Background studies in neutrinoless double beta decay and dark matter searches

Pia Loaiza

université PARIS-SACLAY

Background studies in neutrino double beta decay and dark matter searches

Habilitation à diriger des recherches de l'Université Paris-Saclay

présentée et soutenue à Paris-Saclay, le 20 mars 2024, par

Pía Loaiza

Habilitation à diriger des recherches

Composition du jury

Sara Bolognesi	Rapporteur & Examinateur
Vitaly Kudryavtsev	Rapporteur & Examinateur
Stefan Schönert	Rapporteur & Examinateur
Sophie Henrot-Versillé	Examinateur
Monica Sisti	Examinateur

Contents

Chapter 1

Neutrinoless double beta decay and dark matter

Break on through (to the other side)

The Doors

Starting in the 1980's, there is a rapid growth of direct dark matter and neutrinoless double beta decay experiments with an increasing number of experimental techniques. In both searches the hypothetical signals are expected to happen at very low rates, if ever to happen at all, competing with the background counts populating the region of interest. My work has been dedicated to reducing and understanding the backgrounds in neutrinoless double beta decay ($0\nu\beta\beta$) and dark matter searches.

Long before the 80's, in 1948 Fireman [1] measured the decay of ^{124}Sn with the aim to detect the double beta decay without or with neutrino emission. He measured some electrons and interpreted the effect as the $0\nu\beta\beta$ decay of ^{124}Sn, with a half-life between $4 - 9 \times 10^{15}$ years. Some years later, in 1952 Fireman and Schwarzer [2] re-investigated the decay and made a new measurement, cautiously interpreting the 3 electrons detected as having a different origin than double beta decay, and gave a lower limit for the half life of the double beta decay process of 10^{17} years, one order of magnitude higher than the previous measurement. They concluded that *the previous result may have been caused by a small trace of an impurity having a coincidence activity in the enriched sample.* We can thus appreciate in these pioneer experiments the predominant role of understanding and controlling the background in neutrinoless double beta decay searches. Later in 1966 E. Der Mateosian and M. Goldhaber performed an experiment featuring for the first time the "source equals detector" approach in which the detector contains the target nuclei [3]. They studied the $0\nu\beta\beta$ decay of ^{48}Ca using CaF_2 as a scintillating crystal. They observed a peak in the spectrum of a first enriched crystal and interpreted it as an impurity : *An impurity of 1 part per million of uranium would be sufficient to give the observed peak in channel 100, and a suitable mixture of thorium and uranium impurities could account for the main features of the spectrum observed* [3]. They sent the ^{48}Ca back to Oak Ridge for purification and a second crystal was grown. They finally placed a lower limit of 2×10^{20} yr on the $0\nu\beta\beta$ decay. The determination of the half-life $2\nu\beta\beta$ was still complicated by impurities in the ^{48}Ca and they could establish a lower limit of 5×10^{18} years for the $2\nu\beta\beta$ mode. We had to wait another 20 years for the rapid growth of direct double beta decay experiments. At that time, the double beta community fully realized the importance of low background in $0\nu\beta\beta$

searches in laboratories.

My work in the neutrinoless double beta decay field started with the SuperNEMO demonstrator, a tracking-calorimeter technique in which the $0\nu\beta\beta$ source and detectors are separated. The baseline $0\nu\beta\beta$ isotope is ^{82}Se. One of the main sources of background for SuperNEMO is a possible contamination of ^{208}Tl and ^{214}Bi in the $0\nu\beta\beta$ source foils. I have worked on the radiopurity of the foils and in particular I was in charge of the BiPo-3 detector, a new generation low radioactivity detector developed in the framework of the SuperNEMO program.

I moved then to the CUPID-Mo and CUPID experiments, based on bolometers, a realization of the calorimetric approach in which the source is embedded in the detector. Both experiments exploit the scintillating bolometer technology based on lithium molybdate ($Li_2{}^{100}MoO_4$) with simultaneous readout of heat and light, and ^{100}Mo as double beta isotope. I started working on CUPID-Mo at the moment of the construction of the experiment, which was built as a demonstrator for a next generation bolometric experiment, CUPID. Later on, CUPID-Mo was in operation between 2019- 2020. I have developed, together with my PhD and my master student, a background model describing the features of the CUPID-Mo experimental data. I am currently dedicated to CUPID where I am in charge of the background studies group.

On the dark matter field A. Drukier and L. Stodolsky proposed in 1983 the initial idea of a neutral-current detector for the detection of neutrinos exploiting elastic neutral-current scattering of nuclei [4]. Two years later in 1985, Goodman and Witten [5] proposed that Drukier and Stodolsky's idea could be used to detect dark matter from galactic halos. Drukier and Stodolsky initial idea was a detector that consists of superconducting grains of a few microns radius placed in a magnetic field, maintained just below their superconducting-to-normal transition boundary. The energy deposit in a granule makes it become normal conducting, and the penetration of the magnetic field leads to a flux change detected by a pick-up coil. My PhD thesis was devoted to such a dark matter experiment, ORPHEUS. Ideally, the active background rejection was based on the fact that a dark matter particle would cause the transition of a single granule, while γ's or muons would induce the transition of multiple grains. But in practice background particles induced single flips and the technique was limited by the overwhelming background, limiting its sensitivity [6].

The first experiment to place constrains on the scattering of WIMPs with nuclei was conducted by Ahlen, Avignone, Brodzinsky, Drukier, Gelmini and Spergel in 1987 [7] using a Ge spectrometer. In their work, entitled *Limits on cold dark matter candidates from an ultralow background germanium spectrometer*, the dominant role of the low background that will characterize all future searches, is anticipated in the title.

My work in the dark matter field after my PhD was pursued in the EDELWEISS dark matter experiment, which used germanium bolometers with dual read out of heat and ionization. Here I have participated in the construction of EDELWEISS-III, where I was in charge of the low radioactivity group and I have developed a background model for the gamma events.

In this chapter section 1 gives a theoretical introduction to the Majorana neutrino and neutrinoless double beta decay, section 2 provides some elements on the formalism of the two neutrino double beta decay, section 3 refers to the experimental signature of $0\nu\beta\beta$ decay, section 4 describes non-exhaustively current and future $0\nu\beta\beta$ experiments. Finally section 5 introduces briefly direct dark matter searches.

1.1 Neutrinoless double beta decay

Though it has been known for more than twenty years that neutrinos have mass, they are assumed to be massless in the Standard Model (SM) of particle physics. The simplest way to extend the Standard Model is the generation of neutrino masses via a Majorana mass term and to allow lepton number violation [8, 9]. Neutrinos, as the only neutral fermions, can get their masses either by Dirac or Majorana terms, while for charged fermions the conservation of the electric charge allows only Dirac type mass terms. The possible Majorana nature of the neutrino is an open fundamental question in particle physics.

Starting with the general Dirac equation for any fermion of spin 1/2, we can write the 4-component field Ψ in terms of two 2-component objects [10]:

$$\Psi = \begin{pmatrix} \Psi_L \\ 0 \\ \Psi_R \\ 0 \end{pmatrix} \tag{1.1}$$

to obtain the coupled equations [10]:

$$i\gamma^\mu \partial_\mu \Psi_L = m\Psi_R \tag{1.2}$$

$$i\gamma^\mu \partial_\mu \Psi_R = m\Psi_L. \tag{1.3}$$

where γ^μ are the contravariant Dirac gamma matrices. Majorana proposed that the right-handed component of a massive neutral spin-1/2 field can be just the C conjugate of its left-handed component: $\Psi_R = (\Psi_L)^c$. Generally speaking, the operator $\hat{C}$ changes a particle by its antiparticle, with the charge conjugate field given by: $\Psi^C = \mathrm{C}\ \overline{\Psi}^T$ where C is the charge conjugation matrix and T denotes the transpose. Acting on a chiral field $\hat{C}$ flips its chirality: $(\Psi_L)^c = (\Psi^c)_R$ and $(\Psi_R)^c = (\Psi^c)_L$ [10].

Coming back to the Majorana condition, we can write now the last term in the equality $\Psi_R = (\Psi_L)^c = (\Psi^c)_R$. Thus, it follows that

$$\Psi^c = \Psi \tag{1.4}$$

meaning that Majorana particles are their own antiparticles.

Neutrinoless double beta decay is a very rare hypothetical nuclear process, which, if observed, would demonstrate the Majorana nature of the neutrino, fix the absolute neutrino mass scale and provide valuable information on the neutrino mass ordering. The existence of a Majorana neutrino would also have crucial consequences in cosmology, as it could explain the baryon asymmetry (prevalence of matter over antimatter in the Universe) through leptogenesis [11]. In neutrinoless double beta decay an even-even nucleus decays into a lighter one with the emission of two electrons carrying the discrete energy of the Q-value of the reaction: (A,Z) $\rightarrow$ (A,Z+2) + $2e^-$. (Explicitely, the Q-value or $Q_{\beta\beta}$ = (m(A,Z) - m(A, Z+2) - $2m_e$)c^2).

Neutrinoless double beta decay may be induced by a number of mechanisms beyond the SM. Considering all possible decay channels i, the decay rate of $0\nu\beta\beta$, $\Gamma_{0\nu}$, would relate to new physcis parameters η_i by [8]:

$$\Gamma_{0\nu} = \ln 2 \sum_i G_i \cdot g_i^4 \cdot |M_{0\nu,i}|^2 \cdot \eta_i + \text{interference terms}. \tag{1.5}$$

Here G_i is the phase-space factor relating to the kinematics of the decay, g_i is the hadronic matrix element and $|M_{0\nu,i}|$ the nuclear matrix element. Fig 1.1, left shows the Feynman diagram of a $0\nu\beta\beta$ decay through a blackbox representing the variety of operators which can contribute to the decay.

The most general mass term for the neutrino has the form [12]

$$\mathcal{L}_m = -\frac{1}{2}\left(\left(\overline{\Psi_L}\right)^C \overline{\Psi}_R\right) \mathbb{M} \begin{pmatrix} \Psi_L \\ \Psi_R^C \end{pmatrix} + hc \tag{1.6}$$

Equivalently, if $\Psi^T = (\Psi_L, \Psi_R^C)$ we can write eq 1.6 [8]

$$\mathcal{L}_m = -\frac{1}{2}\overline{\Psi}\mathbb{M}\Psi^C + h.c \tag{1.7}$$

where $\mathbb{M}$ is the mass matrix (in the general case $\mathbb{M} = \mathbb{U}$ diag(m_1, m_2, m_3, ..., m_n) $\mathbb{U}^T$, and m_i are the masses of the neutrinos [8]).

Recall that (ν_e, ν_μ, ν_τ) are not eigenstates of the mass and that, similarly to the quarks, they are a linear combination of the mass eigenstates ν_i, with $i = 1, 2, 3$, through U, a unitary matrix called Pontecorvo-Maki-Nakagawa-Sakata (PMNS) :

$$\begin{pmatrix} \nu_e \\ \nu_\mu \\ \nu_\tau \end{pmatrix} = \begin{pmatrix} c_{12}c_{13} & s_{12}c_{13} & s_{13}e^{-i\delta_{CP}} \\ -s_{12}c_{23} - c_{12}s_{23}s_{13}e^{i\delta_{CP}} & c_{12}c_{23} - s_{12}s_{23}s_{13}e^{i\delta_{CP}} & s_{23}c_{13} \\ s_{12}s_{23} - c_{12}c_{23}s_{13}e^{i\delta_{CP}} & -c_{12}s_{23} - s_{12}c_{23}s_{13}e^{i\delta_{CP}} & c_{23}c_{13} \end{pmatrix} \begin{pmatrix} \nu_1 \\ \nu_2 \\ \nu_3 \end{pmatrix}, \tag{1.8}$$

where $c_{ij} = \cos\theta_{ij}$, and $s_{ij} = \sin\theta_{ij}$, with θ_{12}, θ_{13}, θ_{23} the mixing angles, and δ_{CP} the Dirac phase of CP violation. Today a large number of neutrino oscillation experiments, with a variety of techniques, obtained precision measurements of the mixing angles and of the neutrino squared-mass difference m_2^2 - m_1^2 [13]. However the CP violating phase and the sign of m_3^2 - m_1^2, the so-called Mass Ordering, remain unknown [14, 15].

Each neutrino flavor eigenstate is thus a linear combination of the mass eigenstates:

$$|\nu_\alpha\rangle = \sum_{i=1}^{3} U_{\alpha i}^* |\nu_i\rangle , \tag{1.9}$$

If neutrinos are Majorana one has to add supplementary phases of CP violation in the lepton sector, called Majorana phases, ϕ, that cannot be proved by oscillation experiments:

$$|\nu_\alpha\rangle = \sum_{i=1}^{3} U_{\alpha i}^* e^{i\phi_i} |\nu_i\rangle , \tag{1.10}$$

In the case when $0\nu\beta\beta$ is mediated by a light neutrino, Fig1.1 center, the neutrino propagator can be any mass eigenstate therefore the amplitude of the process should be written as a sum over i as shown in Fig.1.1 right, in particular it must be proportional to the electron-electron entry. The modulus is usually called Majorana mass :

$$m_{\beta\beta} = \left| \sum_{i=1}^{3} \left|U_{ei}^2\right| e^{i\phi_i} m_i \right| , \tag{1.11}$$

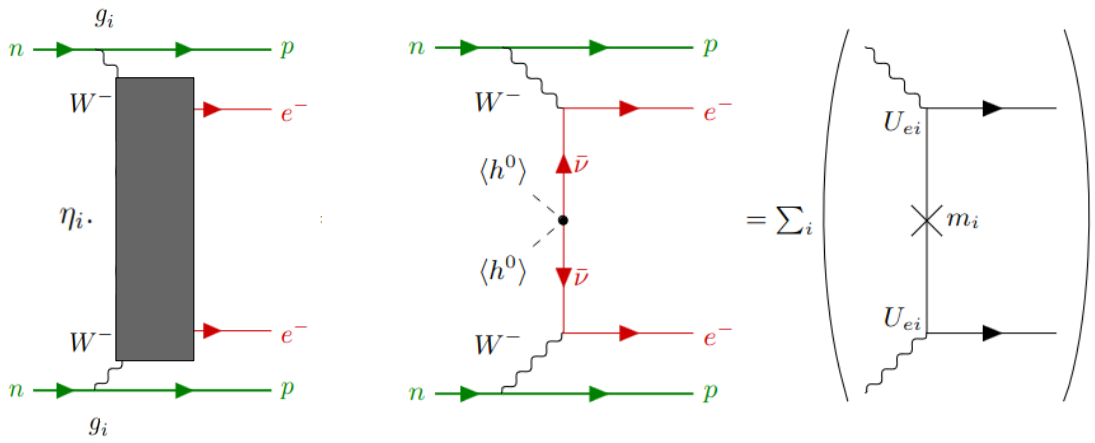

Figure 1.1: Left: Feynman diagram for $0\nu\beta\beta$ where the decay mechanism is visualized as black box with some parameter η_i. Center: The same diagram with light neutrino exchange model. Right: the decomposition in terms of neutrino mass eigenstates and the PMNS matrix U. Adapted from [8].

From eq.1.8 this is:

$$m_{\beta\beta} = \left|\cos^2\theta_{12}\cos^2\theta_{13}m_1 + \sin^2\theta_{12}\cos^2\theta_{13}e^{i\phi_2}m_2 + \sin^2\theta_{13}e^{-2i\delta_{CP}}e^{i\phi_3}m_3\right|. \tag{1.12}$$

Thus in this model the decay rate of $0\nu\beta\beta$ is written as

$$\left(T^{0\nu}_{1/2}\right)^{-1} = g_A^4 \cdot G_{0\nu} \cdot |M_{0\nu}|^2 \cdot \langle m_{\beta\beta}\rangle^2/m_e^2, \tag{1.13}$$

Equation 1.13 highlights the complex interplay in double beta decays which are necessary to interpret the observed decay rate in terms of neutrino mass:

- The phase space factors $G_{0\nu}$ represent the kinematic of the disintegration, and depend on the $Q_{\beta\beta}$ = E_f - E_i of the transition. They can be calculated with good accuracy, but still depend on some assumptions (see section 1.1.1).
- $M_{0\nu}$, the nuclear matrix elements (NME) relate to the fact that the disintegration takes place in a nucleus with a certain number of protons and neutrons, and, thus, that we need to consider an N-body problem. These calculations are complicated and differ by about a factor 3 [16].
- g_A is the hadronic matrix element for a pure Gamow-Teller beta decay. It is common to use the value for a bare nucleon, $g_A = 1.27$, however this value could be 'quenched' with respect to that of a free nucleon [17].

In the next subsection I describe briefly these parameters.

1.1.1 Phase space factors, nuclear matrix elements and the 'g_A problem'

The phase space factors $G_{0\nu}$ represent the kinematic of the disintegration, and depend on the $Q_{\beta\beta}$ of the transition. They can be calculated with good accuracy [18]:

$$G_{0\nu}(Q_{\beta\beta}, A) = \frac{\left(G_F\cos\theta_c\right)^4 \cdot m_e^2}{\ln 2 \cdot (2\pi)^5 \cdot R^2} \int_{m_e}^{Q_{\beta\beta}+m_e} p_1\ p_2\ E_1\ E_2\ F(E_1, E_2, R)\ dE_1, \tag{1.14}$$

where p_i and E_i are the momentum and the energy of the electron i respectively, $R = r_0 \cdot A^{1/3}$ ($r_0 = 1.2$ fm), G_F is Fermi's coupling constant and θ_c the Cabibbo angle. F is a function of E_i and R which involves electron wave functions. Two different approximation schemes are considered in the literature: i) a uniform charge distribution in the nucleus and ii) the exact Dirac wave functions with finite nuclear size and electron screening [19]. Fig. 1.2 and Table 1.1 show the phase space factors for several isotopes calculated using the exact solution for the Dirac equation with finite nuclear size and electron screening obtained in [18]. Table 1.1 is also indicating the $Q_{\beta\beta}$ of some $0\nu\beta\beta$ isotopes.

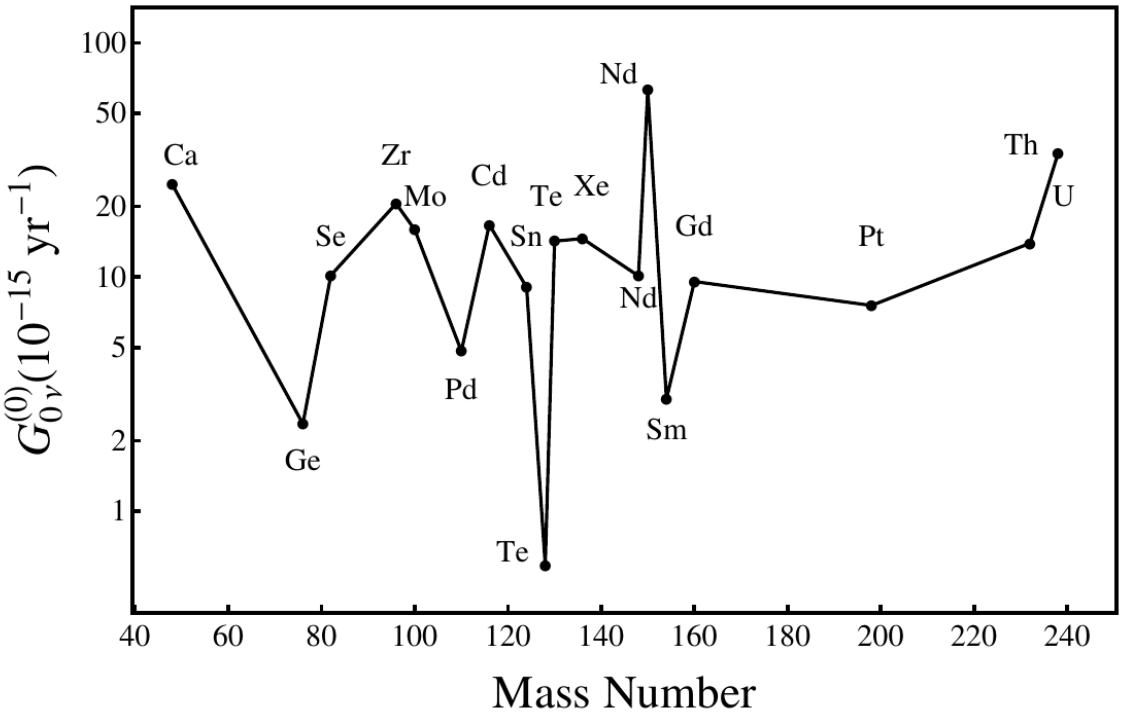

Figure 1.2: Phase space factors calculated in [18].

Nuclear matrix elements are the result of complicated many body calculations. There are several models based on different approximations, each one with advantages and disadvantages which may depend on the nuclei. The nuclear matrix elements calculated by the different nuclear models differ by about a factor 3 [16], shown in Fig. 1.3.

A useful test of the models consists in comparing the predicted theoretical $2\nu\beta\beta$ decay rates with experimental data. The theoretical values are always overestimated with respect to the experiments, in other words, the theoretical product NME $\times$ g_A is too large. This indicates that something is not correct in the theoretical approaches. We may think that the g_A value is smaller than the one for a free nucleon, and we speak about the g_A quenching. The approach that most nuclear models follow today is to use matrix elements that depend on an effective g_A, labelled as g_A^{eff}, which is renormalized in the nuclear medium [20]. Some models then tune g_A^{eff} to match the experimental half life. This approach using $M_{0\nu}(g_A^{eff})$ is also applied to some β decays [21, 17]. On the other hand relatively recent *ab initio* [22] approaches calculated single beta decay Gamow Teller transitions for light nuclei including additional nuclear correlations and found that no quenching is needed. I will come back to the 'g_A' problem in Chapter 5.2.

The theoretical description of the two neutrino double beta decay $2\nu\beta\beta$ is similar to $0\nu\beta\beta$

Isotope	$Q_{\beta\beta}$ [keV]	$G_{0\nu}$ [10^{-15} yr^{-1}] [18]
^{48}Ca	4272.26(404)	24.81
^{76}Ge	2039.061(7)	2.363
^{82}Se	2995.12(201)	10.16
^{96}Zr	3350.37(289)	20.58
^{100}Mo	3034.40(17)	15.92
^{116}Cd	2813.50(13)	16.70
^{130}Te	2526.97(23)	14.22
^{136}Xe	2457.83(37)	14.58
^{150}Nd	3371.38(20)	63.03

Table 1.1: $Q_{\beta\beta}$ values and phase space factors (from [18]).

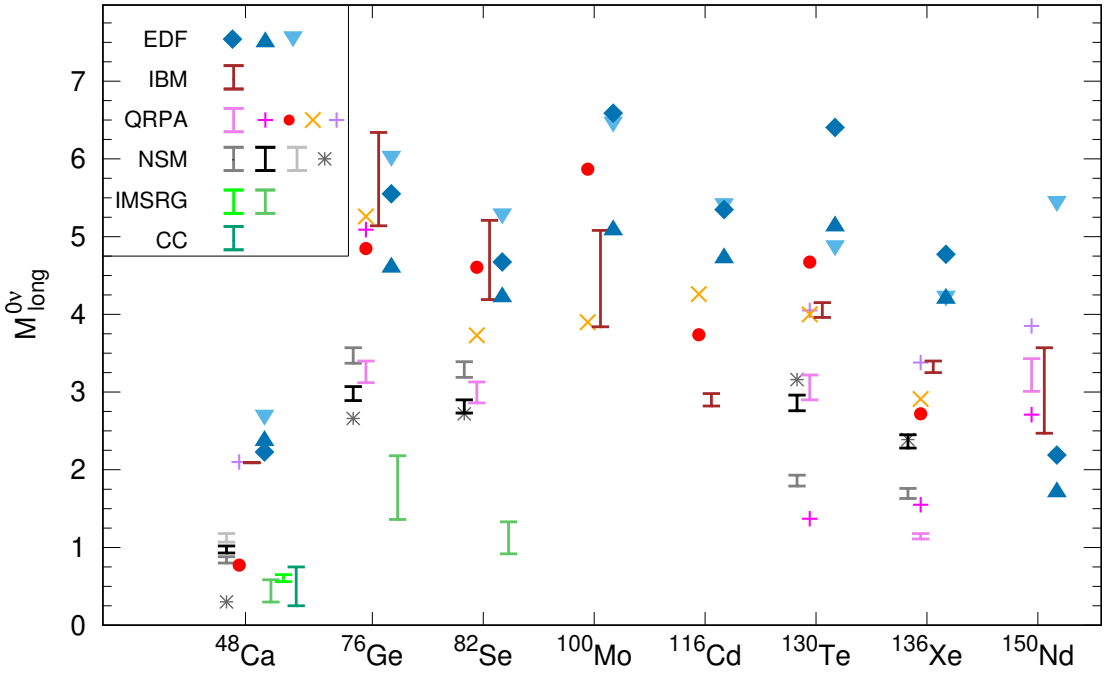

Figure 1.3: Nuclear matrix elements for $0\nu\beta\beta$ decay in the framework of a light neutrino exchange, calculated in several nuclear models. Reproduced from [8].

and probes complementary physics. The $2\nu\beta\beta$ decay, allowed in the standard model, is a test for the theoretical calculations involving many bodies.

1.2 Two neutrino double beta decay

The two neutrino mode is important to understand nuclear structure models and to give inputs for the calculation of $0\nu\beta\beta$ NMEs. Both $2\nu\beta\beta$ and $0\nu\beta\beta$ decays share the same initial and final states but they differ in the momentum transfer, which is much larger for $0\nu\beta\beta$ and thus the decay proceeds through higher energy intermediate states.

It has been observed that nuclear models often predict $2\nu\beta\beta$ decay rates higher than the experiment [17]. To account for this, g_A can be replaced by an effective value g_A^{eff} [21, 23, 24, 25, 26, 27, 28]. The normalized value of g_A with respect to the free nucleon value 1.27 would account for nucleon-nucleon interactions. There is still the possibility that the overpredictions arise from theoretical approximations in the theoretical calculations. The issue of the g_A quenching has significant impact on the interpretation of the $T^{0\nu}_{1/2}$ in terms of effective Majorana mass. Sensitivities for $m_{\beta\beta}$ could be lower than expected for an unrenormalized value of g_A, as currently used in the community. This would have a significant impact on the discovery probability of next generation $0\nu\beta\beta$ experiments. Measurements of the two neutrino mode are necessary to obtain reliable estimates of $0\nu\beta\beta$ NMEs.

The correlation between $0\nu\beta\beta$ NMEs, $M_{0\nu}$, and $2\nu\beta\beta$ NMEs, $M_{2\nu}$, was studied in [29]. Here the authors found a linear correlation between $M_{2\nu}$ and $M_{0\nu}$ NME's both in the pnQRPA and shell models. Fig.1.4 (a) shows $M_{2\nu}/q^2$ vs $A^{-1/6}$ $M_{0\nu}$ for pnQRPA. The normalization by $A^{-1/6}$ is done to remove the mass dependence. The denominator q^2 notes the need to quench the $M_{2\nu}$ values. Within pn-QRPA a g_{pp} parameter, the strength of the particle-particle interaction, is tuned using measurements of the half-life. In other words, the quenching of $M_{2\nu}(g_A^{eff})$ is tuned through the g_{pp} values [19].

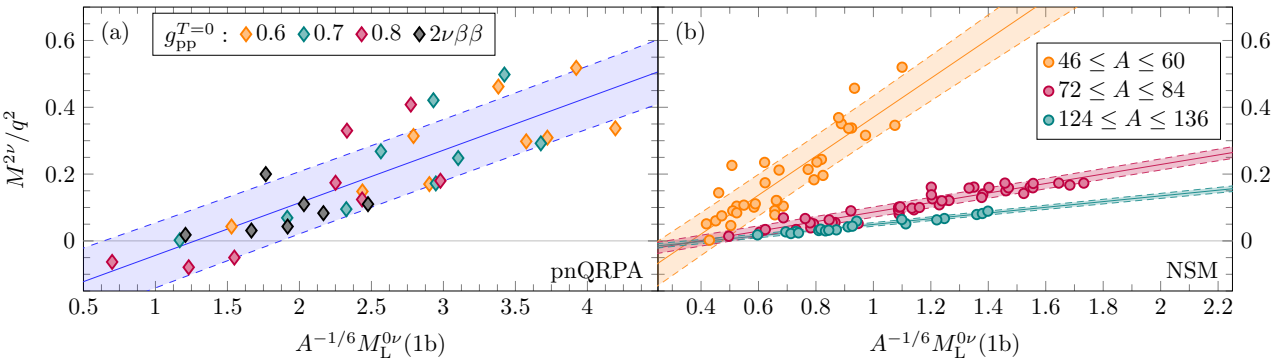

Figure 1.4: $2\nu\beta\beta$ NMEs vs $0\nu\beta\beta$ decay NMEs obtained with (a) pnQRPA with different g_{pp} values (see text) and (b) nuclear shell model (NSM)s for three regions of the nucleon number A. $0\nu\beta\beta$ results are multiplied by $A^{-1/6}$ to remove the mass dependence, and the denominator q^2 notes the need to quench $M_{2\nu}$ values. Solid and dashed lines correspond to linear fits and their 68% CL prediction bands, respectively. Reproduced from [29].

The two neutrino $2\nu\beta\beta$ decay rate can be described with a similar expression as 1.13 :

$$\left(T^{2\nu}_{1/2}\right)^{-1} = G_{2\nu} \cdot |M_{2\nu}|^2 \cdot g_{2\nu}^4. \tag{1.15}$$

However this factorization in a phase space factor times a nuclear matrix element is based on some approximations. In full generality the differential rate of $2\nu\beta\beta$ is given by [19]:

$$\frac{\Gamma}{dE_1 dE_2} \propto F_0(Z,E_1)F_0(Z,E_2)p_1p_2 \int_0^{E_i-E_f-E_1-E_2} E_{\nu_1}^2 E_{\nu_2}^2 A^{2\nu} dE_{\nu_1}, \tag{1.16}$$

where $F_0(Z, E_1)$ is the Fermi function, E_1, E_2, p_1, p_2 are the two electron energies and momenta, E_{ν_2}, E_{ν_1} are the two neutrino energies and E_i, E_f the energies of the initial and final states. $A^{2\nu}$ involves matrix elements which depend on the lepton energies and on the sum over possible states of the intermediate nucleus. In fact, even if the $2\nu\beta\beta$ is the decay of a nucleus (A, Z) to a nucleus (A, Z+2), theoretically one describes the decay through the intermediate nucleus (A, Z+1). As an example, for the decay of ^{100}Mo to ^{100}Ru, the intermediate state nucleus ^{100}Tc is considered, as shown in Fig 1.5.

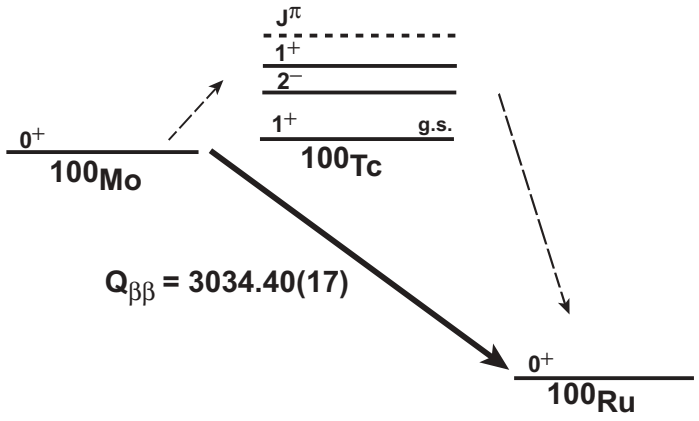

Figure 1.5: Sketch of the decay of ^{100}Mo to ^{100}Ru via the intermediate states of ^{100}Tc.

To understand how the decay rate in eq. 1.16 may be factorized, let's start with the expression for $A^{2\nu}$:

$$A^{2\nu} = \frac{1}{4}|M^K_{GT} + M^L_{GT}|^2 + \frac{1}{12}|M^K_{GT} - M^L_{GT}|^2. \tag{1.17}$$

Here $M^{K,L}_{GT}$ are the Gamow Teller matrix elements given by:

$$M^{K,L}_{GT} = m_e \sum_n \left\langle 0^+_F \right| |\tau^+_m \vec{\sigma_m}| \left|1^+_n\right\rangle | \left\langle 1^+_n \right| |\tau^+_m \vec{\sigma_m}| \left|0^+_I\right\rangle \frac{C_n}{C_n^2 - \epsilon^2_{K,L}}, \tag{1.18}$$

where the sum goes over all possible states of the intermediate nucleus. $\left\langle 0^+_F\right|$ is the state of the final nucleus, $|1^+_n\rangle$ are all possible states of the intermediate nucleus and $\left|0^+_I\right\rangle$ is the state of the initial nucleus. $\vec{\sigma}$ are the Pauli matrices and τ^+ the isospin matrix, $C_n = E_n - (E_i + E_f)/2$. The lepton energies are taken into account in the matrix elements in the terms:

$$\epsilon_K = (E_2 + E_{\nu_2} - E_1 - E_{\nu_1})/2, \tag{1.19}$$

$$\epsilon_L = (E_1 + E_{\nu_2} - E_2 - E_{\nu_1})/2. \tag{1.20}$$

The dependence of the Gamow Teller matrix $M^{K,L}_{GT}$ is a problem because it is not possible to factorize the decay rate into the product of a phase space factor and a matrix element. However, the simplification is possible under the Higher State Dominance (HSD) and the Single State Dominance (SSD) hypothesis.

In the HSD hypothesis we neglect the lepton energies, $\epsilon_{K,L}$, which is possible if the energies of the intermediate states are much higher than the lepton energies. In this case eq.1.18 becomes:

$$M_{GT}^{K,L} = M_{GT}^{2\nu} = m_e \sum_n \left\langle 0_F^+ \right| |\tau_m^+ \vec{\sigma_m}| \left| 1_n^+ \right\rangle | \left\langle 1_n^+ \right| |\tau_m^+ \vec{\sigma_m}| \left| 0_I^+ \right\rangle \frac{1}{C_n}, \tag{1.21}$$

which does not depend on the lepton energies and can be taken out of the integral in eq. 1.16:

$$\frac{\Gamma}{dE_1 dE_2} \propto \overbrace{|M_{GT}^{2\nu}|^2}^{\text{matrix element}} \underbrace{F_0(Z,E_1)F_0(Z,E_2)p_1p_2 \int_0^{E_i-E_f-E_1-E_2} E_{\nu_1}^2 E_{\nu_2}^2 dE_{\nu_1}}_{\text{phase space}}. \tag{1.22}$$

There is still left to evaluate the sum over the intermediate states in $M_{GT}^{2\nu}$, which the nuclear models are not able to calculate. To be able to do this, we replace the energy of the states of the intermediate nucleus with the value for a single, average energy $\bar{E_n}$, known as the *closure energy approximation*. We can thus write:

$$M_{GT-cl} = \frac{\left\langle 0_F^+ \right| |\tau_m^+ \vec{\sigma_m}| \left| 0_I^+ \right\rangle}{\bar{E_n} - (E_i + E_f)/2} \tag{1.23}$$

In the SSD hypothesis we assume the decay proceeds through the lowest 1^+ state of the intermediate states. The matrix elements expression in eq.1.18 becomes:

$$M_{GT}^{K,L} = m_e \left\langle 0_F^+ \right| |\tau_m^+ \vec{\sigma_m}| \left| 1_n^+ \right\rangle | \left\langle 1_n^+ \right| |\tau_m^+ \vec{\sigma_m}| \left| 0_I^+ \right\rangle \frac{C_1}{C_1^2 - \epsilon_{K,L}^2}, \tag{1.24}$$

and the numerator can be taken out of the integral in the expression of the decay rate 1.16. This allows to factorize a nuclear matrix element and the phase space factor separately. This latter includes the evaluation of the integral. The denominator in eq 1.24, involving the lepton energies, still needs to be computed inside this integral. The information on the shape of the $2\nu\beta\beta$ spectrum enters in the phase space factor. The choice of one of the two hypothesis has an impact on spectral shape studies and may affect the experimental values obtained for $2\nu\beta\beta$ half life. An improved formalism attempting a more accurate description of the $2\nu\beta\beta$ decay has been developed recently [19]. We will come back to this improved model in section 5.2.

1.3 $0\nu\beta\beta$ decay experimental signatures

In order to observe $0\nu\beta\beta$ decay, experimentalists aim at the detection of the two emitted electrons, which share the total transition energy corresponding to the $Q_{\beta\beta}$ of the process. The minimal signature of $0\nu\beta\beta$ is therefore a peak at the $Q_{\beta\beta}$ in the sum energy spectrum of the two electrons, enlarged by the detector energy resolution and competing with the background counts populating the region of interest (ROI). Fig. 1.6 shows the expected $0\nu\beta\beta$ signal. Energy resolution is important since the peak signal must be discriminated over the background and therefore it is an asset if it is as narrow as possible. The desirable features of an experimental technology adapted to $0\nu\beta\beta$ search are: high number of investigated nuclei (large mass source and high efficiency); high energy resolution; optimal choice of the $0\nu\beta\beta$ candidate, which should have a $Q_{\beta\beta}$ as high as possible to decrease the background and increase the decay probability, and very low background.

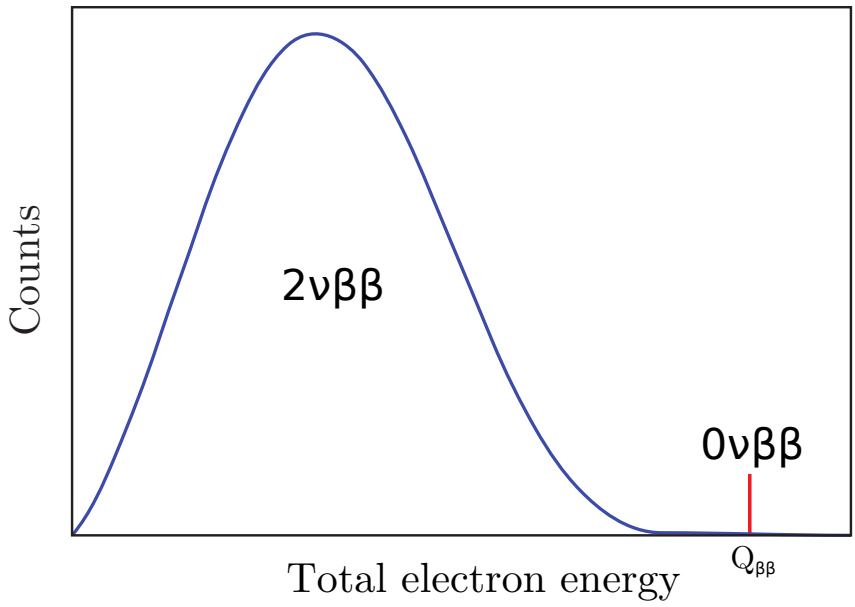

Figure 1.6: Schema of the experimental signal in double beta searches. The $2\nu\beta\beta$ decay produces a continuum spectrum of the sum energy of the two electrons. The $0\nu\beta\beta$ experimental signature would be a peak at the energy of the decay, or the difference in mass between the parent and the daughter nucleus, coinciding with the endpoint of the $2\nu\beta\beta$ spectrum.

The backgrounds can be reduced either by passive or active technologies. Passive techniques aim at reducing the particles that may produce events in the $0\nu\beta\beta$ energy region, through shielding and material selection. Active techniques rely on discrimination capabilities specific to each experimental approach, including reconstruction of event topology, discrimination by pulse shape analysis, combination of two experimental quantities (e.g heat and scintillation).

1.4 $0\nu\beta\beta$ experiments

Neutrinoless double beta decay projects can be broadly classified into two categories: experiments using a fluid-embedded $0\nu\beta\beta$ source (featuring large sensitive masses and easy scalability) and experiments using a crystal-embedded $0\nu\beta\beta$ source (featuring high energy resolution and efficiency). In the first class we have Xe-based TPC projects like nEXO [30] (evolution of the closed EXO-200), NEXT [31, 32, 33] (evolution of NEXT-100), and Panda-X-III [34]. This also includes experiments which dissolve the source in a large liquid-scintillator matrix exploiting existing infrastructures like KamLAND2-Zen [35, 36, 37] (evolution of the current KamLAND-Zen-800) and SNO+phase-II [38] (evolution of the imminent SNO+phase-I). In the second class we have experiments based on germanium diodes: LEGEND-1000 [39] (evolution of the current LEGEND-200) and those which exploit the bolometric technique: CUPID. The most prominent projects in this rich scenario are LEGEND-1000, nEXO, and CUPID, which have a 3σ discovery sensitivity that, at least for some matrix element calculations, reaches below 20 meV for $m_{\beta\beta}$ (see Fig.1.7). In what follows I will briefly describe each of these techniques with some emphasis on the background sources. For the comparison of the background levels I will use a parameter introduced in [8], the *sensitive background* $\mathcal{B}$. This parameter describes the number

of events in the ROI after all selection cuts, normalized by the product of : number of moles of isotope, livetime and signal detection efficiency.

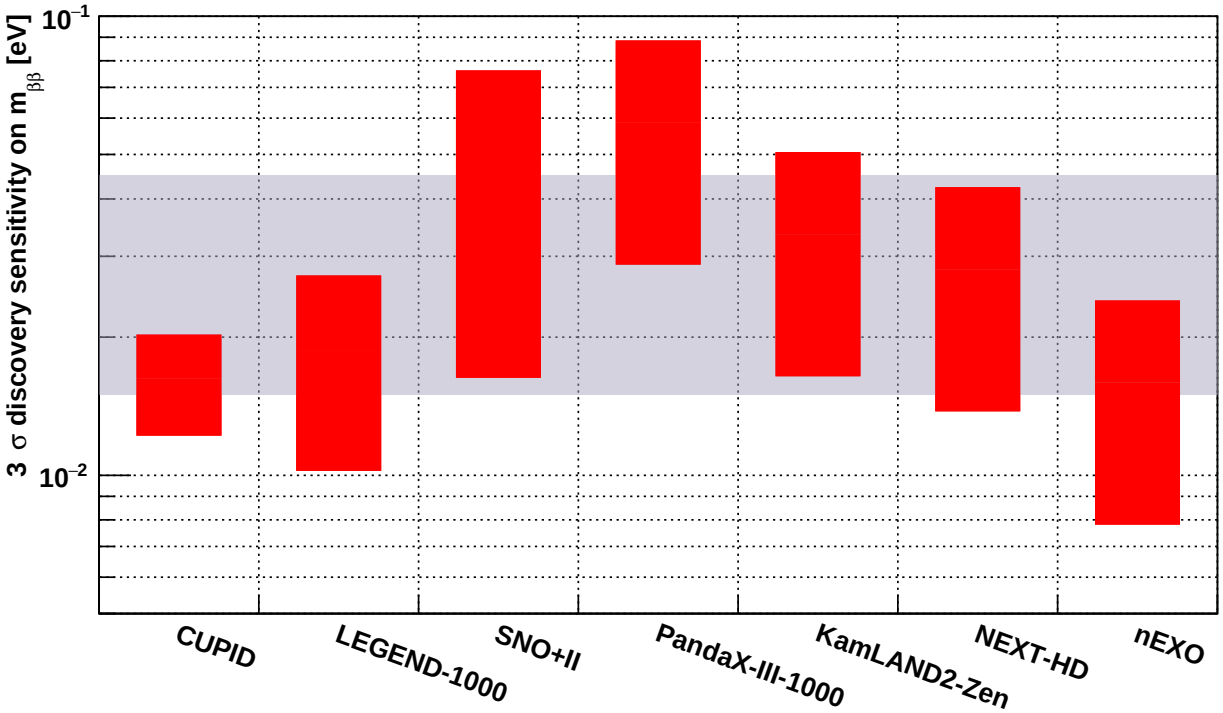

Figure 1.7: Discovery sensitivity for a selected set of next-generation ton-scale experiments at a time scale of 10 years from now. The grey shaded region corresponds to the parameter region allowed in the Inverted Hierarchy of the neutrino mass. The red error bars show the $m_{\beta\beta}$ values such that an experiment can make at least a 3σ discovery within the range of the nuclear matrix elements for a given isotope. Parameters from experiments other than CUPID taken from [40, 41, 42]. From [43].

1.4.1 Liquid scintillators: large sensivitive masses

The experimental technique in KamLand-Zen and SNO+ relies on loading of the double-beta isotope into a liquid scintillator. The organic liquid scintillator gets excited when a particle interacts and fluorescence light is emitted when the molecules of the scintillator de-excite. The amount of fluorescence light is used to measure the energy deposited. Other information, as timing, position and particle identification can be also obtained under some conditions. The big advantage of the technique is the possibility to have large mass of double beta isotope (700 kg for the present KamLand-Zen 800 [36]). Another advantage is that organic scintillators are intrinsically radiopure, with levels of U, Th or K of $\mathcal{O}(10^{-17}$ g/g) [38, 36]. These detectors have the possibility to use the liquid scintillator as self-shielding, thus considerably reducing the background. On the other hand, the main drawback is a modest energy resolution. The photons emitted by the scintillator are detected by PMTs. Typically an organic liquid scintillator emits $\sim$ 10000 photons/MeV of energy deposited, though not all the photons are detected by the PMTs.

KamLand-Zen

KamLand-Zen-800 is looking for $0\nu\beta\beta$ decay of ^{136}Xe. It is presently running and has set a limit for the $0\nu\beta\beta$ decay half-life of 2.3 $\times$ 10^{26} years, 90% CL corresponding to $m_{\beta\beta} <$ 36 - 156 meV [36], the most stringent limit at present on the effective neutrino mass. The energy resolution at $Q_{\beta\beta}$ is $\sigma/E = 4.5\%$ [36]. The main identified backgrounds are the $2\nu\beta\beta$ of ^{136}Xe, getting into the $0\nu\beta\beta$ region due to the poor energy resolution, and the Xe spallation products [36]. From the published number of events in the fiducial region we can extract a background index 2. $\times$ 10^{-4} events/(keV kg yr) which can be translated in terms of a sensitive background $\mathcal{B} = 1.4 \times 10^{-3}$ events/(mol yr) [8]. The future evolution KamLand2-Zen will contain 1 ton of ^{136}Xe and an improved energy resolution of $\sim 2\%$ at $Q_{\beta\beta}$ [37] thanks to a liquid scintillator with higher light yield, PMTs with higher quantum efficiency and more radiopure liquid scintillator. The collaboration does not indicate an estimated background but gives a projected sensitivity of $\sim$ 20 meV for $m_{\beta\beta}$. An effective background of $\mathcal{B} = 3 \times 10^{-4}$ events/(mol yr) reproduces the expected sensitivity [8].

SNO+

SNO+ will use much of the original SNO infrastructure and will operate in three phases [38]. The first phase was the "water phase" in which the SNO+ detector was filled with light water. The experiment is currently operating the second phase, the "scintillator phase", with the inner detector volume replaced with 780 tonnes of organic liquid scintillator. Fig. 1.8 shows the spherical acrylic vessel containing the scintillator. For the third operation phase or "tellurium phase", the scintillator will be loaded with 3.9 tonnes of natural tellurium, corresponding to 1.3 tonnes of ^{130}Te [44]. The expected energy resolution at $Q_{\beta\beta}$ is $\sigma/E = 4.5$ % [44]. The main background are the solar neutrinos from ^{8}B undergoing elastic scattering with an electron in the detector. From the published total number of expected events per year [44] and a fiducial volume equal to 20% of the total, we can derive the expected background 1 $\times$ 10^{-4} counts/(keV·kg·yr) The projected sensitive background is $\mathcal{B} = 7.8 \times 10^{-3}$ events/(mol yr) [8].

SNO+I is expected to be followed by SNO+II by increasing the Te loading to reach a mass of ^{130}Te of 6.6 tons. The predicted background corresponds to 5.7 $\times$ 10^{-3} events/(mol yr) [8].

1.4.2 Xe based TPC: large masses and topology reconstruction capabilities

In these detectors an electric field is applied to the volume containing liquid or gaseous Xe. When a particle interacts in the volume, the electrons and ions produced by ionization are drifted to the end of the TPC where the charges are collected. The time of the drift provides information on the position of the event. The interaction of particles in Xe is followed by the emission of scintillation light. As with the liquid scintillators, liquid Xe based TPCs have the advantage that they feature large masses. They use part of their detectors as self-shielding to reduce the backgrounds. In these detectors, the energy resolutions are better than those of the liquid scintillators, but they are still not as good as the Ge detectors or the bolometers.

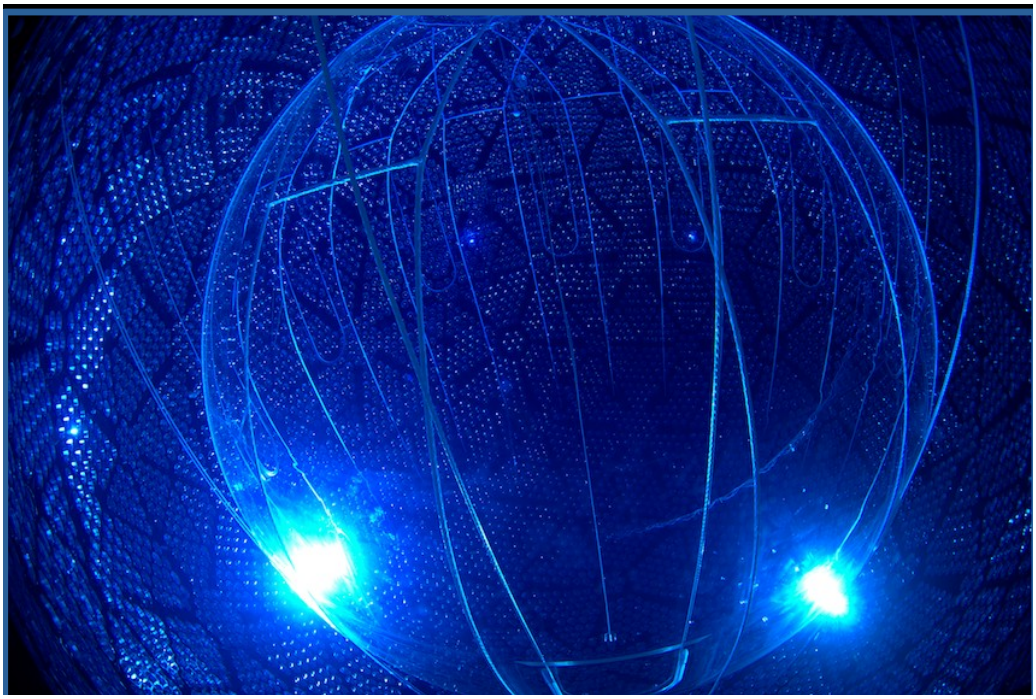

Figure 1.8: The SNO+ detector showing the acrilic vessel filled with scintillator, reproduced from [45]

nEXO

nEXO will use liquid Xe and it will read simultaneously the ionization and the scintillation signals. The energy measurement uses the anticorrelation between scintillation and ionization signals, improving the energy resolution [30]. The nEXO detector will use 5000 kg of Xe enriched at 90% in ^{136}Xe. The energy resolution derived from simulations is $\sigma/E \sim 0.8$ % [30]. In their current model the largest background contribution is from ^{222}Rn, with 50% of the total budget. Specifically ^{214}Bi following a ^{222}Rn decay on the cathode leads to $\sim$ 30 % of the total budget [30]. The collaboration does not give a value for the background index, the published discovery sensitivity is $T_{1/2} = 7.4 \cdot 10^{27}$ yr after 10 years of livetime. The effective background index that reproduces nEXO's published discovery sensitivity, taken from [8] is $\mathcal{B} = 4 \times 10^{-5}$ events/(mol yr).

NEXT

The NEXT detector is a single phase high pressure gas TPC [31]. It exploits the fact that when the electric field is strong enough the collision between the drifting electrons and the gas molecules produce secondary scintillation light, called electroluminiscence. The EL signal largely improves the energy resolution as its intensity is proportional to the number of ionization electrons and it is used for track reconstruction. The previous phase of the NEXT detector, NEXT-White contained an active mass of 5 kg of Xenon. NEXT-White measured an energy resolution at $Q_{\beta\beta}$ of $\sigma/E = 0.5\%$ [32] and it has shown the capability of the technique to discriminate between single electron and double electron tracks, Fig. 1.9. The next phase, NEXT-100, containing 100 kg of Xenon, is under construction. The evolution at the ton-scale, NEXT-1t features a detector with 1109 kg of ^{136}Xe. The most important change is the replacement of the photomultipliers which measure the event energy, going from standard PMTs

to SiPMTs. This will reduce the complexity and will reduce the radioactive background due to the PMTs. The other difference in the design is the change from an asymmetric configuration to a symmetric one. This will ease the requirements on gas purity and high voltage [32]. The dominant source of background are the gamma's from ^{208}Tl and ^{214}Bi which produce single electron tracks by bremsstrahlung or Compton scatterings. The total predicted background is 4×10^{-5} cts/(ROI kg y) largely dominated by the singe electron tracks from gammas in the inner shielding [32].

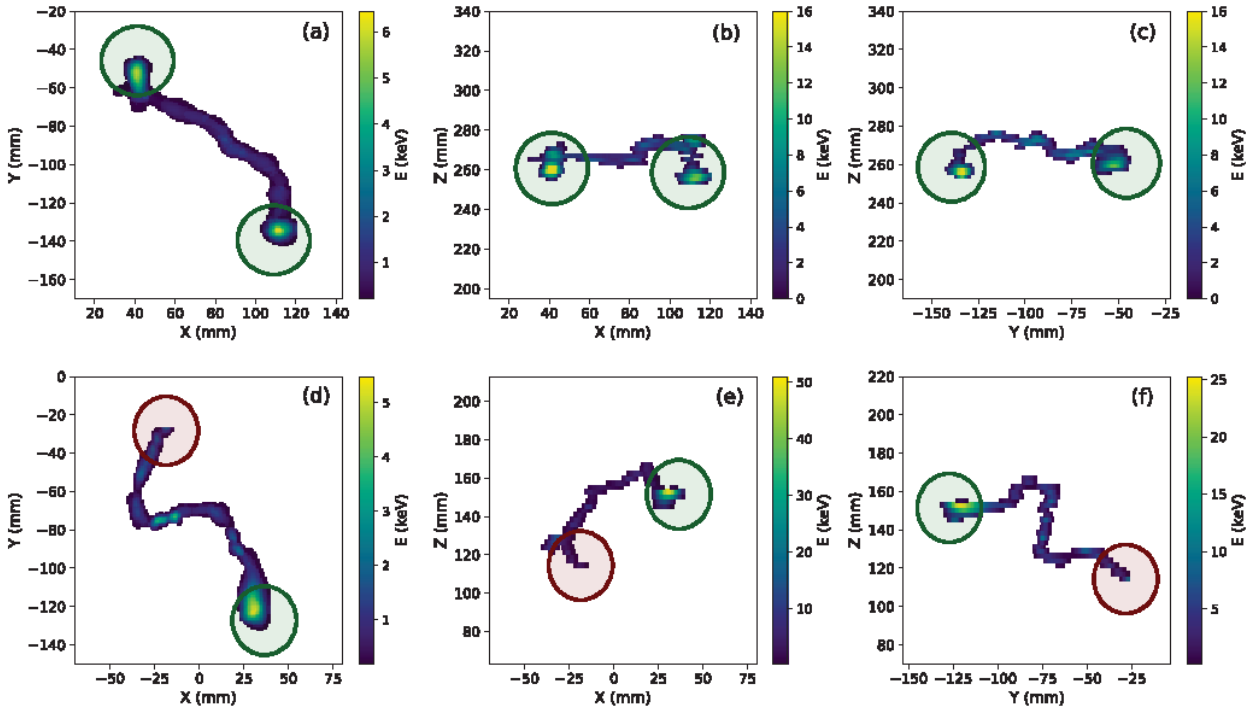

Figure 1.9: Reconstructed events in NEXT-White. The upper pannels are the XY, XZ and YZ projections of a double beta decay event. The lower pannels are the projections of a single-electron track of 1.7 MeV. The circles mark the energy integration region, defined as blobs. Two Bragg peaks are present in the $\beta\beta$ candidate and only one is observed in the single electron track. Reproduced from [46]

.

1.4.3 Ge detectors: high energy resolution

Germanium detectors enriched in ^{76}Ge have been developed over more than $\sim$ 30 years [47, 48, 49]. These experiments employ High Purity Germanium (HPGe) crystals, which are semiconductor detectors. When electrons interact in the detector, electron-hole pairs are produced which are then drifted along an electric field, inducing a current. The integral of the signal is proportional to the energy deposited and its shape depends on the event topology. This technique provides excellent energy resolution. The average energy resolution achieved in GERDA was $\sigma = 1.4$ keV [49] or equivalently $\sigma/E = 0.07\%$. The event topology, for example the number of interaction vertexes or the position of the interaction, can be used to significantly reduce the background. A significant improvement of this technique was obtained by GERDA by immersing the Ge detectors into a liquid argon veto. Scintillation light from interactions in the argon can be readout significantly reducing the backgrounds. The background index achieved

in GERDA was 5×10^{-4} counts/(keV·kg·yr) corresponding to $\mathcal{B} = 4\times 10^{-3}$ events/(mol yr) [49], presently the lowest sensitive background in the field. The final result of GERDA is a constraint on the $0\nu\beta\beta$ decay half-life of 1.8×10^{26} years, 90% CL corresponding to $m_{\beta\beta} < 79$ - 180 meV.

The MAJORANA demonstrator also employs HPGe crystals. MAJORANA is employing electroformed copper and very low radioactivty front-end electronic boards very close to the detectors. They obtained an excellent energy resolution of $\sigma/E = 0.05\%$ ($\sigma = 1.1$ keV) at $Q_{\beta\beta}$, the best of any $0\nu\beta\beta$ experiment.

LEGEND

The GERDA and MAJORANA collaborations are developing the next generation Ge based detectors in the framework of the LEGEND project, which will be developed in two stages, the current LEGEND-200 and the ton scale LEGEND-1000. LEGEND will combine the best elements of GERDA and MAJORANA, it will adopt the MAJORANA electronics, and the expected energy resolution is thus $\sigma/E = 0.05\%$ [39]. LEGEND-200 began stable data taking in March 2023 with 140 kg of HPGe detectors, with complete 200 kg array planned in 2024.

The projected backgrounds in LEGEND-1000 are estimated from radioactivity measurements of the detector components and Monte Carlo simulations, detailed in Fig. 1.10, reproduced from [39]. The anticipated background index is 9.1×10^{-6} counts/(keV·kg·yr) [39], which translates to sensitive background of $\mathcal{B} = 4.9 \times 10^{-6}$ events/(mol yr) [8]. The dominant background component is attributed to the cosmogenic ^{42}Ar in the liquid Argon, which decays to ^{42}K with a $Q_{\beta\beta}$ value above the $Q_{\beta\beta}$ of ^{76}Ge. Backgrounds originating in optical fibers are the next-leading contributor. Finally, cosmogenic activation of ^{68}Ge in the detectors is the remaining background component estimated to contribute at a level above 1×10^{-6} counts/(keV·kg·yr).

1.4.4 Bolometers: good energy resolution and versatility

Bolometers are low temperature detectors (operated at 10-20 mK) sensitive to single particle interactions. The deposited energy is measured as a temperature increase of the detector sensitive part. The advantages of the technique are an excellent energy resolution, second only to the Ge, the possibility to use a wide variety of isotopes and a high detection efficiency. CUORE is at present the largest $0\nu\beta\beta$ bolometric detector. It is based on a pure bolometric technique, via the detection of the heat deposited in a particle interaction with the detection crystal.

CUORE and CUPID

The bolometer technology has been scaled up over the last ~ 30 yrs [50, 51, 52, 53, 54] from tests of individual detectors to the CUORE experiment, an array of 988 crystals of TeO_2 embedding ^{130}Te as double beta isotope. CUORE has achievied an energy resolution $\sigma/E = 0.1\%$ [55] at $Q_{\beta\beta}$. Currently the CUORE sensitivity is limited by the surface α background [52], as shown in Fig. 1.11. The α particles on the surface of the copper crystal holders produce a flat continuum that reaches the ^{130}Te $Q_{\beta\beta}$ at 2526 keV. The background in CUORE is 1.5×10^{-2} counts/(keV·kg·yr) corresponding to a sensitive background of $\mathcal{B} = 9.1 \times 10^{-2}$ events/(mol yr) [8].

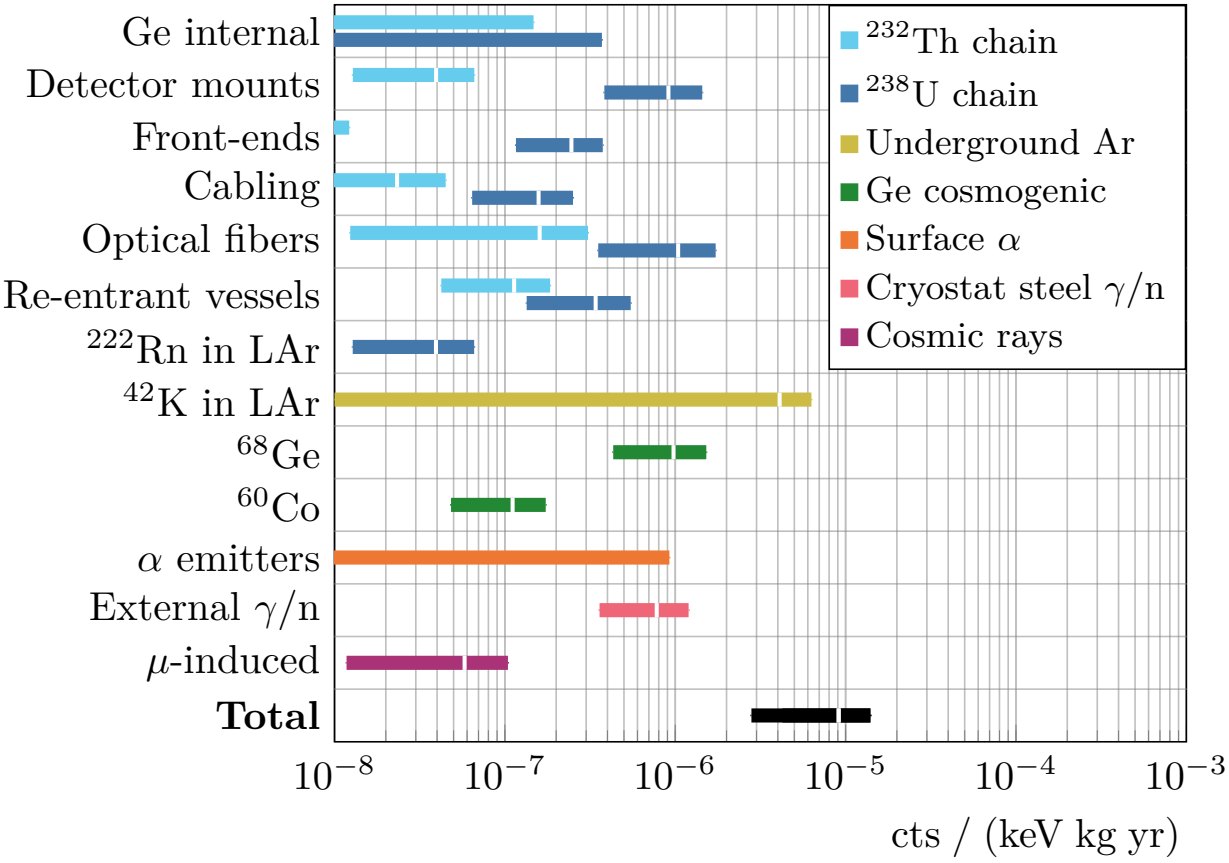

Figure 1.10: Projected backgrounds for LEGEND-1000. The broken bars indicate 1 σ uncertainties due to assay and Monte Carlo estimations. For Ge and alpha emitters the upper limit is shown. Reproduced from [39].

CUPID, the next generation bolometric experiment, will reduce this background by two orders of magnitude thanks to scintillating bolometers. The simultaneous readout of heat and light allows the discrimination between γ/β's and α's. Several smaller-scale arrays, LUMINEU [56], CUPID-0 [57] and CUPID-Mo [58] have demonstrated that crystal radiopurity and α rejection meet the requirements for CUPID. The double beta isotope in CUPID is ^{100}Mo embedded in scintillating $Li_2{}^{100}MoO_4$ crystals. Changing the double beta isotope from ^{130}Te ($Q_{\beta\beta}$ = 2526 keV) to ^{100}Mo ($Q_{\beta\beta}$ = 3034 keV) will help in reducing the background, because the $0\nu\beta\beta$ signal is located outside the bulk of gamma natural radioactivity (see Fig. 1.11). The projected background is 1×10^{-4} counts/(keV·kg·yr) or equivalently $\mathcal{B} = 2.3 \times 10^{-4}$ events/(mol yr) [8]. The CUPID experiment and its backgrounds will be the subject of Chapter 6.

AMORE

This bolometric experiment, looking for $0\nu\beta\beta$ decay of ^{100}Mo, exploits the scintillating bolometer technique, as in CUPID, but employs a different sensor to read the heat and scintillating signals. The first phase of the project, AMORE-I, employed $^{48depl}Ca^{100}MoO_4$ and $Li_2{}^{100}MoO_4$ crystals [59]. The second phase AMORE-II will use 100 kg of ^{100}Mo embedded in $Li_2{}^{100}MoO_4$ crystals [60].

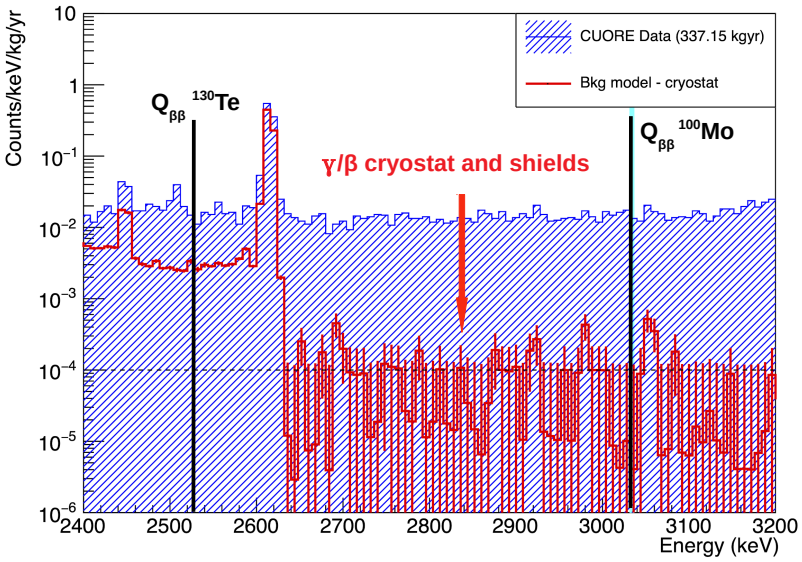

Figure 1.11: CUORE background spectrum from 337 kg yr exposure, in blue. The red spectrum shows the contribution of the radioactivity in the cryostat and shields from MC simulations. The dominant background comes from the α particles on the surfaces of the copper holders directly facing the crystals, producing a flat continuum.

1.4.5 Tracking-calorimeters : full topological reconstruction

The technique developed in the saga of NEMO and SuperNEMO detectors combines tracking and calorimetry that allows to track and identify particles individually. This unique feature allows in particular to measure the single electrons in the $2\nu\beta\beta$ and $0\nu\beta\beta$ decays. However, it is also the only technique featuring the double beta source separated from the detector which reduces the efficiency drastically.

In the tracker calorimeter technique the thin $0\nu\beta\beta$ source ($\sim$ 40 mg/cm^2) is vertically suspended between two particle-tracking modules consisting of a grid of Geiger cells. When a charged particle crosses a cell the ionized gas yields secondary electrons that drift towards the anode wire, the drift times are used to reconstruct the transverse position of the particle in the cells. The avalanche near the anode wire develops into a Geiger plasma which propagates along the wire. The arrival of the plasma at the two ends of the wire is detected with cathode rings. The two propagation times of the plasma are used to determine the longitudinal position of the particle as it passes through the cell [61]. The energy and time-of-flight of particles are measured in a segmented calorimeter, which consists of a wall of optical modules, each formed of a photomultiplier coupled to polystyrene scintillators, surrounding the tracking detector. The time-of-flight is used to discriminate between signal events emitted from the foil and background events where particles crossed the foil.

NEMO-3 operated between 2003 and 2011. Thanks to the identification of γ and electrons, internal and external backgrounds are measured [61] exploiting the characteristic particles emitted in each radioactive decay. Fig. 1.12 shows the NEMO-3 data and the sum of the expected background from: $2\nu\beta\beta$ decays of ^{100}Mo, the radon, the external backgrounds, and from internal ^{214}Bi and ^{208}Tl contaminations inside the foils. Only the $2\nu\beta\beta$ contribution is fitted to the data, while the other background components are set to values measured with the NEMO-3 detector [61]. The data agrees with the expectations. The dominant backgrounds in the ROI

are the $2\nu\beta\beta$ decay of ^{100}Mo, accounting for 56% of the observed events and Radon (30% of the events).

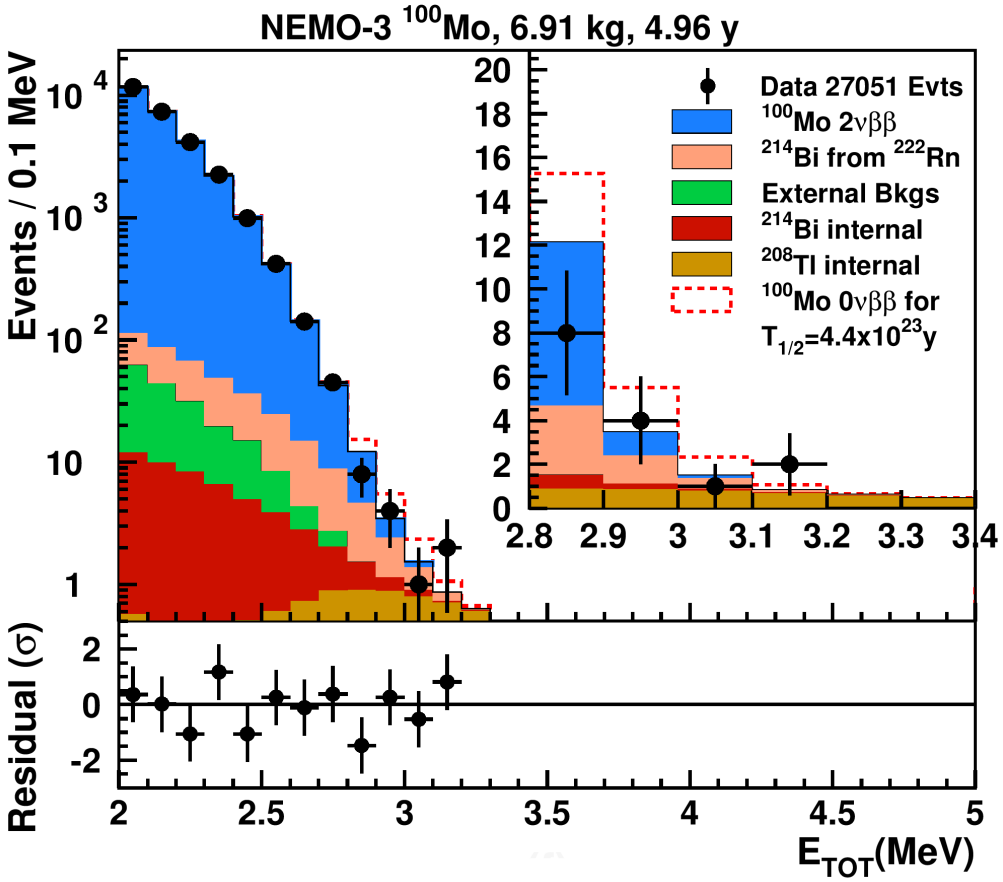

Figure 1.12: Total energy of the two electron distribution for ^{100}Mo in NEMO-3. The experimental data from a total exposure 34.3 kg.y is compared to the expected backgrounds. From [61]

The SuperNEMO demonstrator is under construction at the Laboratoire Souterrain de Modane. The source foils, adding up to 7 kg of ^{82}Se, are shown in Fig. 1.13, left, together with the tracker. The calorimeter consists of 712 optical modules with improved energy resolution, $\sigma/\mathrm{E} = 3$ % for 1 MeV, compared to $\sigma/\mathrm{E} = 6 - 7$ % in NEMO-3 [62]. To further reduce backgrounds, an anti-radon tent has been installed around the detector.

A critical background comes from the internal contamination of the source foils. We will detail the measurement and results of the ^{214}Bi and ^{208}Tl in the SuperNEMO foils in Section 3.4.

Though the technique has several unique features, the low efficiency makes a next generation experiment very difficult to realize and, as such, the demonstrator is not being pursued for a larger experiment, for now.

1.4.6 The present landscape and perspectives for $0\nu\beta\beta$ searches

At present there is a rich variety of experimental techniques and isotopes looking for $0\nu\beta\beta$ decay. Present limits on the $0\nu\beta\beta$ half-life are of the order 10^{26} ys and the limits on the effective neutrino mass are in the range 36 - 156 meV [36]. None of the current experiments

Figure 1.13: Left: Source foils and tracker in SuperNEMO demonstrator. Right: calorimeter wall

has the potential to explore fully the inverted-ordering region of the neutrino mass pattern – corresponding to the range 15 – 50 meV for $m_{\beta\beta}$. This is in fact the objective of next-generation $0\nu\beta\beta$ experiments on ten years time scale.

It is usual to plot the possible values of the effective neutrino mass as a function of the lightest, m_l, neutrino mass eigenvalue among m_1, m_2 and m_3 (see equation 1.12). In the case $\Delta m^2_{31} > 0$ and $\Delta m^2_{32} > 0$, such that $m_1 < m_2 < m_3$ we speak about the normal hierarchy and if $\Delta m^2_{31} < 0$ and $\Delta m^2_{32} < 0$, such that $m_3 < m_1 < m_2$, we speak about the inverted hierarchy, leading to two bands in the space $m_{\beta\beta}$ as a function of m_l, Fig. 1.14 (reproduced from [63], who adapted from [8]). In general, the normal hierarchy leads to smaller $m_{\beta\beta}$ values and therefore longer $0\nu\beta\beta$ decay half-lives. The present $m_{\beta\beta}$ range from KamLand-Zen-800 is shown as the straight brown band and the future ton scale $0\nu\beta\beta$ experiments sensitivities with the dashed brown line.

Recall however, that the main goal of $0\nu\beta\beta$ experiments is the discovery of the Majorana nature of the neutrino, evidencing lepton number violation. The direct observable is the $0\nu\beta\beta$ half life. The sensitivity of our experiments to the half life depends mainly on the background and on the exposure. Fig. 1.15, reproduced from [8], shows the general picture for present and future experiments in terms of sensitive background and sensitive exposure, as defined in [8]. The sensitive background corresponds to the events in the ROI per mol of isotope and per year, therefore embedding the performances on the energy resolution. The sensitive exposure is the product of the number of moles of isotope, livetime and signal detection efficiency. Lower backgrounds and larger exposures would follow an arrow from the top left to the bottom right of the plot. Past experiments populate the top left part, with exposures about thousands of mol year and backgrounds about 10^{-2}–10^{-3} cts/mol year. Experiments with the same discovery sensitivity on the $0\nu\beta\beta$ half life are situated on the 'iso-discovery' lines shown as dashed grey lines. The sensitivities of past experiments are situated in the region around 10^{25} - 10^{26}ys. Future experiments will reduce the backgrounds and increase the exposure, reaching sensitivities in $0\nu\beta\beta$ half-life about 10^{27} – 10^{28} years, for 10 years of exposure. The double beta isotopes are shown in Fig. 1.15: yellow for ^{136}Xe, blue for ^{130}Te, green for ^{100}Mo and red for ^{76}Ge. Each technique relies on a different strategy to increase sensitivity: Xe based experiments, like nEXO, rely mainly on increasing the exposure, by increasing the mass, Ge based detectors, LEGEND-1000 will have somewhat smaller exposure but much better backgrounds, given the excellent energy resolution and background discrimination, CUPID, based on bolometers relies

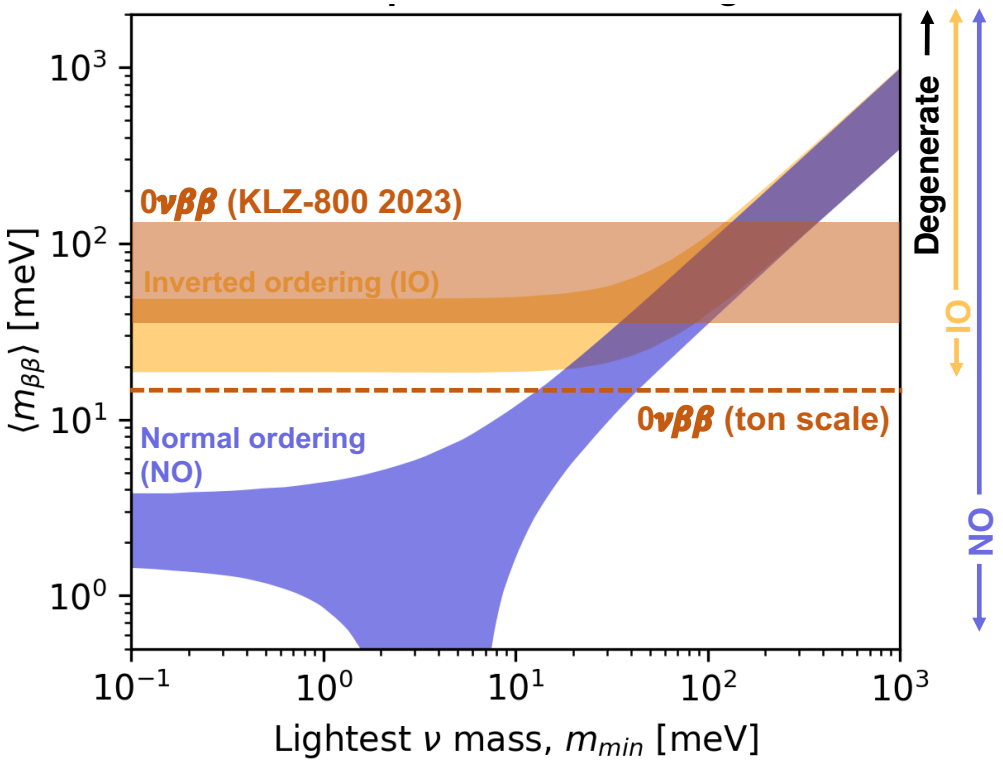

Figure 1.14: Effective neutrino mass $m_{\beta\beta}$ as a function of the lightest neutrino mass (among m_1, m_2 and m_3), for the inverted (yellow band) and normal hierarchy (blue band). The spread in the bands is due to the uncertainty in the Majorana phases. Also shown in the plots are the present $m_{\beta\beta}$ ranges from KamLand-Zen-800 (brown band) and for the future ton scale $0\nu\beta\beta$ experiments (dashed brown line) Reproduced from [63].

on background reduction.

Equal sensitivities in half life translate in different sensitivities for $m_{\beta\beta}$, as the phase space factor and the nuclear structure of the isotopes affect the relation between half-life and $m_{\beta\beta}$. This can be seen in Fig 1.15, where the colored lines correspond to the sensitivities required to test $m_{\beta\beta} = 18.4$ meV corresponding to the bottom of the normal hierarchy, green for ^{100}Mo, blue for ^{130}Te, orange for ^{136}Xe and red for ^{76}Ge (under the assumption of a $0\nu\beta\beta$ decay mediated by the exchange of light Majorana neutrinos and the largest NME value of QRPA calculations [64, 65, 19, 66]). We can see that ^{100}Mo based experiments, like CUPID with somehow lower sensitivity to $0\nu\beta\beta$ half life have a discovery potential for $m_{\beta\beta}$ similar to those of LEGEND and nEXO.

The uncertainty arising from the theoretical predictions in the nuclear matrix elements is potentially the largest uncertainty to anticipate $m_{\beta\beta}$ discovery potential of future experiments. This prevents to foresee if next generation experiments will fully cover the inverted neutrino mass hierarchy. Theoretical uncertainty in the NMEs need to be reduced and $2\nu\beta\beta$ and β^- provide precious inputs to constrain nuclear models employed in $0\nu\beta\beta$ calculations.

1.5 Direct dark matter searches

The hypothesis of dark matter emerged to explain several observations: i)The galactic rotation curves, in which velocities after a rise near the centre r=0 remain almost constant as far as they can be measured, instead of following Kepler's law falling of as $r^{-1/2}$, as expected from

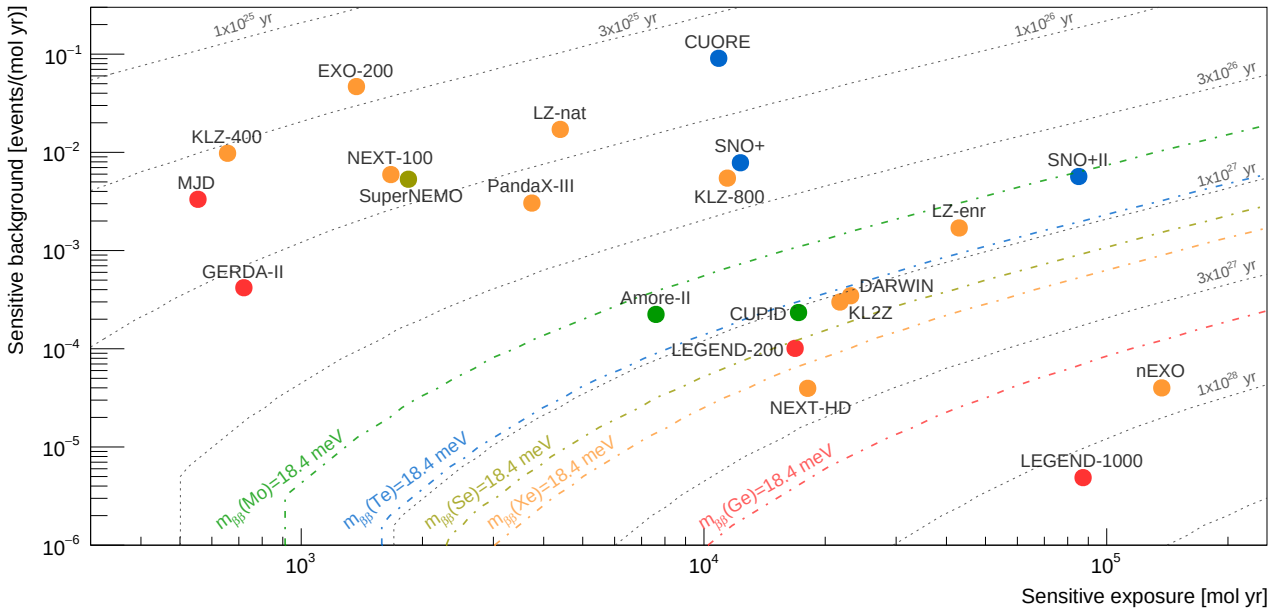

Figure 1.15: Sensitive background vs sensitive exposure for present and future $0\nu\beta\beta$ experiments. The grey lines correspond to the discovery of $0\nu\beta\beta$ decay half life, and the colored lines the sensitivities required to test $m_{\beta\beta}$ = 18.4 meV corresponding to the bottom of the normal hierarchy, under the assumption of the largest NME value of QRPA calculations [64, 65, 19, 66]. For the definition of sensitive exposure and sensitive background we refer to the text. A lifetime of 10 years is assumed for the future experiments. Reproduced from [8]

the luminous mass, ii) Following the virial theorem we can link the gravitational potential to the kinetic energy in clusters of galaxies, $< U > \ + 2 \ < T > = 0$, thus the cluster mass M is determined by measuring the velocity dispersion $< v^2 >$ and the mean galaxy separation $< r >$: $M \approx (< v^2 >< r >)/G$, where G is Newton's gravitational constant. The total mass found in this way was much larger than that of the luminous matter in the clusters iii) There is also the problem of the structure formation in the universe where the small initial density perturbations cannot be reproduced to grow sufficiently to produce the observed large scale structure, iv) The heights of the acoustic peaks in the Cosmic Microwave Background (CMB) angular power spectrum [67] would need a dark matter term.

The description of the evolution of the universe is based on the isotropic and homogeneous Friedmann Lemaître Robertson Walker model. The Friedmann equation describes the evolution of the Universe by the scale factor $a(t)$ which measures how much the universe stretches as a function of time:

$$\left(\frac{\dot{a}}{a}\right)^2 + \frac{k}{a^2} = \frac{8\pi G\rho_{tot}}{3} \tag{1.25}$$

where k is the spacial curvature, G Newton's gravitational constant and ρ_{tot} the energy density. The energy density may contain several components, for example, a mass density and a vacuum energy density.

The expansion rate of the universe is measured by the Hubble parameter, H, defined as $H = \dot{a}/a$. Using this definition, Eq.1.25 is rewritten as:

$$\frac{k}{H^2a^2} = \frac{\rho_{tot}}{(3H^2/8\pi G)} - 1 \tag{1.26}$$

In this form it is easy to see that the critical density ρ_c needed for a flat universe (k=0) is given

by:

$$\rho_c \equiv 3H^2/8\pi G. \tag{1.27}$$

Notice that the Hubble parameter changes with time, its present value is usually written as H_0. Thus, the critical density is also changing with time, with a current value of the order:

$$\rho_c \equiv 3H_0^2/8\pi G \cong 8 \times 10^{-30} g/cm^3 \tag{1.28}$$

The density parameter, Ω, is defined as the ratio of the energy density to the critical density, i.e $\Omega = \rho/\rho_c$. Considering a universe composed by matter and vacuum energy, the Friedmann equation in terms of the density parameter becomes:

$$\frac{k}{H^2a^2} = \Omega_m + \Omega_\Lambda - 1 \tag{1.29}$$

where $\Omega_m \equiv \rho_m/\rho_c$ is the total mass density parameter and $\Omega_\Lambda \equiv \rho_\Lambda/\rho_c \equiv \Lambda/3H^2$ with Λ the cosmological constant.

The cosmological results combining Cosmic Microwave Background (CMB) lensing and baryon acoustic oscillations is consistent with the standard, spatially flat, ΛCDM model, with a Hubble constant H_0= (67.4 $\pm$ 0.5) km s^{-1} Mpc^{-1} [67] and:

$$\Omega_b = 0.0493 \quad \text{and} \quad \Omega_{\text{CDM}} = 0.264. \tag{1.30}$$

where the indices b stand for 'baryonic' and, 'CDM' for cold dark matter. As we are considering a flat universe, the dark energy density gives $\Omega_\Lambda = 0.6847$ [67].

So, we can imagine that dark matter (DM) consists of particles. CMB properties indicate that dark matter is non-baryonic. Secondly, most DM models favour cold dark matter, particles that are non-relativistic around the time when galaxies started to form. Lastly, DM particles should be electrically neutral and stable [68]. The dark matter paradigm has changed in the last 20 years. When I did my PhD thesis in 2004 working in a direct dark matter search experiment, the favorite dark matter candidate by far was a heavy WIMP, with masses in the range 10 GeV-a few TeV. This thermal WIMP is eletrically neutral, interacts weakly with ordinary matter and is cold at the time of the freeze-out. It was a very attractive dark matter candidate because, in a completely independent framework, the supersymmetric theory predicts the existence of a particle with the same properties, the neutralino, the lightest supersymmetric particle, which is of course stable. At that time, we looked for WIMP masses above $\sim$ 30 GeV, following LHC lower limits for the neutralino masses. But time passed by and LHC did not find the expected heavy WIMPs. The WIMP miracle, concealing supersymmetry and cosmology did not happen. Today the truth is that we have no idea of what can dark matter be and the premise is that 'since we do not know where to look, let us look everywhere'. The dark matter candidates masses spans over nearly 50 orders of magnitude, from tiny values 10^{-21} eV to the reduced Planck scale 2×10^{18} GeV, shown in Fig 1.16 (reproduced from [68]). Our old thermal WIMP lies on the heavy dark matter candidate side. Light dark matter candidates span the sub-GeV region. Candidates in this regime include light WIMPs and hidden-sector particles [69]. Ultra-light dark matter, bosonic particles with sub-keV mass, includes the QCD axion and generic light scalars [69]. QCD axion dark matter is a particularly motivated case, predicted by the axion solution to the strong CP problem. Axions would have been produced in the early Universe and they can be easily accommodated in supersymmetric and grand unification theories [68].

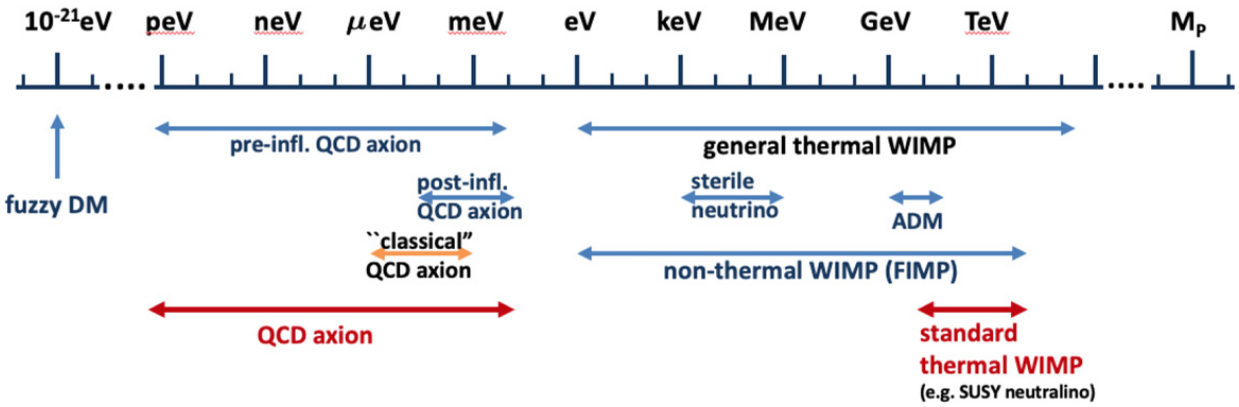

Figure 1.16: Masses of particle dark matter candidates, reproduced from [68]

1.5.1 Experimental signature and dark matter experiments

We focus here on WIMP dark matter searches. For direct searches the experimental signature is the recoiling of the target nucleus produced by the elastic or inelastic scattering of WIMPs off a nucleus. The rate of recoiling nuclei scattered by WIMPs in a detector depends on the density ρ_0 of WIMPs near the Earth, the scattering cross-section σ and the number of target nuclei. Qualitatively, the event rate per kilogram of detector material is simply:

$$R \approx \frac{\rho_0}{m_\chi} \sigma < v > \frac{1}{m_N} \tag{1.31}$$

where m_χ is the WIMP mass, ρ_0/m_χ the WIMP number density, $< v >$ is the average speed of the WIMP relative to the target, and the detector mass divided by the target nucleus mass m_N, gives the number of target nuclei. The expected rate dR in the recoil energy interval E, $E + dE$ is given by the integration over all possible incoming velocities:

$$\frac{dR}{dE} = \frac{\rho_0 \sigma_0}{2 m_\chi m_r^2} F^2(E) \int_{v_{min}}^{v_{max}} \frac{f_1(v)}{v} dv \tag{1.32}$$

where $m_r = m_N m_\chi/(m_N + m_\chi)$ is the reduced mass, σ_0 is the total scalar cross-section at zero momentum transfer, $F(E)$ is a form factor, and $f_1(v)$ is the distribution of velocities relative to the detector. v_{min} is the minimum WIMP velocity necessary to contribute to a particular energy in the recoil spectrum, and v_{max}, the maximum velocity that WIMPs in the halo can have, is given by $v_{max} = v_E + v_{esc}$, where v_E is the Earth velocity relative to the halo and v_{esc} is the escape velocity from our galaxy.

In the case of inelastic scattering of dark matter, the expected signature is a nuclear recoil followed by an electronic de-excitation of the target nucleus. WIMPs with very low mass, in the MeV/c^2 range and below, do not transfer sufficient momentum to the target nucleus to generate nuclear recoils of detectable energy. The coupling of WIMPs to atomic electrons is thus used to search for such particles [68].

Nowadays more than 30 experiments worldwide based on a rich variety of targets and techniques are searching for dark matter WIMPs by direct detection. Fig 1.17, reproduced from [68] shows the current status of searches for spin-independent elastic WIMP-nucleus scattering. Shown are the limits of the experiments looking for light WIMPS: CDEX, CDMSLite, COSINE-100, CRESST, DAMA/LIBRA, DAMIC, EDELWEISS, SuperCDMS, NEWS-G. Searches for

heavy WIMPs require very large masses, and the only techniques that can reach the required exposures nowadays are based on liquid Xenon or liquid Argon : DarkSide, DEAP-3600, LUX, PandaX-II and XENON (see [68] and References therein).

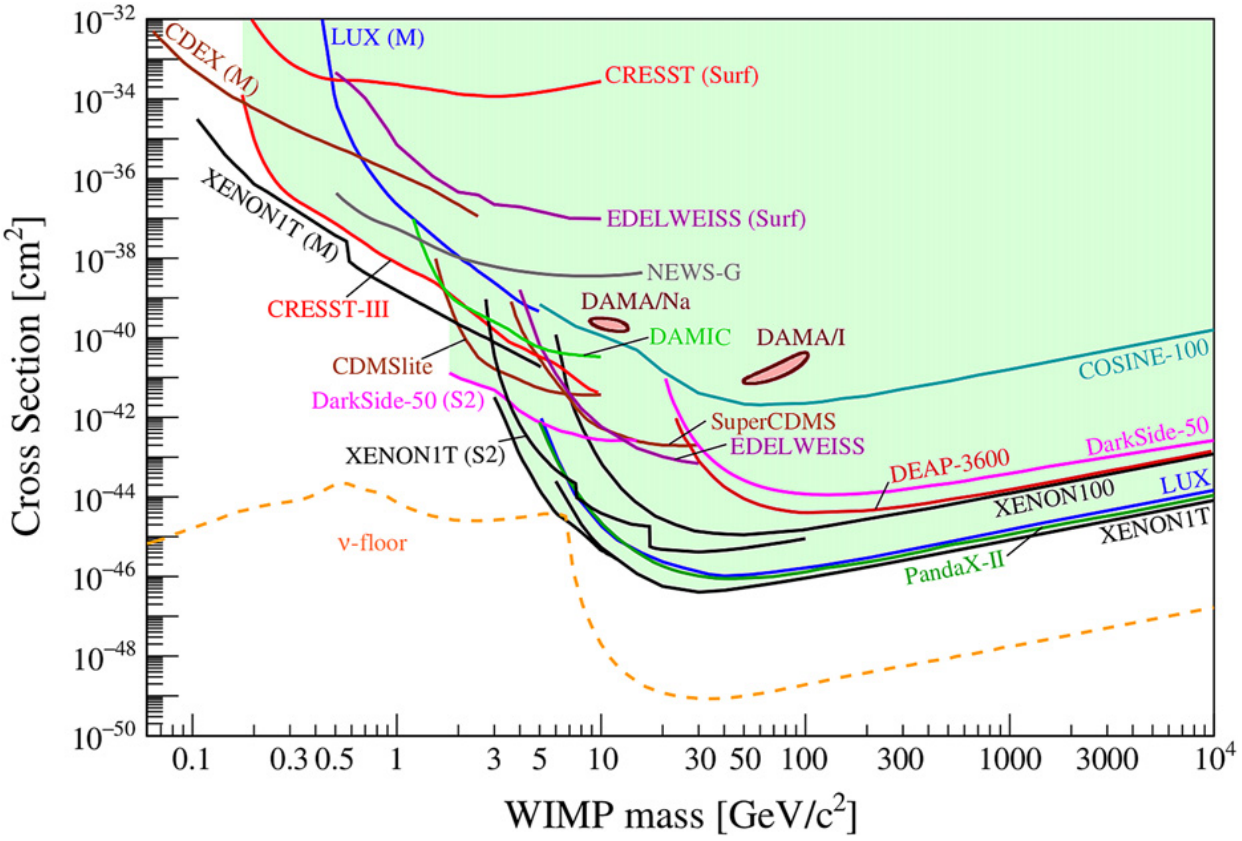

Figure 1.17: Current limits for spin-independent elastic WIMP-nucleus scattering cross-section, scattering assuming the standard parameters for an isothermal WIMP halo: $\rho_0 = 0.3$ GeV cm $^{-3}$, $v_0 = 220$ km s^{-1}, $v_{esc} = 544$ km s^{-1}, reproduced from [68].

Chapter 2

Background sources

> Mais comment croire à notre paix? Les vents alizés glissaient sans repos vers le Sud. Ils essuyaient la plage avec un bruit de soie.
>
> *Courier Sud,* A. de Saint-Exupéry

Background reduction is a key ingredient in neutrinoless double beta decay and dark matter searches. In this chapter I describe the main background sources and the methods to reduce them.

2.1 Cosmic rays

Cosmic rays may induce backgrounds directly by the energy deposition of muons or through neutron interactions. In $0\nu\beta\beta$ searches muons may induce a background through the energy deposition of gammas with energies in the region of interest $\sim 2.5 - 3$ MeV, produced by muon radiative energy loss. Neutrons produced by muons represent a significant background in dark matter searches because they mimic the WIMP nuclear recoil.

Fig. 2.1 shows the flux of muons and the cosmic nucleonic component as a function of depth, up to 1000 meters water equivalent (m.w.e). The nucleonic component of cosmic rays, composed by more than 97% of neutrons, can be effectively reduced with an overburden of about 10 m.w.e, as in a cellar of a building. To reduce the muon flux, experiments must be placed deeper underground. The muon flux at sea level, $\sim 10^{-2}$ /cm^2/s, is reduced by at least six orders of magnitude at sites below 2000 m.w.e. Fig. 2.2 shows the muon flux in several underground laboratories worldwide. At present the Laboratori Nazionali del Gran Sasso (LNGS) in Italy is the largest laboratory in Europe at a depth of 3700 m.w.e. LNGS together with the Laboratoire Souterrain de Modane (LSM) in France (4800 m.w.e), Boulby (2800 m.w.e) in UK and the Laboratorio Subterráneo de Canfranc (2450 m.w.e) in Spain are hosting the majority of the double beta and dark matter experiments in Europe. SNOlab (5890 m.w.e) and SURF (4300 m.w.e) are the deepest underground laboratories in North America. In Asia the main underground laboratories are Kamioka (1750 m.w.e) in Japan, Jinping, CPL ($\sim$ 6500 m.w.e) in China and Yang-Yang (1800 m.w.e) in Korea (a deeper underground laboratory in Korea, Yemilab, is foreseen to be soon in operation). The first multipurpose underground laboratory in the Southern hemisphere is located in Australia. The Stawell Underground Physcis Laboratory, SUPL, at a depth of $\sim$ 2900 m.w.e is presently installing the electricity, air condition, and will

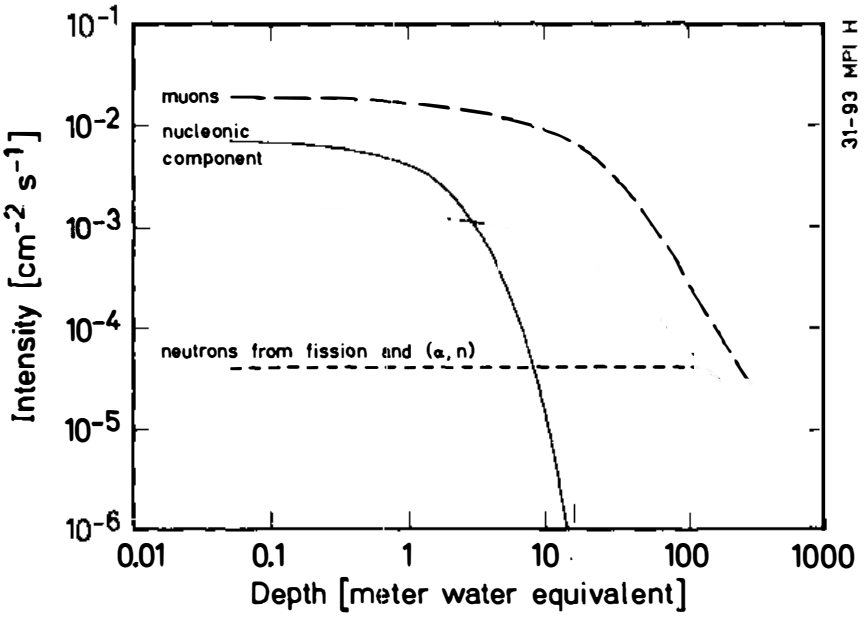

Figure 2.1: Cosmic ray muons and nucleonic component as a function of the depth, for shallow depths. The nucleonic component is more than 97% neutrons. Reproduced from [70].

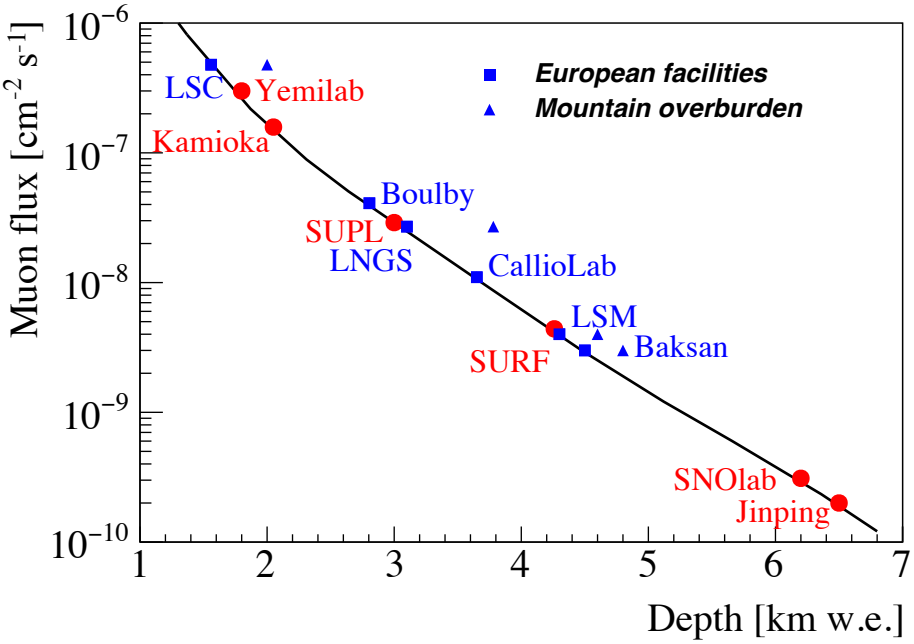

Figure 2.2: Muon flux in selected underground laboratories in the world, reproduced from [71].

soon be in full operation. The ANDES project foresees an underground laboratory between Argentina and Chile at a depth $\sim$ 4700 m.w.e. The laboratory will be built at the same time as a road tunnel between the two countries, but unfortunately the tunnel construction is in stand by due to economical and political instability in Argentina [72].

The energy spectrum of the muons is shifted towards higher energies with increasing depth. The average muon energy at sea level is 4 GeV, while for example at LNGS the single muon average energy is 270 GeV [73] and 327 - 356 GeV [74] at SNOLab.

Cosmic rays can also produce backgrounds by cosmogenic activation. Neutrons and protons in the atmosphere may produce radionuclides by neutron capture or fission. If the radionuclide has a relatively long half life and the Q-value is above the ROI, then they may become a sizeable background source. Several isotopes of cobalt are produced in copper, a material commonly used in detector construction, by cosmogenic activation via n + $^{63,65}_{29}\mathbf{Cu} \rightarrow {}^{56,57,58,60}_{27}\mathbf{Co} + \alpha +$ Xn. Other common elements in detector construction that are cosmogenically activated are Al, Si, Xe, Ge, As, Au, Fe, Nb, W, Mo. In the case of $Li_2{}^{100}MoO_4$ crystals the potentially dangerous cosmogenic isotopes are produced by cosmic interaction with ^{100}Mo. In particular ^{82}Sr ($T_{1/2}$= 25.3 days) with Q-value = 178 keV, much lower than the $0\nu\beta\beta$ signal, is not dangerous by itself but decays to ^{82}Rb ($T_{1/2}$= 1.26 min) which has a Q-value = 4403 keV above the $0\nu\beta\beta$ signal region. Similarly, the activation product ^{88}Zr ($T_{1/2}$= 83 days, Q-value= 673 keV) decays to ^{88}Y ($T_{1/2}$= 106.6 days) which has a Q-value = 3622 keV. Another potentially worrisome cosmogenic in ^{100}Mo are ^{56}Co ($T_{1/2}$= 77 days, Q-value= 4566 keV) and ^{42}K ($T_{1/2}$= 12 hours, Q-value= 3525 keV). We will come back to these background contributions in Chapter 6. In general, to mitigate the production of cosmogenic radionuclides it is common to store the detectors and materials underground whenever possible. Other strategy consists to fabricate the materials directly underground. As an example, the dominant background in LEGEND-1000 is expected to be the cosmogenic ^{42}Ar, produced by cosmic ray interaction with ^{40}Ar, the predominant isotope of atmospheric Argon. Though ^{42}Ar is not dangerous by itself, it decays to ^{42}K with has a Q-value=3525 keV. To minimize the level of ^{42}Ar the baseline plan for LEGEND-1000 is to use Underground Liquid Argon, directly fabricated underground [75].

Once underground the residual muons can generate neutrons through different processes. These muon-induced neutrons can produce radioactive isotopes in-situ. The production rate is of course much lower than on the surface, however given the sensitivity levels aimed for the future experiments they can still be relevant. We will discuss in section 2.3 the muon-induced neutrons and their mitigation.

2.2 Radioactivity

2.2.1 Natural radioactivity

The earth was formed 4.5 billion years ago from clouds of interstellar dust released by the explosion of supernovas. Significant quantities of uranium, thorium and potassium, long-lived radioactive elements, were present, and today they are part of the earth crust with average concentrations of 44 Bq/kg for ^{232}Th, 36 Bq/kg for ^{238}U and 850 Bq/kg for ^{40}K.

^{238}U and ^{232}Th decay through a series of daughter isotopes, producing β and α particles and γ-rays as shown in Fig.2.3. In the upper part of the ^{238}U chain we find α emitters with energies $\sim 4-5$ MeV. Then ^{226}Ra decays subsequently to short-lived daughters, up to ^{210}Pb. The first of those is ^{222}Rn, a gas that can diffuse through the materials and is present in the air. Radon

represents a background to all experiments as it diffuses through liquids or deposits on surfaces of the detector components. We will discuss radon backgrounds in the next subsection. The ^{226}Ra short-lived daughters include γ and β emitters and, in particular, ^{214}Bi that β decays with an endpoint of 3.3 MeV. This isotope is of particular concern for $0\nu\beta\beta$ experiments, since its Q-value is above the $Q_{\beta\beta}$ of most $\beta\beta$ isotopes (see Table 1.1). The ^{226}Ra/^{222}Rn short-lived descendants decay to ^{210}Pb ($T_{1/2}$= 22 years), which is particularly dangerous for dark matter experiments. The ^{210}Pb daughters includes ^{210}Bi, a pure β emitter with Q-value= 1.1 MeV, producing a continuous background up to this energy.

In the thorium chain, the parent radionucleide decays through ^{228}Ra and ^{228}Ac to ^{228}Th. This isotope decays subsequently to short-lived radionuclides untill ^{208}Pb, which is stable. ^{228}Th daughters includes in particular ^{208}Tl which emits a gamma at 2614 keV, the highest relevant γ line in natural radioactivity. It is particularly dangerous for $0\nu\beta\beta$ experiments, since, as shown in Fig 2.4, a 583 keV gamma may be in coincidence with the 2614 keV gamma line (with 100% probability of emission) summing up to an energy near the $0\nu\beta\beta$ signal.

The decay of uranium, thorium and potassium in the rock and concrete, typically at levels $\mathcal{O}$(10 Bq/kg), leads to an environmental background of γ's, β's , α's and neutrons. As an example, in Table 2.1 we show the flux of several γ lines measured by a portable HPGe detector at the Laboratoire Souterrain de Modane.

	^{40}K	^{214}Pb	^{214}Bi	^{212}Pb	^{208}Tl	^{208}Tl	^{137}Cs
Energy [keV]	1460	352	609	238	583	2614	662
	Flux [10^{-3} photons/s/cm^2]						
	207	47	72	17	18	51	1

Table 2.1: γ flux measured at the Laboratoire Souterrain de Modane with a portable HPGe detector.

Environmental γ's are shielded with high Z materials, usually lead, iron and copper, where γ's loose their energy by Compton scattering and full energy deposition. Fig 2.5 (reproduced from [76]) shows the spectrum at the boundary of the rock in Boulby underground laboratory, spectrum A, where the total flux of gammas from the rock boundary is about 0.09/s/cm^2. Spectrum B), C), D) and E) shows the resulting spectrum after 5 cm , 10 cm, 20 cm and 30 cm of lead shielding, from GEANT4 simulations. A shielding of 20 cm of lead reduces the environmental background in average by about 5 orders of magnitude. On the same Fig. 2.5 spectrum F) shows the spectrum after 20 cm of Pb and 40 g/cm^2 of CH_2 (corresponding to about 40 cm of PE).

Radon

^{222}Rn mixed in the air deposits on the surfaces of the detector materials, and further decays through short lived daughters up to ^{210}Pb. This isotope emits only one low energy γ of 46 keV. Its daughters, ^{210}Bi and ^{210}Po are β and α emitters respectively, which represent a sizeable background in dark matter searches.

The recoil ($\sim$ 100 keV) of the ^{210}Pb nucleus may implant ^{210}Pb atoms in a sub-surface layer. Implantation depths in copper are in average about 20 nm and follow a function similar to a Landau function, according to a simulation using SRIM [77] and GEANT4, as shown in Fig 2.6 (reproduced from [78]). The implantation of ^{210}Bi and ^{210}Po descendants is much more complicated to model.

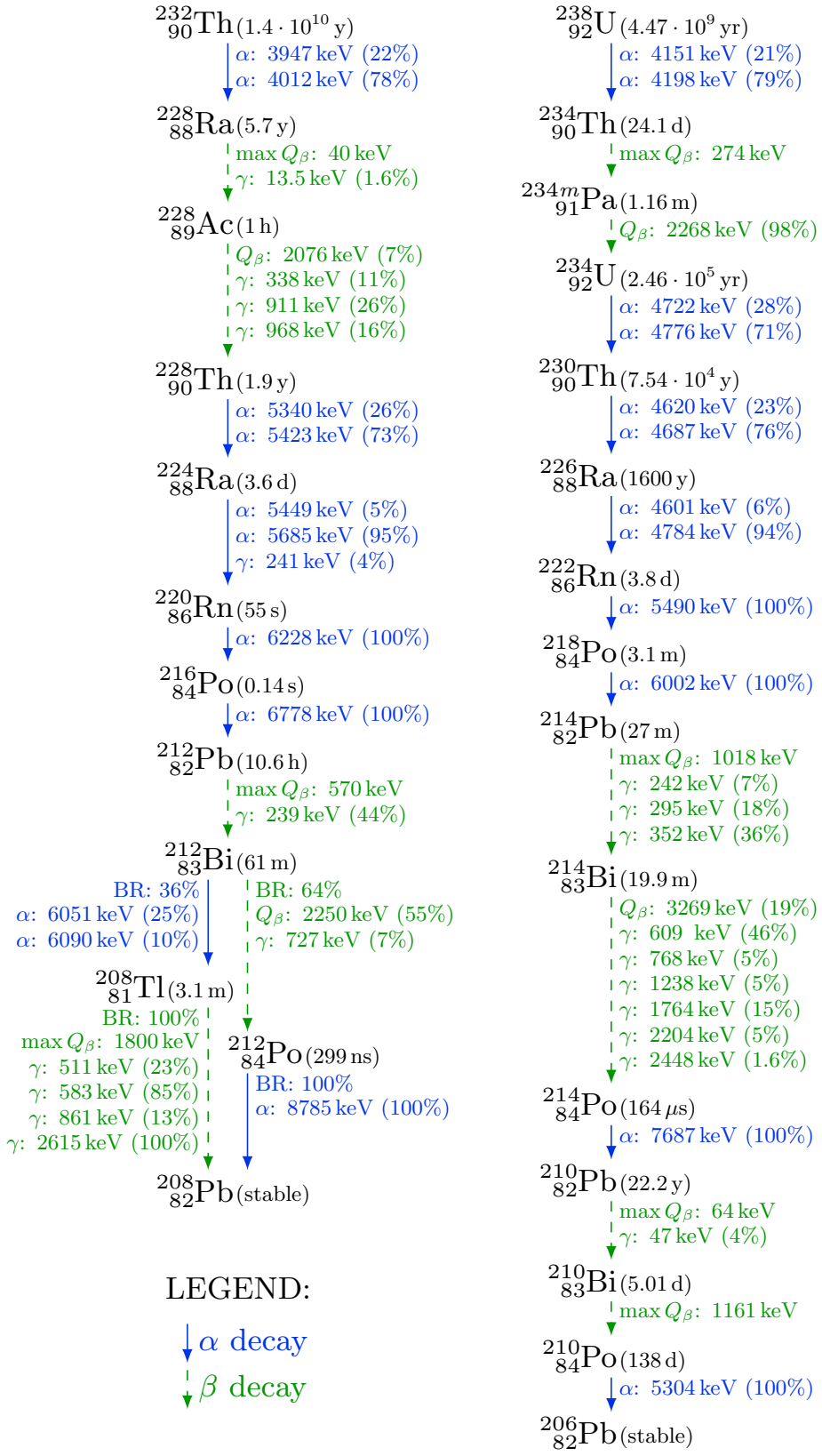

Figure 2.3: The ^{238}U and ^{232}Th decay chains. Probability emissions of gamma $P_\gamma > 5$ % and alpha $P_\alpha > 1$ % are reported. 'Max Q_β' stands for the maximum available β energy excluding γ transitions. Adapted from [8].

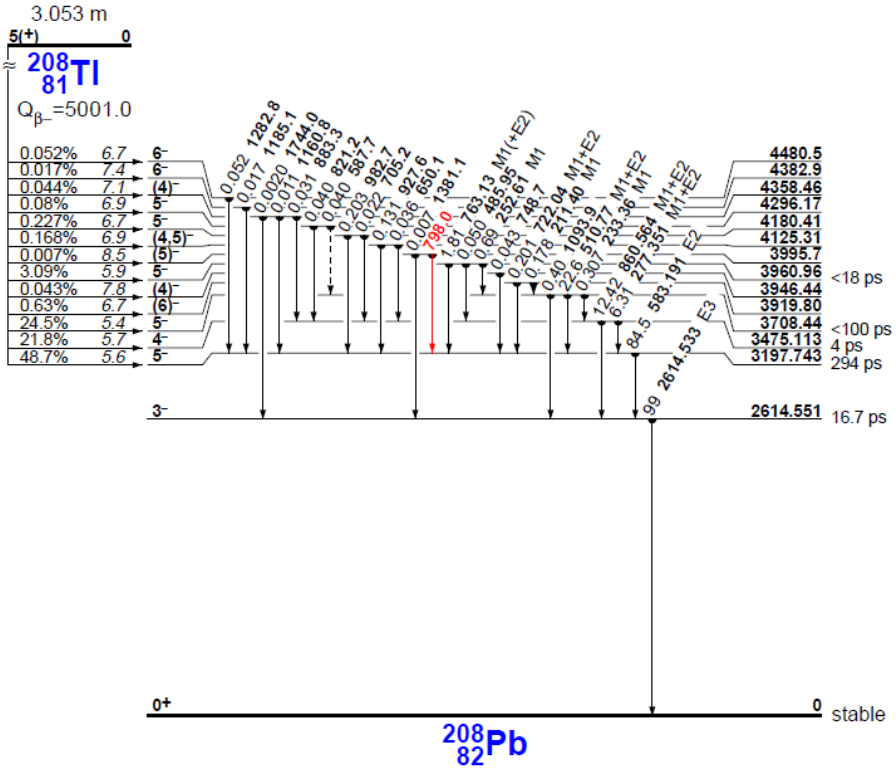

Figure 2.4: ^{208}Tl decay scheme. 100 % of the disintegration goes through the 2614 keV level, 49% with the emission of a 583 keV gamma. If both decays occur, the gamma may create an event in the $0\nu\beta\beta$ region, mimicking the double beta decay signature.

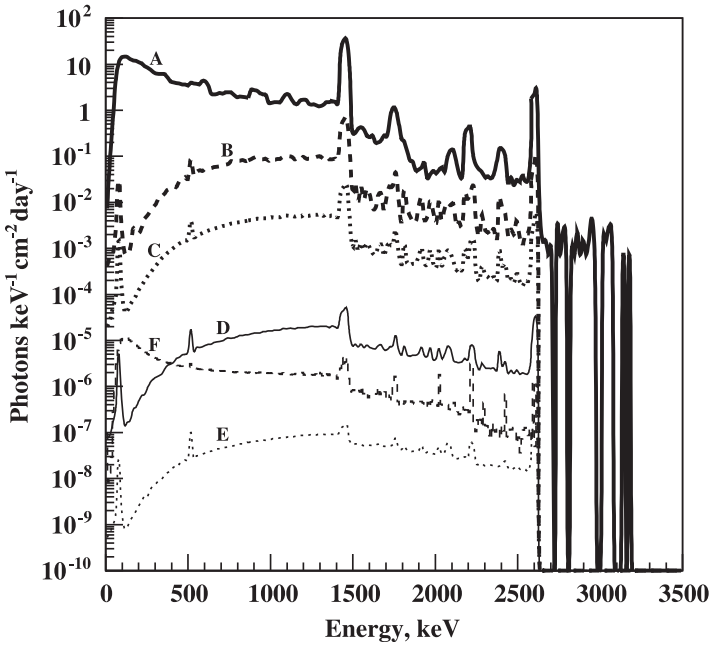

Figure 2.5: Gamma spectrum from Boulby rock/cavern (A) and after 5 cm (B), 10 cm (C), 20 cm (D) and 30 cm (E) of Pb shielding. The usual U/Th peaks can be seen as well as the peak at 1460 keV from ^{40}K. Line (F) is the spectrum after 20 cm Pb and 40 g/cm^2 of CH_2 . Reproduced from [76].

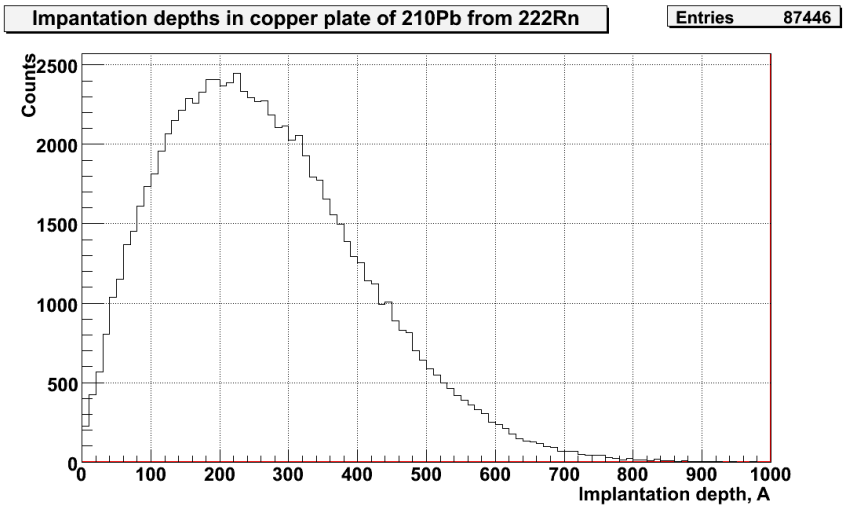

Figure 2.6: Implantation depth profile of ^{210}Pb deposited by radon in copper obtained with SRIM and GEANT4 simulations. Reproduced from [78].

Methods to remove ^{210}Pb and its descendants in copper have been extensively developed, showing that recontamination of the surfaces after cleaning is an issue and should be prevented. Removing 20 mg/cm^2 of the copper surface by chemical etching or electropolishing effectively removes ^{210}Po from copper surfaces [79].

2.2.2 Anthropogenic radioactivity

Human activity can produce radioactive isotopes in the environment, usually fission products from nuclear accidents or nuclear weapon testing. Anthropogenic radionucleides represent a background for dark matter searchers looking for low mass WIMPS at low energies and also for $0\nu\beta\beta$ when the Q-value of the isotope is greater than the one of the $0\nu\beta\beta$ isotope.

The massive nuclear weapon tests in the 60's, the Chernobyl and Fukushima accidents released γ and β emitters. At the Laboratoire Souterrain de Modane, we measured radionucleides released by the Fukushima accident in 2011 with a HPGe detector dedicated to material screening [80]. We detected fission products ^{131}I, ^{132}Te, ^{134}Cs and ^{137}Cs in filters that we placed in the laboratory ventilation system. For ^{131}I, which is relatively short lived ($T_{1/2}$= 8 d), we found about 100 μBq/m^3, more than 100 times higher than the concentrations of the other fission products. However, this gamma ray emitter decays rapidly and does not represent a background for rare event searches. The activity concentration of ^{134}Cs ($T_{1/2}$= 2 years) and ^{137}Cs ($T_{1/2}$= 30 years) ranged from 5 to 30 μBq/m^3. We could establish that the period with highest activity concentration recorded for ^{134}Cs and ^{137}Cs corresponded to the same period as for ^{131}I, an increase consistent with simulation models of the movement of the air masses in the atmosphere [81]. The aforementioned activity concentration found for ^{134}Cs and ^{137}Cs in the air near Modane following the Fukushima accident was about 1000 times lower than the average levels of ^{137}C measured in France due to the Chernobyl accident. In fact, as a result of the nuclear weapon tests and the Chernobyl accident we still find in France residual ^{137}Cs present in the air and in the materials (^{134}Cs has already decayed and it is not usually found in the materials any more). In the same work after the Fukushima accident [80], we did not detect

other γ-emitting radionuclides in the air near Modane. We set upper limits for the activity concentration of ^{95}Nb , ^{95}Zr, ^{140}Ba/La and ^{103}Ru of 0.4 μBq/m^3 and < 3 μBq/m^3 for ^{106}Ru.

However, near the Fukushima reactor the radioactive isotopes did produce backgrounds in rare event search experiments. The main background in KamLand Zen phase I was a fallout from the Fukushima accident present in the Internal Balloon, fabricated 100 km from the Fukushima-I reactor [82] . The sensitivity of the Phase-I was limited by the presence of the unexpected background peak from ^{108m}Ag ($T_{1/2}$= 360 days, $Q_{\beta\beta}$ = 3.01 MeV), just above the 2.458 MeV Q-value of ^{136}Xe $0\nu\beta\beta$ decay. After completing Phase-I, the collaboration embarked on a Xe-LS purification campaign and in December 2013, they started the Phase-II, and found a reduction of ^{108m}Ag by more than a factor of 10 [83].

However, γ emitting radionucleides are not particularly dangerous for techniques with good energy resolution since they can be identified by the gamma lines or directly tagged in experiments capable of event reconstruction. The most dangerous backgrounds in this case are pure β emitters. We have found anthropogenic ^{90}Sr ($T_{1/2}$= 28.8 years, Q-value = 546 keV) in $Li_2{}^{100}MoO_4$ bolometers for $0\nu\beta\beta$. ^{90}Sr decays to ^{90}Y, $T_{1/2}$= 64 h and Q-value= 2279 keV, which represents a background for the $2\nu\beta\beta$ decay and the spectral shapes analysis.

2.2.3 Radioactivity in detector materials

Once the experiments are shielded from environmental γ radioactivity, the main background arises from the radioactivity in the materials constituing the experimental set-up. I devote Chapter 3 to the subject.

2.3 Neutrons

Neutrons represent a background for dark matter searches looking for heavy WIMPs because they mimic the WIMP nuclear interaction. They are also a potential background for $0\nu\beta\beta$ searches because neutrons may be captured, the de-excitation of the resulting nucleus emits high energetic gammas which may produce energy depositions in the $0\nu\beta\beta$ signal region.

Neutrons can be produced by muon interactions or from reactions involving the decay chains of ^{238}U and ^{232}Th. At low energies, typically E < 8 MeV, neutrons from radioactivity dominate. These neutrons are produced in the rock or in the detector materials by (α,n) reactions or fission. When an α particle from the decay of the U or Th chain interacts with an element, neutrons may be produced if the energy threshold for (α,n) production in the element is low enough. For example, the reaction is naturally occurring for ^{18}O present in the rock :

$$^{18}O + \alpha \rightarrow n +^{21} \text{Ne} \tag{2.1}$$

The (α,n) reactions in the rock come from ^{9}Be, ^{13}C, ^{17}O, ^{18}O, ^{25}Mg, ^{43}Ca and the less abundant elements aluminum and sodium. Even the most energetic alpha particle (8.8 MeV from the thorium chain) cannot overcome the energy threshold for (α, n) production in ^{40}Ca, ^{16}O, ^{28}Si which constitute more than 75% of the Earth's crust by weight [84].

The energy of these radiogenic neutrons peaks around 1 MeV and their flux depends on the composition of the rock. The spectrum and yield of radiogenic neutrons can be computed, for example, with the SOURCES4 code [85]. The rock composition in the Laboratoire Souterrain de Modane has a density =2.65 g/cm^3, the activity ^{238}U: 10.4 Bq/kg, ^{232}Th: 10 Bq/kg, and its composition is [86] :

(%)	O	Ca	C	Si	Al	Mg	Fe	H	Na	K	Ti	P	Mn
	49.4	30.6	5.94	6.93	2.58	0.84	1.9	1	0.44	0.21	0.07	0.06	0.03

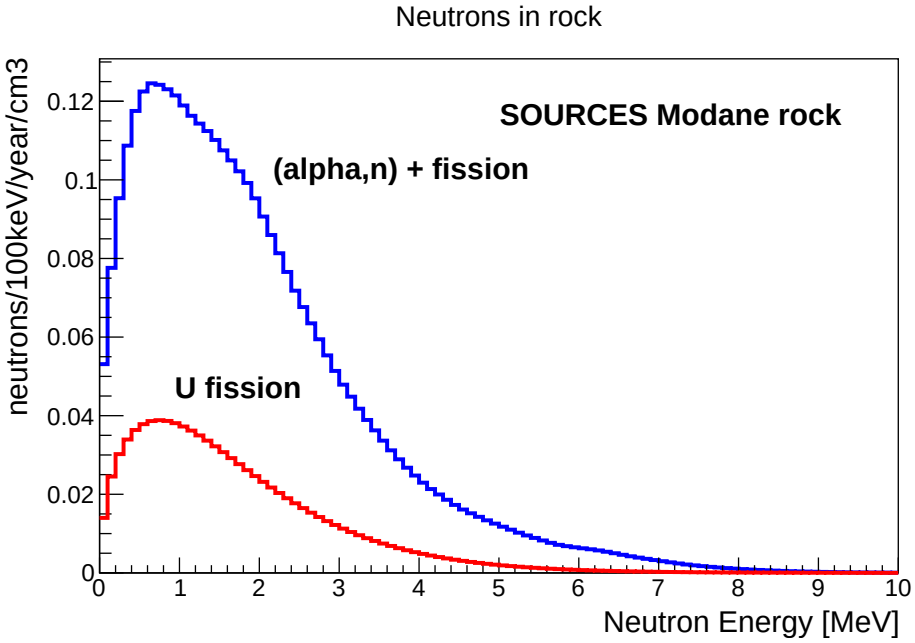

Figure 2.7: Neutron spectra produced in the rock at the Modane Underground Laboratory, at the point of production, obtained with the code SOURCES4A.

We can use these parameters to get the neutron spectrum at the point of the production shown in Fig. 2.7. The spectrum peaks at $\sim$ 1 MeV and (α,n) reactions contribute to 77% of neutron yield and fission to 23 %. By integrating the spectra, the neutron production rate in Modane rock resultsin 1.13 $\times$ 10^{-7} neutrons/sec/cm^3.

Neutrons produced in the rock or the concrete are thermalized with hydrogenated materials, like water or Polyethylene, capable of effectively slowing down radiogenic neutrons. Fig. 2.8, reproduced from [87], shows the reduction of the neutron flux from the rock by a hydrogenated material, obtained from GEANT4 and MCNPX simulations. The flux is taken at the surface of the cavern at the Boulby underground laboratory. A neutron shielding equivalent to 50 g/cm^2 (about 45 cm of Polyethylene) should suppress the neutron flux from radioactivity in the rock by more than 6 orders of magnitude.

Neutrons from (α, n) or fission can be produced also in the detector materials, typically in materials containing fluorine or Be, with low thresholds for (α, n) interactions. Radioactivity in the material itself may thus give rise to neutrons which can not be shielded by a shielding around the set-up. As an example, in the Edelweiss-III dark matter experiment, about 50% of the background in the WIMPs signal region (20 -200 keV), the highest background contribution, came from (α,n) reactions in a CuBe part (press-fit) in connectors very close to the detectors.

The neutron production rate due to muons at large depths is 2 to 3 orders of magnitude lower than that of neutrons from local radioactivity. However, muon-induced neutrons are fast, with a very hard energy spectrum, extending to several GeV [74], and can penetrate to significant depth in the detector set-up. Fast neutrons represent an important background for dark matter searches. Muons can generate neutrons through different processes [84, 88]:

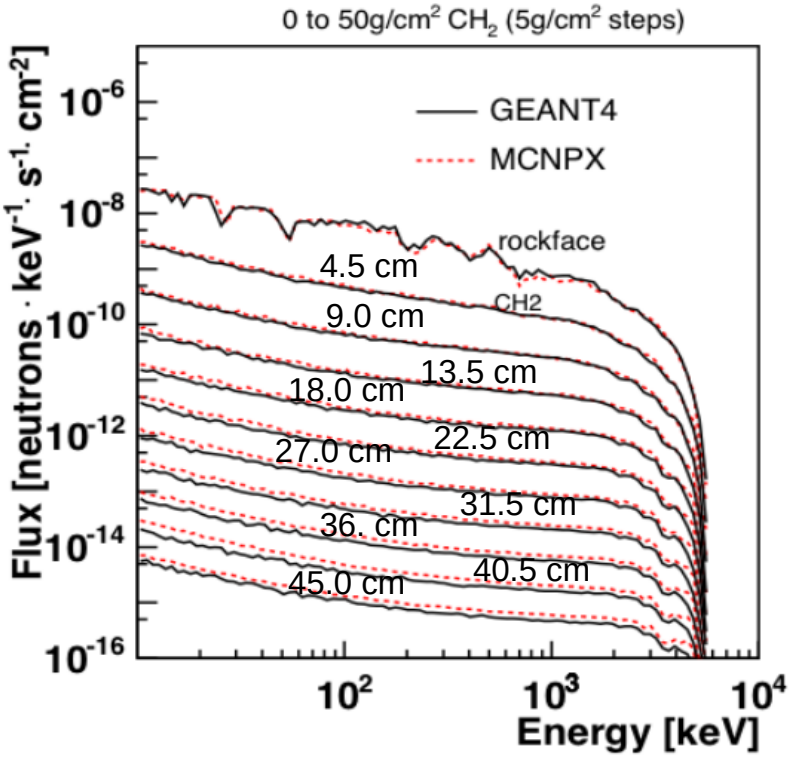

Figure 2.8: Neutron spectra at the surface of the rock of and the attenuation with several thickness of a material containing CH_2, in steps of 5 g/cm^2. The thickness corresponds to 4.5 cm, 9 cm, 13.5 cm, 18 cm, 22.5 cm, 27 cm, 31.5 cm, 36 cm, 40.5 cm and 45 cm of polyethylene. Reproduced from [87]

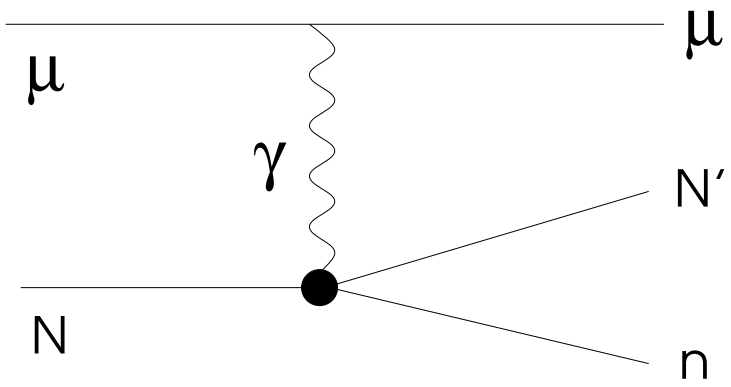

Figure 2.9: Feynman diagram of a muon spallation reproduced from [88]

- By interactions with nuclei via a virtual photon, which produces a nuclear disintegration as shown in Fig. 2.9, also known as "muon spallation".
- Neutrons can be produced by stopping muons, which are captured, resulting in highly excited isotopes emitting one or more neutrons [88]:

$$\mu^- + {}^{A}_{Z}X \rightarrow \nu_\mu + {}^{A}_{Z-1}X \qquad {}^{A}_{Z-1}X \rightarrow {}^{A-M_N}_{Z-1}X + M_N n \tag{2.2}$$

- Neutron production in electromagnetic showers: electromagnetic showers generated by muon ionization produce electrons, e^+e^- pairs. The neutron production occurs mostly via inelastic charge exchange and photoproduction. The cross sections grow as Z^2, and thus become more important for high-Z targets, such as lead [84].
- Muon-nucleon quasi inelastic scattering: the quasielastic scattering of muons on nuclei produces knock-on neutrons with energies in the order of 100 MeV .
- Neutron production in hadronic showers: the main source for hadronic showers are pions from muon-induced photonuclear interactions – either via real or virtual photon exchange.

Muon induced neutrons are a dangerous background because they can not be shielded. However, muon-induced neutrons originating in the experimental set-up, mostly in the lead shield, are very much reduced by tagging the parent muon with a muon-veto system.

2.3.1 Cosmogenic activation by neutrons underground

As introduced in section 2.1, neutrons produced by muons underground can be captured in the materials and produce radiactive isotopes [89]. These background is subdominant for present experiments but it may become important for next generation experiments, with even higher sensitivities. For example in LEGEND-1000 neutrons may produce in-situ the radioactive isotopes ^{77}Ge ($T_{1/2}$= 11.2 h) and ^{77m}Ge ($T_{1/2}$= 53.7 s) by neutron capture in ^{76}Ge. ^{77}Ge decays with a γ cascade of minimum 195 keV, thus it can be rejected but ^{77m}Ge decays predominantly via pure ground-state decay, which can not be identified by the standard cuts in LEGEND-1000 [39]. The ^{77m}Ge (Q-value = 2.7 MeV) represents a sizeable background at LNGS site (it is two orders of magnitude lower at SNOLab) [39]. However a coincidence cut substantially suppress the ^{77m}Ge contribution [90].

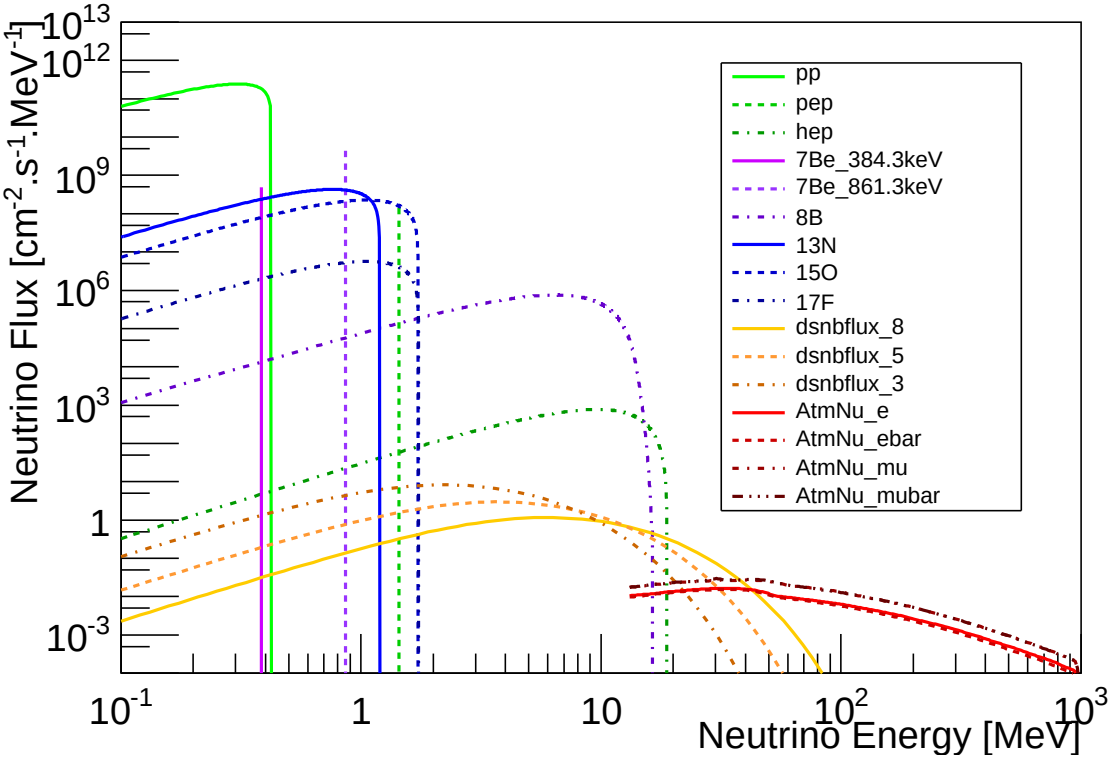

Figure 2.10: Solar, atmospheric and diffuse supernova neutrinos fluxes, which are backgrounds for dark matter and $0\nu\beta\beta$ experiments. Reproduced from [91]

2.4 Neutrinos

Cosmic neutrinos may produce a background in dark matter and $0\nu\beta\beta$ decay experiments. The sources that are relevant are solar neutrinos, atmospheric neutrinos and the diffuse supernova neutrino background. Solar neutrinos are composed by several contributions corresponding to the primary reaction in the sun. Atmospheric neutrinos are produced through cosmic ray collisions in the Earth's atmosphere. The collisions produce pions which then decay to muons and electron neutrinos and antineutrinos. The diffuse supernova neutrino background (DSNB) is the flux from the past history of all supernova explosions in the Universe. The neutrino flux spectra from these sources are shown in Fig. 2.10.

Solar neutrinos become a significant background for $0\nu\beta\beta$ experiments with large liquid scintillator masses as SNO+, but they are negligible in experiments where the active detector is mainly the double beta decay isotope. Given the higher flux and the solar neutrino energies, the only relevant contribution to $0\nu\beta\beta$ experiments is that from ^{8}B (see Fig. 2.10) , which arise from the decay $^8\mathrm{B} \rightarrow {}^7\mathrm{B}^* + \mathrm{e}^+ + \nu_e$. The scattering of the ν_e with an electron in the SNO+ detector produces a flat, continuum spectrum in $0\nu\beta\beta$ region [44].

Direct dark matter detection experiments will be sensitive to the flux of solar, atmospheric, and diffuse supernova neutrinos. The cosmic neutrino background poses a hard limit on the discovery potential of future direct detection experiments [91]. The maximal sensitivity that light WIMP searches could reach is $\sim 10^{-45}$ cm^2 and heavy WIMP searches $\sim 10^{-49}$ cm^2, assuming no directional sensitivity [91]. Fig 1.17 shows the neutrino floor extending from 0.1 GeV to thousands of GeV (thick dashed orange) compared with current limits for spin-

independent elastic WIMP-nucleus cross-sections. Progress beyond this line would require a combination of better knowledge of the neutrino background, annual modulation, and/or directional detection.

2.5 Background from $2\nu\beta\beta$ decay

The standard process of double beta decay with neutrino emission has a continuous spectrum extending up to $Q_{\beta\beta}$. The minimal experimental signature of $0\nu\beta\beta$ decay is a peak at the energy $Q_{\beta\beta}$. For this reason, $2\nu\beta\beta$ decay represents a background for the techniques with modest energy resolution, since the tail of the $2\nu\beta\beta$ spectrum containing the highest energy $2\nu\beta\beta$ events may extend up to the $0\nu\beta\beta$ signal region. This is the case for example in KamLandZen-800 [36], in which $2\nu\beta\beta$ ^{136}Xe represented one of the most important backgrounds. Another possible background arises from the random coincidence of two or more $2\nu\beta\beta$ events happening so close in time that the signal is equivalent to that of the sum of the two events, summing up to an energy in the $0\nu\beta\beta$ signal region. In practice, the experiments that encounter this background are the ones using ^{100}Mo with a relatively fast $2\nu\beta\beta$ decay time of 7.1×10^{18} yr [92], like CUPID. We will discuss the $2\nu\beta\beta$ background in CUPID in chapter 6.

Chapter 3

How to measure radioactivity in materials?

Todo sirve para algo
Pero nada sirve para todo

Mafalda (& Felipe)

Material selection in terms of radiopurity is crucial to restrain the background counting to the required levels. This chapter describes the techniques that are commonly used to asses the radioactive impurities in materials, one of the main backgrounds in present and future $0\nu\beta\beta$ decay and direct dark matter searches. The chapter is organized as follows: section 3.1 gives a general overview of the radioactivity in materials and the radionucleides that are measured with each technique, showing that they are complementary. Section 3.2 describes gamma-ray spectrometry, including two articles on the development and construction of two low background detectors. Section 3.3 presents the principles of Inductively Coupled Mass Spectrometry and Neutron Activation Analysis. Section 3.4 describes surface screening, including an article on the BiPo-3 detector. Finally, we conclude in section 3.5 with the Conclusion and perspectives.

3.1 Introduction

We speak of secular equilibrium if the activity of ^{238}U and ^{232}Th, the progenitors of the uranium and thorium chains, is the same as that of their daughters. This is the case if the material has been undisturbed during a period of about 10 $\times$ the half life of the daughter radionuclides, which happens in materials found in nature, for example, rocks, soils, or ores from which metals are extracted. However, the fabrication of man-made materials requires chemical processes which remove either the parent radionuclide, or its decay product because of their different chemical properties, and therefore secular equilibrium is usually broken in the materials used in the detector construction. It is thus important to asses the radioactivity of the progenitors as well as the descendants.

Once a radionucleide is extracted from the chain, which happens typically for radium in the uranium and thorium chains, subsequent short-lived daughters reach equilibrium within a short time scale. We define this group as a subchain. Fig 3.1 shows the ^{238}U and ^{232}Th chains, where the subchains are shown with blue circles. In the uranium chain, the ^{226}Ra subchain includes short-lived radionucledes from ^{226}Ra to ^{214}Po. Radionucleides from ^{210}Pb to ^{206}Pb constitute

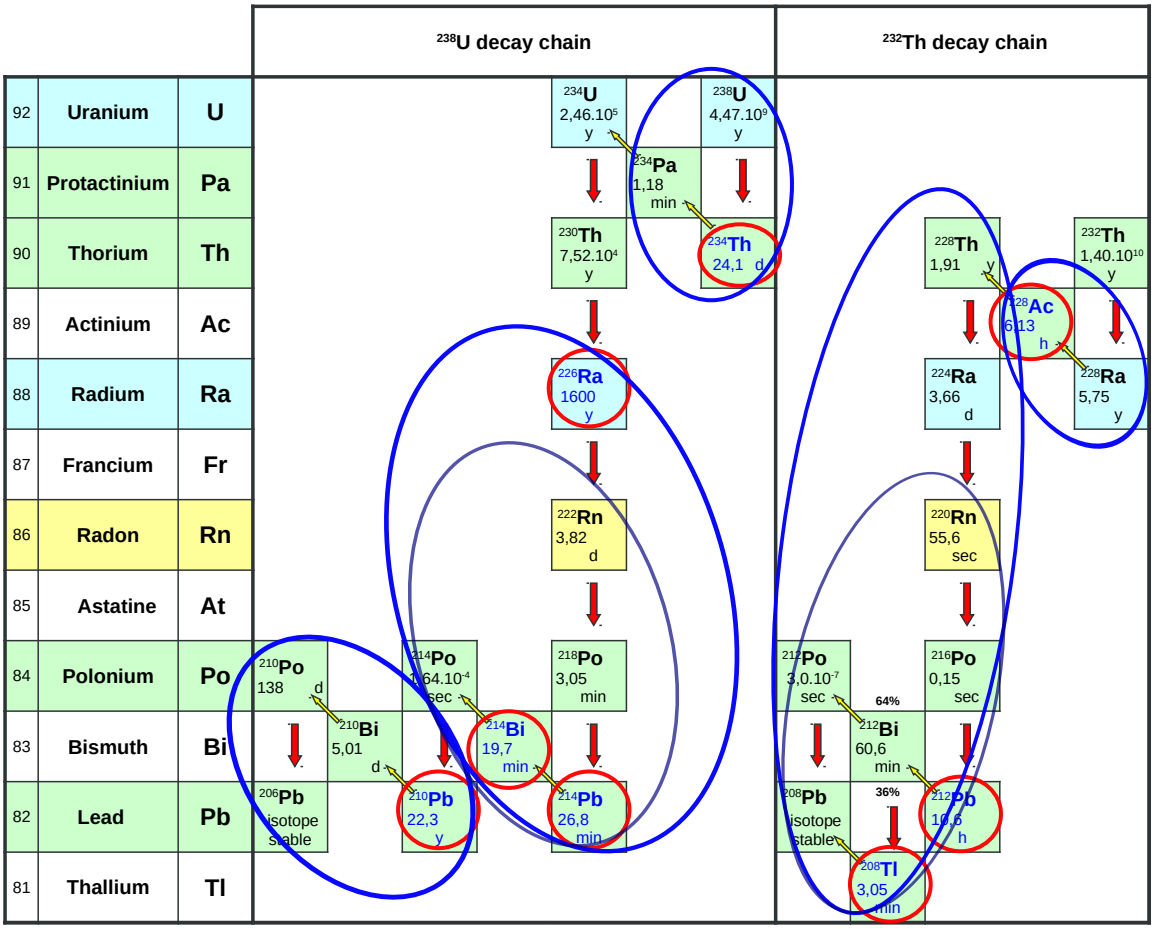

Figure 3.1: The ^{238}U and ^{232}Th decay chains. β and α disintegrations are indicated with a yellow and red arrow respectively. The break of secular equilibrium is shown and the subchains are marked with a blue circle: ^{226}Ra and ^{210}Pb subchains in the uranium chain and ^{228}Ra and ^{228}Th subchains in the thorium chain. If the material allows radon diffusion then equilibrium is broken at the level of ^{222}Rn/^{220}Rn, indicated with a dark blue circle. The activity of ^{238}U and ^{232}Th, the progenitors, can be measured with Mass Spectrometry or Neutron Activation Analysis. Gamma emitters used in γ-ray spectrometry are indicated with red circles. This technique is able to asses the lower parts of the chains, ^{226}Ra, ^{210}Pb and ^{228}Ra and ^{228}Th subchains. Additionally, ^{214}Bi and ^{208}Tl contaminations can be measured via the delayed coincidences of the β and the α particles in the BiPo cascade.

the ^{210}Pb subchain. In the thorium chain, secular equilibrium may be broken at the level of ^{228}Ra; its daughter,^{228}Ac, soon reaches equilibrium with it. Finally ^{228}Th decays subsequently with short-lived isotopes till ^{208}Pb which is stable.

Inductively Coupled Plasma Mass Spectrometry (ICPMS) and Neutron Activation Analysis (NAA) are able to measure the progenitors ^{238}U and ^{232}Th (section 3.3), and γ-ray spectrometry (section 3.2) can measure the lower part of the chains through the γ emitting radionuclides shown with red circles in Fig. 3.1.

Gamma ray spectrometry is a non-destructive technique able to measure large quantities, up to some tens of kg, while ICPMS and NAA are destructive and measure low amounts of material of the order of mg. However, γ-ray spectrometry typical sensitivities are about 0.1 – 1 mBq/kg while ICPMS and NAA reach typically μBq/kg.

3.2 Ultra low background gamma ray spectrometry

Ultra-low background germanium γ-spectrometers have been developed since many years for material selection in rare event searches in astroparticle and neutrino physics [93, 94]. The low background detectors are also widely exploited in environmental sciences [95, 80], geology, biology and also in the research of software errors in microelectronics [96, 97].

The detection limit that high purity germanium (HPGe) detectors can reach is given by:

$$\text{Detection Limit} = \frac{1}{\varepsilon \cdot M \cdot P_\gamma}\sqrt{\frac{B \cdot \Delta E}{t}} \tag{3.1}$$

with ε the detection efficiency, M the sample mass, t the measuring time, B the background, ΔE the energy resolution and P_γ the probability of emission of the γ quanta.

To be able to reach low sensitivities, HPGe's need to reduce their backgrounds, and thus are placed underground. Besides the necessity to reduce the cosmic-ray flux, HPGe's have also to be protected against background gamma-rays with appropriate shields, and they are generally flushed with a radon-free gas. Finally, many developments involve also the selection of the construction materials.

Fig. 3.2 shows the integral background rates of HPGe detectors at several underground depths together with the muon flux. Below 500 m.w.e the background reaches a plateau, we conclude that the muon background is relevant for depths above 500 m.w.e while below this depth, the driving background source is the radioactivity from detector components. Several efforts have been made to reduce the intrinsic background of γ-spectrometers [98, 99] by selection of very low radioactive materials and new configuration designs.

Fig. 3.3 shows schematically the internal configuration of a low background HPGe developed for material screening at LSM. The Ge crystal is operated at nitrogen temperature. The signal is read by a FET, a first stage of amplifier also at nitrogen temperature. The crystal and the FET are cooled down with a cold finger and the whole detector is housed in a vacuum tight endcap. Typicallly HPGe's are operated at 2000 - 3000 V voltage bias and the energy resolutions are 1 – 2 keV at 1332 keV.

HPGe detectors can be classified according to the shape of the Ge crystal as: planar, coaxial or well type, shown schematically in Fig. 3.4. Large volume p-type crystals are used in coaxial shapes and they may accommodate Marinelli shaped samples allowing to measure high masses. They are well suited for the detection of the 2614 keV ^{208}Tl γ line, one of the main

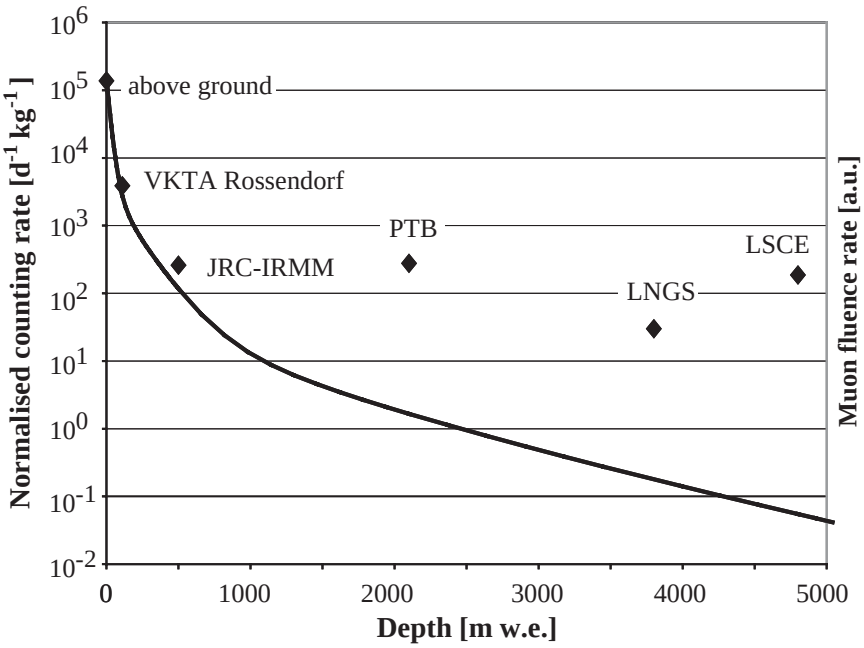

Figure 3.2: Integral background rate in the energy range [40 – 2700] keV normalized by the Ge crystal mass, for some HPGe detectors at different locations. The solid line is the muon flux in arbitrary units. Reproduced from [100].

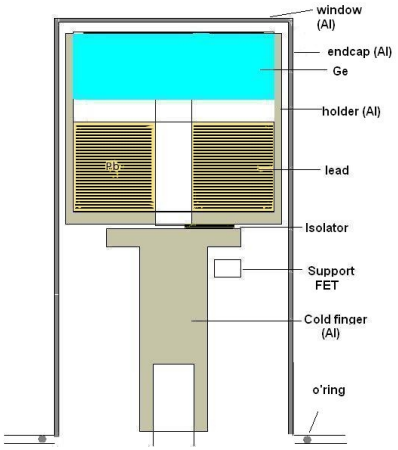

Figure 3.3: Scheme of a HPGe detector for low background gamma ray spectrometry.

backgrounds in $0\nu\beta\beta$ decay experiments. The planar geometries using point-contact detectors feature improved energy resolutions and are able to measure lower γ energies, down to ~ 30 keV, in particular the 46 keV γ line of ^{210}Pb which is useful for dark matter experiments material selection. Well-type detectors can place only small sample masses but have large detection efficiencies.

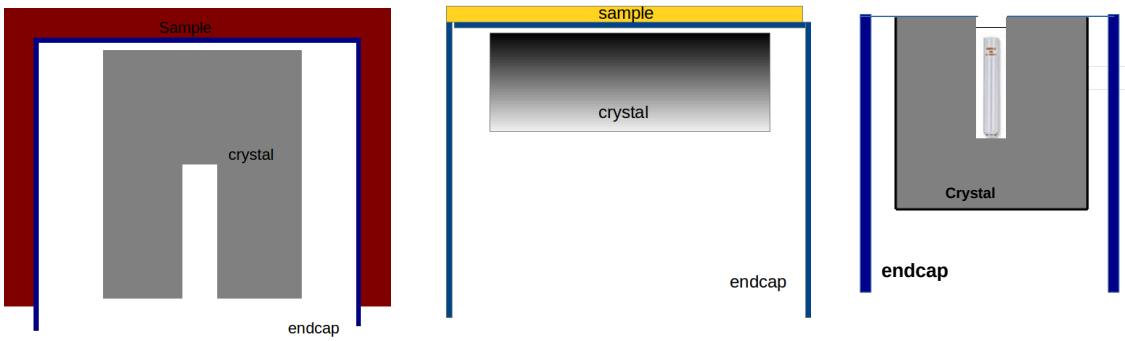

Figure 3.4: Schemes of HPGe types according to the Ge crystal (in grey) shape. Left: the coaxial detectors may accommodate Marinelli shaped samples (in brown) allowing to measure high masses. Center: the planar geometries using point-contact detectors feature improved energy resolutions and are able to measure lower γ energies, down to ~ 30 keV. Right: well-type detectors can measure small masses, with detection efficiencies much higher than the coaxial or planar HPGe's.

In practice we measure the activity of the ^{226}Ra subchain through the gamma emitters ^{214}Pb and ^{214}Bi[1]. The activity of ^{210}Pb and its descendants can be assessed through ^{210}Pb itself. On the thorium decay chain, we have access to the activity of ^{228}Ra through the decay of ^{228}Ac (since ^{228}Ra has a rather short period of 5.7 y, it is possible that the secular equilibrium with ^{232}Th is restored). In the lower part of the thorium chain, we assess the activity of the ^{228}Th subchain through ^{212}Pb and ^{208}Tl.

3.2.1 Development, construction and performances of a low background planar HPGe

This section presents the development of a low background planar HPGe now in operation at LSM, published in the article included below [101]. The detector, built in close collaboration with Mirion technologies, former CANBERRA, has a Ge crystal 30 mm high, 80 mm diameter and mass = 800 g. The innovation in the design consisted in the addition of a roman lead cylinder just below the crystal, to shield it from the first stage of the preamplifier components. The increase in the distance between the crystal and the preamplifier slightly worsened the energy resolution, however this did not affect the spectral analysis performances. This was the first time such configuration was used in a HPGe for γ spectrometry. The innovative design reduced the intrinsic background to 140 counts/day in the energy range [20,1500] keV (after the decay of the cosmogenic isotopes). A photo of the detector is shown in Fig. 3.5. On the left, we see the endcap and the pulse tube used to cool down, and on the right, the lead shielding previous to the installation of the detector. The planar detector, named Mafalda, was initially

[1]also ^{226}Ra but this is much less used because the most intense gamma has only 3% emission probability and it interferes with a ^{235}U γ-line

employed for material selection in the EDELWEISS dark matter search. The reduced dead layer compared to a coaxial detector allows for measurement of low energies gammas, 46 keV from ^{210}Pb and also 63 keV and/or 93 keV γ-lines of ^{234}Th (in equilibrium with ^{238}U). The planar geometry allows in particular to assess ^{210}Pb on surfaces due to the radon deposition.

Figure 3.5: Mafalda, the planar low background HPGe for gamma spectrometry installed at LSM. Left: the detector endcap, the cold finger and the pulse tube. Right: lead shielding.

Article: P. Loaiza *et al*, NIMA 634, 64 (2011)

Nuclear Instruments and Methods in Physics Research A 634 (2011) 64–70

Contents lists available at ScienceDirect

Nuclear Instruments and Methods in Physics Research A

journal homepage: www.elsevier.com/locate/nima

Low background germanium planar detector for gamma-ray spectrometry

P. Loaiza [a,*], C. Chassaing [d], Ph. Hubert [b], A. Nachab [b], F. Perrot [b], J.-L. Reyss [c], G. Warot [a]

[a] Laboratoire Souterrain de Modane, CEA-CNRS, 1125 route de Bardonnèche, 73500 Modane, France
[b] Centre d'Etudes Nucléaires Bordeaux Gradignan, CNRS/IN2P3 et Université de Bordeaux1, UMR 5797, Gradignan F-33175, France
[c] Laboratoire des Sciences du Climat et de l'Environnement, Av. Terrasse Bat 12, F-91198 Gif sur Yvette, France
[d] CANBERRA France, 1 chemin de la Roseraie, BP 311, F-67834 Tanneries, France

ARTICLE INFO

Article history:
Received 19 August 2010
Received in revised form
3 January 2011
Accepted 4 January 2011
Available online 15 January 2011

Keywords:
gamma – ray spectrometry
Low-background
Monte Carlo simulation

ABSTRACT

A new ultra-low background planar germanium spectrometer has been developed. The planar geometry improves the sensitivity and energy resolution below 600 keV. The integral background counting rate in the Laboratoire Souterrain de Modane (4800 m water equivalent) in the energy range from 20 to 1500 keV for the planar Ge (mass=800 g) is 140 count/day. After 40 days of statistics, the background counting rates for all expected single lines are below 0.5 count/day with the exception of ^{210}Pb(46-keV line) which was measured to be (1.76 ± 0.25) count/day. Monte Carlo simulations have been performed to explain the origin of the remaining background and to calculate the detection efficiencies. Sensitivities around 1 mBq/kg are obtained within few days of statistics for ^{226}Ra and ^{228}Th. The main achievement is the high sensitivities for ^{210}Pb (46-keV line) and ^{238}U (^{234}Th: 63 and 93 keV lines). For an aluminium sample (mass=1 kg) the limits obtained in 15 days are ^{210}Pb < 9 mBq/kg and ^{238}U < 3 mBq/kg.

1. Introduction

Ultra-low background germanium-spectrometers have been in development for many years for the purpose of providing low radioactivity measurements for material selection in rare event searches in astroparticle and neutrino physics [1,2]. The capability to measure very low radionuclide concentrations is also applied to environmental measurements [3,4] and other applications [5]. Several efforts have already been made in the last years to reduce the intrinsic background of coaxial and well-type germanium-spectrometers [6]. Nowadays it is well known that in order to reach low background levels the cryostat must be built with very low radioactive materials, surrounded with low radioactive shielding and operated in a deep underground laboratory. In this paper, we present the development of a low background planar germanium spectrometer now in operation at the Laboratoire Souterrain de Modane, LSM (4800 m water equivalent), which has been built in the framework of the ILIAS European program [7]. This new spectrometer is mainly dedicated to material selection for the dark matter experiment EDELWEISS-II [8] and to the R&D of the double beta decay experiment SuperNEMO [9].

2. Detector description and design considerations

The high purity germanium crystal has a diameter of 80 mm and a thickness of 30 mm (150 cm^3 active volume). This type of detector, called BEGe-detectors, has been chosen to enhance low-energy gamma-rays efficiency and energy resolution. This feature is particularly important in order to measure the 46-keV gamma-line of ^{210}Pb and 63 and 93-keV lines of ^{234}Th, a descendant of the ^{238}U chain. These two radionuclides are a substantial background in experiments for rare-event searches. Although these low-energy gamma-rays can be measured with high efficiency using well-type Ge spectrometers, the planar geometry allows much better energy resolution (typically FWHM=700 eV at 122 keV), higher sample masses and a variety of sample shapes.

The detector construction was performed in close cooperation with CANBERRA France. The endcap and crystal holder, shown on Fig. 1, have been made of aluminium specially selected for its high radiopurity (Al–(4%)Si). This special alloy has been chosen since this low Z material contains almost no cosmogenic activity (only ^{26}Al $= 0.38 \pm^{0.19}_{0.14}$ mBq/kg). However the main drawback is the thorium contamination at the level of 0.3 ppb. For the window the same aluminium alloy was chosen, as a compromise between minimizing the radioimpurities and keeping a high transmission at low energies. The window is 1.7 mm thick, determined by mechanical stress constraints. Carbon or beryllium windows were not chosen since, while they allow good transmission, they may contain U and K contaminations [10]. The transmission at 46-keV

* Corresponding author.
E-mail address: ploaiza@lsm.in2p3.fr (P. Loaiza).

0168-9002/$ - see front matter © 2011 Elsevier B.V. All rights reserved.
doi:10.1016/j.nima.2011.01.017

is reduced only by 10 % for the aluminium with respect to the carbon window.

From our previous experience in low background detectors the main contributions to the intrinsic background come from the aluminium, the isolators, the first stage of the cold preamplifier, and the O-ring of the cryostat (see Fig. 1). Other components include mechanical parts such as screws specially made of lead-free brass and plastic holders. The radioimpurities of all components have been measured using HPGe spectrometers in LSM, Centre d'Etudes Nucléaires Bordeaux Gradignan (CENBG) and Gran Sasso and a selection of results are presented in Table 1.

The contributions of the cryostat components to the intrinsic detector-background were studied by means of simulations using GEANT 3 Monte Carlo codes (details on the Monte Carlo are given in Section 3.2). The radionuclide concentrations that were used are listed in Table 1.

Table 2 shows the results of the simulation of the expected background at the 238-keV gamma-line due to the main materials involved in the construction of the cryostat, for the standard configuration shown in Fig. 1 as Config. I. The 238-keV gamma-line from ^{212}Pb in the thorium chain is the most intense line in the background spectrum if there is an internal thorium pollution.

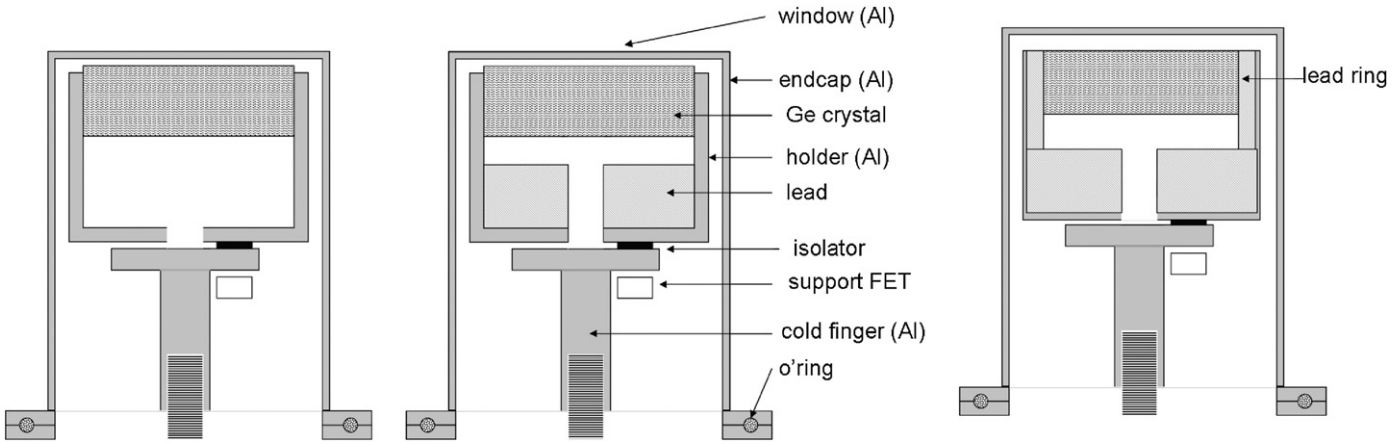

Fig. 1. Configurations studied for the Ge spectrometer. Config. I (left), Config. II (centre), Config. III (right), not to scale. The crystal and the cryostat are placed inside the endcap. Config. I corresponds to the standard configuration. Different detector configurations were tested to reduce the intrinsic background. A roman lead cylinder was placed below the crystal (Config. II) and, additionally, a roman lead ring was placed around the crystal (Config. III).

Table 1
Radionuclide concentrations (in mBq/kg, otherwise stated) in some materials used in the cryostat construction measured by gamma-ray spectrometry, except for ^{210}Pb in Roman lead, which was measured using radiochemistry followed by α spectrometry. The ^{210}Pb content in aluminium was measured at LSM.

Material	Det. loc.	^{238}U	^{226}Ra	^{228}Ra	^{228}Th	^{40}K	Others
Aluminium	Gran Sasso	<9.3	0.27 ± 0.19	<0.11	1.4 ± 0.2	$1.1\pm^{0.2}_{0.1}$	^{137}Cs 1.3×10^{-4} ^{26}Al $0.38\pm^{0.19}_{0.14}$ ^{235}U <0.3 ^{210}Pb <9
Isolators	LSM	<160	13.2 ± 0.9	65 ± 15	293 ± 20	<170	
FET support	Bordeaux	<3 mBq/unit	1.6 ± 0.2 mBq/unit	2.9 ± 0.6 mBq/unit	<0.5 mBq/unit	<5 mBq/unit	^{207}Bi 1.7 ± 0.7 mBq/unit
O-ring	LSM		1500 ± 40	300 ± 30	170 ± 20	3200 ± 200	
Roman lead	LSM		<0.3 [12]	<0.3 [12]			^{210}Pb <121

Table 2
Simulation results of the 238 keV gamma-line contributions to intrinsic background of the Ge planar detector for the three configurations presented in Fig. 1. The activities of the materials used have been measured and are given in Table 1. The quoted upper limits $<10^{-5}$ result from no events in the background obtained from a simulation equivalent to 10^5 days of counting. The statistical uncertainties are 10–20% for values between 10^{-3} and 10^{-1} and 1% for values between 0.5 and 1. For the FET support the expected contributions are indicated as limits since the Th contamination measurement gives a limit to this concentration.

Component	Mass (g)	Contribution to intrinsic background at 238 keV (count/day)					
		Config. I	Config. II				Config. III:
			1 cm	2 cm	3 cm	4 cm	4 cm + 5 mm lead ring
Al endcap	374	0.86	0.62	0.61	0.58	0.56	0.11
Al holder	263	1.06	0.91	0.82	0.746	0.683	0.012
Al cold finger	234	0.182	$1.4\ 10^{-4}$	$<10^{-5}$	$<10^{-5}$	$<10^{-5}$	$<10^{-5}$
Isolator	12	5.34	$3.3\ 10^{-3}$	$<10^{-5}$	$<10^{-5}$	$<10^{-5}$	$<10^{-5}$
FET support	1.1	<0.34	$<2.2\ 10^{-4}$	$<10^{-5}$	$<10^{-5}$	$<10^{-5}$	$<10^{-5}$
O-ring	5.9	0.200	0.007	0.005	$<10^{-5}$	$<10^{-5}$	$<10^{-5}$
Total		**7.98**	**1.54**	**1.44**	**1.33**	**1.24**	**0.12**

The aim is to obtain an intrinsic background of about 0.1 count/day. The ^{228}Th contamination in the isolators (293 ± 20) mBq/kg would increase the intrinsic background to the unacceptable level of 5 count/day, even for the small masses involved in the construction. The aluminium endcap and holder also show non-negligible contributions of about 1 count/day. The O-ring used for the vacuum, even containing high radioactivity levels, gives minor contributions since it is placed far from the crystal. The total expected background is 8 count/day at 238-keV, which is an unacceptably high background level. Therefore, the standard configuration has been modified by the addition of a roman lead cylinder to shield the crystal against the radioactivity of the materials placed below, as shown in Config. II in Fig. 1. Several lead thicknesses have been studied, as shown in Table 2. Simulations showed that the addition of 1 cm of lead should reduce the intrinsic background by a factor 5, the most important effect being the shielding of the radioactivity of the isolators. Table 2 shows the effect of increasing the lead thickness. The contribution of all the components should result in a background counting rate of 1.24 count/day at 238-keV for a thickness of 4 cm. Nevertheless, the addition of the lead has almost no effect in the reduction of the background induced by the Al endcap and holder. Hence, 5 mm of lead was added around the Ge crystal, as shown in Fig. 1, Config. III. With this last modification the contributions from the Al endcap and holder are noticeably suppressed. Simulations of Config. III showed that the intrinsic background should be reduced to 0.12 count/day at 238-keV.

As can be deduced from Table 2, a lead thickness of 1 cm below the crystal (shielding the Al cold finger, the isolators, the FET support and the O-ring) plus a 5-mm lead ring around the crystal (shielding the Al endcap and holder) would be enough to achieve the required intrinsic background levels at 238-keV. Nevertheless, the contributions at higher energy-lines should also be considered. Table 3 shows the simulation results for the intrinsic background at 583-keV produced by the most radioactive materials in our cryostat. The background peak rate induced by the isolators, the materials containing the highest thorium impurities, is still unacceptably high if 1 cm of lead is used, but drops below 10^{-4} count/day for a lead thickness of 4 cm (Config. II). With the further addition of the lead ring around the crystal, the total count rate at the peak is expected to be about 0.1 count/day, which reaches the background level goal. Therefore, the chosen configuration includes the addition of 4 cm of lead below the crystal plus a lead ring of 5 mm around the crystal (Config. III).

The 4-cm-thick internal lead cylinder has been made of roman lead dated to the fourth century, recovered near Ploumanac'h, in French Brittany [11]. The shielding inner layer is made out of roman lead as well. Radioactivity measurements of the roman lead are presented in Table 1. The ^{210}Pb content has been measured by radiochemical separation of the ^{210}Po and subsequent spectrometry (decision threshold given according to ISO 11929-3:2000 with $=0.025$ [13], see also Ref. [23]).

3. Detector installation and performance

The spectrometer is installed in the underground laboratory LSM, where the overburden of 4800 m water equivalent reduces the cosmic muon flux to 4 $\mu/m^2/day$ [16]. The shielding is made of lead that has been cast in a cylindrical shape in order to minimize the free air-spaces. The innermost layer consists of 5 cm of roman lead. The outer layer consists of 15 cm "low activity" lead with a ^{210}Pb contamination of 10–20 Bq/kg. The whole system is flushed permanently by de-radonised air ($Rn \approx 20$ mBq/m^3) provided by a facility at LSM [14]. The cryostat is cooled down by means of a Pulse Tube CP5© (Canberra) [15]. Tests showed that there is no degradation in the energy resolution due to vibrations.

3.1. Background measurements

The background count rate was measured immediately after the installation of the detector underground in April 2008, some months later in January 2009 and in October 2009. The integral count rate [20–1500 keV] decreased from an initial value of 226 to 141 count/day in October 2009 due to the decay of short living cosmogenic nuclei (Table 4).

Table 5 lists the count rates of the cosmogenic radionuclides present in the Ge crystal during the measuring periods given in Table 4. The 143-keV line of ^{57}Co (corresponding to the sum of the 122 keV gamma-line, a 14.4-keV gamma from de-excitation and a 6.4-keV X-ray) and the 1124-keV line from ^{65}Zn decreased between the two measurements, while the ^{58}Co (817-keV) completely disappeared.

Fig. 2 shows the background spectrum measured during the Period 2, corresponding to 40 days of measurement. The single lines

Table 4
Integral background count rates (20–1500 keV) for two measurement periods. Uncertainties are purely statistical.

	Measuring period	Measurement time (days)	Integral count rate (day^{-1})
Period 1	April 2008	20	226 ± 3
Period 2	January/ February 2009	40	164 ± 1
Period 3	October 2009	13	141 ± 3

Table 3
Simulation results of the 583 keV gamma-line contributions to intrinsic background of the Ge planar detector for the three configurations presented in Fig. 1. The activities of the materials have been measured and are given in Table 1. The quoted upper limits $<10^{-4}$ result from no events in the background obtained from a simulation equivalent to 10^4 days of counting. The statistical uncertainties are 20% for values between 10^{-3} and 10^{-2} and 1–3% for values between 10^{-1} and 1. For the FET support the contributions to the background are indicated as limits since the Th concentration used as input is measured as a limit.

Component	Mass (g)	Contribution to intrinsic background at 583 keV (count/day)					
		Config. I	Config. II				Config. III
			1 cm	2 cm	3 cm	4 cm	4 cm + 5 mm lead ring
Al. endcap	374	0.197	0.142	0.135	0.128	0.109	0.06
Al. holder	263	0.225	0.18	0.164	0.150	0.134	0.06
Al. cold finger	234	0.057	0.014	0.003	$<10^{-4}$	$<10^{-4}$	$<10^{-4}$
Isolator	12	1.40	0.339	0.080	0.019	$<10^{-4}$	$<10^{-4}$
FET support	1.1	<0.12	<0.032	<0.008	<0.003	$<10^{-4}$	$<10^{-4}$
O-ring	5.9	0.07	0.018	0.006	0.002	$<10^{-4}$	$<10^{-4}$
Total		**2.07**	**0.73**	**0.4**	**0.3**	**0.25**	**0.12**

that appear are only the 46-keV, the Pb X-rays and the cosmogenic radionuclide lines at 143-keV from ^{57}Co and at 1124-keV from ^{65}Zn. The presence of a single peak at 238-keV and at 511-keV from the 40 days-measurement-spectrum inspection is not obvious.

Table 5
Background count rates for cosmogenic radionuclides. The measuring periods correspond to the measuring periods given in Table 4. Uncertainties are purely statistical.

Isotope	$T_{1/2}$	Energy ($E_{\gamma+X}$)	Peak counting rate (per day)		
			Period 1	Period 2	Period 3
^{57}Co	271 days	122+14.4+6.4=143 keV	3.4 ± 0.4	1.9 ± 0.3	< 0.7
^{58}Co	71 days	810 + 7= 817 keV	0.8 ± 0.2	< 0.3	< 0.5
^{65}Zn	244 days	1115+9.5=1124.5 keV	2.2 ± 0.3	0.7 ± 0.2	< 0.6

The background count rates for single lines of several nuclides are given in Table 6. All count rates are below 0.5 count/day, except for ^{210}Pb.

3.2. Origin of the background

To understand the origin of the remaining background, extensive Monte Carlo simulations have been performed as detailed in the next subsection.

3.2.1. Monte carlo simulations

The Monte Carlo simulation used the GEANT 3.21 code [17] together with the DECAY code developed by the University of Southampton [18]. This latter code simulates nuclide decays, taking into account the physical information from the decay

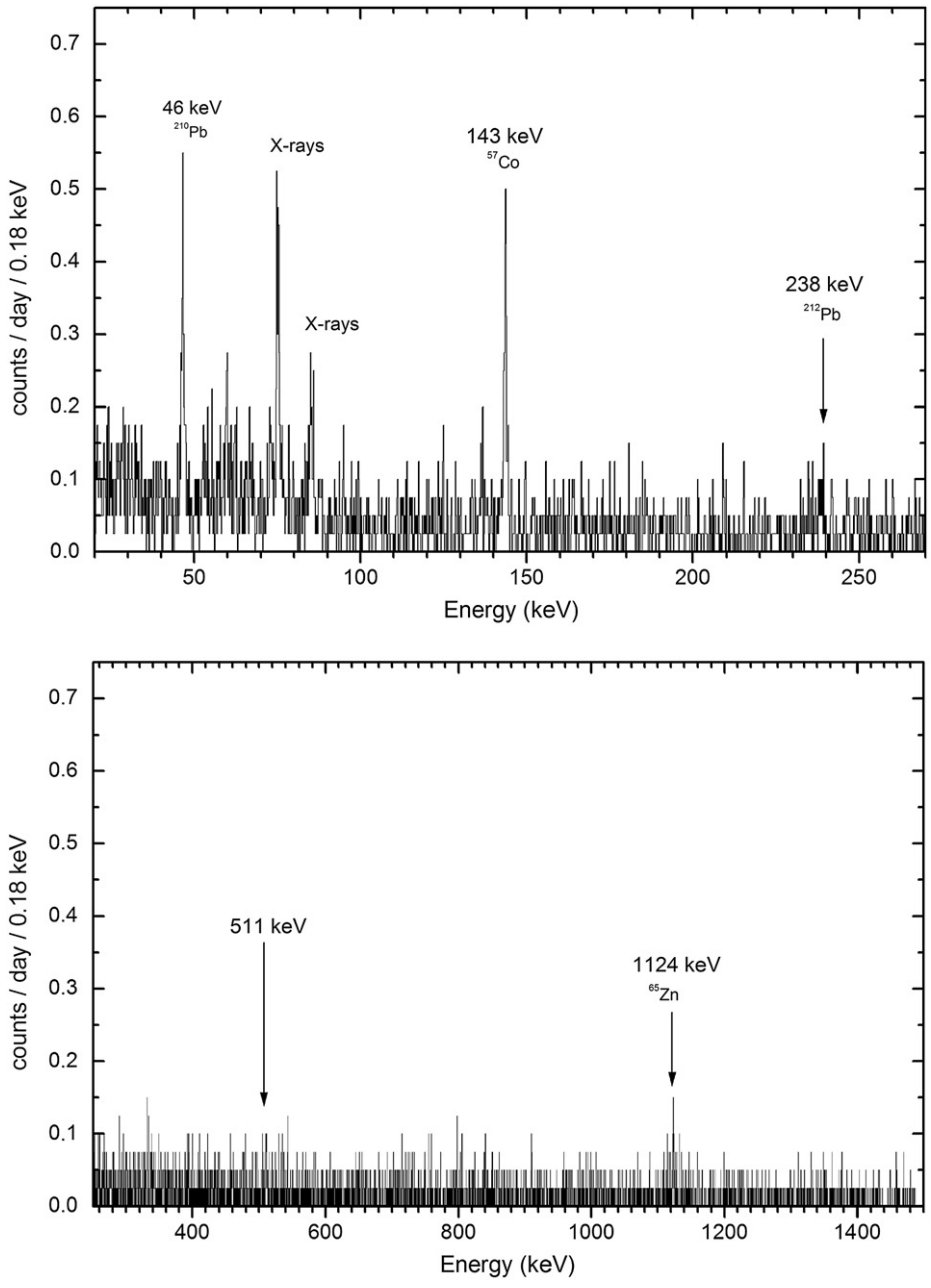

Fig. 2. Background spectrum of the planar germanium spectrometer measured in January 2009 (8 months after its installation underground) at LSM (measurement time = 40 days).

schemes. Basically, a decay is 'followed' through the decay scheme, the branching ratios being respected through Monte Carlo techniques. It was designed to handle all kinds of decays (α, β^-, β^+, EC), the emission of the associated particles and energy distribution, the following de-excitation of the nucleus (γ, IT) and the accompanying X-rays and Auger electrons [19]. The information concerning the decay schemes of more than 2200 isotopes have been taken from the NNDC's Evaluated Nuclear Structure Data File (ENSDF) [20], the Table of Isotopes [21] and the Decay Data Evaluation Project [22]. All the particles generated through a single decay are then fed into the GEANT simulation.

3.2.2. Single lines

The background due to the main components of the cryostat has been obtained using the Monte Carlo simulations described above. Table 7 shows the expected contributions for the main gamma-lines, assuming the activity levels given in Table 1. A blank is quoted when there is no activity measurement available, as in the case of ^{234}Th in lead. All individual contributions to the intrinsic background (with exception of lead ring) are below 1 count/day achieved by a rigorous material selection. The calculated lead ring contributions are up to ≈ 1 count/day since this piece is critically placed in close contact with the Ge crystal.

The expected single-line background rates are obtained by summing-up the individual contributions and are indicated in the second-to-last column in Table 7. These results are consistent with the measured values shown in the last column in Table 7.

It can be noted that some measured background levels are below the expected background from simulations, as in the case of ^{214}Pb, ^{228}Ac or ^{210}Pb. An inspection of the values in Table 7 shows that this effect is due to the predicted simulated contributions from the lead parts. Therefore, the simulation results may be used to constrain the radioimpurity levels in the lead. For the 352-keV line, the experimental background rate is below the result predicted by the simulation by a factor 5. Thus, the limit on the ^{226}Ra activity in lead can be lowered by a factor 5, which leads to a ^{226}Ra contamination in roman lead to be <0.06 mBq/kg.

In a similar way, the comparison between the simulation results and the experimental data at 911-keV constrains the ^{228}Ra in lead to be <0.1 mBq/kg.

The measured background at 238-keV has a relatively large statistical uncertainties due to the low counting rates even for 40 days of live-time. The measured background is compatible within the statistical uncertainties with the Monte Carlo predictions used to design the cryostat as described in Section 2.

The results in Table 7 obtained for the 46-keV line show that the ^{210}Pb in the aluminium window as part of the Al endcap gives a negligible contribution to the single peak background. The ^{210}Pb level in the internal roman lead is below 121 mBq/kg, as a result of the measurement detailed in Table 1. Using this number the background expected from the internal lead parts is <3.5 count/day, about a factor 2 higher than the measured background. Thus, the ^{210}Pb level in the roman lead can be constrained to 60 mBq/kg. While the roman lead cannot be excluded as the origin of the ^{210}Pb contamination, other non-controlled contaminations must be considered as possible sources, such as surface contaminations very close to the crystal.

3.2.3. Continuous background

In an effort to understand the origin of the continuous intrinsic background, the effects of some potential sources were simulated.

Table 6
Background count rates for single lines (measurement time = 40 days). The count rates are reported with statistical uncertainties. Decision thresholds are given according to ISO 11929-3:2000, with $\alpha = 0.025$ [13,23].

Nuclide	E_γ (keV)	Counts/day
^{238}U-chain:		
^{234}Th	63	<0.48
	93	<0.37
^{226}Ra + ^{235}U	186	<0.34
^{214}Pb	242	<0.31
	295	<0.30
	352	<0.30
^{214}Bi	609	<0.30
^{210}Pb	46	1.76 ± 0.25
^{232}Th-chain:		
^{228}Ac	338	<0.32
	911	<0.23
^{212}Pb	238	0.28 ± 0.18
^{208}Tl	583	<0.29
^{137}Cs	662	<0.26
^{60}Co	1173	<0.24
	1332	<0.22
^{40}K	1460	<0.36
β^+	511	0.58 ± 0.18

Table 7
Results of the simulated background count rates for single lines. The quoted upper limits $<10^{-3}$ result from no events in the background obtained from a simulation equivalent to 10^3 days of counting. The blanks state that there is no activity measurement available. The statistical uncertainties in the simulation results are about 10% for values $\approx 10^{-1}$ and 20%-30% for values $\approx 10^{-2}$. In order to compare with the experimental results, the right column shows the measured values.

Nuclide	E_γ (keV)	Contribution to intrinsic background obtained by MC simulation (count/day)								Meas. bckg (count/day)
		Lead ring $M = 556$ g	Lead $M = 3228$ g	Al endcap $M = 374$ g	Al holder $M = 263$ g	Isolator $M = 12$ g	Support FET $M = 1.13$ g	O-ring $M = 5.9$ g	Total	
^{238}U chain:										
^{234}Th	63	–	–	<0.07	$<10^{-3}$	$<10^{-3}$	$<10^{-3}$	$<10^{-3}$	<0.07	<0.48
	93	–	–	<0.08	$<10^{-3}$	$<10^{-3}$	$<10^{-3}$	$<10^{-3}$	<0.08	<0.37
^{214}Pb	295	<0.71	<0.07	0.01	0.01	$<10^{-3}$	$<10^{-3}$	$<10^{-3}$	<0.80	<0.30
	352	<1.38	<0.16	0.02	0.01	$<10^{-3}$	$<10^{-3}$	$<10^{-3}$	<1.57	<0.30
^{214}Bi	609	<1.27	<0.23	0.025	0.023	$<10^{-3}$	$<10^{-3}$	$<10^{-3}$	<1.55	<0.30
^{210}Pb	46	<2.5	<1.0	<0.3	$<10^{-3}$	–	–	–	<3.8	1.76 ± 0.25
^{232}Th-chain:										
^{228}Ac	338	<0.43	<0.05	$<10^{-3}$	$<10^{-3}$	$<10^{-3}$	$<10^{-3}$	$<10^{-3}$	<0.48	<0.32
	911	<0.67	<0.14	<0.01	<0.01	$<10^{-3}$	0.01	$<10^{-3}$	<0.83	<0.23
^{212}Pb	238	–	–	0.11	0.01	$<10^{-3}$	$<10^{-3}$	$<10^{-3}$	0.12	0.28 ± 0.18
^{208}Tl	583	–	–	0.07	0.06	$<10^{-3}$	$<10^{-3}$	$<10^{-3}$	0.12	<0.29
^{40}K	1460	–	–	0.01	0.02	<0.12	<0.01	0.04	<0.21	<0.36

Fig. 3 shows the simulated background contribution from the internal roman lead with a ^{210}Bi activity of 50 mBq/kg. The value of 50 mBq/kg is chosen since, according to the discussion in Section 3.2.2, the measured 46-keV background peak rate correspond to a ^{210}Pb activity <60 mBq/kg. The bremsstrahlung from the ^{210}Bi daughter produces a continuous background up to 750 keV.

Also shown in Fig. 3 is the expected background from the maximum possible content in thorium in the standard lead, ^{228}Th <10 mBq/kg, which produces an almost flat background. The measured background spectrum is partially explained by the two sources mentioned above.

Some other sources have been investigated. Table 8 details the results of the simulations of the integral background count rate of the detector for the contributions from the cryostat materials. The ^{210}Bi and ^{40}K contaminations in the external lead shielding and ^{40}K

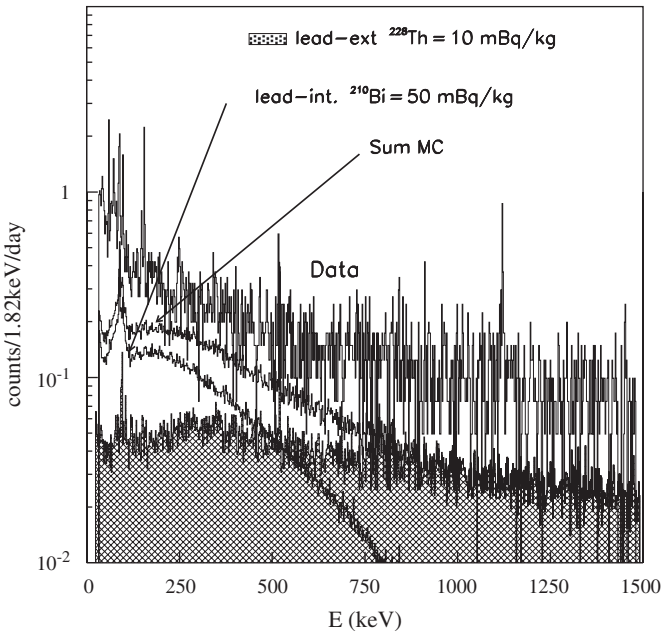

Fig. 3. Background spectra of the planar germanium spectrometer. From top to bottom: Experimental data, sum of the two simulated MC contributions, simulated contribution from ^{210}Bi = 50 mBq/kg in the internal roman lead, and simulated contribution from ^{228}Th = 10 mBq/kg in the external lead shielding.

Table 8
Contributions to the integral background count rate of the planar spectrometer obtained by Monte Carlo simulations.

Material	Radioimpurities assumed	Integral count rate $20 > keV < E < 1500$ keV (count/day)
Cryostat materials	See Table 1	<7
Roman lead internal	^{210}Bi <50 mBq/kg	<42
Lead external shielding	^{210}Bi $=20$ Bq/kg	<1
Lead external shielding	^{228}Th <10 mBq/kg	<33
Lead external shielding	^{40}K <15 mBq/kg	<3
Environmental Radioactivity	^{208}Tl, 2614 keV: 40×10^3 photons/cm^2/s [24]	11
Environmental Radioactivity	^{40}K, 1460 keV: 120×10^3 photons/cm^2/s [24]	1
Total simulation		**<98**
Total measured		**164**

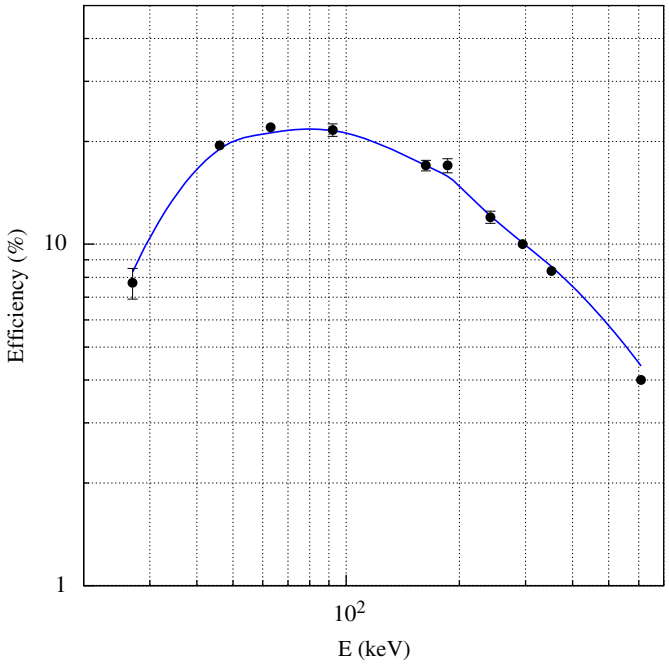

Fig. 4. Full Energy Peak detection efficiency of the planar germanium spectrometer measured with the RGU-1 sample described in the text (dots). Shown also are the results of the simulation (solid line).

and ^{208}Tl radioactivities from the environment were simulated. The external shielding lead contains 20 Bq/kg of ^{210}Bi which gives a negligible contribution to the background (<1 count/day). The environmental background, in particular ^{40}K and ^{208}Tl should generate just a few counts per day: 1 count/day from ^{40}K and 11 count/day from ^{208}Tl.

Clearly the measured background spectrum can not be accounted for only by the studied sources. The contribution from the cosmogenic radionuclides in the crystal, radon present in the sample-chamber air, surface contaminants, neutron-induced gammas and muon-induced gammas is currently under study.

3.3. *Efficiency and energy resolution*

Fig. 4 shows the result of the detection efficiency measurement using the IAEA-RGU-1 [25] reference material of 40 mm diameter and 3 mm height. The lowest energy point corresponds to 27 keV line from ^{231}Pa in the ^{235}U series, which is a remarkably low-energy line measured by gamma-ray spectrometry. The efficiency has been simulated using the GEANT3.21 Monte Carlo code described in Section 3.2.1. The comparison between the measured and the simulated efficiency shows an agreement better than 5%. The Monte Carlo simulation is used to determine the efficiencies for the different sample geometries and materials.

The resolution of the detector at 122 keV is 890 eV. Since the construction of the spectrometer has been made giving priority to the background reduction, some choices were made which resulted in a degradation of the energy resolution.

4. Sample measurements

This new planar spectrometer was used to measure the activity of different materials and a few are presented here as evidence of the detector's performance (Table 9). The measurement of $CaWO_4$ powder was made in the framework of a study aiming at minimizing the intrinsic radioactivity of crystal scintillators for dark matter

Table 9
Measured samples. The uncertainties given are expanded combined standard uncertainties, decision threshold according to Ref. [13].

Material	Weight (g)	Time (days)	Activity (mBq/kg)				
			^{210}Pb	^{234}Th	^{226}Ra	^{228}Ra	^{228}Th
$CaWO_4$	46	13	<30	<10	15 ± 3	<10	<7
Epoxy slab	47	16	35 ± 7	14 ± 3	9 ± 2	<6	10 ± 3
Aluminium	1025	15	<9	<3	<0.9	<1	0.98 ± 0.24

searches. The crystals are grown from the $CaWO_4$ powder, therefore it is necessary to asses the radiopurity of the raw material as a first stage. Table 9 shows results from $CaWO_4$ powder purchased from the NeoChem company (Moscow, Russia) specially synthesized to reduce the level of impurities. The powder is placed in a plastic box, with 80 mm diameter and 4 mm thickness. The crystal contamination levels required for the next generation of dark matter searches is about 0.01 mBq/kg, while the radioactive contamination of present $CaWO_4$ crystals remains 3–4 orders of magnitude higher [26]. Efforts are currently undergoing to reduce the intrinsic contaminations during the crystal production process [27].

As a second example, the contaminations of two superimposed ceramic slabs ($55\times54\times4$ mm each) are presented. This material is a compound in microelectronic integrated circuits (ICs). Alpha-particle have been known to produce Single-Event Upset in integrated circuits for many years. With the downscaling of CMOS technologies, the sensitivity of ICs to alpha contamination is a crucial question because of the constant reduction of the supply voltage and node capacitance [28]. Thus, it becomes necessary to minimize the radioactive impurities in the circuit materials. The sample for which the results are shown here has not undergone any particular fabrication process to assure its radiopurity, therefore the levels in Table 9 should be considered as normal contamination levels in this material.

The last measurement shown in Table 9 is for high purity aluminium used in the construction of low background detectors. In this case, the sample is an aluminium cylinder with a diameter of 110 mm and height of 40 mm. Specifically fabricated to decrease its radioactive contaminants, this aluminium is effectively used in dark matter search experiments (electronic boxes) or in the construction of low background HPGe detectors.

The sensitivities achieved in the ^{210}Pb and the ^{234}Th (thus, in ^{238}U) measurements are remarkably high sensitivities obtained with the gamma-ray spectrometry technique.

5. Conclusion

The low-level planar germanium spectrometer developed at LSM has an extremely low background achieved by modifying the standard commercial configuration and by careful selection of materials. The counting rates of single background lines are below 0.5 per day except for ^{210}Pb. The background at the single lines of U and Th and progeny are consistent with the Monte Carlo simulation of the background originating from the cryostat components radio-impurities. The integral background counting rate in the energy range from 20 to 1500 keV is 141 count/day as of October 2009, and keeps decreasing due to the decay of short living cosmogenic nuclei present in the crystal.

Acknowledgements

The authors would like to gratefully acknowledge the LSM technical staff for their help. Matthias Laubenstein is warmly thanked for helpful discussions and for the aluminium measurement. Rodolfo Gurriaran has kindly provided the initial Monte Carlo code. This work was supported by the ILIAS integrating activity (Contract n: RII3-CT-2004-506222) as part of the European Union FP6 programme in Astroparticle Physics.

References

[1] Arpesella, et al., Astropart. Phys. 18 (2002) 1.
[2] Arnold, et al., Nucl. Instr. and Meth. A 536 (2005) 79.
[3] M. Hult, et al., Appl. Radiat. Isot. 53 (2000) 225.
[4] J.-L. Reyss, et al., Nucl. Instr. and Meth. A 357 (1995) 391.
[5] F. Perrot, in: P. Loaiza (Ed.), American Institute of Physics Conference Proceedings, vol. 897, 2007, p. 131.
[6] H. Neder, G. Heusser, M. Laubenstein, Appl. Radiat. Isot. 53 (2000) 191; G. Heusser, M. Laubenstein, H. Neder, Radionucleides in the environment, International Conference on Isotopes and Environmental Studies, vol. 8, Elsevier, 2006, p. 495.
[7] ILIAS—Integrated Large Infrastructures for Astroparticle Science. European Union FP6 programme in Astroparticle Physics ⟨http://www-ilias.cea.fr⟩.
[8] E. Armengaud, et al., Phys. Lett. B 687 (2010) 294.
[9] Yu. Shitov on behalf of the SuperNemo coll, Proceedings of XXth Rencontres de Blois, 2008.
[10] M. Hult, et al., Environmental Radiochemical Analysis II, Special Publication No. 291, The Royal Society of Chemistry, Cambridge, UK, 2003, p. 373.
[11] M. l'Hour, Rev. Archéol. Ouest. 4 (1987) 113.
[12] Ph. Hubert, F. Hubert, in: P. Loaiza (Ed.), American Institute of Physics Conference Proceedings, vol. 897, 2007, p. 3.
[13] DIN 25482-5, 1993. Limit of Detection and Limit of Decision for Nuclear Radiation Measurements – Part 5: Counting Measurements by High Resolution Gamma Spectrometry, Neglecting the Influence of Sample Treatment.
[14] A. Nachab, et al., in: P. Loaiza (Ed.), American Institute of Physics Conference Proceedings, vol. 897, 2007, p. 35.
[15] ⟨http://www.canberra.com/pdf/Products/Detectors_pdf/C37147-CryoPulse5-SS.pdf⟩.
[16] Fréjus Collaboration, Nucl. Instr. and Meth. A 262 (1987) 463.
[17] R. Brun, et al., GEANT3: Detector Description and Simulation Tool, CERN Program Library, W5013, CERN, Geneva, Switzerland.
[18] N. Diallo, et al., in: Proceedings of 4th Integral Workshop 'Exploring the Gamma-Ray Universe' Alicante, Spain, 4–8 September 2000.
[19] R. Gurriaran, et al., Nucl. Instr. and Meth. A 524 (2004) 264.
[20] Available online ⟨http://www.nndc.bnl.gov/ensdf⟩.
[21] R.B. Firestone, et al., Table of Isotopes, eighth ed., Wiley, New York, 1996.
[22] Decay Data Evaluation Project [Online] Available ⟨http://www.bnm.fr/bnm-lnhb/DDEP.htm⟩, 2003, October 15, Bureau National de Mtrologie, Laboratoire National Henri Becquerel, France.
[23] M. Köhler, et al., Appl. Radiat. Isot. 67 (2009) 736.
[24] Rodolfo Gurriaran, Result of a measurement of gamma environmental background at LSM with a portable Ge detector, Private Communications.
[25] ⟨http://www.iaea.org/programmes/aqcs/pdf/rl_148.pdf⟩.
[26] Yu. Zdesenko, et al., Astropart. Phys. 23 (2005) 249; C. Cozzini, et al., Phys. Rev. C 70 (2004) 064606.
[27] F. Danevich, et al., Nucl. Instr. and Meth. A, accepted for publication, doi:10.1016/j.nima.2010.11.118.
[28] S. Martinie, et al., in: D.F. Heidel et al.(Ed.), IEEE International Conference on IC Design and Technology ICICTD10, IBM J. Res. Dev., vol. 52 N3, 2008, p. 225.

3.2.2 Development, construction and performances of a low background coaxial HPGe

We developed a low background HPGe coaxial detector based on a p-type crystal with a sensitive volume of 600 cm^3 and mass of approximately 3 kg. The detector was financed jointly by the Joint Institute for Nuclear Research in Russia, IEAP of the Czech Technical University in Czech Republic and LSM. The development is described in [102] and in the conference proceedings included below [103]. To keep the detector background as low as possible the design of the internal part of the cryostat integrates the modification introduced for the planar HPGe. We added a 10 mm thick roman lead cylinder at the bottom of the holder to shield the crystal against the radioactivity of the FET. All the materials involved in the construction were screened and selected in terms of low radioactive contaminations. This allowed to reduce the intrinsic background to a level comparable to the most sensitive HPGe worldwide, achieving an integral count rate in the region of 40—3000 keV of 73 counts/kg/d. The energy resolution of the detector is 1.2 keV at 122 keV (^{57}Co) and 2 keV at 1332 keV (^{60}Co).

The sensitivity of the coaxial detector, called OBELIX, allowed us to perform some nuclear studies in addition to material screening. We have studied the $2\nu\beta\beta$ decay of ^{100}Mo to the excited states of ^{100}Ru, through the measurement of the γ-ray lines corresponding to the decay scheme. We measured the half-life of the $2\nu\beta\beta$ decay of ^{100}Mo to the excited 0^+ state and we derived the NME value of the transition (with fixed g_A) [104]. We also investigated other rare nuclear processes, such as resonant neutrinoless double electron capture (0νEC/EC) of ^{106}Cd [102, 105]. This spectrometer is also dedicated to material selection, for SuperNEMO and other rare event searches.

Article: P. Loaiza *et al*, AIP Conf. Proc. 1672, 130002 (2015)

Obelix, a new low-background HPGe at Modane Underground Laboratory

P. Loaiza[*,†], V. Brudanin[**], F. Piquemal[*,‡], E. Rukhadze[§], N. Rukhadze[**], I. Stekl[§], G. Warot[*] and M. Zampaolo[*]

[*]*Laboratoire Souterrain de Modane, CNRS-CEA, 1125 route de Bardonnèche, 73500 Modane, France*
[†]*LAL, Univ. Paris-Sud, CNRS/IN2P3, 91405 Orsay, France*
[**]*JINR, Joint Institute for Nuclear Research, 141980, Dubna, Russia*
[‡]*CENBG, Univ Bordeaux, CNRS/IN2P3, 33175 Gradignan, France*
[§]*IEAP, Czech Techincal University in Prague, 12800 Prague, Czech Republic*

Abstract. An ultra-low background coaxial HPGe detector for gamma-ray spectrometry with a relative efficiency of 160%, corresponding to a 600 cm^3 Ge crystal, was installed at the Laboratoire Souterrain de Modane, France (4800 m.w.e). To reduce the instrinsic detector background, all parts involved in the detector cryostat were selected for their low radioactivity contamination. A shielding, composed of an inner layer of roman lead and an external layer of regular lead was installed, together with a system to reduce the Rn level inside the sample chamber. The shielding was designed to allow the measurement of Marinelli-shaped samples. We present the constructional details which lead to a remarkable low detector background of 73 cts/kg·d in [40, 3000] keV. Measured samples showed that sensitivities about 100 μBq/kg in ^{226}Ra and ^{228}Th are reached for samples of some kg and 30 days of lifetime.

Keywords: γ -ray spectrometry, Low-background
PACS: 29.30Kv,29.40Wk

INTRODUCTION

Ultra-low background germanium gamma-ray spectrometers have been developed since many years for material selection in rare event searches in dark matter and neutrino physics. To reach low background levels the cryostat must be built with selected very low radioactive materials, it must be surrounded with low radioactive shielding and it must be operated in a deep underground laboratory. In this work, we present the development of a low background coaxial germanium spectrometer now in operation at the Laboratoire Souterrain de Modane (4800 m.w.e). The new spectrometer is dedicated to material screening for the SuperNemo $2\beta0\nu$ experiment [1] and to the investigation of rare nuclear processes such as resonant neutrino-less double electron capture and double beta decay processes to the excited states of daughter nuclei.

DETECTOR DESIGN

The cryostat

The p-type high purity germanium crystal has a sensitive volume of 600 cm^3, corresponding to a mass of approximately 3 kg and a relative effic ciency of 160%. The cryostat was developed in close cooperation with Canberra France. To achieve the maximum efficiency in the gamma-ray detection, the germanium crystal is placed at a minimun distance (4 mm) from the entrance window of the endcap of the aluminium cryostat and the thickness of the entrance window is about 1.6 mm. To minimize the radioactive background the radioactivity levels of all components were measured and high radioactive components were replaced by their low radioactive counterparts when possible. The crystal is mounted in a holder made of aluminium specially selected for its high radiopurity (Al-(4%)Si). This special alloy has been chosen since this low Z material contains almost no cosmogenic activity, only ^{26}Al = 0.38 $\pm^{0.19}_{0.14}$ mBq/kg [2]. However the main drawback is the thorium contamination at the level of 1.4 mBq/kg. All other parts inside the holder are made of plastic or lead-free brass, in particular, all the screws are homemade out of lead-free brass (^{210}Pb<100 mBq/kg). The first stage of the amplifier with a Field Effect Transistor (FET) is placed below the holder and gives one

Low Radioactivity Techniques 2015 (LRT 2015)
AIP Conf. Proc. 1672, 130002-1–130002-4; doi: 10.1063/1.4928012

TABLE 1. Radioactive contaminations of materials used in the cryostat construction.

Material	Activity (mBq/kg)				
	^{226}Ra	^{228}Ra	^{228}Th	^{40}K	Others
Aluminium	0.27±0.19	<0.11	1.4±0.2	$1.1\pm^{0.2}_{0.1}$	^{26}Al: $0.38\pm^{0.19}_{0.14}$
Lead-free brass	4.9 ±1.3	<5	< 3	< 40	^{210}Pb<100
FET support*	1.6 ±0.2	2.9±0.6	<0.5	<5	^{207}Bi 1.7±0.7
O-ring	910 ± 80	320 ± 70	350 ± 30	1360 ± 400	
Roman lead	<0.3	<0.3			^{210}Pb<60

* The radioactivity levels of the FET support are given in mBq/unit.

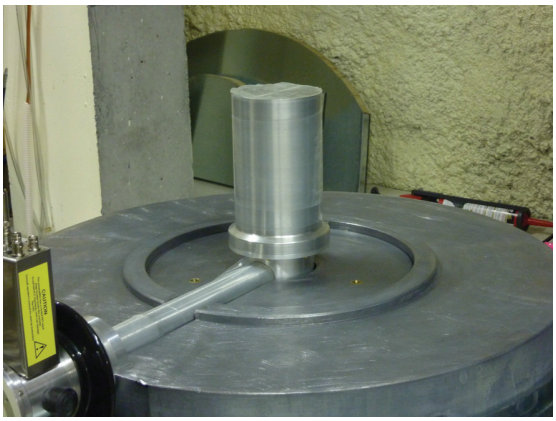

FIGURE 1. Detector cryostat and shielding

of the main contributions to the instrinsic background. We have modified the standard design to include a 10 mm thick roman-lead (^{210}Pb<60 mBq/kg) cylinder at the bottom of the holder to shield the radioactivity of the FET support. The endcap, made of the same aluminium as the crystal holder, is sealed at the bottom part by an O-ring which, even containing high radioactivity levels, gives minor contributions since it is placed far from the crystal. Table 1 gives the radioactivity measured in some of the materials used in the cryostat construction.

Shielding

The detector is shielded from environmental radioactivity by concentrical cylindrical layers of lead, as shown in Fig.1. The innermost layer allows different configurations to place samples of different volumes: the maximum shielding thickness consists of 12 cm of roman lead (^{210}Pb<60 mBq/kg), while the minimum thickness, with a sample chamber of 9800 cm^3, is 5 cm. The outermost layer is made of 20 cm of low activity lead with ^{210}Pb activity between 10-20 Bq/kg. To reduce the Radon inside the sample chamber, the shielding is flushed with Radon depleted air with a Radon concentration of $\sim$ 20 mBq/m^3.

RESOLUTION AND BACKGROUND MEASUREMENTS

The detector has a measured resolution of 1.2 keV at 122 keV and 2 keV at 1332 keV.

After the installation of the detector underground at the end of 2010, the integral count rate has decreased due to the decay of cosmogenic isotopes which are produced in the Ge crystal during its exposure on the Earth's surface. The integral count rate in the region [40 - 3000] keV decreased from 173 counts/kg·d to 73 counts/kg·d. The remaining background shows traces of ^{226}Ra, ^{228}Ra, ^{228}Th and ^{40}K, as shown on Fig. 2. Table 2 gives the count rates for single lines of several nuclides measured in May 2014, where uncertainties correspond to the statistical uncertainties (25 days measurement). Decision limits are given at 95% CL according to [3]. All lines are below 1 count/kg·d, and the higher

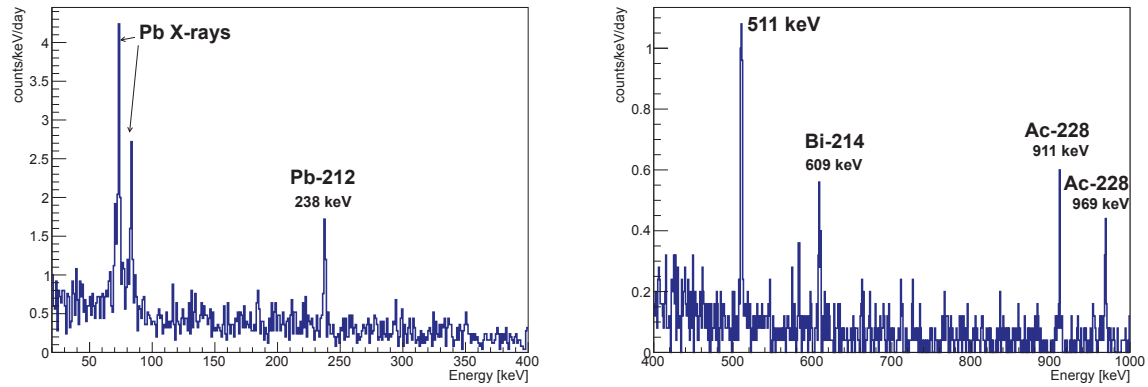

FIGURE 2. Background spectra of Obelix in the region [20-400] keV (left) and [400-1000] keV (right) measured in May 2014.

TABLE 2. Background count rates for single lines, see text for details.

Nucleide	**E_γ (keV)**	**Cts/kg·d**
^{238}U-chain:		
^{214}Pb	295	< 0.14
	352	0.20 ± 0.09
^{214}Bi	609	0.35 ± 0.08
^{232}Th-chain:		
^{228}Ac	338	<0.15
	911	0.25 ± 0.05
^{212}Pb	238	0.9 ± 0.1
^{208}Tl	583	0.18 ± 0.07
	2615	0.17 ± 0.06
^{60}Co	1173	<0.08
	1332	<0.08
^{40}K	1460	0.46 ± 0.09
β^+	511	1.0 ± 0.1

rates correspond to the 238 keV line from ^{212}Pb with (0.9 ± 0.1) cts/kg·d and 1460 keV from ^{40}K with (0.46 ± 0.09) cts/kg·d.

RESULTS: MATERIAL SCREENING

The spectrometer has a sensitivity of ∼100 μBq/kg in ^{226}Ra, ^{228}Th for samples of about 5 kg and 30 days of lifetime. The result of some measurements is given in Table 3, where upper limits are given at 95% CL according to [3].

TABLE 3. Some material screening results.

Material	**Mass (kg)**	**Time (d)**	**Activity (μBq/kg)** ^{226}**Ra**	^{228}**Th**	^{40}**K**	^{60}**Co**
Copper endcaps	5.6	6.5	< 200	< 170	< 2000	110 ±40
Polyethylene	3.9	28	650±80	300±70	< 1000	< 60
Pure Iron	0.6	20	500 ±30	<900	< 5000	340 ±120

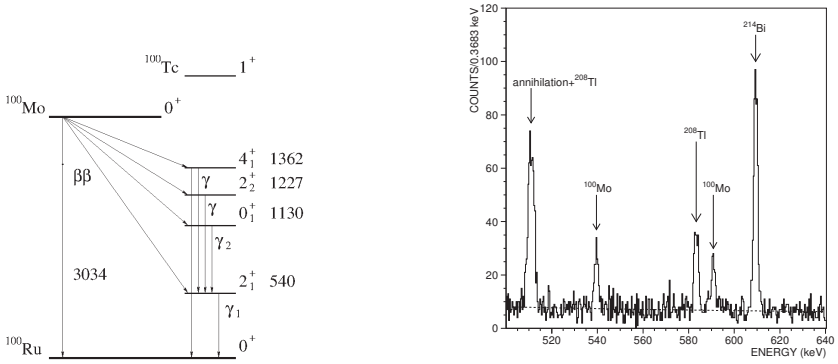

FIGURE 3. Decay scheme of ^{100}Mo (left) and measured energy spectrum with enriched Mo in the region [500-640] keV (right).

RESULTS: $2\beta2\nu$ DECAY OF ^{100}MO

The $2\beta2\nu$ decay of ^{100}Mo to the excited states of ^{100}Ru provides the possibility to determine experimentally the nuclear matrix elements involved in $2\beta0\nu$ decays. As shown in Fig. 3, left, the decay to the excited 0^+_1 state is accompanied by two γ-rays with energies 539.5 keV and 590 keV. Both peaks are clearly visible in the measured spectrum, leading to a half-life for the two-neutrino double beta decay of $T_{1/2} = [7.5 \pm 0.6(stat) \pm 0.6(syst)] \cdot 10^{20}$ yr. This work was reported in [4] and it is the most precise value ever obtained for this transition [5].

CONCLUSION

An ultra-low background coaxial HPGe was developed and installed in the Laboratoire Souterrain de Modane. Thanks to the selection of all cryostat and shielding components regarding the radiopurity, a remarkable low intrinsic background was achieved, i.e, 73 cts/kg·d in [40, 3000] keV, placing this spectrometer as one of the most sensitive in the world. Typical sensitivities of $\sim$100 μBq/kg in ^{226}Ra, ^{228}Th are achieved for regular measurements of samples of about 5 kg and 1 month of lifetime. The $2\beta2\nu$ decay of ^{100}Mo to the excited 0^+_1 state of ^{100}Ru was measured leading to the most precise value ever obtained for the half-life of this transition.

ACKNOWLEDGMENTS

The authors would like to thank the technical staff of the Laboratoire Souterrain de Modane for their unvaluable help in the installation and running of the detector.

This activity is supported by the grants No. LM 2011027, LG 14003, RFBR No. 14-02-00568.

REFERENCES

1. R. Arnold *et al.*, *Eur. Phys. J. C* **70**, 927, DOI 10.1140/epjc/ s10052-010-1481-5 (2010).
2. P. Loaiza *et al*, *Nucl. Instr. and Methods A*, **634**, 64 (2011).
3. Ch. Hurtgen *et al*, *Appl. Rad. Isot.* **53**, 45 (2000).
4. NEMO collaboration, *Nucl. Phys. A*, **925**, 25 (2014).
5. A. Barabash, *Nucl. Phys. A*, **935**, 52-64 (2015).

3.2.3 Worlwide HPGe sensitivities

HPGe detectors for γ-ray spectrometry have typical sensitivities $\sim$100 μBq/kg – 1 mBq/kg. The sensitivity depends on the radionucleide, the sample mass and the measurement time. For ^{226}Ra and ^{228}Th subchains the sensitivity is around a few 100 μBq/kg with a 1 kg sample and 2-4 weeks measurement time. The lowest limits measured so far were obtained with the GeMPI detector at LNGS [98, 99], at the level of 10 μBq/kg for ^{226}Ra and ^{228}Th for a copper sample [100] of 125 kg and about 3 months measurement.

Table 3.1 shows some measurements performed with HPGe detectors. The planar HPGe Mafalda can asses low energy gammas from ^{210}Pb and ^{234}Th/^{238}U, the coaxials are not able to measure low energies, but can measure ^{238}U through ^{234}Pa. Large volume coaxials HPGe are more sensitive for higher energies thanks to higher efficiencies and larger sample masses.

Detector	Sample	M	T meas.	^{210}Pb	^{234}Th	^{226}Ra	^{228}Th
		[kg]	[d]	[mBq/kg]	[mBq/kg]	[mBq/kg]	[mBq/kg]
Mafalda (Planar)	Al	1.0	5.5	<9	<3	< 0.9	1 ± 0.3
Obelix (Coaxial)	PE	3.9	28	-	-	0.65 ± 0.08	0.30 ± 0.07
GeMPI2 (Coaxial)	Cu	125	100.5	-	<7	< 0.016	<0.012

Table 3.1: Examples of measurements with HPGe detectors. Mafalda and Obelix are at LSM and GeMPI is at LNGS.

3.3 Mass Spectrometry and Neutron Activation Analysis

3.3.1 Inductively Coupled Plasma Mass Spectrometry

Inductively Coupled Plasma Mass Spectrometry (ICPMS) is based, as all mass spectrometry techniques, on atom counting. The sample to be measured by ICPMS is dissolved into a solution using acids or bases. A flow of gas, usually Argon, converts the liquid sample into a fine aerosol. A portion of the aerosol is directed through the center of an argon plasma torch at high temperature, where the aerosol particles are ionized. Then the ions are extracted into a mass spectrometer where they are separated according to their mass/charge ratio. For the same activity concentration, mass spectrometry is more sensitive for longer-lived radionuclides, as this corresponds to a higher number of atoms. In addition, the possibility to measure a certain radionucleide depends as well on the interferences. The key interferences to consider are: isobaric, stable or radioactive isotopes with a similar mass that cannot be resolved by the detector e.g. ^{238}Pu and ^{238}U; polyatomic, formed by reactions of elements with gases in the plasma including Ar, O and H, e.g. ^{226}Ra measurements may suffer several polyatomic interferences [106] ^{88}Sr^{138}Ba, ^{40}Ar^{40}Ar^{146}Nd, ^{87}Sr^{139}La, ^{86}Sr^{140}C, and thus is not effectively measured in the case of very low concentrations. The measurement of ^{40}K with ICPMS was difficult due to isobaric interferences at the same m/z, mainly ^{40}Ar. Thanks to advances in instrument design, low levels of ^{40}K can be measured for some materials, employing a "triple quadrupole" ICPMS [107].

Low level counting ICPMS requires all chemicals and reagents to be of the highest purity and clean-room conditions. This technique may measure extremely low radioactivities, typically in the range 1 - 10 μBq/kg, and it is able reach below the μBq/kg level. For example, the limits for electroformed copper ^{238}U: 0.024×10^{-12} g/g and ^{232}Th: 0.075×10^{-12} g/g were reported (equivalent to < 0.3 μBq/kg for both ^{232}Th and ^{238}U) [108].

3.3.2 Neutron activation analysis

The principle in Neutron Activation Analysis (NAA) consists of first irradiating the sample with neutrons to produce an excited, unstable nucleus, which de-excites by emitting gamma rays that are measured by a HPGe detector. The concentration of the isotopes of interest is obtained based on the concentration of the nucleus produced by activation. The most usual sources of neutrons are nuclear research reactors.

NAA can be applied to measure ^{232}Th and ^{238}U and ^{40}K if the material does not produce long-lived neutron activation products, because of the Compton continuum from higher energy γ's than those of interest. The concentrations of these three isotopes are measured from the reactions:

$$\begin{aligned} {}^{232}Th(n,\gamma)^{233}Th \rightarrow {}^{233}Pa \quad & \tau_{1/2} = 27 \text{ d}, E_\gamma = 312 \text{ keV} \\ {}^{238}U(n,\gamma)^{239}U \rightarrow {}^{239}Np \quad & \tau_{1/2} = 2.35 \text{ d}, E_\gamma = 106 \text{ keV}, 222 \text{ keV}, 228 \text{ keV} \\ {}^{41}K(n,\gamma)^{42}K \quad & \tau_{1/2} = 12.36 \text{ d}, E_\gamma = 1524 \text{ keV} \end{aligned}$$

Since ^{41}K and ^{40}K isotopic abundances are 6.7%, and 0.01% respectively, the ^{40}K concentration is calculated from the ^{41}K one. [109].

NAA can achieve extremely low sensitivity levels. As an example, in a measurement of PMMA the following limits could be reached: ^{238}U: $< 0.3 \times 10^{-12}$ g/g, ^{232}Th: $< 0.5 \times 10^{-12}$ g/g and ^{40}K $< 0.016 \times 10^{-12}$ g/g [109] (equivalent to < 4 μBq/kg for ^{238}U, < 2 μBq/kg for^{232}Th and < 4 μBq/kg for ^{40}K)

3.4 Surface contamination measurements, the BiPo-3 detector

Surface contaminations are the driving background in $0\nu\beta\beta$ decay pure bolometric searches and they are a concern in many other techniques in $0\nu\beta\beta$ and dark matter searches. Unfortunately at present only a few technologies are able to measure low level contaminations on surfaces.

Current technologies include the XIA's alpha counter, UltraLo-1800, a commercial detector, based on a drift chamber filled with Ar. In this device the α's, emitted from the sample with surfaces up to 1.8 m^2, are drifted towards the anode. The α background from the walls and ceilings are discriminated through pulse shape analysis. The backgrounds at the sea level are 10^{-3} α/cm^2/h and 10^{-4} α/cm^2/h underground[2]. These detectors reach sensitivities of about 10 nBq/cm^2 for ^{210}Po [110] .

An innovative detector concept, based on cryogenic calorimeters is the SURFACE detector, an array of Si wafers operated as bolometers [111]. The 20 keV energy resolution would allow

[2]Personal communication from Brendan McNally, XIA

to distinguish most α lines from ^{238}U and ^{228}Th chains. The detector is under development, the background measured in preliminary R&D tests is 10^{-7}cts/cm^2/s in the [2.5 – 10] MeV region.

The most sensitive detector to my knowledge for the measurement of ^{208}Tl and ^{214}Bi contamination on surfaces is the BiPo-3 detector, developed in the frame of the SuperNEMO experiment (Fig.3.6). Together with a post-doc we have written a detailed paper [112] which describes the detector and its performances. I include here below another shorter article summarizing the detector performances [113]. The BiPo-3 detector, operated between 2013 and 2019 at the Laboratorio Subterraneo de Canfranc, measured ^{208}Tl and ^{214}Bi contaminations on thin materials with surfaces up to 3.6 m^2 through the study of delayed coincidences related to bismuth-polonium cascade disintegrations. The material under investigation is sandwiched between two plastic scintillators, which provide a very clear time-topology signature. The first source of intrinsic background is the scintillator surface contamination, $\mathcal{A}(^{208}\text{Tl}) = 0.9 \pm 0.2$ μBq/m^2 and $\mathcal{A}(^{214}\text{Bi}) = 1.0 \pm 0.3$ μBq/m^2.

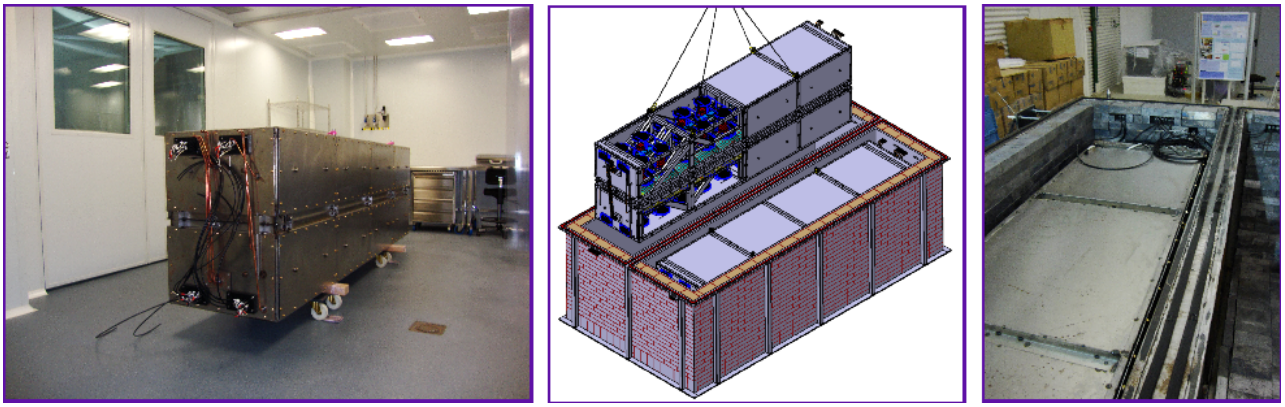

Figure 3.6: Left: one of the two BiPo-3 modules in the clean-room of LSC. Center: placement of one of the modules inside the shielding. Right: the module inside the shielding in the LSC hall.

The second source of background is the random coincidences between opposite scintillators. Although the coincidences are negligible for the ^{208}Tl measurement, they represent the dominant background for the ^{214}Bi measurement, with a level of about 0.10 counts/day/m^2 of scintillator surface area.

The detector was mainly dedicated to the measurement of the SuperNEMO $0\nu\beta\beta$ source foils, which consist of ^{82}Se powder mixed with a PVA glue and deposited between Mylar foils. Fig 3.7 shows a picture of the SuperNEMO foils in one of the detector modules. The measurement campaign included the characterization and selection of the raw materials prior to the fabrication and measurement of the final foils. The detector could reach sensitivities of the order of few μBq/kg for ^{208}Tl and $\sim$100 μBq/kg for ^{214}Bi, in terms of bulk radioactivity. In terms of surface contaminations, as an example, we set upper limits for the raw Mylar radiopurity of <0.3 nBq/cm^2 for ^{208}Tl and <1.2 nBq/cm^2 for ^{214}Bi for a measurement of 76 days and a sample with 1.6 m^2 surface. Besides the SuperNEMO foils, we have assessed also other samples, e.g. the Vikuiti reflecting foil used in CUPID-Mo, for which we obtained a limit for ^{208}Tl <0.2 nBq/cm^2 and a value for ^{214}Bi = 1.0 $\pm$ 0.4 (stat)nBq/cm^2.

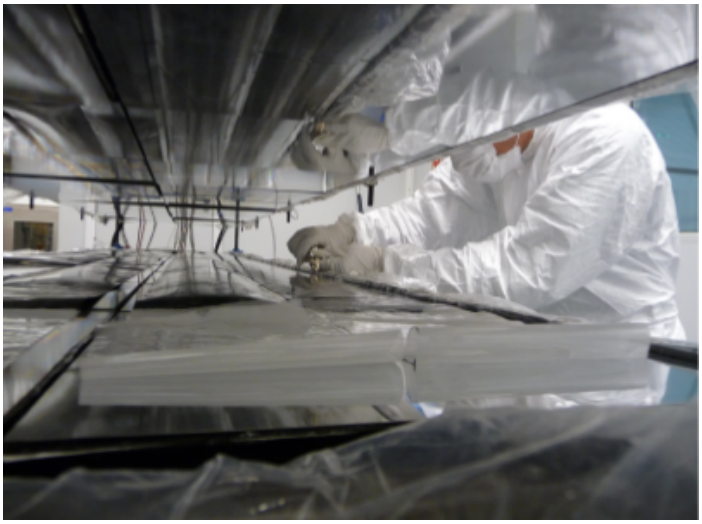

Figure 3.7: The BiPo-3 detector opened in the clean-room of LSC during the installation of the SuperNEMO enriched ^{82}Se $0\nu\beta\beta$ source foils.

Article: P. Loaiza *et al* [SuperNEMO coll.], Appl. Rad. and Isot. 123, 54 (2017)

Applied Radiation and Isotopes 123 (2017) 54–59

Contents lists available at ScienceDirect

Applied Radiation and Isotopes

journal homepage: www.elsevier.com/locate/apradiso

The BiPo-3 detector

P. Loaiza[a,*], A.S. Barabash[b], A. Basharina-Freshville[c], E. Birdsall[d], S. Blondel[a], S. Blot[d], M. Bongrand[a], D. Boursette[a], V. Brudanin[e,v], J. Busto[f], A.J. Caffrey[g], S. Calvez[a], M. Cascella[c], C. Cerna[h], E. Chauveau[h], A. Chopra[c], S. De Capua[d], D. Duchesneau[i], D. Durand[k], V. Egorov[e], G. Eurin[a,c], J.J. Evans[d], L. Fajt[j], D. Filosofov[e], R. Flack[c], X. Garrido[a], H. Gómez[a], B. Guillon[k], P. Guzowski[d], K. Holý[l], R. Hodák[j], A. Huber[h], C. Hugon[h], A. Jeremie[i], S. Jullian[a], M. Kauer[c], A. Klimenko[e], O. Kochetov[e], S.I. Konovalov[b], V. Kovalenko[e], K. Lang[m], Y. Lemière[k], T. Le Noblet[i], Z. Liptak[m], X.R. Liu[c], G. Lutter[h], M. Macko[l], F. Mamedov[j], C. Marquet[h], F. Mauger[k], B. Morgan[n], J. Mott[c], I. Nemchenok[e], M. Nomachi[o], F. Nova[m], H. Ohsumi[p], G. Oliviéro[k], R.B. Pahlka[m], J. Pater[d], F. Perrot[h], F. Piquemal[h,q], P. Povinec[l], P. Přidal[j], Y.A. Ramachers[n], A. Remoto[i], B. Richards[c], C.L. Riddle[g], E. Rukhadze[j], R. Saakyan[c], X. Sarazin[a], Yu. Shitov[e,r], L. Simard[a,s], F. Šimkovic[l], A. Smetana[j], K. Smolek[j], A. Smolnikov[e], S. Söldner-Rembold[d], B. Soulé[h], I. Štekl[j], J. Thomas[c], V. Timkin[e], S. Torre[c], Vl.I. Tretyak[t], V.I. Tretyak[e], V.I. Umatov[b], C. Vilela[c], V. Vorobel[u], D. Waters[c], A. Žukauskas[u]

[a] LAL, Université Paris-Sud, CNRS/IN2P3, Université Paris-Saclay, F-91405 Orsay, France
[b] NRC "Kurchatov Institute", ITEP, 117218 Moscow, Russia
[c] University College London, London WC1E 6BT, United Kingdom
[d] University of Manchester, Manchester M13 9PL, United Kingdom
[e] JINR, 141980 Dubna, Russia
[f] Aix Marseille Univ., CNRS, CPPM, Marseille, France
[g] Idaho National Laboratory, Idaho Falls, ID 83415, United States
[h] CENBG, Université de Bordeaux, CNRS/IN2P3, F-33175 Gradignan, France
[i] LAPP, Université de Savoie, CNRS/IN2P3, F-74941 Annecy-le-Vieux, France
[j] Institute of Experimental and Applied Physics, Czech Technical University in Prague, CZ-12800 Prague, Czech Republic
[k] LPC Caen, ENSICAEN, Université de Caen, CNRS/IN2P3, F-14050 Caen, France
[l] FMFI, Comenius University, SK-842 48 Bratislava, Slovakia
[m] University of Texas at Austin, Austin, TX78712, United States
[n] University of Warwick, Coventry CV4 7AL, United Kingdom
[o] Osaka University, 1-1 Machikaney arna Toyonaka, Osaka 560-0043, Japan
[p] Saga University, Saga 840-8502, Japan
[q] Laboratoire Souterrain de Modane, F-73500 Modane, France
[r] Imperial College London, London SW7 2AZ, United Kingdom
[s] Institut Universitaire de France, F-75005 Paris, France
[t] Institute for Nuclear Research, MSP 03680 Kyiv, Ukraine
[u] Charles University, Prague, Faculty of Mathematics and Physics, CZ-12116 Prague, Czech Republic
[v] National Research Nuclear University MEPhI, 115409, Moscow, Russia

ARTICLE INFO

Keywords:
Low-radioactivity measurements
Double beta-decay detectors

ABSTRACT

The BiPo-3 detector is a low radioactive detector dedicated to measuring ultra-low natural contaminations of ^{208}Tl and ^{214}Bi in thin materials, initially developed to measure the radiopurity of the double β decay source foils of the SuperNEMO experiment at the μBq/kg level. The BiPo-3 technique consists in installing the foil of interest between two thin ultra-radiopure scintillators coupled to low radioactive photomultipliers. The design and performances of the detector are presented.

* Corresponding author.

http://dx.doi.org/10.1016/j.apradiso.2017.01.021
Received 12 August 2016; Received in revised form 29 December 2016; Accepted 23 January 2017
Available online 29 January 2017

In this paper, the final results of the ^{208}Tl and ^{214}Bi activity measurements of the first enriched ^{82}Se foils are reported for the first time, showing the capability of the detector to reach sensitivities in the range of some μBq/kg.

1. Introduction

The BiPo-3 detector, running in the Canfranc Underground Laboratory, Spain, since 2013, has been initially developed to measure ultra low natural contaminations of ^{212}Bi (^{208}Tl) and ^{214}Bi in the SuperNEMO source foils. The goal of the SuperNEMO experiment is to search for the neutrinoless double β decay, $\beta\beta0\nu$ (Arnold, 2010) as an experimental proof that the neutrino is a Majorana particle, i.e. identical to its own antiparticle. SuperNEMO will measure 100 kg of $\beta\beta0\nu$ isotopes with a sensitivity of $T_{1/2}(\beta\beta0\nu) > 10^{26}$ years. The baseline isotope is ^{82}Se with a $Q_{\beta\beta}$ value = 2.998 MeV. One of the main sources of background for SuperNEMO is a possible contamination of ^{208}Tl (Q_β = 4.99 MeV) and ^{214}Bi (Q_β = 3.27 MeV) produced inside the $\beta\beta0\nu$ source foils. The required radiopurities of the $\beta\beta0\nu$ foils are $\mathscr{A}(^{208}\text{Tl}) < 2$ μBq/kg and $\mathscr{A}(^{214}\text{Bi}) < 10$ μBq/kg in order to achieve the desired SuperNEMO sensitivity (Arnold, 2010). To measure such low levels in the $\beta\beta0\nu$ foils the collaboration has developed the BiPo-3 detector. We show in this paper that the BiPo-3 performances have been achieved: the BiPo-3 detector can measure the radiopurity of double beta metallic foils with a total surface at the level of some μBq/kg. We show also that the BiPo-3 detector becomes a generic low radioactive detector, which can measure the natural radioactivity of Tl and Bi in general thin materials with an unprecedent sensitivity.

2. Measurement principle of the BiPo-3 detector

In order to measure ^{208}Tl and ^{214}Bi contaminations, the underlying concept of the BiPo-3 detector is to detect with organic plastic scintillators the so-called BiPo process, which corresponds to the detection of an electron followed by a delayed α particle (Bongrand et al., 2011; Gomez, 2013). The ^{214}Bi isotope is a (β,γ) emitter decaying to ^{214}Po, which is an α emitter (E_α = 7.69 MeV (Bé et al., 2008)) with a half-life of 162 μs. The ^{208}Tl isotope is measured by detecting its parent, ^{212}Bi. Here ^{212}Bi decays with a branching ratio of 64% (Bé et al., 2004) via a β emission (Q_β = 2.25 MeV) towards the daughter nucleus ^{212}Po which is a pure α emitter (E_α = 8.79 MeV (Bé et al., 2004)) with a short half-life of 300 ns, as summarized in Fig. 1.

The BiPo-3 experimental technique consists in installing the foil of interest between two thin ultra radiopure organic plastic scintillators, as illustrated in Fig. 2. The ^{212}Bi (^{208}Tl) and ^{214}Bi contaminations inside the foil are measured by detecting the β decay followed by the delayed α particle within a time window which depends on the isotope to be measured. The energy of the delayed α particle provides information on whether the contamination is on the surface or in the bulk of the foil.

3. Description of the BiPo-3 detector

The detector is composed of two modules. Each module (see Fig. 3) consists of 20 pairs of optical sub-modules, positioned in two rows. Each optical sub-module consists of a scintillator plate coupled with a polymethyl methacrylate (PMMA) optical guide to a 5 in. low radioactive photomultipliers (Bongrand et al., 2011). The optical sub-modules are arranged face-to-face to form a pair. The size of each scintillator is 300 × 300 × 2 mm^3. The BiPo-3 detector corresponds to a total number of 80 optical sub-modules and a total detector surface of 3.6 m^2. The surface of the scintillators facing the source foil is covered with a 200 nm thick layer of evaporated ultra radiopure aluminium in order to optically isolate each scintillator from its neighbours, and to improve the light collection efficiency. The two BiPo-3 modules are installed inside a low-radioactivity shield. The shield is built out of a radon-tight stainless steel tank with the upper part composed of a pure iron lid (2 cm thick). Low-activity lead bricks are assembled inside the tank and above the upper iron plate for a total thickness of 10 cm. Pure iron plates, 18 cm thick, are added under the tank and on its lateral sides. The radiopurity of all the materials used for the detector have been measured to ensure high radiopurity. A selection of results is shown in Table 1.

4. Background measurement

4.1. Sources of the background

The first source of background are the random coincidences between two opposite scintillators, giving a background signal within the delay time window, as illustrated in Fig. 4(a). The delay time distribution of the random coincidences is flat and the energy distributions of both the prompt and delayed signals are localized at low energy, since the single counting rate is dominated by Compton electrons due to external γ's.

The second source of background comes from ^{212}Bi and ^{214}Bi contaminations on the surface of the scintillator in contact with the sample foil, hereafter called surface background, as illustrated in Fig. 4 (b). The delayed α particle, emitted from the surface of the scintillator, deposits all its energy inside the scintillator.

The third potential source of background is the ^{212}Bi or ^{214}Bi bulk contamination inside the scintillator volume. In this case, the delayed α particle deposits also all its energy inside the scintillator but the prompt electron first triggers this scintillator block before escaping and entering the opposite one, as illustrated in Fig. 5. Therefore two prompt signals are detected in coincidence in the two opposite scintillators, allowing the rejection of this class of background events.

Thus the background can be defined by two components: the random coincidences and the surface background.

The energy spectrum of the delayed signal is the most sensitive observable to discriminate the two background components. For surface background, the delayed α particle deposits all its energy inside the scintillator, corresponding to a peak at around 800 keV for ^{214}Bi and around 1 MeV for ^{212}Bi, while random coincidence signals are dominant at low energy.

4.2. Measurement conditions

The background is measured by closing the detector, without any sample between the scintillators. Opposite scintillators are directly in contact.

The background has been measured separately for each of the two BiPo-3 modules. The background of the Module 1 has been measured from July 2012 to September 2012 at the beginning of the commissioning with a preliminary shield, and from July 2013 to September 2013

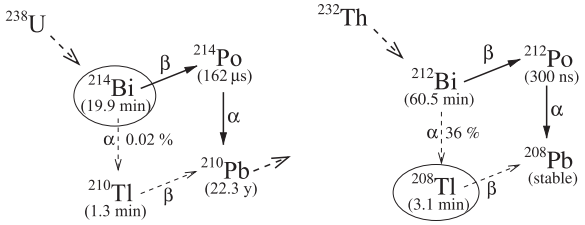

Fig. 1. The ^{214}Bi-^{214}Po and ^{212}Bi-^{212}Po cascades used for the ^{214}Bi and ^{208}Tl measurements.

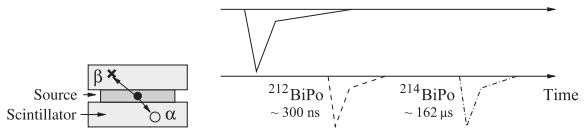

Fig. 2. Schematic view of the BiPo detection technique with the source foil inserted between two plastic scintillators plate, and the scintillation signal waveforms acquired for a BiPo event. The prompt β signal and the delayed α signal observed by the top and bottom scintillators respectively are schematically illustrated.

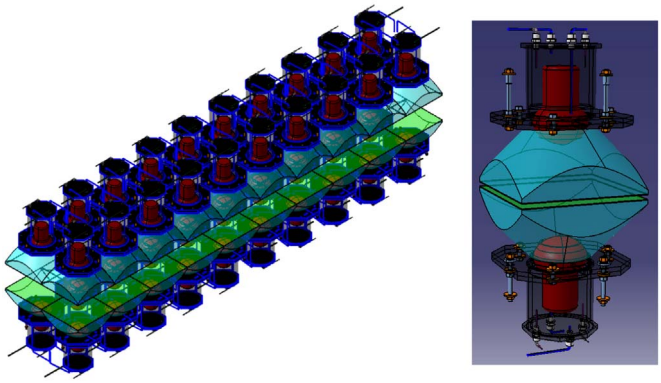

Fig. 3. Details of the assembly of the 40 optical sub-modules inside a BiPo-3 module. On the right, a pair of optical sub-modules with the two thin scintillators (in green) face-to-face, coupled with a PMMA optical guide (blue) to a low radioactive 5 in. PMT (red).

Table 1
Radioactivity measurements using HPGe of the BiPo-3 components. The mass of one photomultiplier (PMT) is 385 g.

Activity (mBq/kg)	^{40}K	^{214}Bi	^{228}Th
Al. on scintillators	–	–	<0.6
Scintillators	17 ± 2	<0.1	<0.1
PMTs	1377	623	104
PMMA	<109	<6	<7
RTV glue 615	490 ± 150	<18	<11
Iron shield	<11	<1	<3

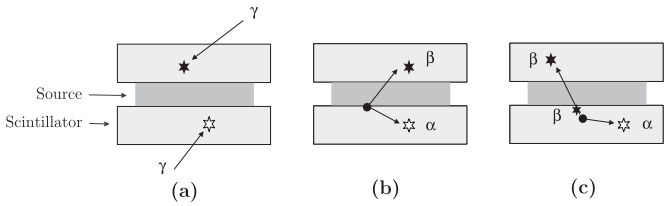

Fig. 4. Illustration of the possible sources of background: (a) random coincidences due to the γ flux, (b) ^{212}Bi or ^{214}Bi contamination on the surface of the scintillators, (c) ^{212}Bi or ^{214}Bi contamination in the volume of the scintillators.

with the final shield and after having introduced and measured several samples. The background of Module 2 has been measured from February 2013 to May 2013, with the final shield. The measurements allow to characterize at the same time the backgrounds for ^{212}Bi and ^{214}Bi.

4.3. Event selection

Only the events with β and α particles entering different scintillators on opposite sides of the detection volume, *back-to-back* events, are considered (as the one in Fig. 2, left). Events with β and α particles entering in the same scintillator, *same-side* events, are not used since the level of background is much higher than the one measured in the *back-to-back* topology. This is because the bulk contamination inside the scintillators can mimic the *same-side* events.

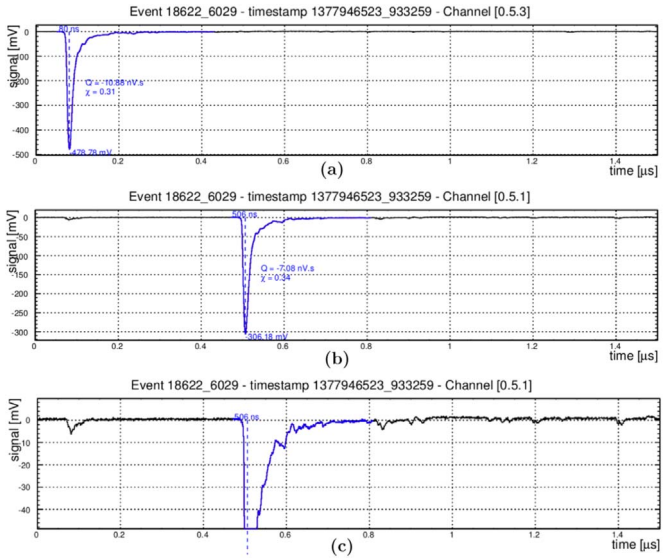

Fig. 5. Display of a BiPo event identified as a bulk contamination inside the scintillators, with a signal in coincidence with the prompt signal in the opposite scintillator: (a) the prompt signal, (b) the delayed signal, (c) a zoom of the delayed signal with the coincidence signal. Using the coincidence of the prompt signals, these kind of background events are rejected.

The coincidence time window for the delay time between the prompt and the delayed signal, Δt, is 20 ns < Δt < 1500 ns for ^{212}BiPo events, and 10 µs < Δt < 1000 µs for ^{214}BiPo events. The criteria to select the *back-to-back* BiPo events are described in the following. The energy of the prompt signal is greater than 200 keV. The energy of the delayed signal is greater than 150 keV for ^{212}BiPo events, and greater than 300 keV for ^{214}BiPo events. The higher energy threshold for the ^{214}BiPo measurement is set in order to reduce the random coincidence background. A pulse shape analysis based on the charge over amplitude Q/A ratio of the prompt and delayed signals is applied to reject noise pulses. If a signal greater than 3 mV (about 10 keV) is detected in coincidence with the prompt signal in the opposite scintillator, the BiPo event is recognized as a bulk contamination background event and is rejected (see Fig. 5).

4.4. Analysis method

The observed data are compared to the expected background by fitting simultaneously the energy spectra of the delayed α signal of the two background components. The α energy spectrum of a contamination sitting on the surface of the scintillators is calculated by simulating BiPo decay cascades, uniformely distributed on the surface. The BiPo-3 Monte Carlo simulations are performed with a GEANT4 (Agostinelli et al., 2003; Allison et al., 2006, 2016) based package using the DEC AY0 event generator (Ponkratenko et al., 2000) and the SuperNemo simulation sofware. Detection efficiencies are also obtained from the Monte-Carlo simulations. The detector efficiency for the contamination on the surface of the scintillators, without any sample between, is 32% for ^{212}BiPo events and 28% for ^{214}BiPo events.

The α energy spectrum of the random coincidence background is measured using the single counting events. The rate of random coincidences is also determined independently by measuring the single counting rate of the scintillator plates, using the single counting events. The single rate is calculated by using all the data available and by averaging over all the scintillators. The expected number of random coincidences is equal to $2 \times r_p \times r_d \times \Delta T \times T_{obs}$, where r_p is the single rate measured by applying the prompt energy threshold (200 keV), r_d is the single rate measured by applying the delayed energy threshold (150 keV for ^{212}Bi and 300 keV for ^{214}Bi), ΔT is the time window (1480 ns for ^{212}Bi and 990 µs for ^{214}Bi), and T_{obs} is the duration of the

measurement. Comparing the expected number of random coincidences with its fitted value gives a cross-check and a validation of the fitting procedure.

4.5. Results of the background measurements in the ^{212}BiPo and ^{214}BiPo channels

The results of the background measurements in the ^{212}BiPo and ^{214}BiPo channel are presented in Table 2. For ^{212}BiPo, the level of random coincidences, calculated by measuring the single rate, is about 6×10^{-4} counts/day/m^2 of surface area of scintillator, and is negligible. For the ^{214}BiPo measurement, the random coincidence background becomes larger due to the longer ^{214}Po decay half-life, leading to BiPo events with preferentially low energy signals. Therefore an energy threshold of 300 keV on the delayed signal is systematically applied for the ^{214}BiPo measurement. The counterpart is that the ^{214}BiPo efficiency is reduced when measuring samples. The expected rate of random coincidences, calculated by measuring the single rate, as explained in Section 4.4, is 0.13 counts/day/m^2 of surface area of scintillator for the first BiPo-3 module with the final shielding, and 0.10 counts/day/m^2 for the second BiPo-3 module. As presented in Table 2, the number of random coincidences estimated by the fit is in agreement with the expected rate calculated from the single rates. It demonstrates the reliability of the fit and the reliability of the estimated activity in ^{214}Bi on the surface of the scintillators.

We note that the levels of surface background measured separately in the two BiPo-3 modules are equal, within the statistical uncertainties (with the exception of the ^{214}BiPo background measurement with the temporary shielding with a higher surface background, due to a poor tightness of this shield against external radon. This measurement is not taken into account for the estimation of the detector surface background.) For ^{212}BiPo combining the three distinct sets of dedicated background measurements, corresponding to 200.4 days of data collection and a scintillator surface area of 3.10 m^2, 29 ^{212}BiPo background events have been observed. The fitted ^{208}Tl activity for the contamination on the surface of the scintillators is $\mathscr{A}$(^{208}Tl) = 0.9 ± 0.2 μBq/m^2 of surface area of scintillator. For ^{214}BiPo combining the two distinct sets of background measurements of the two modules with the final shield, corresponding to 111.9 days of data collection and a scintillator surface area of 3.24 m^2, the fitted ^{214}Bi activity for the contamination on the surface of the scintillators is $\mathscr{A}$(^{214}Bi) = 1.0 ± 0.3 μBq/m^2 of surface area of scintillator. The background level has been controlled during sample measurements, by keeping half of the module empty and it is stable.

5. Measurement of the first SuperNEMO ^{82}Se double β source foils

The SuperNEMO foils are in the form of strips, 270 cm long, 13.5 cm wide and ~200 μm thick. To produce enriched ^{82}Se foils for the SuperNEMO experiment, thin and chemically purified ^{82}Se powder is mixed with Polyvinyl alcohol (PVA) glue and then deposited between Mylar foils. The Mylar foil is 12 μm thick and has been irradiated at JINR Dubna (Russia) with an ion beam and then etched in a sodium hydroxide solution. This produces a large number of microscopic holes in order to ensure a good bond and to allow water evaporation during the drying of PVA.

5.1. Analysis method

The criteria to select the *back-to-back* BiPo events and the analysis method for the ^{212}Bi and ^{214}Bi contamination measurements inside the samples is similar to the method used for the background (described in Sections 4.3 and 4.4). For the samples, we search for an excess of BiPo events above the background expectation in the delayed energy spectrum. The background components are random coincidences and the contamination on the scintillator surface. For the ^{82}Se foils, the contamination inside the irradiated Mylar is added as an extra component of the background. The delayed α energy spectra of the background components are then simultaneously fitted to the observed data. The surface background and the irradiated Mylar fit values are allowed to vary within the range given by the dedicated measurements. For the surface background these values are quoted in Table 2, and for the irradiated Mylar they are given in Section 5.2. The number of random coincidences is allowed to vary within the 1 σ range given by the expected value calculated from the single rates (as explained in Section 4.4).

For the ^{214}Bi measurement, the delay time between the prompt and the delayed signal is required to be lower than 492 μs (three times the ^{214}Po half-life), to reduce the random coincidences background.

5.2. Measurement of the raw materials

Before producing the ^{82}Se foils, the raw materials have been first measured separately with the BiPo-3 detector (PVA and Mylar). The PVA is very pure in ^{208}Tl and upper limits of $\mathscr{A}$(^{208}Tl) < 12 μBq/kg and $\mathscr{A}$(^{214}Bi) < 505 μBq/kg are obtained (using the statistical analysis approach described by Feldman and Cousins (1998). For the irradiated Mylar the following values are measured:

$$\mathscr{A}(^{208}\mathrm{Tl}) = 100 \pm 53\ \mu\mathrm{Bq/kg}.\mathscr{A}(^{214}\mathrm{Bi}) < 690\ \mu\mathrm{Bq/kg}$$

5.3. Measurement of the enriched ^{82}Se foils

Four first SuperNEMO ^{82}Se strips with thickness ~40 mg/cm^2, have been measured from August 2014 to June 2015. The total duration of this measurement is 262 days for the ^{212}BiPo measurement (after rejecting the three first days to suppress the background induced by the

Table 2
Results of the ^{212}BiPo and ^{214}BiPo background measurements: separate and combined results of the three dedicated background measurements.

	^{212}BiPo				^{214}BiPo			
	Module 1 Temp. shield	Module 1 Final shield	Module 2 Final shield	**Combined**	Module 1 Temp. shield	Module 1 Final shield	Module 2 Final shield	**Combined Final shield**
Duration (days)	73.5	51.2	75.7	200.4	73.5	36.2	75.7	111.9
Scint. surface (m^2)	2.7	3.06	3.42	3.10	2.7	3.06	3.42	3.24
Data events	9	8	12	29	27	18	30	48
Surf. Bkg (fit)	7.4	8.0	12.0	27.7	11.7	2.5	6.9	9.4
Coinc. (fit)	1.6	0.0	0.0	1.3	15.3	15.5	23.1	38.5
Coinc. (single rate)	0.20	0.10	0.14	0.44	18.2	14.3	25.0	39.3
$\mathscr{A}$(^{208}Tl) μBq/m^2	0.8 ± 0.3	1.0 ± 0.4	1.0 ± 0.3	0.9 ± 0.2				
$\mathscr{A}$(^{214}Bi) μBq/m^2					2.5 ± 0.7	1.0 ± 0.6	1.0 ± 0.4	1.0 ± 0.3

^{220}Rn deposition) and 241.1 days for the ^{214}BiPo measurement (after rejecting the fifteen first days to suppress the background induced by the ^{222}Rn deposition). The total effective mass of the ^{82}Se + PVA mixture is 359 g (352 g), and the effective scintillators surface area is 2.13 m^2 (1.97 m^2) for the ^{212}BiPo (^{214}BiPo) measurement. A second set of four strips with thickness ~55 mg/cm^2, have been measured from October 2015 to May 2016. The total duration of this measurement is 161.3. days for the ^{212}BiPo measurement and 109.7 days for the ^{214}BiPo measurement, the total effective mass of the ^{82}Se + PVA mixture is 777 g (726 g), and the effective scintillators surface area is 2.7 m^2 (2.52 m^2) for the ^{212}BiPo (^{214}BiPo) measurement. Combining the two set of measurement, the total duration is 423.3 days for the ^{212}BiPo measurement and 350.8 days for the ^{214}BiPo measurement.

The energy spectra of the prompt and delayed signals are presented in Fig. Fig. 6. The number of fitted events from each background component and from bismuth contamination inside the ^{82}Se + PVA mixture are summarized in Table 3. To reject the surface background and to reduce the background contribution from the irradiated mylar, an upper limit on the delayed energy is added (700 keV for ^{212}BiPo and 600 keV for ^{214}BiPo), allowing to increase the signal over background ratio.

With a delayed energy lower than 700 keV, 18 ^{212}BiPo events are observed and 4.3 background events are expected from the fit. The excess of observed events above the fitted background is in agreement with a ^{212}Bi contamination inside the ^{82}Se + PVA mixture. Taking into account the detection efficiency of 2.65% for the first four strips and 1.55% for the second set of four strips (calculated by simulating ^{212}BiPo events emitted uniformely inside the ^{82}Se + PVA mixture), this corresponds to a 90% confidence level (C.L.) interval for the ^{208}Tl activity of the ^{82}Se + PVA mixture of:

$$\mathscr{A}(^{208}\mathrm{Tl}) = 20[10.5 - 32.0]\ \mu\mathrm{Bq/kg}\ (90\%\ \mathrm{C.\ L.})$$

For the ^{214}BiPo measurement, with a delayed energy lower than 600 keV, 87 ^{214}BiPo events are observed and 66.5 background events are expected from the fit. Taking into account the detection efficiency of 0.66% for the first four strips and 0.32% for the second set of four strips, an upper limit at 90% C.L. is set to the ^{214}Bi contamination of the ^{82}Se + PVA mixture:

$$\mathscr{A}(^{214}\mathrm{Bi}) < 290\ \mu\mathrm{Bq/kg}\ (90\%\ \mathrm{C.\ L.})$$

6. Conclusion

The BiPo-3 detector is a low radioactive detector dedicated to the measurement of ultra-low ^{208}Tl and ^{214}Bi contaminations in thin materials. Surface activities of $\mathscr{A}(^{208}\mathrm{Tl}) = 0.9 \pm 0.2\ \mu\mathrm{Bq/m^2}$ and $\mathscr{A}(^{214}\mathrm{Bi}) = 1.0 \pm 0.3\ \mu\mathrm{Bq/m^2}$ have been measured. It has been shown that this background can be strongly suppressed by analysing the delay alpha energy spectrum. The measurement of the first SuperNEMO $\beta\beta0\nu$ source foils shows a low ^{208}Tl contamination inside the ^{82}Se mixture with an activity $\mathscr{A}(^{208}\mathrm{Tl}) = [10.5 - 32]\ \mu\mathrm{Bq/kg}$ (90% C. L.). For ^{214}Bi an upper limit (at 90% C.L.) is set $\mathscr{A}(^{214}\mathrm{Bi}) < 290\ \mu\mathrm{Bq/kg}$ (90% C. L.). The BiPo-3 detector has become a generic detector and will be available in 2017 to measure samples for various purposes.

Acknowledgements

We acknowledge support by the grant agencies of the Czech

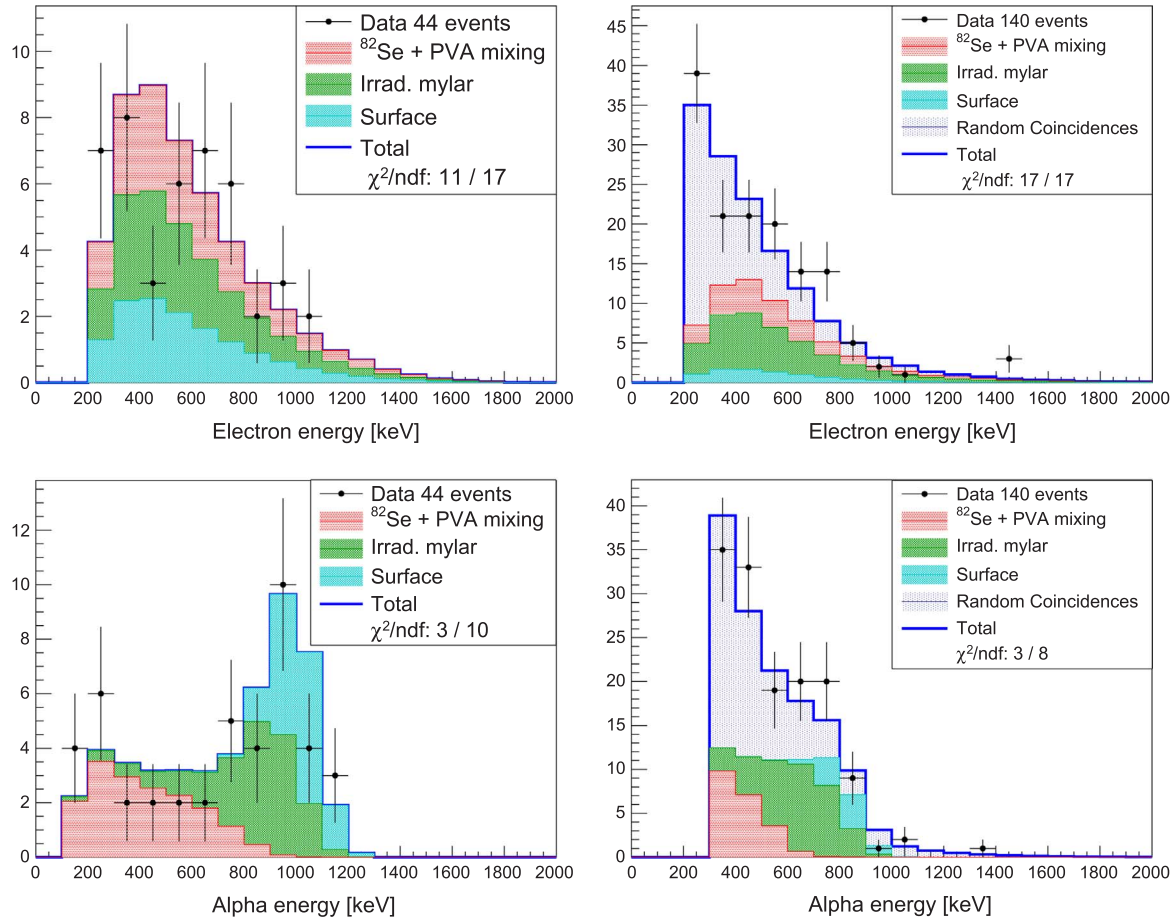

Fig. 6. Distributions of the electron and alpha energy, for the ^{212}BiPo (left) and ^{214}BiPo (right) measurement of the eight first enriched ^{82}Se SuperNEMO foils, with 423.3 days and 350.8 days of data collection respectively. The data is compared to the expected background from the contamination on the surface of the scintillators (light blue histogram), the irradiated Mylar (green histogram) and random coincidences (dark blue histogram).

Table 3
Number of expected background events(surface background, irradiated Mylar and random coincidences) calculated from separate measurements, number of fitted events (background events and signal events from BiPo decays inside the ^{82}Se + PVA mixture) and number of observed events, after 423.3 days(350.8 days) of measurement of the first SuperNEMO ^{82}Se source foils. The number of expected and fitted events are also given in the delayed energy range $150 < E_\alpha < 700(600)$ keV allowing to reduce to zero the surface background, thus increasing the signal to noise ratio.

	^{212}BiPo				^{214}BiPo			
	$E_\alpha > 150$ keV		$150 < E_\alpha < 700$ keV		$E_\alpha > 300$ keV		$300 < E_\alpha < 600$ keV	
	Expected	Fitted	Expected	Fitted	Expected	Fitted	Expected	Fitted
Surf. Bkg.	15.6 ± 2.8	13.9	0.13 ± 0.01	0.12	5.3 ± 3.7	8.8	0.08 ± 0.05	0.12
Irrad. Mylar	21.0 ± 12.0	17.5	4.6 ± 2.5	3.8	<36	36.0	<14.4	14.4
Rand. Coinc.	0.48	0.48	0.41	0.41	65.7 ± 8.1	71.9	47.0 ± 6.9	53.2
^{82}Se + PVA		16.8		15.1		21.2		20.5
Total Fit		48.6		19.4		137.9		88.1
Total Data		44		18		140		87

Republic, by CNRS/IN2P3 in France, RFBR 16-52-16018 in Russia, APVV in Slovakia, STFC in the U.K. and NSF in the U.S.

References

Agostinelli, S., 2003. Geant4 - a simulation toolkit. Nucl. Inst. Meth. A 506, 250–303.
Allison, J., et al., 2006. Geant4 developments and applications. IEEE Trans. Nucl. Sci. 53 (1), 270–278.
Allison, J., et al., 2016. Recent developments in Geant4. Nucl. Inst. Meth. A 835, 186–225.
Arnold, R., et al., 2010. Probing new physics models of neutrinoless double beta decay with SuperNEMO. Eur. Phys. J. C 70, 927–943.
Bé, M.-M. et al., 2008. Table of Radionuclides, Vol 4, ed. Bureau International des Poids et Mesures, Sèvres, France.
Bé, M.-M., et al., 2004. Table of Radionuclides, Vol 2, ed. Bureau International des Poids et Mesures, Sèvres, France.
Bongrand, M., et al., 2011. The BiPo detector for ultralow radioactivity measurements, Proceedings Low Radioactivty Techniques, LRT Workshop, AIP Press, 1338, 49–58.
Feldman, G.J., Cousins, R.D., 1998. Unified approach to the classical statistical analysis of small signals. Phys. Rev. D 57, 3873–3889.
Gomez, H., et al., 2013. BiPo: a dedicated radiopurity detector for the SuperNemo experiment. Nucl. Instr. Meth. A 718, 52–55.
Ponkratenko, O., Tretyak, V.I., Zdesenko, Y., 2000. The event generator DECAY4 for simulation of double beta processes and decay of radioactive nuclei. Phys. At. Nucl. 63, 1282–1287.

3.5 Conclusion and perspectives

We have reviewed in this chapter the main methods to assay the radioimpurities in materials: γ-ray spectrometry, mass spectrometry, neutron activation analysis and surface contamination measurements. To meet the goals of future $0\nu\beta\beta$ searches we need to construct large scale experiments with backgrounds below 1 count/(ROI ton y). Generally speaking, contaminations at the level of 1 to 100 μBq/kg are required (the radioimpurities of the components required to reach the background goals depend of course on the amount of material and their location in the set-up). Unlike ICPMS and neutron activation analysis, γ-ray spectrometry is a non-destructive method that can asses the radioactivities of the worrisome radionucleides in $0\nu\beta\beta$ searches: ^{214}Bi and ^{208}Tl from ^{238}U and ^{232}Th chains. However, γ-ray spectrometry sensitivity, typically in the range 100 μBq/kg – 1 mBq/kg, is not enough for many detector parts, to meet the requirements of present, up-coming and future $0\nu\beta\beta$ and dark matter searches. On the other hand, mass spectrometry and neutron activation sensitivities are low enough, below 1 μBq/kg, but they can only measure the concentration of the parents ^{232}Th and ^{238}U. We are thus confronted with a lack of techniques capable to assess the isotopes of interest at the required low levels of radioactivity. Today the most sensitive assay of the radioactivity of the materials is achieved with the $0\nu\beta\beta$ or dark matter experiments themselves. We need innovative low radioactivity techniques. One way to go could be to perform a chemical separation that would concentrate the radioisotopes of interest prior to their measurement in a HPGe detector.

Chapter 4

Bolometers

La glace chantait dehors dans l'obscurité ...

Henning Mankell

A very sensitive approach for discovering $0\nu\beta\beta$ is to develop a device that is at the same time the source and the detector of the $0\nu\beta\beta$ decay. Furthermore, the detector must exhibit high energy resolution and low radioactive background. Energy resolution is important since the $0\nu\beta\beta$ signal is a peak in the energy spectrum positioned exactly at the $Q_{\beta\beta}$ of the transition, due to the absorption of the two emitted electrons. The peak must be discriminated over the background and therefore it is an asset if it is as narrow as possible. The bolometric technology fulfils all the required features. Bolometers are low temperature detectors (operated at 10-20 mK) sensitive to single particle interactions. This chapter gives a brief introduction to the bolometer detection principle and focuses on the bolometer materials and sensors employed in the EDELWEISS and CUPID experiments.

4.1 Detection principle

A bolometer basically detects the excitation produced by a particle interaction in the lattice of the absorber material at very low temperatures and reads it by a sensor, which converts the information to an electric signal. A bolometer can be modeled as an absorber of heat capacity C, where particles interact, thermally linked by a conductance G to a heat sink, kept at constant temperature T_0. The particle interaction produce a temperature rise, which is translated by the sensor into an electric signal. This model is shown schematically in Fig. 4.1.

A bolometer registers the excitations produced in the crystal lattice, the phonons, which are the quanta of the lattice vibrational states. The temperature increase is proportional to the released energy E, and inversely proportional to the heat capacity C:

$$\Delta T(t) = \frac{E}{C(T)} e^{-t/\tau}. \tag{4.1}$$

Here $\tau = C/G$ is the thermal time constant of the detector, so the conductance G should be sufficiently high in order to provide fast signals but low enough to measure the temperature rise before the heat is evacuated to the thermal bath. In any case, the detector-to-bath coupling must be weak compared to the absorber-sensor coupling. The material and size of the absorber must be carefully chosen so that the overall heat capacity is small enough. The specific heat

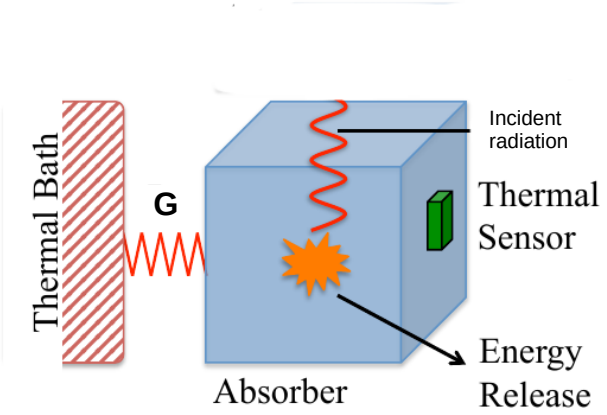

Figure 4.1: Model of the detection principle in a bolometer.

of a crystal is the sum of the lattice and electronic contributions. If the material is dielectric, there is no electronic contribution and the specific heat is given only by the lattice contribution. This is the case for bolometers in $0\nu\beta\beta$ decay experiments and for the EDELWEISS detectors. The lattice heat capacity is expressed as:

$$C_{lattice} = \frac{12\pi^4 k_B N}{5}\left(\frac{T}{\theta_D}\right)^3 \tag{4.2}$$

where k_B is the Boltzmann constant, N the number of atoms in the crystal and θ_D the Debye temperature of the crystal. As we can see from the equations above, bolometers must be operated at low temperatures, about 10- 30 mK, in order to have a measurable temperature rise. Even at cryogenic temperatures the temperature variations are very small: $\sim$0.1 mK per 1 MeV deposited energy.

Any particle interaction ends up releasing its energy into the crystal lattice: nuclear scattering directly transfers its energy to the crystal lattice and electronic interactions produce ionization with the creation of electron-hole pairs and finally relax through their coupling with the lattice. When the crystal lattice is excited, high energy or athermal phonons are produced in the first ns, then they degrade their energy to thermal phonons.

4.2 Thermal sensors

Thermal sensors collect the phonon excitations from the absorber and convert them into an electrical signal. Different types of sensors are available and they measure different signals, voltage, current, magnetic field.

- Transition edge sensors (TES) are superconduting films operated within the temperature range of the superconducting to normal phase transition. The temperature rise produce a change in the resistance. The bias current variation is usually read by a SQUID. They directly measure athermal phonons, therefore their response is fast, featuring signal rise

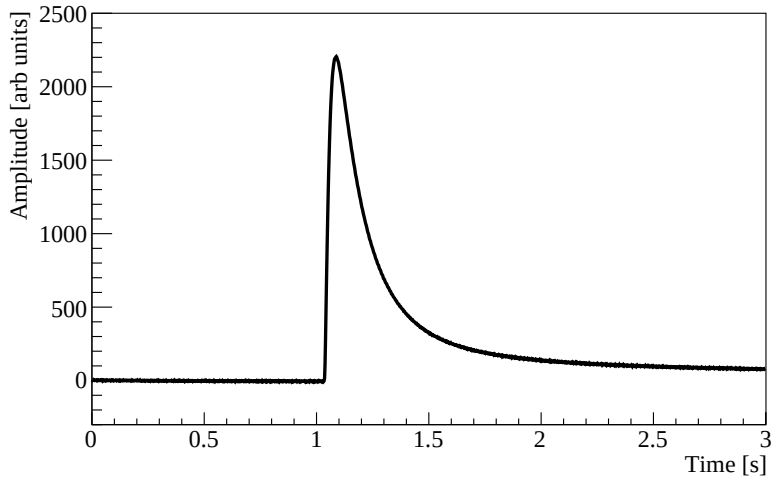

Figure 4.2: A heat signal from a $Li_2{}^{100}MoO_4$ bolometer instrumented with a semiconductor thermistor

time of ~ 100 μs, depending on the implementation. TES are employed, e.g, in the CDMS and CRESST dark matter experiments.

- Metallic Magnetic Calorimeters (MMC) are paramagnetic temperature sensors whose magnetization, in a small magnetic field, varies strongly with temperature. The variation in magnetization is measured with a SQUID. They are chips that are coupled to a film on the crystal, directly collecting athermal phonons, thus their signal is fast, of the order of 100 μs. The AMORE $0\nu\beta\beta$ experiment is using MMCs to read the heat and light signals of scintillating bolometers.

- Semiconductor thermistors are doped semiconductors in which the resistance depends on the temperature.The bolometers in CUORE, CUPID and EDELWEISS utilize this type of sensors, on which we will focus the discussion.

In a semiconductor material, the intrinsic carrier concentration depends exponentially on the temperature T and is given by the fraction of electrons in the conduction band. The conduction occurs when the excitation energy is equal or greater than the energy gap, which never occurs at cryogenic temperatures. In this regime, conduction happen thanks to impurities and depends on the net doping level. The phonons couple to the sensor via the conduction electrons provided by the doping. Due to the low electron density the coupling is relatively slow, of the order of some ms. Fig. 4.2 shows a typical signal from a semiconductor thermistor on a $Li_2{}^{100}MoO_4$ crystal.

At temperatures much lower than 10 K the resistivity of a semiconductor is given by:

$$R(T) = R_0 e^{(T_0/T)^\gamma} \tag{4.3}$$

where R_0 and T_0 depend on the doping level, and γ on the ratio of acceptor to donor impurities.

CUPID bolometers use Neutron Transmutation Doped (NTD) Ge, obtained by irradiation of Ge wafers with neutrons from a nuclear reactor. This technique allows to control the doping level to get the required conduction properties. Fig. 4.3 shows a calibration of several NTDs for CUPID.

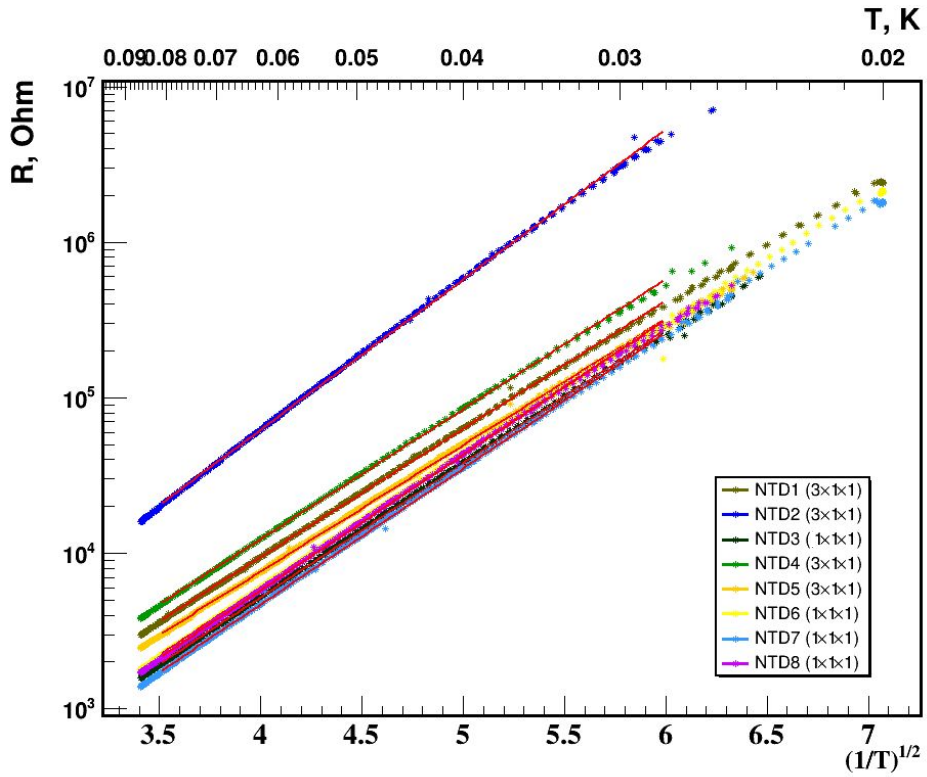

Figure 4.3: A typical resistivity law for NTD thermistors. The data is fit by the function: $\ln R = \ln R_0 + (T_0/T)^{1/2}$

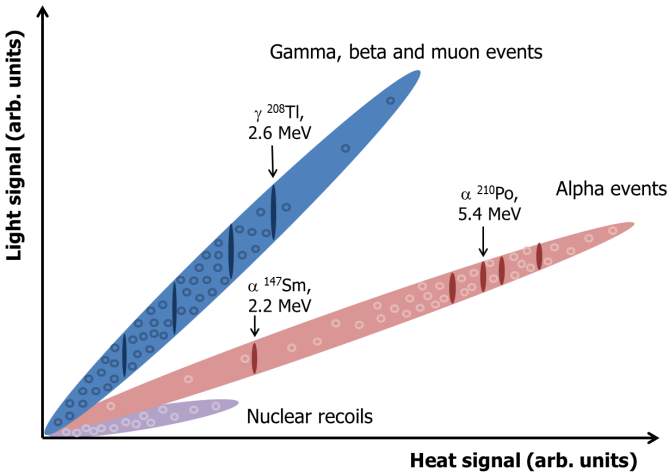

Figure 4.4: Schematic presentation of the light and heat distributions measured by a scintillating bolometer [116].

4.3 Scintillating bolometers

Scintillating bolometers for $0\nu\beta\beta$ searches were developed to reduce the background observed in the current $0\nu\beta\beta$ bolometric experiment CUORE [114]. In CUORE, the background in the region of interest (2527 ± 40) keV) is dominated by surface α's from the copper structure holding the detectors [115]. Bolometric experiments using scintillating bolometers, employing scintillating crystals as absorbers, allow particle identification thanks to the dependence of the scintillation light yield on the type of particle. Like the non-scintillating CUORE detectors, the crystals of the scintillating bolometers are instrumented with NTD Ge thermistors reading a heat signal, but additionally a small fraction of the energy deposited in the crystal is emitted as scintillation light. An equally bolometric light detector (section 4.3.1) facing the scintillating crystal reads the light signal. The response of the scintillating bolometer, both in terms of temperature increase and scintillation light, is proportional to the energy deposited in the material. In a plot of the light signal vs. the heat signal, the slope, i. e. the ratio of the proportionality factors for the two signals, is different for ions, electrons, γ's or nuclear recoils. Fig. 4.4 shows a schematic representation of the light yield distributions in a $Li_2{}^{100}MoO_4$ scintillating bolometer (reproduced from [116]). In particular, the light emitted in the $Li_2{}^{100}MoO_4$ by α particles is about a factor 5 smaller compared to the light emitted by β/γ's of the same energy [56, 116].

The sequence of processes leading to scintillation in a medium can be described as: 1- energy conversion: initial energy release with formation of electrons and holes, 2- thermalization: inelastic processes of interaction of electrons and holes and their thermalization, 3- transfer to luminescent centers: formation of excitonic states and groups of excited luminescent centers and 4- light emission: relaxation of excited luminescent centers and emission of scintillation light [117]. In a way, a scintillator can be therefore defined as a wavelength shifter. It converts the energy (or wavelength) of an incident particle into a number of photons of much lower energy (or longer wavelength) in the visible or near visible range [117]. $Li_2{}^{100}MoO_4$ crystals are weak scintillators that yield scintillation light of λ=590 nm, in the visible range [116] (the typical photon energy is 2.05 eV).

4.3.1 Light detectors

In CUPID and its predecessors the light detectors are Ge wafers instrumented with NTD sensors. Such configuration features typical rise times of about 1 ms, as illustrated in Fig. 4.5.

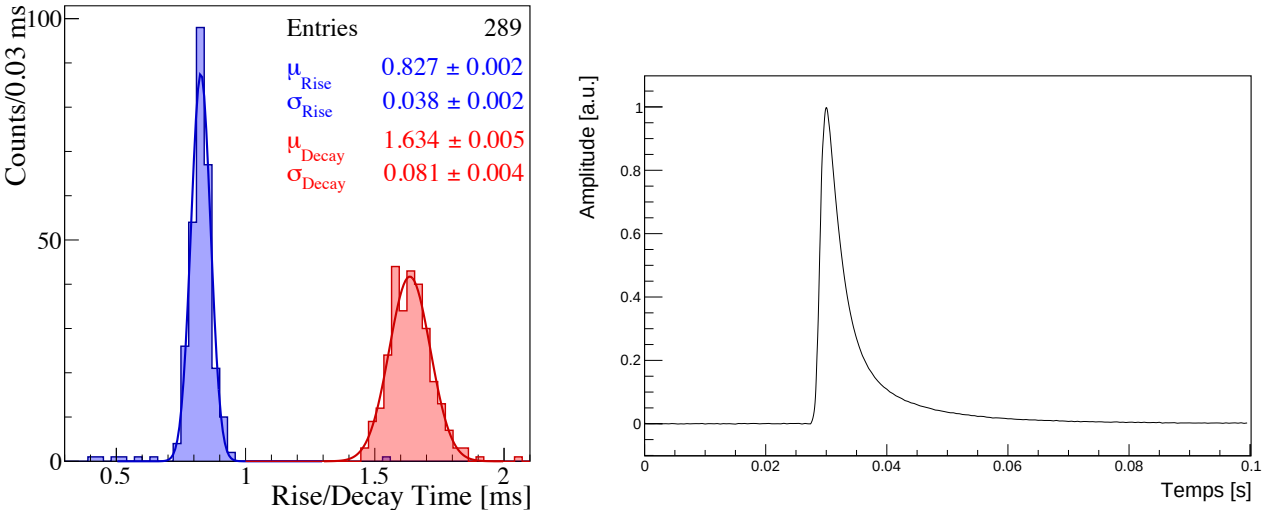

Figure 4.5: Left: Performance of a Ge-LD tested at LNGS in the framework of the CUPID R&D program [118], showing the rise and decay time distributions for ^{55}Fe X-rays. Right: Light signal obtained from the average of 100 pulses.

We define the light yield of scintillation as the amount of light emitted by the scintillator, and collected by the light detector, per unit energy deposited by ionizing radiation in the medium. Tests performed in CUPID R&D configuration show that the light yield for γ/β is $\sim$ 0.3 keV/MeV, when Ge wafers are coated with an anti-reflective layer. This means that when a γ or β particle deposits 1 MeV in the $Li_2{}^{100}MoO_4$ crystal, a signal of 0.3 keV is observed in the light detector. This light yield corresponds to $\sim$ 100 photons/MeV. This light yield is enough to ensure 99.9% α rejection, keeping $\sim$ 100% acceptance of β events. However, the ratio of the light signal to the RMS baseline noise is modest, S/N $\sim$ 10 (900 eV/100 eV) at 3 MeV. Due to this, the rejection of the background induced by random coincidences of $2\nu\beta\beta$ events is insufficient. This motivated to improve the pileup rejection capabilities of the NTDs with Neganov Trofimov Luke amplification. This amplification mechanism [119] appears when the charge carriers in a semiconductor are drifted in an electric filed. Recall that a particle which interacts in the bolometer ionizes the medium and produces electron-hole pairs. The number of charge carriers is $N{=}E/\epsilon$, where ϵ is the energy that is needed to produce one electron-hole pair. If the charge carriers are drifted by a potential V, additional phonons are created by the interactions of the electrons with the lattice, corresponding to a thermal energy $E_{NL} = N \cdot e \cdot V$, where e is the elementary charge. The total energy is then:

$$E_{tot} = E_0(1 + e \cdot V/\epsilon) \tag{4.4}$$

Our standard light detectors, instrumented with NTD sensors, will also be instrumented with charge drift electrodes to apply the voltage V. A prototype is shown in Fig. 4.6.

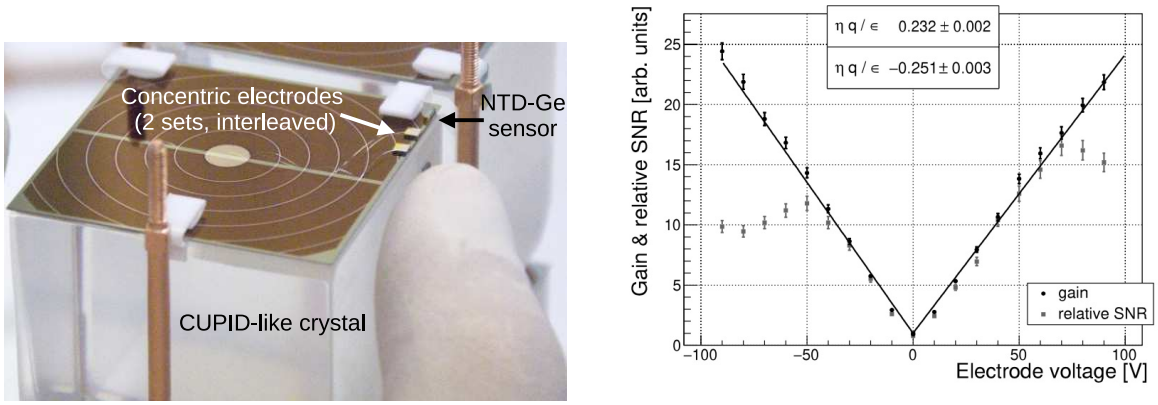

Figure 4.6: (Left) Picture of a germanium light detector instrumented with concentric electrodes to exploit the NTL amplification mechanism. The absorber is a Ge wafer, 175 μm-thickness. This detector has also a SiO coating layer to enhance the absorption of photons in visible wavelength. (Right) Gain and S/N-ratio gain for NTL-assisted LD, as a function of the ΔV applied on the charge-collecting electrode sets. (The deflection in the S/N curves at 55 V is related to spurious infrared photons impinging the absorber, which contribute to increase the baseline noise).

4.4 Ge detectors for heavy WIMP dark matter search

The EDELWEISS dark matter used germanium detectors, with simultaneous read out of heat and ionization to discriminate γ/β induced electronic recoils from potential WIMP-induced nuclear recoils. The particle identification is based on the different ionization yields from electrons and nuclear recoils. The ionization, produced by the free charges induced by a particle interaction, is collected by electrodes, evaporated on the surface on the germanium. The electrodes are biased with a voltage to create an electric field in the crystal. The application of this voltage affects the heat signal as well. The heat signal results from the sum of the heat deposited by the incident particle and of the heat generated by the charge carriers during their drift by the Neganov-Trofimov-Luke effect. From eq. 4.4 we can observe that, as bias voltage increases, the fraction of the heat signal directly correlated to the ionization signal increases, hindering separation of the electron recoils from the nuclear recoils. In practice the bias voltages are of the order of a few volts to ensure the particle discrimination. The heat signals are measured by NTD sensors glued to the crystal. Fig. 4.7 shows a schema of the detection in a Ge detector for dark matter search. Details on the configuration of the EDELWEISS-II Ge detectors are given in section 5.1.

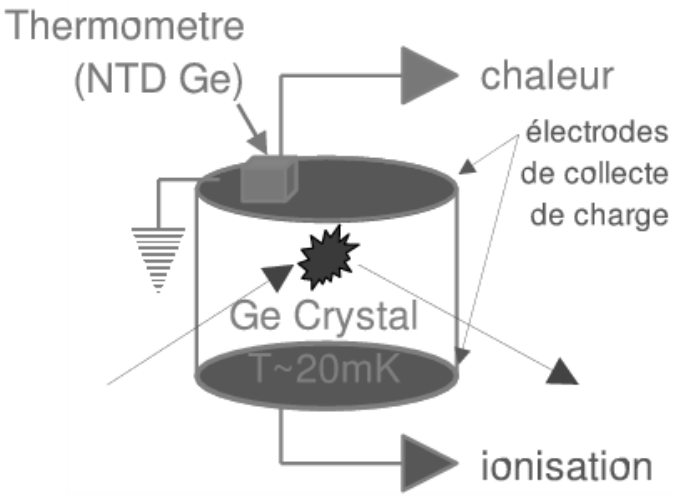

Figure 4.7: Schema showing the principle of the dual read out ionization-heat in a Ge detector for dark matter search.

Chapter 5

Background studies and main results of the EDELWEISS and CUPID-Mo experiments

> Me ocurría a veces que todo se dejaba andar, se ablandaba y cedía terreno, aceptando sin resistencia que se pudiera ir así de una cosa a otra.
>
> *El otro cielo*, Julio Cortázar

5.1 The EDELWEISS-II dark matter experiment : a search for WIMPs with Ge detectors

EDELWEISS-II was a low-background cryogenic experiment aiming at the direct detection of the local WIMPs, which may constitute the dark matter of our Milky Way. The elastic collisions of WIMPs on ordinary matter target nuclei would generate deposits of $\leq$ 100 keV with an exponential-like spectrum.

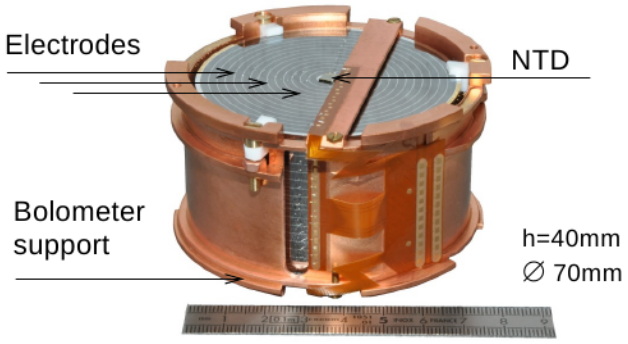

Figure 5.1: Picture of an EDELWEISS-III Ge detector

The EDELWEISS-II setup was located at the Laboratoire Souterrain de Modane where the 4800 m water-equivalent rock overburden reduces the cosmic muon flux down to $\sim$ 5 $\mu \cdot \mathrm{m}^{-2} \cdot \mathrm{d}^{-1}$. The central part of the experiment was a reversed geometry dilution cryostat which could host

up to 40 kg of detectors. A 20 cm thick lead shield surrounded the cryostat to attenuate the external γ radioactivity, with an inner layer of 2 cm made of roman lead. A 50 cm thick polyethylene shielding protected the detectors against the external neutron flux. The shielding materials and detector construction materials were screened by gamma spectrometry. A muon veto made of plastic scintillators with a geometric efficiency for thoroughgoing muons of more than 98% allowed tagging neutrons produced by the residual flux of muons interacting mostly in the lead shield. Additional background monitoring was realized using a Radon detector near the cryostat, a ^{3}He-gas detector to measure the thermal neutron flux, and a Gd-loaded liquid scintillator outside the shielding to study muon-induced neutrons [120].

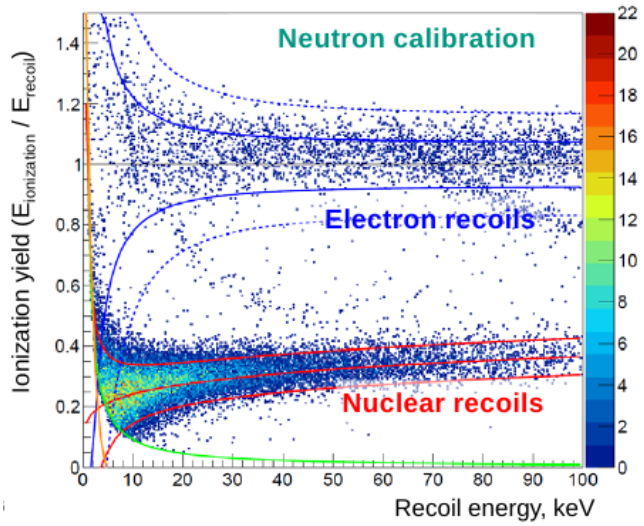

Figure 5.2: $E_{ionization}/E_{recoil}$ versus E_{recoil} from a neutron calibration measurement, showing the electron and the nuclear recoil bands.

EDELWEISS detectors are ultrapure germanium crystals equipped with a dual heat and ionization measurement in order to discriminate γ/β-induced electronic recoils from potential WIMP-induced nuclear recoils, a technology with proven rejection efficiency since the beginning of the 2000s [121]. The heat sensors are NTD (neutron transmutation doped) Ge thermistors glued on the surface of each detector, while the ionization is measured using electrodes polarized at a few volts, Fig. 5.1. The ionization yield is defined as $E_{\rm ionization}/E_{\rm recoil}$. For nuclear recoils it is a factor ~ 3 lower with respect to electron recoils in the energy region of interest, enabling a complete event-by-event discrimination for the bulk of γ-ray radioactivity, as shown in Fig. 5.2. Still, the charge collection is incomplete and difficult to control when an interaction takes place near the surface of the detector. Such surface events 'leak' into the nuclear recoil band and they cannot be discriminated from potential WIMP-induced signals. Surface events originate on copper surfaces facing the crystal, from Radon deposited on them. Radon decays to the long lived ^{210}Pb ($T_{1/2}$= 22 years), which decays subsequently to ^{210}Bi and ^{210}Po, Fig. 5.4, left.

In order to reject these events, new-generation detectors called "ID" (InterDigit) were developed. The principle of these detectors is shown on Fig. 5.3: the concentric electrodes A to D are alternatively polarized with potentials e.g of -1.5V, 4V, 1.5V, -4V, on the A,B, C, D electrodes, respectively. In the bulk of the detector (in green on the Fig.), the field lines are vertical and all the charges are collected on the B and D electrodes. Near the top and bottom surfaces (in brown on the Fig.), the field lines are roughly parallel to the surface and the charge is collected on either A and B, or C and D. Thus, the rejection of events with a signal on either

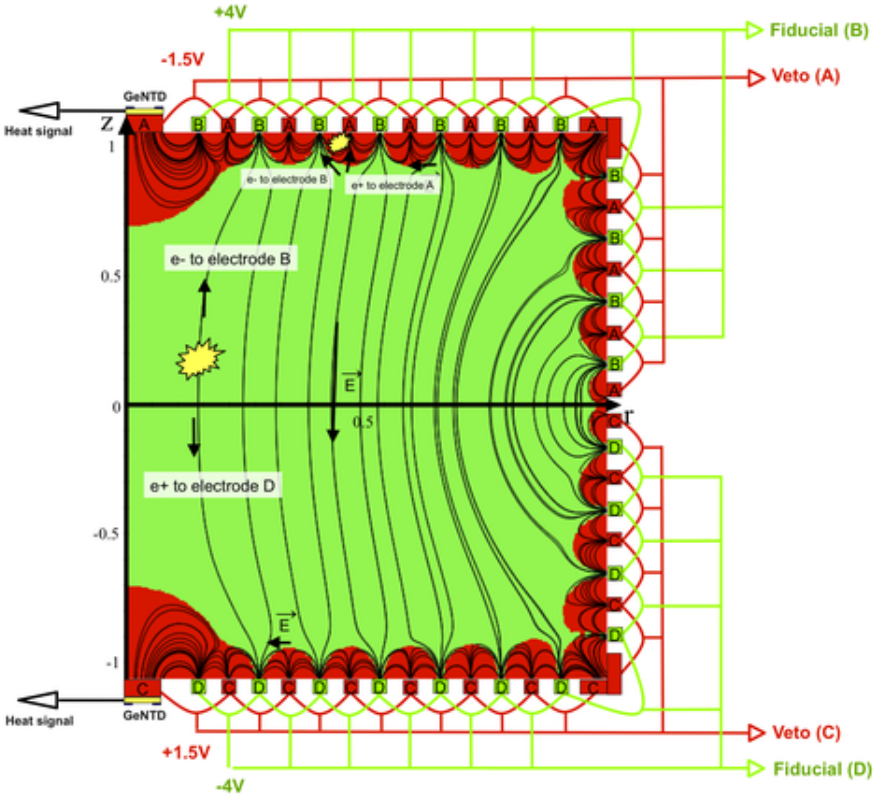

Figure 5.3: Left: Sectional view illustrating the principle of an ID detector. The interleaved electrodes on the top and bottom of the Germanium crystal create an electric field whose equipotential lines are represented in thin lines. The collected signals in the different electrodes enables to isolate interactions taking place within the fiducial volume, in green.

the A or C electrode effectively removes all interactions occurring at depths of less than ∼1 mm below the detector surface.

Fig 5.4 shows on the top right the scatter plot of ionization yield vs recoil energy from a calibration with a ^{210}Pb source on a ID detector of second generation. A total of $\sim 10^5$ β events are detected. The bottom right shows the events passing the fiducial cut to reject surface events. The bands of electron recoil (β and γ interactions) and nuclear recoil (neutrons and WIMPs interactions) are also indicated. From the total of $\sim 10^5$, 1 event is found in the nuclear recoil band, in the energy region E_R >15 keV. The β rejection factor of the these detectors was determined as $4 \cdot 10^{-5}$ in E_R >15 keV, at 90% CL.

The EDELWEISS-II collaboration completed a direct search for WIMP dark matter using 10 cryogenic Ge detectors (400 g each) and 384 kg×days of effective exposure. A cross-section of 4.4×10^{-8} pb was excluded at 90% C. L. for a WIMP mass of 85 GeV [122].

5.1.1 EDELWEISS-III

In the next phase of the experiment, EDELWEISS III, the interdigit detectors were replaced by second generation detectors. The interleaved set of electrodes surrounded also the lateral faces of the crystal, hence they were called Full InterDigit (FID), shown in Fig. 5.5. By using both

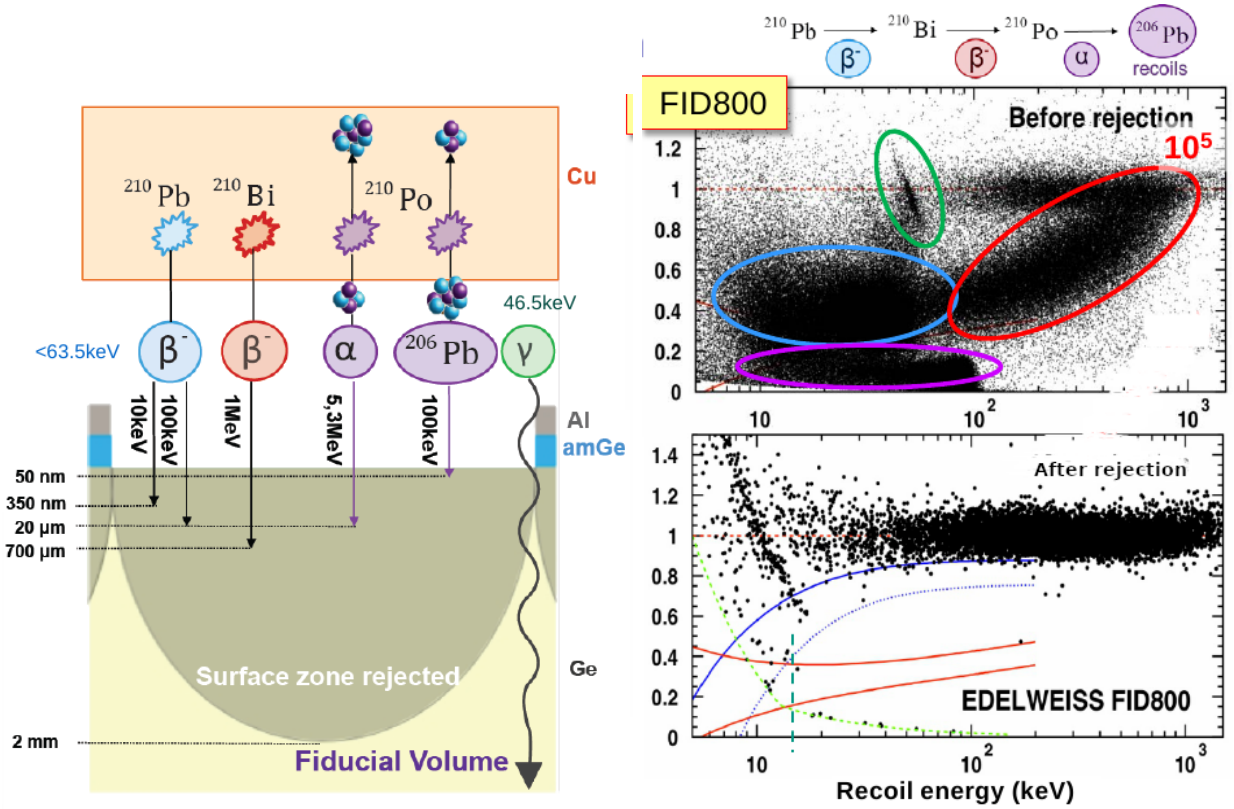

Figure 5.4: Left: Scheme of the decay of ^{210}Pb implanted in the copper casings facing the detectors. The decays of ^{210}Pb and its daughters are shown, together with their maximum energies. The penetration depth of β's, α's and nuclear recoils are indicated; they are much smaller than the surface zone region rejected thanks to the interleaved electrodes design of the FID detectors. Right: Ionization yield as a function of recoil energy (in keV) for a ^{210}Pb calibration. Top: Events passing standard quality cuts. Bottom: events passing the standard quality cuts and the fiducial cut to reject surface events. Only 1 event above 15 keV is within the 90% C.L. band for nuclear recoils (red lines).

the FID design and a mass of 800 g, the fiducial mass for a detector was significantly increased with respect to the EDELWEISS-II detectors of mass = 400 g.

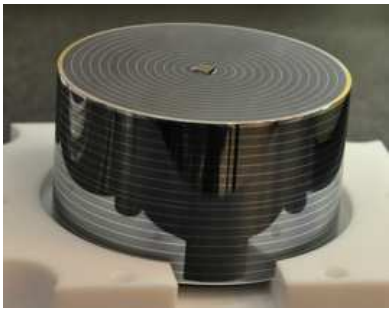

Figure 5.5: Picture of a 800 g Full InterDigit bolometer.

EDELWEISS-III involved the upgrade of several parts of the EDELWEISS-II setup. The background studies presented in the article included below [123] contributed to the design of this new phase. One of the results was that the cryostat thermal shields, made of copper type CuC2, were the main source of gamma background. We replaced all cryostat shields by new ones made of a more radiopure copper, of NOSV type. Additionallly, we installed an extra 10 cm polyethylene shield below the detectors to reduce internal neutrons from materials inside the cryostat. We have also replaced the cabling at the 10 mK stage by new kapton cables and connectors.

We have performed a screening campaign of all new materials in the set-up. The vast majority of the measurements were done by gamma spectroscopy. Selected results are shown in Table 5.1.

Table 5.1: Radioactive contaminations in materials in the EDELWEISS-III set-up. Most measurements were assessed by gamma-ray spectrometry at LSM with the HPGe's Mafalda, Gentiane and Obelix. The NOSV copper of the screens and casings were measured at LNGS. ^{238}U in connectors assesed by ICPMS and the polyethylene shielding by NAA [124].

Component(Material)	Mass (kg)	Radioactivity in materials (mBq/kg) ^{238}U	^{226}Ra	^{228}Th	^{210}Pb
Cables (apical,Cu)	0.5	-	<6	12±3	549±111
Connectors (brass, CuBe)	0.018	1055 ± 211	32±20	<53	18132 ±2720
Screws (Brass)	0.4	<16	8±5	<5	524±102
Screens,casings (Cu)	295		<0.04	0.024±0.012	
Shielding (PE:CH_2)	151	0.8±0.2	0.65±0.08	0.30±0.07	<3
Connectors (Al, resin)	428	2635±406	<186	450±44	6014±460
Cables (PTFE)	3.5	-	4±3	5±2	138±53
Cold electronics (PCB)	0.6	7507±1537	7565±158	10117±132	13986±3094
Warm electronics (PCB)	-		26500±1500*	19300±1100	

* For the whole set (not in mBq/kg).

Fig. 5.6 shows the FID detectors installed in the EDELWEISS cryostat and the completed upgraded set-up.

EDELWEISS-III started taking data in July 2014. About that time, the bolometric technique faced the fact that the slow scalability did not allow to place competitive results in the

search of high mass WIMPS, contrary to liquid noble gas experiments, who consolidated their role as the leaders in the high mass WIMP searches. The EDELWEISS detectors were thus dedicated for low mass WIMP searches [125].

Figure 5.6: The EDELWEISS-III set-up

The article included below presents a study of the gamma and neutron background in EDELWEISS-II and an estimation of the expected background in EDELWEISS-III.

Article: E. Armengaud *et al* [**EDELWEISS coll.**], **Astroparticle Physics 47, 1 (2013)** [Corresponding authors V. A. Kudryatsev and P. Loaiza]

Astroparticle Physics 47 (2013) 1–9

Contents lists available at SciVerse ScienceDirect

Astroparticle Physics

journal homepage: www.elsevier.com/locate/astropart

Background studies for the EDELWEISS dark matter experiment ☆,☆☆

E. Armengaud [a], C. Augier [b], A. Benoît [c], A. Benoît [b], L. Bergé [d], T. Bergmann [e], J. Blümer [f,g], A. Broniatowski [d], V. Brudanin [i], B. Censier [b], M. Chapellier [d], F. Charlieux [b], F. Couedo [d], P. Coulter [k], G.A. Cox [f], M. De Jesus [b], J. Domange [d,a], A.-A. Drilien [d], L. Dumoulin [d], K. Eitel [g], D. Filosofov [i], N. Fourches [a], J. Gascon [b], G. Gerbier [a], M. Gros [a], S. Henry [k], S. Hervé [a], G. Heuermann [f], N. Holtzer [d], A. Juillard [b], M. Kleifges [e], H. Kluck [f], V. Kozlov [g], H. Kraus [k], V.A. Kudryavtsev [l,*], H. Le Sueur [d], P. Loaiza [j,*], S. Marnieros [d], A. Menshikov [e], X-F. Navick [a], C. Nones [a], E. Olivieri [d], P. Pari [h], B. Paul [a], O. Rigaut [d], M. Robinson [l], S. Rozov [i], V. Sanglard [b], B. Schmidt [f], S. Scorza [b,1], B. Siebenborn [g], S. Semikh [i], D. Tcherniakhovski [e], A.S. Torrento-Coello [a], L. Vagneron [b], R.J. Walker [a,f], M. Weber [e], E. Yakushev [i], X. Zhang [k]
The EDELWEISS Collaboration

[a] CEA, Centre d'Etudes Saclay, IRFU, 91191 Gif-Sur-Yvette Cedex, France
[b] IPNL, Université de Lyon, Université Lyon 1, CNRS/IN2P3, 4 rue E. Fermi, 69622 Villeurbanne Cedex, France
[c] CNRS-Néel, 25 Avenue des Martyrs, 38042 Grenoble Cedex 9, France
[d] CSNSM, Université Paris-Sud, IN2P3-CNRS, bat 108, 91405 Orsay, France
[e] Karlsruhe Institute of Technology, Institut für Prozessdatenverarbeitung und Elektronik, 76021 Karlsruhe, Germany
[f] Karlsruhe Institute of Technology, Institut für Experimentelle Kernphysik, 76128 Karlsruhe, Germany
[g] Karlsruhe Institute of Technology, Institut für Kernphysik, 76021 Karlsruhe, Germany
[h] CEA, Centre d'Etudes Saclay, IRAMIS, 91191 Gif-Sur-Yvette Cedex, France
[i] Laboratory of Nuclear Problems, JINR, Joliot-Curie 6, 141980 Dubna, Moscow Region, Russia
[j] Laboratoire Souterrain de Modane, CEA-CNRS, 1125 route de Bardonnèche, 73500 Modane, France
[k] University of Oxford, Department of Physics, Keble Road, Oxford OX1 3RH, UK
[l] Department of Physics and Astronomy, University of Sheffield, Hounsfield Road, Sheffield S3 7RH, UK

ARTICLE INFO

Article history:
Received 19 July 2012
Received in revised form 8 March 2013
Accepted 15 May 2013
Available online 23 May 2013

Keywords:
Dark matter
WIMPs
Background radiation
Radioactivity
The EDELWEISS experiment

ABSTRACT

The EDELWEISS-II collaboration has completed a direct search for WIMP dark matter using cryogenic Ge detectors (400 g each) and 384 kg × days of effective exposure. A cross-section of 4.4×10^{-8} pb is excluded at 90% C. L. for a WIMP mass of 85 GeV. The next phase, EDELWEISS-III, aims to probe spin-independent WIMP-nucleon cross-sections down to a few $\times 10^{-9}$ pb. We present here the study of gamma and neutron background coming from radioactive decays in the set-up and shielding materials. We have carried out Monte Carlo simulations for the completed EDELWEISS-II setup with GEANT4 and normalised the expected background rates to the measured radioactivity levels (or their upper limits) of all materials and components. The expected gamma-ray event rate in EDELWEISS-II at 20–200 keV agrees with the observed rate of 82 events/kg/day within the uncertainties in the measured concentrations. The calculated neutron rate from radioactivity of 1.0–3.1 events (90% C. L.) at 20–200 keV in the EDELWEISS-II data together with the expected upper limit on the misidentified gamma-ray events ($\leqslant 0.9$), surface betas ($\leqslant 0.3$), and muon-induced neutrons ($\leqslant 0.7$), do not contradict five observed events in nuclear recoil band. We have then extended the simulation framework to the EDELWEISS-III configuration with 800 g crystals, better material purity and additional neutron shielding inside the cryostat. The gamma-ray and neutron backgrounds in 24 kg fiducial mass of EDELWEISS-III have been calculated as 14–44 events/kg/day and 0.7–1.4 events per year, respectively. The results of the background studies performed in the present work have helped to select better purity components and improve shielding in EDELWEISS-III to further reduce the expected rate of background events in the next phase of the experiment.

☆ This is not an open-access article, I have never indicated that we wanted an open access publication.
☆☆ GANAPATHYS1 29-MAY-13 Open Access Yes in EES, but no funding form. OA and CC undone.
* Corresponding authors. Tel.: +44 (0)114 2224531; fax: +44 (0)114 2223555 (V.A. Kudryavtsev), tel.: +33 (0) 1 64 46 86 90; fax: +33 (0) 1 69 07 94 04 (P. Loaiza).
E-mail addresses: v.kudryavtsev@sheffield.ac.uk (V.A. Kudryavtsev), ploaiza@lsm.in2p3.fr (P. Loaiza).
[1] Present address: Department of Physics, Southern Methodist University, Dallas, TX 75275, USA.

0927-6505/$ - see front matter © 2013 Published by Elsevier B.V.
http://dx.doi.org/10.1016/j.astropartphys.2013.05.004

1. Introduction

The reduction and discrimination of the background is one of the most important tasks in any dark matter experiment as the signal rate expected from WIMPs is extremely low. EDELWEISS-II is a direct dark matter search experiment based on Ge bolometers. The combined measurement of the ionisation and heat in a particle interaction allows the rejection of the gamma background at the level of $(3 \pm 1)\times10^{-5}$ [1]. Interleaved electrode design, recently developed by the collaboration [2], enables an efficient rejection (6×10^{-5} [3]) of near-surface interactions. Using 10 detectors representing a total mass of 4 kg and with a total effective exposure of 384 kg $\times$ days, EDELWEISS-II has recently published its final WIMP search result [1]. A cross-section of 4.4 x 10^{-8} pb has been excluded at 90% C. L. for a WIMP mass of 85 GeV/c^2. To reach the sensitivity to WIMP-nucleon cross-section significantly below 10^{-8} pb in the next phase of the experiment, the background has to be further reduced.

The sources of background are neutrons, gamma-rays and surface beta contaminants. Neutrons may be induced by cosmic-ray muons or generated by the decay of the natural radioactive elements present in the cavern walls and in the set-up components. Details on the muon-induced neutron studies using the EDELWEISS-II setup are given in Ref. [4], an additional liquid scintillator detector dedicated to the measurement of muon-induced neutrons is described in Ref. [5]. Gamma-rays and beta contaminants are produced by the radioactivity in the construction materials. Surface events induced by surface contaminants are discriminated using the interleaved electrodes. Ref. [1] gives details on the surface event background. We present in this paper studies of the gamma-ray and neutron background coming from radioactive decays in the set-up and shielding of EDELWEISS-II and EDELWEISS-III. Extensive Monte Carlo simulations have been performed and combined with radiopurity measurements of all materials. These background studies have been used for optimisation of the configuration of the next stage WIMP search experiment at Modane – EDELWEISS-III.

2. Experimental set-up and simulations

EDELWEISS-II is located in the Laboratoire Souterrain de Modane (LSM) where the rock overburden of 4800 m w.e. reduces the cosmic muon flux down to about 5 muons/m^2/day [4]. The environmental gamma-ray flux below 4 MeV is dominated by natural radioactivity in the rock and concrete. The uranium, thorium and potassium concentrations have been reported in [6]: 0.84 ± 0.2 ppm and 1.9 ± 0.2 ppm of ^{238}U, 2.45 ± 0.2 ppm and 1.4 ± 0.2 ppm of ^{232}Th, 230 ± 30 Bq/kg and 77.3 ± 13 Bq/kg of K in the rock and concrete, respectively. The neutron flux above 1 MeV is about 10^{-6} n/cm^2/s [7]. The radon level in the laboratory is $\sim$20 Bq/m^3 thanks to a ventilation system renewing the entire laboratory volume 1.5 times per hour. Further reduction of the radon level (down to $\sim$20 mBq/m^3) inside the shielding is achieved by the radon trap facility.

EDELWEISS-II uses cryogenic germanium detectors installed in the 10 mK chamber of a dilution refrigerator specially designed for the experiment. Each detector is enclosed in an individual casing made of electrolytic copper of type CuC2 as termed by the manufacturer and characterised by high purity (99.99% pure) and concentration of oxygen limited to 5 ppm. The radiopurity of this copper has been measured at LNGS (Italy) using gamma-spectrometry [8] and the results are shown in Table 1. Only Teflon (PTFE) is used to hold the detectors inside the casings in a design specially developed to obtain the lowest possible radioactive background [9]. The detectors are arranged on disks supported by three vertical bars. The disks and the vertical bars are themselves supported by a thick plate at 10 mK and surrounded by a 10 mK thermal screen. The 10 mK plate also plays the role of shielding the Ge crystals from the radioactivity beneath the plate. The 10 mK plate and the 10 mK thermal screen will be referred to hereafter as the 10 mK chamber. The disks, the bars and the 10 mK chamber are made of electrolytic copper of type CuC1 (with oxygen concentration less than 1 ppm and purity of 99.95%). The radiopurity of CuC1 copper has been measured at LSM. The results of the measurements are shown in Table 1. To simulate the response of the detec-

Table 1
Radioactive contaminations in materials of the EDELWEISS-II set-up and shielding. All contaminations have been assessed by gamma-ray spectrometry, except for ^{238}U and ^{232}Th in lead and mild steel which have been measured by mass spectrometry, and ^{238}U and ^{232}Th in polyethylene measured by neutron activation. The radioactivity quoted for the dilution unit is based on measurement of individual components.

Component/Material	Mass (kg)	Radioactivity in materials (mBq/kg)				Other radionuclides
		^{226}Ra	^{228}Th	^{60}Co	^{40}K	
Detector holders/PTFE	0.02	<7	<5	<20	<100	^{210}Pb<80
Electrodes/Al	$<3\cdot10^{-5}$	0.27 ± 0.19	1.4 ± 0.2	-	1.1 $\pm^{0.2}_{0.1}$	^{26}Al: 0.38$\pm^{0.19}_{0.14}$
Detector casings/ CuC2 copper[a]	3	0.025 ±0.015	0.033 ±0.016	0.038 ±0.010	<0.39	^{238}U< 1.4, ^{235}U< 0.9 ^{54}Mn: 0.024 ± 0.010[b]
Disks, bars, 10 mK chamber/ CuC1 copper	90	<1	<0.7	<1	<110	^{210}Pb:180 ± 140
Screens 7–11/copper	320	<3	<2	<2	<25	
Dilution unit	≈1	<20	<20	<20	<100	^{108}Ag:331 ± 32
1 K connectors	0.32	644 ± 65	1353 ± 138	<25	1181 ± 197	^{238}U:1994 ± 204
Coaxial cables	1.4	10 ± 7	<6	<8	120 ± 60	^{210}Pb<110
Bolometer boxes[c] (warm electronics)	50 units	331 ± 17	235 ± 13	-	340 ± 40	^{238}U:134 $\pm^{65}_{15}$ ^{210}Pb:1019 ± 56
Roman lead shield	≈120	<0.3	<0.3	-	<1.3	^{210}Pb<120
Modern lead shield	30,000	<3	<1	-	-	^{210}Pb: $(24 \pm 1)\times10^3$ ^{238}U< 0.01 ppb
Polyethylene shield	40,000	5 ± 1	<2	<3	16 ± 2	^{238}U:1 ppb,^{232}Th:0.1 ppb
Mild steel support	8600	-	-	-	-	^{238}U< 0.01 ppb ^{232}Th< 0.01 ppb

[a] CuC2 copper has been measured at LNGS with the GeMPI detector [8].
[b] The activities of short-lived cosmogenic isotopes in CuC2 copper correspond to (10 ± 2) days of exposure.
[c] The radioactivity levels in bolometer boxes are given in mBq/unit.

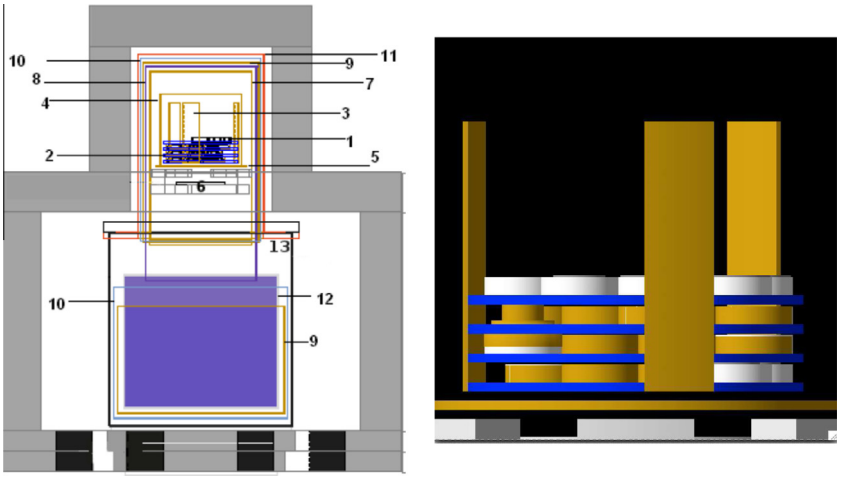

Fig. 1. The GEANT4 geometry of the EDELWEISS-II set-up. Left: 1 – germanium detectors with casings, 2 – copper disks supporting Ge detectors (10 mK), 3 – support bars for the copper disks (10 mK), 4 – 10 mK thermal screen, 5 – 10 mK thick plate supporting inner detector components, 6 – internal roman lead shielding, 7 – 1 K thermal screen, 8 – 4.2 K thermal screen, 9 – 40 K thermal screen, 10 – 100 K thermal screen, 11 – 300 K vacuum chamber, 12 – stainless steel liquid He reservoir, 13 – stainless steel can. The outer lead shielding including modern and roman lead, is shown in grey. The outer polyethylene shielding and the muon veto are not shown. Right: zoom of the central part showing the germanium detectors with casings (dark yellow and grey) stacked on the copper disks (blue), the vertical support bars (dark yellow), the 10 mK thick plate (dark yellow) and, at the bottom, part of the internal roman lead shielding (grey). (For interpretation of the references to color in this figure legend, the reader is referred to the web version of this article.)

tors to various types of particles, the complete set-up has been implemented in the GEANT4 package [10] as shown in Fig. 1.

Below the 10 mK plate, at 1 K, 14 cm of roman lead shields the detectors from the gamma-rays induced by the radioactivity in the cold electronics, the dilution unit and other cryogenic parts. The dilution unit components are made of copper, stainless steel and silver. Four thermal screens at 1 K, 4.2 K, 40 K, 100 K and the vacuum chamber at 300 K, all made of copper which has not been specially selected for its ultra-low radioactivity, complete the cryostat. Hereafter the thermal screens from 1 K to 100 K and the vacuum chamber at 300 K will be referred to as 'screens 7–11' according to the numbering in Fig. 1. EDELWEISS-II uses coaxial cables from the detectors to room temperature. Resistors together with electrical connectors are installed at the 1 K stage below the lead shielding. Cold JFETs are positioned at the 100 K stage. The electronics to bias the JFETs, the DACs to bias the detectors, the final amplification, the anti-aliasing filter and the digitisation are all integrated in a single room-temperature module, called bolometer box, which is attached to the stainless steel can (see Fig. 1 for details of the set-up, bolometer boxes are not shown).

An 18 cm thick outer layer of modern lead shields the cryostat against ambient gamma-ray background. A 2 cm thick inner roman lead layer has been cast directly on the modern lead. An outer 50 cm thick polyethylene shielding protects the detector against ambient neutrons. The lead and polyethylene shielding is mounted on a mild steel structure with rails allowing the opening of the two halves of the shielding structure. In addition an 100 m^2 plastic scintillator active muon veto surrounds the polyethylene [5].

All materials used in the construction have been measured to assess their radioactive contaminations. Table 1 shows a selection of the results. The CuC2 copper of the detector casings was purchased in 2006 and stored in LSM since then. A few samples of this copper have been exposed to cosmic rays for a few days during their transportation from LSM to LNGS for accurate measurements of radiopurity. Decay rates of cosmogenic isotopes (see Table 1) agree with the assumption of a few day activation.

3. Gamma background

The Monte Carlo simulation was based on the GEANT4 code with the Low Energy Electromagnetic Interactions physics list. Cross-sections are determined from evaluated data (EPDL97, EEDL and EADL, stopping power data, binding energy based on data of Scofield) [12]. The particle generator uses the GEANT4 Radioactive Decay Module (GRDM), which was designed to handle all kinds of decays (α, β^-, β^+, EC), the emission of the associated particles and energy distribution, the following de-excitation of the nucleus (γ, internal conversion) and the accompanying X-rays and Auger electrons [12]. The GRDM generator takes into account the total energy loss occurring due to the cascade gamma emission. All emitted particles were followed in GEANT4 and energy depositions in the crystals were stored. Energy depositions occurring in the same crystal within the time window of 50 ms were summed together giving a single event. In a subsequent analysis the fiducial events have been defined in the same way as in real data and the fiducial volume cut was applied to the simulated events.

The decays of ^{226}Ra, ^{228}Ra, ^{60}Co, ^{40}K, ^{54}Mn and ^{210}Pb were simulated in the detector casings, the disks supporting the Ge detectors, the bars supporting the disks, the 10 mK chamber, the cryostat screens 7–11, the dilution unit (as a block for simplicity), 1 K connectors, the coaxial cables and the lead shielding (see Fig. 1). To simplify the simulation task ^{228}Ra was assumed to be in equilibrium with ^{228}Th. In addition, the cosmogenically induced isotopes ^{68}Ge and ^{65}Zn in germanium crystals were considered and their activities were chosen to match the measured intensities of the lines at around 10 keV.

PTFE crystal holders, aluminium electrodes and other small parts located close to the crystals have too small mass to give a measurable contribution to the gamma-ray background but their contribution to the neutron background may be enhanced due to high (α,n) cross-sections, in particular on aluminium and fluorine (see Section 4). The coaxial cables, the dilution unit and 1 K connectors (Table 1) are located below the 14 cm thick lead plate and their contribution was found to be negligible compared to that of the cryostat screens 7–11 despite higher radioactivity levels. The gamma-ray background from bolometer boxes (warm electronics) was not simulated as they were located behind lead. The contribution from ^{210}Bi in the modern lead shielding is negligible but the energetic gammas of about 2.6 MeV from ^{228}Th decay chain may reach the detectors, as shown in Table 2. The background from rock and concrete was shown to be suppressed by several orders of magnitude due to the lead shielding around the cryostat.

Table 2
Ionisation event rate in events/kg/day in fiducial volume obtained from simulations.

Material	Gamma event rate (events/kg/day) at 20–200 keV						
	Fit 1						Fit 2
	^{226}Ra	^{228}Ra (^{228}Th)	^{60}Co	^{40}K	Other radionuclides	Total (%)	Total (%)
Ge crystals	0	0	0	0	^{68}Ge: 1.6	1.6 (2)	1.6 (2)
Detector casings/CuC2 copper	1.2	1	1	0	^{210}Pb: 11	14 (17)	14 (18)
Disks, bars, 10 mK chamber/ CuC1 copper	0.2	1	5	0.3	^{57}Co: 0.7 ^{54}Mn: 2.3	9.5 (12)	13.5 (17)
Screens 7–11/copper	12	15	3	2	^{57}Co: 0.2 ^{54}Mn: 0.3	32.5(40)	17 (22)
Pollution 300 K (see text)	8	14	0	0	0	22 (27)	29 (37)
Modern lead shield	0	2.6	0	0	0	2.6 (3)	4 (5)
Total MC	21	33.6	9	2.3		82	79
Total data						82	82

As only upper limits were obtained in the radioactivity measurements for CuC1 copper and the copper of the screens 7–11, a χ^2 minimisation with 10 free parameters was used to determine those contaminations. The 10 free parameters were: ^{226}Ra and ^{228}Ra in CuC1 copper (disks, bars and 10 mK chamber), ^{226}Ra and ^{228}Ra in copper of the screens 7–11 and ^{226}Ra and ^{228}Ra contamination at 300 K (not shown in Table 1) which could be due to unaccounted radioactivity in cryogenic pipes, electronics, radon or uncontrolled impurities on the 300 K vacuum chamber (6 parameters in total); cosmogenic ^{60}Co and ^{54}Mn in CuC1 and copper of the screens 7–11 (assumed to be the same), ^{40}K in CuC1 and copper of the screens 7–11 (assumed to be the same) and ^{210}Pb on the surface of the detector casings. The radiopurity measurements reported in Table 1 for CuC2 copper were used to calculate the gamma contributions from CuC2 copper parts. The upper limits for other copper parts were taken as upper bounds for the fitting procedure.

Fig. 2 shows the gamma-background in the fiducial volume of the EDELWEISS-II detectors compared to the GEANT4 simulation results. The data were collected with the EDELWEISS-II set-up containing 15 germanium detectors of the type described in Ref. [11] with a total exposure of 310 kg × days. After a cut on the fiducial volume, data with an exposure of 185 kg × days were compared to the simulations. No multiplicity cuts have been applied, i.e. coincident pulses between detectors were included. Multiple-hit events contribute about 30% to the background rate in data and simulations and their rejection does not change the results presented here. Some characteristic peaks are observed in the 0–3000 keV region: ^{60}Co peaks at 1173 and 1332 keV, ^{40}K at 1460 keV, 238 keV and 2614 keV from ^{228}Th (the peaks are linked here to the sub-chain starting with the closest long-lived parent isotope rather than to the gamma-ray emitter). On the right plot of Fig. 2 the 46 keV peak from ^{210}Pb can be seen. The contributions to the gamma background in the low-energy region are presented in Table 2 for two fitting results, corresponding to the minimum and maximum contributions of the thermal cryostat screens. The primary source of gamma background is connected to the U/Th daughters and ^{60}Co in copper screens 7–11 and 10 mK copper parts, which contribute between 39% and 52% to the total gamma-background. The second most important source (between 27% and 37%) is ^{226}Ra and ^{228}Ra decays in some detector parts at 300 K which must be introduced to match the data. This source (marked as 'Pollution 300 K' in Table 2) might be due to radioactivity in cryogenic pipes, bolometer boxes, uncontrolled impurities on the 300 K screen or radon still present in the air in the gap between the cryostat and the lead shielding, in spite of the flushing of radon depleted air. The third most important gamma background source is the ^{210}Pb surface pollution at the level of the detector casings or on the detector's surface (17%).

4. Neutron background

The Monte Carlo simulation used the GEANT4 High Precision (HP) model for neutrons with energies below 20 MeV. Elastic and inelastic scattering, capture and fission were included.

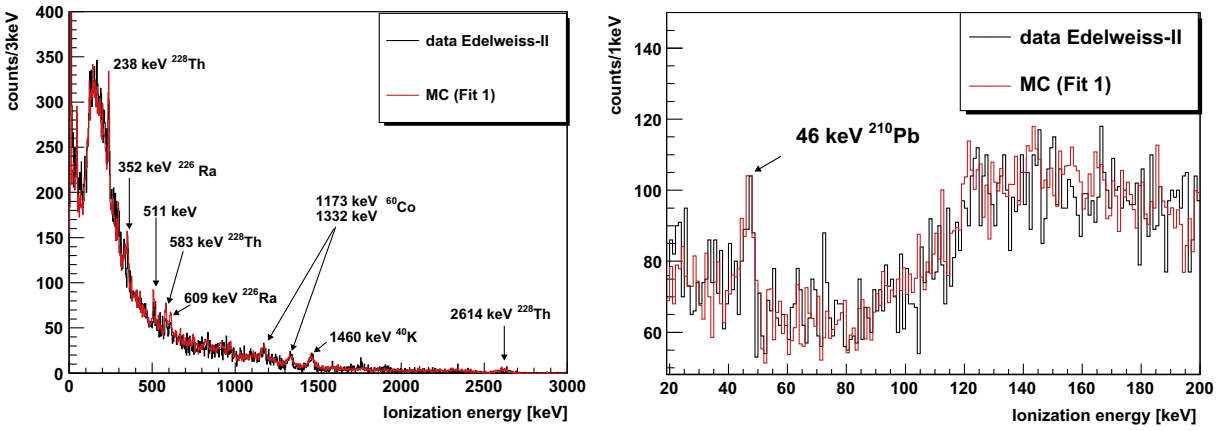

Fig. 2. The background ionisation energy spectrum in the fiducial volume of the EDELWEISS-II detectors from measured data (black line) and Monte Carlo simulation (red line) for 185 kg × days. The full energy range of 0–3000 keV is shown on the left and the relevant range for WIMP search (20–200 keV) is shown on the right. (For interpretation of the references to color in this figure legend, the reader is referred to the web version of this article.)

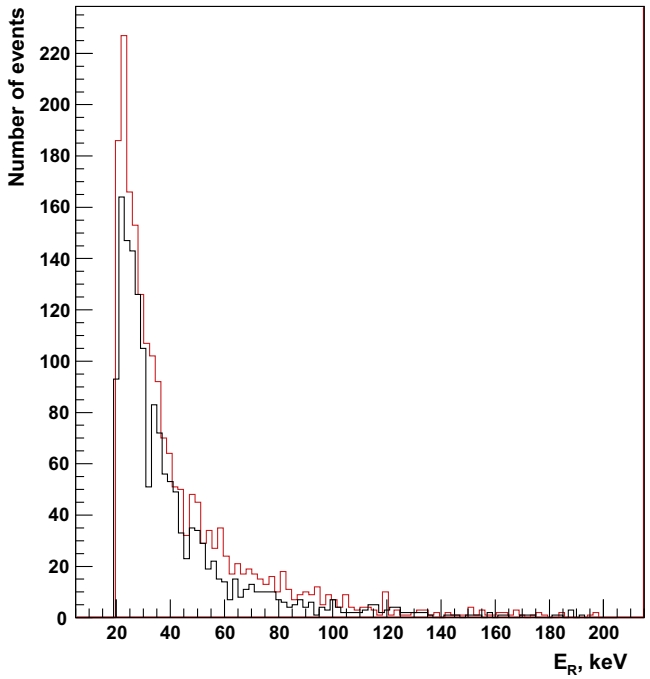

Fig. 3. Energy spectra of neutrons from the Am-Be source used in the detector calibration. Black histogram – data from calibration run with the neutron source; red histogram – spectrum obtained in the simulations of neutrons from this source. Data have not been corrected for the detector dead time of DAQ for this particular run which has been found to be $30 \pm 10\%$. (For interpretation of the references to color in this figure legend, the reader is referred to the web version of this article.)

To check the accuracy of the model, simulations of neutrons from Am-Be source placed inside the Pb shielding on the top of the cryostat, were compared to the measured rate and energy spectrum of nuclear recoils. The source has a neutron intensity of 21 ± 4 neutrons/s and the estimated dead time of the DAQ was $30 \pm 10\%$. The data were collected for about 90 h and the typical number of detected events above 20 keV after all cuts was about 2000 per crystal giving a statistical error of about 2%. Similar statistics was accumulated in simulations. Fig. 3 shows the energy spectrum of nuclear recoils observed from the neutron source and obtained in the simulations. Data have not been corrected for the dead time on this plot so lie below the simulated histogram but the overall shapes of the spectra are in good agreement. The ratio of measured-to-simulated event rates above 20 keV after all cuts, corrected for the dead time and averaged over all crystals, was found to be 1.20 ± 0.23, where the error, given at 68% C. L. is dominated by a 19% uncertainty in the source intensity. Statistical and dead time uncertainties are also included. The ratio is consistent with one within errors, proving the validity of the geometrical model of the detector and neutron physics in GEANT4. The deviation of the average ratio from one may serve as an estimate of the uncertainty of the evaluated neutron rate if the source of background neutrons is located inside the polyethylene shielding.

Further tests of the simulation model were done with a strong neutron source giving about 2×10^5 neutrons/s, positioned outside the polyethylene and lead shielding. 50 cm of polyethylene should attenuate the fast neutron flux by 5–6 orders of magnitude. The neutron source was placed at several positions around the shielding to check the shielding model and neutron transport in GEANT4. The thickness of the shielding was not exactly the same for different source positions, the difference being as much as 5 cm of polyethylene. Also some small holes in the shielding are unavoidable due to pipes, readout cables, support structure etc., so special attention was paid to neutrons which could squeeze through these holes inside the shielding. To check the effect of the holes, the neutron source was also positioned close to the existing holes with pipes, cables and support beams. A difference up to a factor of 50 was observed in the data collected with different source positions and similar effect has also been found in the Monte Carlo simulations. For all source positions the rate of detected events after all cuts was found to be in agreement with the simulated rate within a factor of three with a typical uncertainty of 20% for the measurements and simulations. Bearing in mind the challenge of building precise geometry of all shielding and detector components in GEANT4, the agreement between the measured and simulated rate within a factor of three can be considered as reasonably good. This is quite a small difference on a scale of the overall attenuation of the neutron flux by the polyethylene of 5–6 orders of magnitude (depending on the exact thickness of the shielding and neutron energy). A factor of three difference in the neutron rate (if being due to neutron attenuation in polyethylene) corresponds to a thickness of 5 cm of polyethylene. For half of the source positions tested, the difference between the measured and simulated rates does not exceed 50%. The difference of 50% in neutron flux attenuation by 50 cm of polyethylene was found between GEANT4 and MCNPX [14] showing a good agreement between the two codes on an overall scale of 10^6 for the neutron flux attenuation.

To estimate the event rate due to neutrons in the EDELWEISS-II experiment, we considered the following materials/components as potential sources of neutrons: cavern walls (rock and concrete), lead (shielding), polyethylene (shielding), copper (cryostat and internal parts), stainless and mild steel (support structure), cables, connectors, electronic parts and other components. The results of the simulations are summarised in Table 3. Neutron spectra were generated using SOURCES4A [13] assuming secular equilibrium in the uranium (U) and thorium (Th) decay chains. Further details about neutron production with SOURCES4A for underground experiments can be found in Ref. [15,16]. Fig. 4 shows the energy spectra of neutrons from U/Th decays in stainless steel generated by SOURCES4A. When calculating the neutron-induced event rate, the same cuts have been applied as to the real data: recoil energy threshold of 20 keV, ionisation energy threshold of 3 keV, 90% acceptance in the nuclear recoil band, multiple hit and surface events have been rejected (multiple hit events have been included on the plots).

Apart from the mild steel, the radiopurity of different materials was taken from measurements of decay rates with Ge gamma-spectrometers or from mass-spectrometry data on U and Th concentrations. For mild steel we used the same U/Th concentrations as for the stainless steel. Note that even with five times higher concentrations of U/Th, the contribution of mild steel components will not exceed 0.2 events for the data reported in Ref. [1].

The measurements of the concentrations of U, Th and K (potassium) in the Modane rock and concrete (rock: 0.84 ± 0.2 ppm U and 2.45 ± 0.2 ppm Th, concrete: 1.9 ± 0.2 ppm U and 1.4 ± 0.2 ppm Th), used in the present work, were initially reported in Ref. [6]. The measurements of the neutron flux at LSM [6] require higher values for U/Th (the normalisation requires an additional factor of 2.3 [7]) than measured in the rock/concrete due to a possible non-uniformity in U/Th abundances or rock composition. The uncertainties in the U/Th concentration, in the neutron transport through polyethylene and additional normalisation factor for the neutron flux lead to a large uncertainty (about a factor of 4.7) in the neutron event rate from the cavern walls. The upper limit on the neutron event rate from the walls is given in Table 3 taking into account this possible error.

Since most measurements of U/Th concentrations resulted in upper limits (given at 90% C. L.), normalisation of our simulation results gave upper limits on the neutron-induced event rate in EDELWEISS-II. This gives a significant contribution to the uncer-

Table 3
Number of background events due to neutrons in EDELWEISS-II in the run detailed in [1]. The column "Material" refers to the material in each source which contributes most to neutron production. The column "Composition" gives the chemical composition of the source used to calculate neutron spectra with the abundance of elements (by the number of atoms, not mass) given in brackets. Only elements with the abundance greater than 1% are shown (with the accuracy of 1%). The composition of the mild steel was not known so that of the stainless steel was used instead as giving slightly higher neutron flux than other possible compositions. Neutron yield (columns 4 and 5) is shown as the number of neutrons per gram of material per second per ppb of U and Th concentration. The same cuts as for data have been applied to the simulated events.

Source	Material	Composition (abundance %)	Neutron yield in n/g/s/ppb		Neutron events
			U	Th	
Hall walls	Rock	H (17), C (8), O (53), Mg (1), Al (3), Si (4), Ca (13), Fe (1)	2.88×10^{-11}	7.52×10^{-12}	<0.01
Hall walls	Concrete	H (19), C (11), O (52), Mg (1), Si (2), Ca (15)	2.21×10^{-11}	3.96×10^{-12}	<0.1
Shielding	Polyethylene	H (67), C (33)	2.90×10^{-11}	6.25×10^{-12}	<0.01
Shielding	Lead	Pb (100)	1.35×10^{-11}	–	<0.08
Support	Stainless steel	Cr (17), Mn (0.02), Fe (69), Ni (12)	1.84×10^{-11}	5.92×10^{-12}	<0.01
Support	Mild steel	as above	1.84×10^{-11}	5.92×10^{-12}	<0.04
Warm electronics	PCB	H (22), B (2), C (19), N (6), O (35), Mg (1), Al (4), Si (8), Ca (3)	7.08×10^{-11}	2.21×10^{-11}	1.0 ± 0.5
1 K connectors	Aluminium	Al (100)	1.80×10^{-10}	8.59×10^{-11}	0.5 ± 0.2
Thermal screens, crystal supports	Copper	Cu (100)	1.38×10^{-11}	9.36×10^{-13}	<0.1
Coaxial cables	PTFE	C (33), F (67)	8.40×10^{-10}	3.50×10^{-10}	<0.5
Crystal holders	PTFE	C (33), F (67)	8.40×10^{-10}	3.50×10^{-10}	<0.01
Electrodes	Aluminium	Al (100)	1.80×10^{-10}	8.59×10^{-11}	<0.01
Total					<3.1

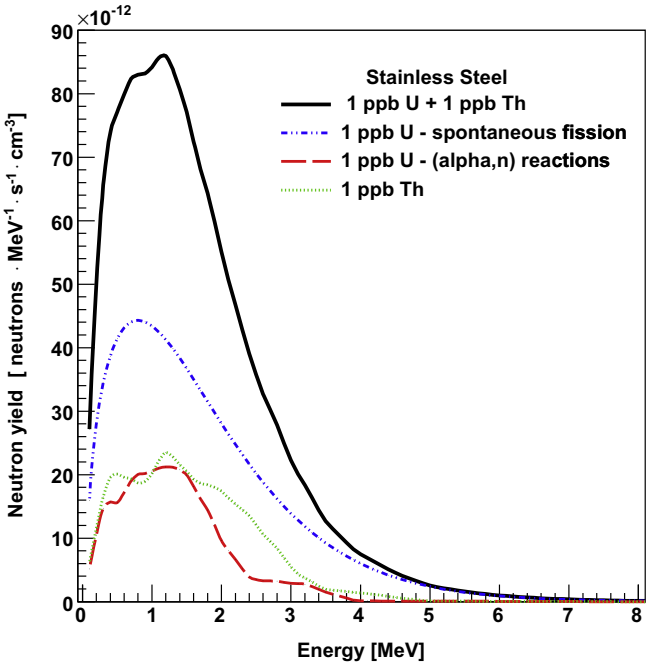

Fig. 4. Energy spectra of neutrons originated in U and Th decay chains in stainless steel. 1 ppb of U and Th were assumed in the calculations and resulting event spectra were later normalised to the measured concentrations. Contributions from different channels (^{238}U spontaneous fission and (α,n) reactions) from the two decay chains are shown separately, together with the total spectrum.

tainty in the neutron background event rate. The uncertainty of the neutron flux and spectra calculations using SOURCES4A has been discussed in [15,17] and found to be 20–30% by comparing calculations with different cross-sections for (α, n) reactions and transition probabilities to excited states. The uncertainty due to the neutron transport and geometry model should not exceed 20% (as follows from the agreement between simulations and data with a neutron source positioned within the shielding). The upper limits shown in Table 3 take into account all these uncertainties. The total rate shown in the last row is the sum of all upper limits and is not strictly the upper limit on the total event rate. Bearing in mind that some of the radioactivity measurements gave positive signals, we can also estimate that the lower limit on the nuclear recoil rate is 1.0 events in data reported in Ref. [1]. The neutron background is potentially dominated by neutrons from materials inside the shields, especially cables and electronics.

Fig. 5 shows an example scatter plot of ionisation yield (ratio of ionisation energy to recoil energy normalised to this ratio for electron recoils) versus recoil energy for simulated nuclear recoils from neutrons originated in the uranium decay chain from contamination in the steel support structure around the main copper vessels. 10^6 neutrons were sampled using the spectrum from SOURCES4A which corresponds to about 4.5×10^4 years of live time for the uranium decay rate of 5 mBq/kg (assuming secular equilibrium). Only events in the fiducial volume of the detectors are shown on the scatter plot. Ionisation yield, Q, has been calculated using the relation $Q = 0.16(E_{rec}(keV))^{0.18}$, where $E_{rec}(keV)$ is the recoil energy. This relation has been proven to be valid for EDELWEISS detectors [11,18].

To conclude, the neutron rate from radioactivity has been calculated as 1.0–3.1 events (90% C. L.) at 20–200 keV in the EDELWEISS-II data run if the same cuts are applied to both data and simulations. Muon-induced neutrons are expected to contribute $\leqslant 0.7$ events [4].

5. Expected background in EDELWEISS-III

The next stage of the EDELWEISS experiment, EDELWEISS-III is currently under construction at LSM. It will contain 40 Ge detectors (800 g each) with improved configuration of electrodes and higher fraction of fiducial mass per crystal (about 600 g) making the total fiducial mass about 24 kg [19]. Larger target mass requires better purity of materials close to the detectors and additional neutron shielding to reduce the expected background and achieve the projected sensitivity of a few $\times 10^{-9}$ pb. Materials and components which could contribute significantly to the gamma-ray or neutron background rate in EDELWEISS-II are being replaced by their counterparts with better radiopurity, for instance the cryostat screens 7–11 and other copper parts at 10 mK (disks supporting the Ge detectors, vertical bars and 10 mK chamber) are made of ultra radiopure NOSV copper [20].

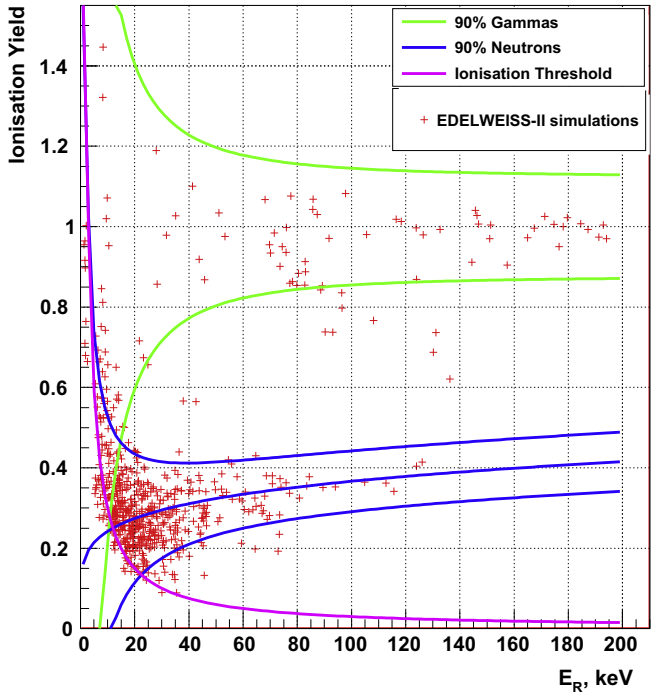

Fig. 5. Ionisation yield (ratio of ionisation to phonons normalised to this ratio for electron recoils) versus recoil energy for simulated nuclear recoils in EDELWEISS-II from neutrons originated in the uranium decay chain from contamination in the steel support structure around the main copper vessels. Blue curves show the average and the edges of the band which contains 90% of nuclear recoils in one of the crystals as calculated from the experimental resolutions, that were also included in the simulations [1]. Green curves show the band which contains 90% of electron recoils. They appear on the plot because of neutron inelastic scattering and capture resulting in gamma-ray production. The pink curve shows the 3 keV software threshold for ionisation, applied as in real data. Statistics corresponds to about 4.5×10^4 years of live time for the uranium decay rate of 5 mBq/kg. (For interpretation of the references to color in this figure legend, the reader is referred to the web version of this article.)

Radioactivity measurements of most new components were done at LSM using low-background gamma-ray spectrometry. Extensive simulations of gamma-rays and neutrons were carried out for a geometry of EDELWEISS-III with additional neutron shielding and the results were normalised to the measured concentrations of radioactive isotopes. The results of the measurements and simulations are shown in Table 4. For some components, such as cables and connectors, various parts were screened separately using a HPGe detector. We present in Table 4 the data for the parts which contribute the most to the background rate. The uncertainties in the radioactivity levels are given at 90% C. L.. Some measurements gave only upper limits leading to large uncertainties in the expected background rates. Neutron event rates were calculated assuming secular equilibrium in the U/Th decay chains except for ^{210}Pb sub-chain. The neutron rate is also affected by a large uncertainty in the chemical composition of the component or its part which may contribute to the background. Since a significant fraction of neutrons may come from (α,n) reactions, exact knowledge of the chemical composition of the material is crucial in the estimate of the neutron event rate. However, in some cases, for instance electronics parts, it is not known precisely which particular part is contaminated the most and hence, it is difficult to predict the expected rate of events with high accuracy. We emphasise that we try to avoid placing materials containing elements with high cross-section of (α,n) reactions (low energy threshold), for example fluorine, close to the crystals. As can be seen from Table 4, a large contamination of printed circuit boards (PCBs) used in electronics (rows eight and nine in Table 4) could compromise the sensitivity of the experiment if crystals were not shielded from their radioactivity by a 14 cm thick lead plate and 10 cm of additional polyethylene shielding.

An example nuclear recoil energy spectrum for neutron events from radioactivity (uranium decay chain) in the inner polyethylene shielding and hit multiplicity distribution are shown in Figs. 6 and 7, respectively. Multiplicity has been defined as the number of hits in different crystals where at least one hit was in the region of interest: recoil energy 20–200 keV, ionisation energy $>$ 3 keV, ionisation yield 0.1–0.5 and hit location is within the fiducial volume; other hits have only been required to have an energy higher than 10 keV. 35–40% of events are single hit events with this selection. Energy spectrum is plotted for all events with any multiplicity. Recoil energy has been calculated as energy deposited in a single crystal. Statistics corresponds to about 2.6×10^4 years of live time.

Table 4
Radioactive contaminations in materials of the EDELWEISS-III set-up. All contaminations have been assessed by gamma-ray spectrometry at LSM, except for NOSV copper of thermal screens that have been taken from the measurements reported in [20]. The last two columns give the expected gamma-induced background in events/kg/day at 20–200 keV and neutron-induced background in a year of running in 24 kg of fiducial mass. For 15 keV threshold the gamma background will change by less than 3% whereas the neutron background will increase by about 15–20%. The first five rows with data show the materials positioned close to the crystals so crystals are directly exposed to the radiation from these components. The next three rows show the materials below the lead plate and polyethylene beneath the detectors. A small gamma rate from warm electronics is due to the additional lead which shields the crystals from the gamma radiation. The gamma-induced rate is given for all events within the fiducial volume without excluding coincidences between different crystals. For neutron-induced rate the coincidences were excluded assuming the threshold for a second hit of 10 keV (35–40% of events are single hit events with this selection).

Component	Material	Mass (kg)	Radioactivity in materials (mBq/kg)					Gammas (kg × days)$^{-1}$	Neutrons Events/year
			^{226}Ra	^{228}Th	^{210}Pb	^{40}K	^{60}Co		
Cables	Apical, Cu	0.2	26 ± 15	<50	346 ± 110	167 ± 126	<25	5–11	0.03–0.07
Connectors	Delrin, brass	0.056	32 ± 20	<53	11,000 ± 1000	680 ± 220	<36	1–8	0.02–0.06
Screws	Brass	0.1	4.9 ± 1.3	<3	<100	<40	<3	<1	<0.003
Screens, support	Cu	~500	<0.016	<0.012	–	<0.11	<0.018	<7	<0.01
Shielding	CH_2	~90	0.65 ± 0.08	0.30 ± 0.07	<3	<1	<0.06	7–14	0.03–0.06
Connectors	Al, resin	1.6	80 ± 9	158 ± 6	743 ± 48	129 ± 33	<4	0.2–0.3	0.3–0.5
Cables	PTFE	~1	<35	<28	190 ± 40	440 ± 110	<19	<1	<0.1
Cold electronics	PCB	0.23	7800 ± 500	12600 ± 1200	4500 ± 400	6500 ± 1200	<120	1–2	0.04–0.06
Warm electronics[a]	PCB	-	26,500 ± 1500	19,300 ± 1100	82,000 ± 5000	27,000 ± 3000	-	<1	0.3–0.5
Total								14–44	0.7–1.4

[a] Decay rates for warm electronics are given for the whole set (not in mBq/kg).

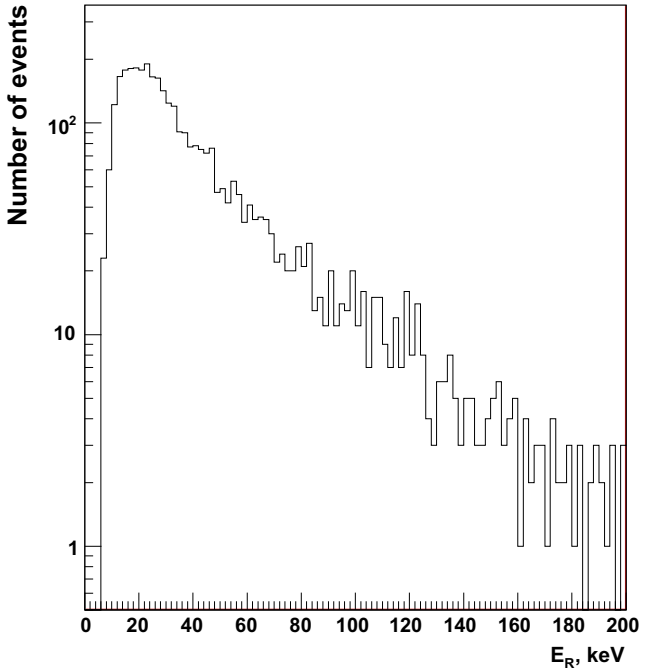

Fig. 6. Simulated energy spectrum of nuclear recoils in EDELWEISS-III detectors from neutrons originated in the uranium decay chain from contamination in the inner polyethylene shielding. Recoil energy has been calculated as energy deposited in a single crystal and events with all hit multiplicities have been included. Statistics corresponds to about 2.6×10^4 years of live time.

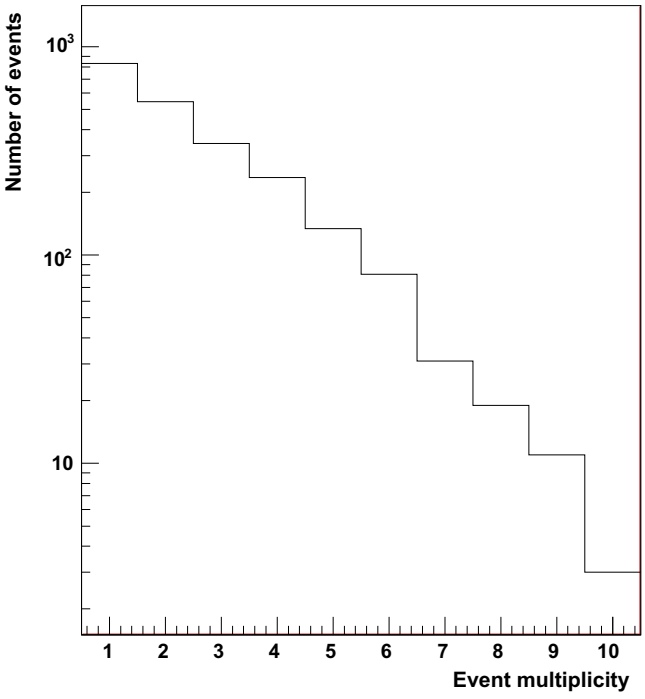

Fig. 7. Hit multiplicity distribution for nuclear recoils in EDELWEISS-III detectors from neutrons originated in the uranium decay chain from contamination in the inner polyethylene shielding. Statistics corresponds to about 2.6×10^4 years of live time. See text for details.

In addition to the components specified in Table 4 we expect to have less than 0.3 neutrons per year from components which were present already in EDELWEISS-II, such as lead shielding, mild and stainless steel support structure etc., bringing the total expected neutron rate to about 0.7–1.7 events per year of running. Decreasing the software energy threshold down to 15 keV will increase the expected neutron rate by 15–20%.

By comparing Tables 2 and 4 we can see that the improvement in the background event rate induced by gamma-rays as measured per unit mass and unit exposure time, will be up to a factor of 6. Even in the worst possible scenario of all contaminations being close to the 90% C. L. upper limits (a factor of 2 improvement in gamma-induced event rate), we expect that better performance of the new "fiducial inter-digitized" (FID) detectors compared to the old type ID detectors will allow us to reach the projected sensitivity of a few $\times 10^{-9}$ pb to WIMP-nucleon cross-section.

Since single nuclear recoil events from neutrons cannot be rejected by any discrimination technique, special measures have been taken in the new design to reduce possible background from neutrons, specifically, an additional polyethylene shielding will be installed in EDELWEISS-III. Our simulations (see Table 4) show that this shielding will suppress the neutron background by more than an order of magnitude (per unit target mass) compared to the EDELWEISS-II setup. The neutron background given in Table 4 corresponds to the rate per unit mass and exposure of $(0.8-1.9) \times 10^{-4}$ events/kg/day in EDELWEISS-III compared to $(2.6-8.1) \times 10^{-3}$ events/kg/day in EDELWEISS-II. An improvement by at least an order of magnitude will allow us to achieve the projected sensitivity with about 3000 kg $\times$ days of statistics with EDELWEISS-III.

6. Conclusions

An extensive study of the gamma and neutron background in the EDELWEISS experiment has been performed, based on Monte Carlo simulations combined with radiopurity data. The primary source of gamma background in EDELWEISS-II is the copper from the cryostat screens and 10 mK parts. The neutron background is potentially dominated by neutrons produced by α-n reactions in materials inside the shields, in particular cables and electronics. The calculated neutron rate from radioactivity of 1.0–3.1 events (90% C. L.) at 20–200 keV in the EDELWEISS-II data run together with the expected upper limit on the misidentified gamma-ray events ($\leqslant 0.9$), surface betas ($\leqslant 0.3$) [1], and muon-induced neutrons ($\leqslant 0.7$) [4], do not contradict five observed events in nuclear recoil band [1]. The background studies performed in the present work have contributed to the design of the next stage of the experiment, EDELWEISS-III. New cryostat screens and 10 mK parts will be built from ultra-pure copper and an inner polyethylene shielding against neutrons from materials inside the external shielding will be installed. The expected gamma-ray and neutron induced background rates from radioactivity in EDELWEISS-III at 20–200 keV are 14–44 events/kg/day and 0.7–1.4 events in 40 detectors per year, respectively. With these improvements and the projected increase by an order of magnitude of the detector mass, the goal is to soon probe the range of spin-independent WIMP-nucleon cross-sections down to a few $\times 10^{-9}$ pb.

Acknowledgments

The help of the technical staff of the Laboratoire Souterrain de Modane is gratefully acknowledged. Matthias Laubenstein has kindly measured the copper of type CuC2 using the GeMPI detector at the Laboratori Nazionale de Gran Sasso, LNGS, developed by the Max-Planck-Institut fuer Kernphysik (MPIK) in Heidelberg. The EDELWEISS project is supported in part by the Agence Nationale pour la Recherche (France) under contract ANR-10-BLAN-0422–03, the Russian Foundation for Basic Research (Russia) and the Science and Technology Facilities Council (UK, Grants ST/I003371/1,

ST/I00338X/1, ST/J000671/1, ST/J000663/1, ST/K003186/1, ST/K006444/1, ST/K003151/1). Background studies for dark matter search are funded in part by the German ministry of science and education (BMBF) within the "Verbundforschung Astroteilchenphysik" Grant 05A11VK2.

References

[1] E. Armengaud et al., The EDELWEISS Collaboration, Phys. Lett. B 702 (2011) 329.
[2] A. Broniatowski et al., J. Low Temp. Phys. 151 (2008) 830.
[3] A. Broniatowski et al., The EDELWEISS Collaboration, Phys. Lett. B 681 (2009) 305.
[4] B. Schmidt et al., The EDELWEISS Collaboration, Astropart. Phys. 44 (2013) 28.
[5] V.Yu. Kozlov et al., Astropart. Phys. 34 (2010) 97.
[6] V. Chazal et al., Astropart. Phys. 9 (1998) 163.
[7] S. Fiorucci et al., The EDELWEISS Collaboration, Astropart. Phys. 28 (2007) 143.
[8] G. Heusser, M. Laubenstein, H. Neder, Radionuclides in the environment, in: P. Povinec, J.A. Sanchez-Cabeza (Eds.), Proceedings of the International Conference on Isotopes in Environmental Studies (Aquatic Forum 2004, 25–29 October, Monaco), Radioactivity in the environment, 8 (2006) 495.
[9] X.-F. Navick et al., Nucl. Instrum. Methods A 444 (2000) 361.
[10] S. Agostinelli et al., Nucl. Instrum. Methods A 506 (2003) 250.
[11] O. Martineau et al., The EDELWEISS Collaboration, Nucl. Instrum. Methods A 530 (2004) 426.
[12] <http://geant4.web.cern.ch/geant4/UserDocumentation/UsersGuides/PhysicsReferenceManual/fo/PhysicsReferenceManual.pdf>.
[13] W.B. Wilson et al. SOURCES4A, Techical Report LA-13639-MS, Los Alamos (1999).
[14] R. Lemrani et al., Nucl. Instrum. Methods A 560 (2006) 454.
[15] V. Tomasello, V.A. Kudryavtsev, M. Robinson, Nucl. Instrum. Methods A 595 (2008) 431.
[16] V. Tomasello, M. Robinson, V.A. Kudryavtsev, Astropart. Phys. 34 (2010) 70.
[17] M.J. Carson et al., Astropart. Phys. 21 (2004) 667.
[18] P.D. Stefano et al., Astropart. Phys. 14 (2001) 329.
[19] E. Armengaud (for the EDELWEISS Collaboration), in: Talk at the 12th International Conference on Topics in Astroparticle and Underground Physics (TAUP2011, Munich, 5–9 September 2011), <http://taup2011.mpp.mpg.de/>.
[20] M. Laubenstein et al., Applied Radiation and Isotopes 61 (2004) 167.

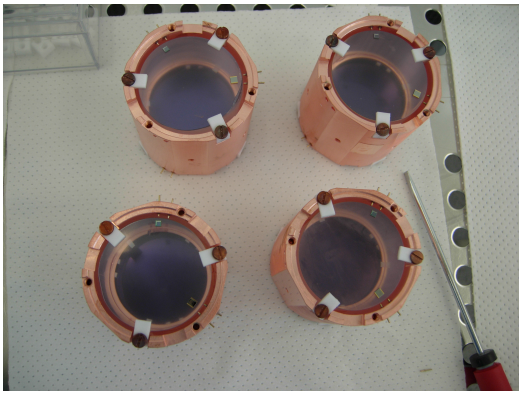

Figure 5.7: CUPID-Mo modules. The transparent $Li_2{}^{100}MoO_4$ crystals are instrumented with NTD thermal sensors (small squares) and supported by PTFE pieces in cylindrical copper holders

5.2 The CUPID-Mo $0\nu\beta\beta$ decay experiment

CUPID-Mo was a demonstrator for CUPID, a next generation $0\nu\beta\beta$ decay experiment. It was located in the Laboratoire Souterrain de Modane, and operated between 2019 and 2020. The basic components of the detection system are $Li_2{}^{100}MoO_4$ crystals coupled to thermal sensors, consisting of NTDs, which read the heat signal. The top and bottom of the crystals are facing light detectors fabricated from Ge wafers, also instrumented with NTDs to read the light signal. The crystals are housed in cylindrical copper holders and supported by PTFE pieces. A reflective foil (3M Vikuiti®) is installed around the crystals, inside the copper holder, to increase the light collection. Four CUPID-Mo modules are shown in Fig. 5.7. These modules were arranged into 5 towers of 4 modules each and mounted in the EDELWEISS cryostat alongside EDELWEISS germanium detectors.

CUPID-Mo has demonstrated that energy resolution, α rejection and radiopurity are at reach to meet the requirements for CUPID. The energy resolution is obtained from Gaussian fits to the full energy γ peaks [126]. Fig 5.8 shows the fit to the 2615 keV line in calibration data. The energy dependence of the resolution in $Li_2{}^{100}MoO_4$ can be described by a typical functional form given by: $\sigma(E) = \sqrt{p_0^2 + p_1 E}$. From the extrapolation of the curve to 3034 keV, we extract the energy resolution at $Q_{\beta\beta}$ [126]:

$$\Delta E(\text{FWHM}) = (7.40 \pm 0.4)\ \text{keV}\ @Q_{\beta\beta} \tag{5.1}$$

The key feature of the CUPID-Mo technology is the capability to discriminate γ/β's from α particles thanks to the simultaneous measurement of heat and light, compared to the existing CUORE approach of heat only measurement. The discrimination capability depends on the light collection efficiency and the performance of the light detectors. Fig. 5.9 shows the light versus heat scatter plot measured with one detector of the CUPID-Mo array [58]. Two separate populations can be seen: a band of γ/β's, and a distribution associated with α events. This happens since the light emitted in a scintillator by an α particle is smaller compared to the light emitted by γ/β's of the same energy. Thus, the commonly used particle identification parameter is the light yield, defined as the ratio of the light signal measured in keV to the heat signal measured in MeV. A light yield ~ 0.5 keV/MeV is necessary in order to attain a rejection goal of more than 99.9%. In CUPID-Mo and its predecessors, with a reflecting foil surrounding the crystals, typical values of 0.75 keV/MeV were obtained for the light yield [56], [58].

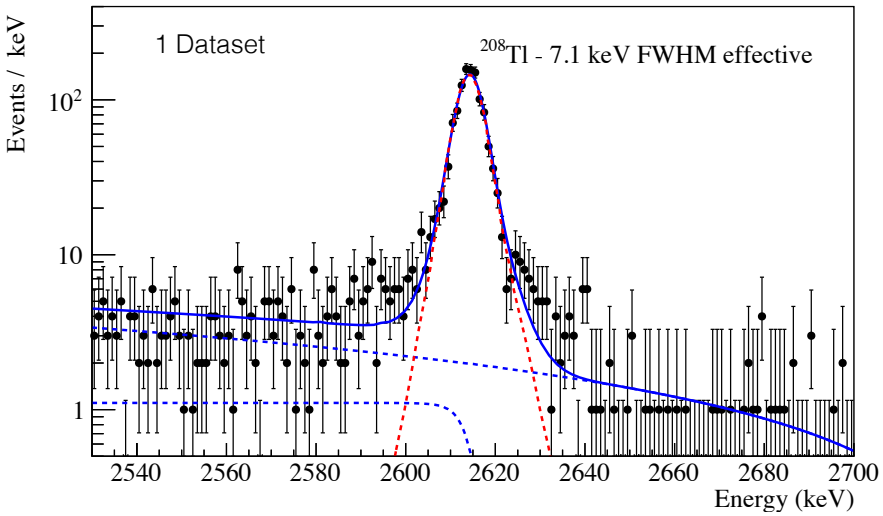

Figure 5.8: Fit of the 2615 keV γ line in calibration data, for all channels in a single dataset, showing the energy resolution.

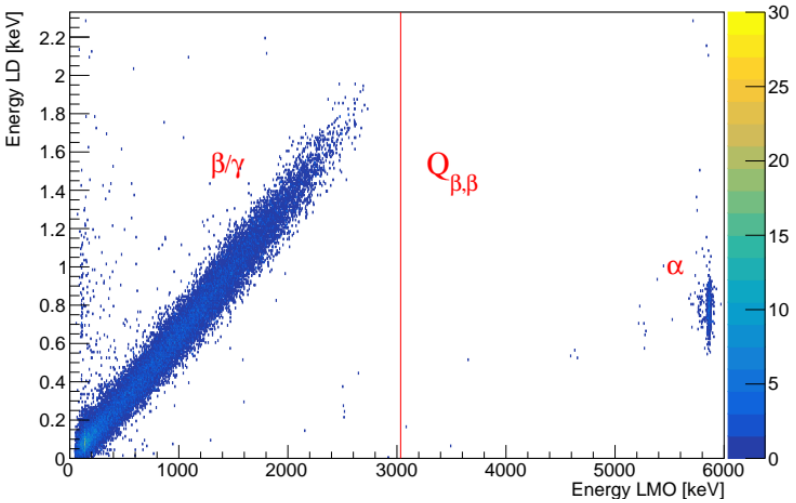

Figure 5.9: Light signal versus heat signal from one $Li_2{}^{100}MoO_4$ crystal (11 days of physics data).

The radioactivity of the $Li_2{}^{100}MoO_4$ crystals is very low, below 1 μBq/kg, which has been measured with the bolometers themselves, by means of the α peaks from bulk contamination and with a detailed model of the CUPID-Mo backgrounds.

5.2.1 Limit on the $0\nu\beta\beta$ decay half life of ^{100}Mo

CUPID-Mo was also an important experiment in its own right. It has set, from 2020 to 2023, the world leading limit on the half life of $0\nu\beta\beta$ decay of ^{100}Mo [127, 126]. The limit was extracted using a blinded Bayesian analysis and, as a counting analysis, it is calculated for the decay rate. At that time, the background model was not finalized, therefore the background index has been evaluated from the still blinded data with a phenomenological fit model that contains an exponential to approximate both the high energy part of the $2\nu\beta\beta$ spectrum as well as tails from U/Th contaminants in the set-up and a constant as a conservative estimate for the coincident detection of two $2\nu\beta\beta$ events in the same crystal, remaining unvetoed muon events and close contamination from the high energy beta decays in the natural U/Th chains [127]. The background index obtained in a region 100 keV around the Q-value is :

$$B = (4.7 \pm 1.7) \times 10^{-3} \text{ counts/keV/kg/year.} \tag{5.2}$$

It was found that in the case of zero events observed, the prior on the background does not change the observed limit [126]. The other parameter involved is the total efficiency defined as the product of the analysis efficiency and the confinement efficiency. The later corresponds to the probability that a $0\nu\beta\beta$ event leaves its energy in only one crystal. Its value, calculated from MC simulations, is $(75.0 \pm 1.1\%)$. The analysis efficiency is $88.4 \pm 1.8\%$ [126].

After the unblinding of the data, zero events were observed in the ROI, and also on a larger energy region [126], as shown in Figs. 5.10 and 5.11. This translates to a limit to the half life :

$$T^{0\nu} > 1.8 \times 10^{24} \text{ years (stat.+syst.) at 90\% C.I.,} \tag{5.3}$$

Using $g_A = 1.27$, the space factors from [18, 128], and the Nuclear Matrix elements in [20, 129, 130, 131, 132, 65, 133, 134], the limit on the Majorana mass is:

$$\langle m_{\beta\beta} \rangle < (0.28 - 0.49) \text{ eV,} \tag{5.4}$$

Fig. 5.12 shows $m_{\beta\beta}$ limits for several experiments as a function of the exposure. CUPID-Mo was able to set competitive limits with a modest ^{100}Mo exposure of 1.19 kg $\times$ yr.

5.2.2 CUPID-Mo background model

The work of my PhD student Léonard Imbert consisted in the development of a background model of the CUPID-Mo data, based on fitting the data with detailed Monte Carlo simulations. This detailed model describing the background sources in the CUPID-Mo experiment is able to reproduce well the features of the experimental data, Fig. 5.13.

We have found that the radiopurity of the $Li_2{}^{100}MoO_4$ crystals is sufficient to reach the goals of the future $0\nu\beta\beta$ experiment CUPID. The radiopurity levels of ^{226}Ra and ^{228}Th are below 0.5 μBq/kg.

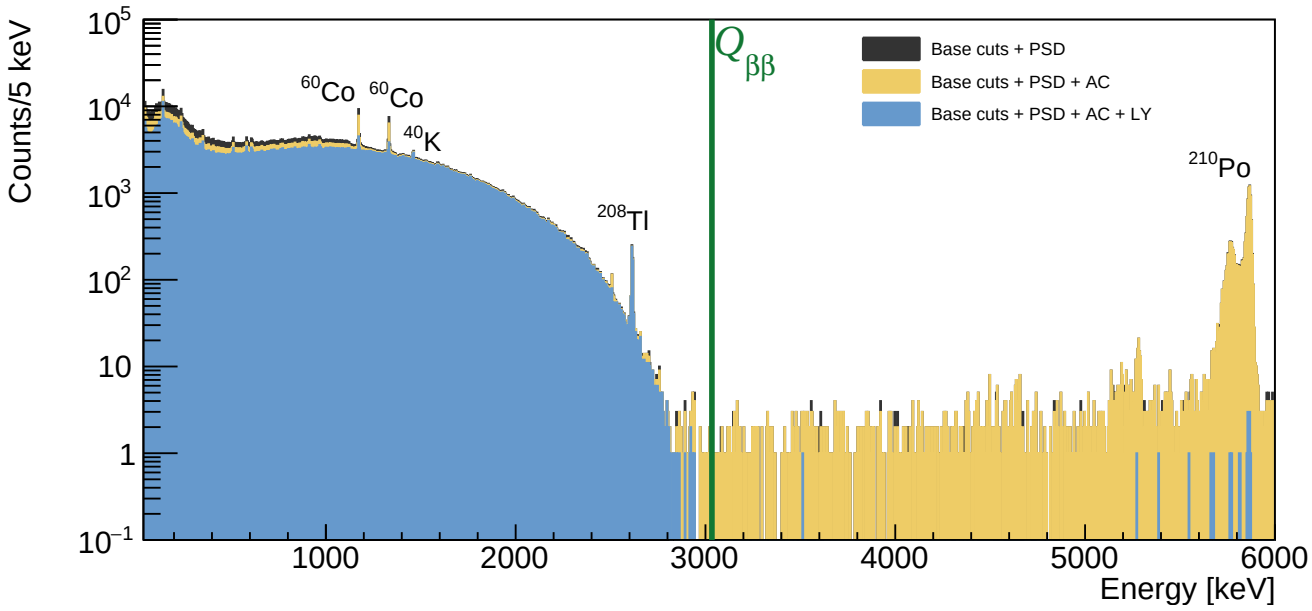

Figure 5.10: Background spectrum showing the analysis cuts [126].

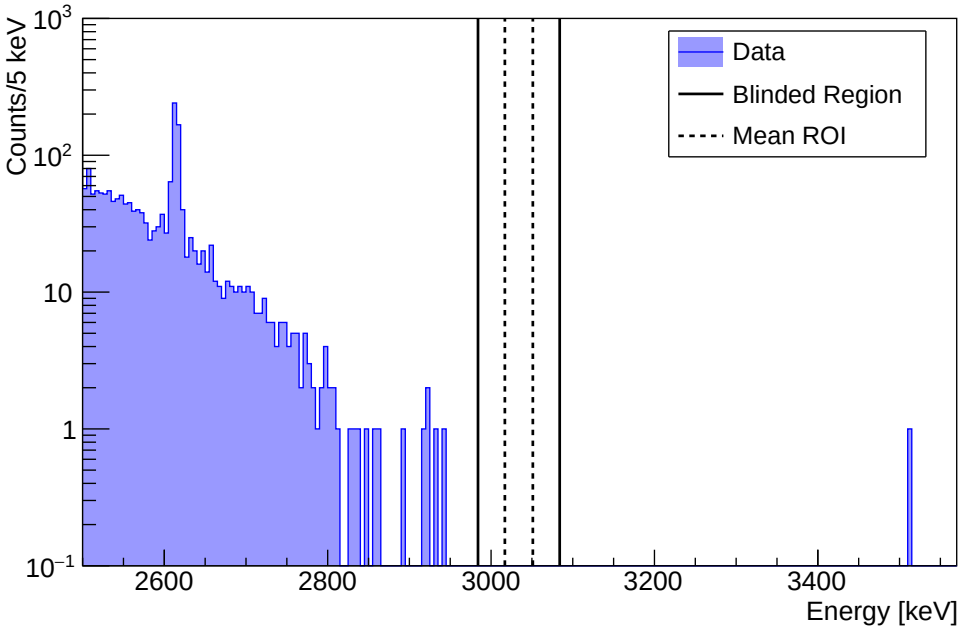

Figure 5.11: Background spectrum in the ROI region. Zero events are observed after the cuts [126]

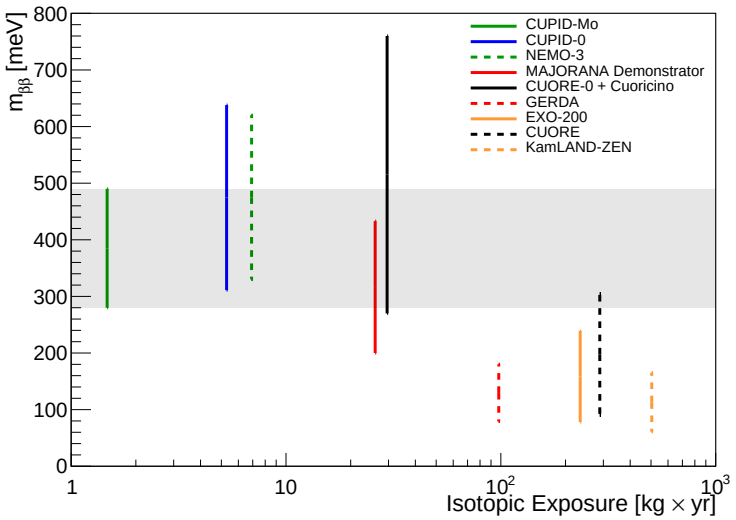

Figure 5.12

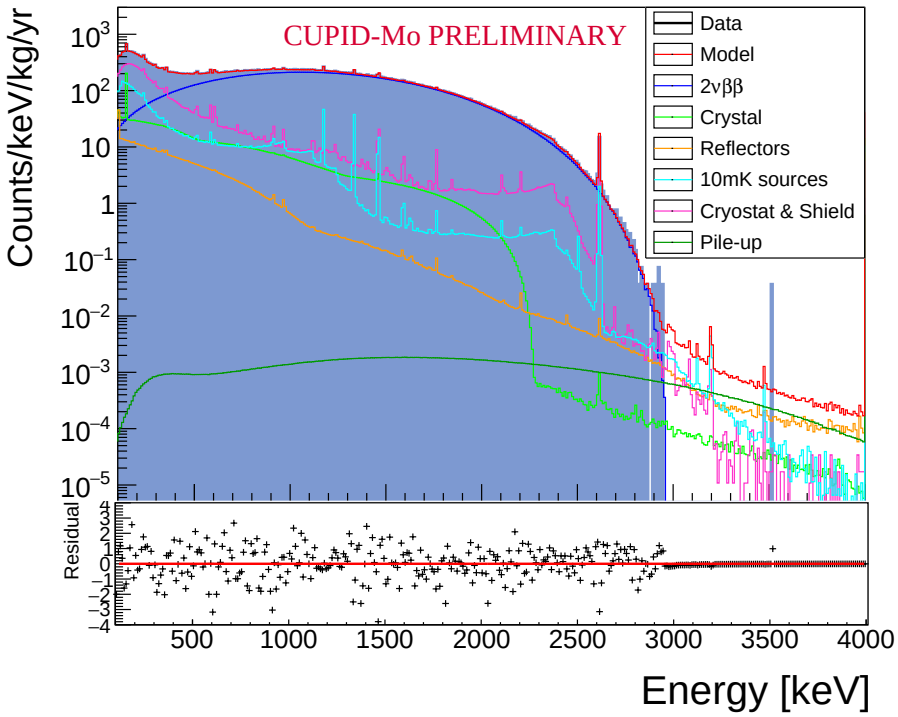

Figure 5.13: Cupid-Mo data and background contributions as obtained from the background model described in [135]

We obtain a background index in the region of interest of $2.7^{+0.7}_{-0.6}(\text{stat})^{+1.1}_{-0.5}(\text{syst})\times10^{-3}$cts/keV/kg/yr. We compare in Fig 5.14 this background, in units of counts per mol of isotope per year, with several experiments. For CUPID-Mo, we obtain $3.7^{+0.9}_{-0.8}$ (stat)$^{+1.5}_{-0.7}$ (syst) $\times$ 10^{-3} counts/ΔE_{FWHM}/mol_{iso}/yr, the lowest in a bolometric $0\nu\beta\beta$ decay experiment.

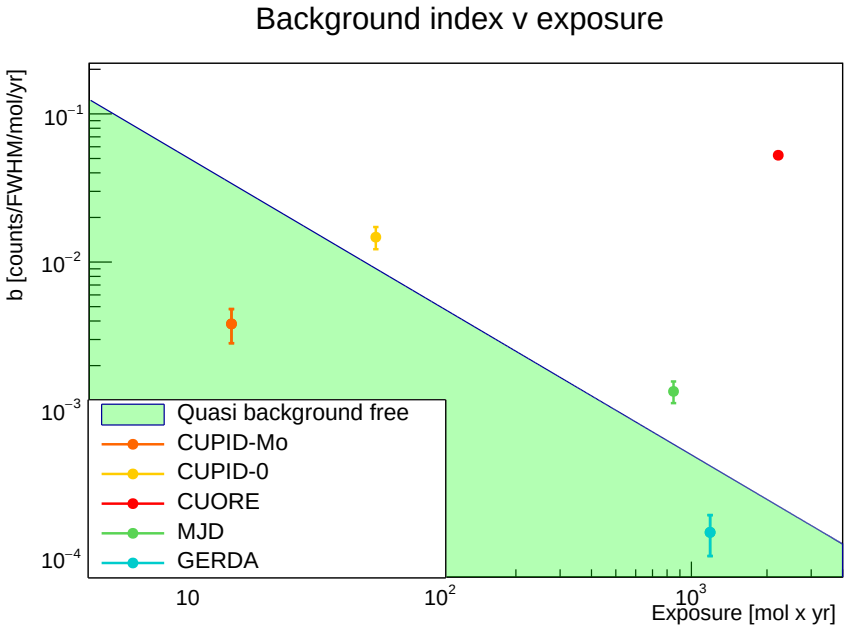

Figure 5.14: Backgrounds of some $0\nu\beta\beta$ experiments, in units of counts/FWHM/mol/yr as a function of exposure. The CUPID-Mo experiment reached the lowest background for a bolometric experiment.

The work was published in Eur. Phys. Journal C [135] and is included below. After the introduction, section 2 describes the CUPID-Mo set-up, including the cryostat and shieldings. Section 3 details the data analysis, which is somewhat different from the $0\nu\beta\beta$ analysis, because it aims at the accurate measurement of the background spectra. Section 4 lists the background sources included in the model and Section 5 describes the Monte Carlo simulations. Section 6 gives the method used for the construction of the background model and section 7 is dedicated to the results.

Article: C. Augier *et al* [**CUPID-Mo coll.**], **Eur. Phys. J. C. 83, 675 (2023)**

Eur. Phys. J. C (2023) 83:675
https://doi.org/10.1140/epjc/s10052-023-11830-2

THE EUROPEAN PHYSICAL JOURNAL C

Regular Article - Experimental Physics

The background model of the CUPID-Mo $0\nu\beta\beta$ experiment

C. Augier[1], A. S. Barabash[2], F. Bellini[3,4], G. Benato[5,6], M. Beretta[7], L. Bergé[8], J. Billard[1], Yu. A. Borovlev[9], L. Cardani[4], N. Casali[4], A. Cazes[1], E. Celi[5,6], M. Chapellier[8], D. Chiesa[10,11], I. Dafinei[4], F. A. Danevich[4,12], M. De Jesus[1], P. de Marcillac[8], T. Dixon[8], L. Dumoulin[8], K. Eitel[13], F. Ferri[15], B. K. Fujikawa[14], J. Gascon[1], L. Gironi[10,11], A. Giuliani[8], V. D. Grigorieva[9], M. Gros[15], D. L. Helis[5,6], H. Z. Huang[16], R. Huang[7], L. Imbert[8,a], J. Johnston[17], A. Juillard[1], H. Khalife[15], M. Kleifges[18], V. V. Kobychev[12], Yu. G. Kolomensky[7,14], S. I. Konovalov[2], J. Kotila[19,20,21], P. Loaiza[8], L. Ma[16], E. P. Makarov[9], R. Mariam[8], L. Marini[5,7], S. Marnieros[8], X.-F. Navick[15], C. Nones[15], E.B. Norman[22], E. Olivieri[8], J. L. Ouellet[17], L. Pagnanini[5,6], L. Pattavina[6,23], B. Paul[15], M. Pavan[10,11], H. Peng[24], G. Pessina[11], S. Pirro[6], D. V. Poda[8], O. G. Polischuk[4,12], S. Pozzi[11], E. Previtali[10,11], Th. Redon[8], A. Rojas[25], S. Rozov[26], V. Sanglard[1], J. A. Scarpaci[8], B. Schmidt[15], Y. Shen[16], V. N. Shlegel[9], V. Singh[7], C. Tomei[4], V. I. Tretyak[6,12], V. I. Umatov[2], L. Vagneron[1], M. Velázquez[27], B. Welliver[7], L. Winslow[17], M. Xue[24], E. Yakushev[26], M. Zarytskyy[12], A. S. Zolotarova[15]

[1] Université Lyon 1, CNRS/IN2P3, IP2I-Lyon, 69622 Villeurbanne, France
[2] National Research Centre Kurchatov Institute, Kurchatov Complex of Theoretical and Experimental Physics, 117218 Moscow, Russia
[3] Dipartimento di Fisica, Sapienza Università di Roma, P.le Aldo Moro 2, 00185 Rome, Italy
[4] INFN, Sezione di Roma Tor Vergata, Via della Ricerca Scientifica 1, 00133 Rome, Italy
[5] Gran Sasso Science Institute, 67100 L'Aquila, Italy
[6] INFN, Laboratori Nazionali del Gran Sasso, 67100 Assergi, AQ, Italy
[7] Department of Physics, University of California, Berkeley, CA 94720, USA
[8] Université Paris-Saclay, CNRS/IN2P3, IJCLab, 91405 Orsay, France
[9] Nikolaev Institute of Inorganic Chemistry, 630090 Novosibirsk, Russia
[10] Dipartimento di Fisica, Università di Milano-Bicocca, 20126 Milan, Italy
[11] INFN, Sezione di Milano-Bicocca, 20126 Milan, Italy
[12] Institute for Nuclear Research of NASU, Kyiv 03028, Ukraine
[13] Institute for Astroparticle Physics, Karlsruhe Institute of Technology, 76021 Karlsruhe, Germany
[14] Nuclear Science Division, Lawrence Berkeley National Laboratory, Berkeley, CA 94720, USA
[15] IRFU, CEA, Université Paris-Saclay, 91191 Gif-sur-Yvette, France
[16] Key Laboratory of Nuclear Physics and Ion-beam Application (MOE), Fudan University, Shanghai 200433, People's Republic of China
[17] Massachusetts Institute of Technology, Cambridge, MA 02139, USA
[18] Institute for Data Processing and Electronics, Karlsruhe Institute of Technology, 76021 Karlsruhe, Germany
[19] Department of Physics, University of Jyväskylä, PO Box 35, 40014 Jyvaskyla, Finland
[20] Finnish Institute for Educational Research, University of Jyväskylä, P.O. Box 35, 40014 Jyvaskyla, Finland
[21] Center for Theoretical Physics, Sloane Physics Laboratory, Yale University, New Haven, CT 06520-8120, USA
[22] Department of Nuclear Engineering, University of California, Berkeley, CA 94720, USA
[23] Physik Department, Technische Universität München, 85748 Garching, Germany
[24] Department of Modern Physics, University of Science and Technology of China, Hefei 230027, People's Republic of China
[25] LSM, Laboratoire Souterrain de Modane, 73500 Modane, France
[26] Laboratory of Nuclear Problems, JINR, 141980 Dubna, Moscow Region, Russia
[27] Université Grenoble Alpes, CNRS, Grenoble INP, SIMAP, 38402 Saint Martin d'Héres, France

Received: 2 May 2023 / Accepted: 10 July 2023 / Published online: 28 July 2023

Abstract CUPID-Mo, located in the Laboratoire Souterrain de Modane (France), was a demonstrator for the next generation $0\nu\beta\beta$ decay experiment, CUPID. It consisted of an array of 20 enriched $Li_2{}^{100}MoO_4$ bolometers and 20 Ge light detectors and has demonstrated that the technology of scintillating bolometers with particle identification capabilities is mature. Furthermore, CUPID-Mo can inform and validate the background prediction for CUPID. In this paper, we present a detailed model of the CUPID-Mo backgrounds. This model is able to describe well the features of the experimental data and enables studies of the $2\nu\beta\beta$ decay and other processes with high precision. We also mea-

[a] e-mail: leonard.imbert@ijclab.in2p3.fr (corresponding author)

sure the radio-purity of the $Li_2{}^{100}MoO_4$ crystals which are found to be sufficient for the CUPID goals. Finally, we also obtain a background index in the region of interest of $3.7\,^{+0.9}_{-0.8}\,(\text{stat})^{+1.5}_{-0.7}\,(\text{syst}) \times 10^{-3}$ counts/ΔE_{FWHM}/mol_{iso}/year, the lowest in a bolometric $0\nu\beta\beta$ decay experiment.

Contents

1 Introduction

Neutrinoless double beta decay ($0\nu\beta\beta$) is a hypothetical nuclear transition that would occur if the neutrino is its own antiparticle, or a Majorana particle. It consists in the transformation of an even-even nucleus into a lighter isobar containing two more protons accompanied by the emission of two electrons and no other particles, with a change of the total lepton number by two units. Thus, the $0\nu\beta\beta$ signal is a peak in the summed electron energy spectrum positioned at the $Q_{\beta\beta}$ (the energy difference between parent and daughter nuclei) of the transition. The detection of this "matter-creating" process would represent the observation of a new phenomenon beyond the Standard Model [1]. Current best limits for $0\nu\beta\beta$ half-life are of the order of 10^{24}–10^{26} year [2–8].

The Standard Model process, two-neutrino double beta decay, $2\nu\beta\beta$, includes also the emission of two $\bar{\nu}_e$ and conserves lepton number. Unlike $0\nu\beta\beta$ decay, $2\nu\beta\beta$ has a continuous energy spectrum and has been observed in more than ten nuclei with half-lives in the range of 10^{18}–10^{24} year [9].

One of the largest challenges in $0\nu\beta\beta$ decay experiments is the control of the radioactive background, that may produce events in the signal energy region. These could mimic the very rare $0\nu\beta\beta$ signal reducing the experimental sensitivity.

During the last 10 years the scintillating bolometer technology has proved that bolometers based on lithium molybdate (Li_2MoO_4), are very promising detectors for next generation $0\nu\beta\beta$ searches [10,11]. Scintillating bolometers were developed to reduce the background observed in the current leading $0\nu\beta\beta$ bolometric experiment, CUORE [12]. In CUORE, the background in the region of interest is dominated by surface α's emitted from the copper structure holding the detectors [13]. The array of 988 TeO_2 bolometers, installed at the Laboratori Nazionali del Gran Sasso, Italy, has observed a background in the ^{130}Te region of interest ($\mathcal{Q}_{\beta\beta}$ = 2527 keV) of $(1.49 \pm 0.04) \times 10^{-2}$ counts/keV/kg/year [4,14,15]. The next generation experiment CUPID (Cuore Upgrade with Particle IDentification) will drastically reduce the background thanks to the simultaneous readout of heat and light signals. The capability to discriminate β/γ from α particles with scintillating bolometers relies on the fact that the light emitted in the $Li_2{}^{100}MoO_4$ by α particles is about a factor 5 smaller compared to the light emitted by β/γ's of the same energy [10,16].

In addition to the particle discrimination, the CUPID strategy to reduce the background relies on the radiopurity of the scintillating crystals and the minimisation of the passive materials [17]. Another key point is that the $\mathcal{Q}_{\beta\beta}$ energy value of ^{100}Mo (3034 keV) is higher than 2615 keV, implying a signal located above the majority of γ lines from natural radioactivity.

The CUPID-Mo experiment [11], located in the Laboratoire Souterrain de Modane (LSM) in France, under an overburden of 4800 m water equivalent, was built as a demonstrator experiment for CUPID. It consisted of 20 $Li_2{}^{100}MoO_4$ (LMO) scintillating bolometers and 20 Ge light detectors (LDs) for a simultaneous read-out of heat and light. One of the aims of CUPID-Mo was to validate the background predictions for CUPID, in particular the LMO crystal radiopurity and residual α background. LMO radiopurity for the U and Th chains of less than 10 and 3 μBq/kg respectively are needed to meet the CUPID goals [17], this can be validated on a mid-scale with CUPID-Mo.

In this paper we present the background model which describes the background sources in the CUPID-Mo experiment. This model is based on fitting the CUPID-Mo data to detailed Monte Carlo simulations. We show that the residual α background contribution and the radiopurity of the LMO crystals are sufficient to meet the CUPID background goal.

CUPID-Mo was also an important experiment in its own right. In particular, it has set the world-leading limits on the half-life of $0\nu\beta\beta$ decay of ^{100}Mo to both ground and excited states [6,11,18]. The detailed study of the experimental backgrounds in the CUPID-Mo experiment enables a high precision measurement of the $2\nu\beta\beta$ decay rate and allows to disentangle between the Single State Dominance (SSD) or High State Dominance (HSD) mechanisms [19,20] of the $2\nu\beta\beta$ decay process in ^{100}Mo. It also provides the basis to study new physics processes outside the Standard Model, which could distort the spectral shape of the $2\nu\beta\beta$ spectrum, such as $0\nu\beta\beta$ decay with emission of Majoron(s), $2\nu\beta\beta$ decay with emission of Bosonic neutrinos, Lorentz invariance violation or sterile neutrinos [21–30].

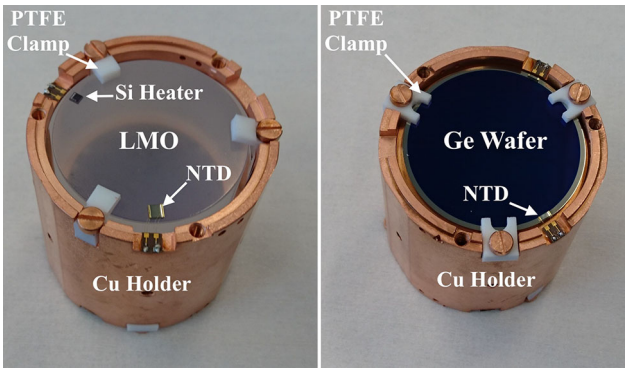

Fig. 1 Left: An individual CUPID-Mo bolometer showing the transparent $Li_2{}^{100}MoO_4$ crystal, the copper holder, the NTD-Ge thermometer and the Teflon clamps. Right: View of the opposite side of the detector, showing the black light detector, fabricated from Ge wafers [6]

2 The CUPID-Mo experiment

CUPID-Mo was installed in the EDELWEISS cryogenic set-up [31] at LSM. The experiment was in operation between March 2019 and June 2020.

CUPID-Mo used ^{100}Mo-enriched LMO crystals, where the ^{100}Mo, the double beta isotope, has been enriched at $\sim$ 97%. The basic detection modules are the crystals coupled to thermal sensors, consisting of a Neutron Transmutation Doped Ge thermistor, NTD. The top and bottom of the crystals are facing light detectors fabricated from Ge wafers, also instrumented with NTDs to readout the scintillation light signal. The crystals are housed in cylindrical copper holders and supported by PTFE pieces, as shown in Fig. 1. A reflective foil (3 M Vikuiti®) is installed around the crystals, inside the copper holder, to increase the light collection. The average weight of the CUPID-Mo crystals is 210 g and the total mass is 4.158 kg corresponding to 2.264 kg of ^{100}Mo.

The array of 20 bolometers is arranged in five towers with four modules each, as shown in Fig. 2. Each tower is suspended by stainless steel springs to mitigate the vibrational noise of the set-up. The signal from the CUPID-Mo detectors are readout with NOMEX® cables, copper and constantan wires on Kapton pads. Situated in the same cryostat, the EDELWEISS detectors, visible behind the five CUPID-Mo towers in Fig. 2, are equipped with Kapton® pads and MillMax® connectors. The detector chamber consists of four copper plates made of NOSV® grade copper[1] to support the bolometers, and is able to accommodate 12 detector towers.

The cryostat involves five thermal copper screens, typically referred to as the 10 mK, 1 K, 50 K, 100 K and 300 K stages respectively. The cryostat screens are made of NOSV and CUC2[2] grade copper. An internal polyethylene (PE) shield, to shield against neutrons produced in the set-up components by (α, n) reactions or induced by muons [32], is mounted between the detectors and the internal lead shield, and has a temperature of $\sim$ 1 K. An internal lead shield of 14 cm Roman lead [33] is installed inside the cryostat at 1 K, between the detector chamber and the dilution unit (see Fig. 3). Its main purpose is to shield the detectors from radioactive background of the warm electronics, the cold electronics and the connectors and cables at the 1 K stage.

The external shielding closest to the cryostat consists of 20 cm thick lead, with the innermost 2 cm made of Roman lead. The empty space between the lead shield and the outermost thermal screen of the cryostat is flushed with radon depleted air from a radon trapping facility. The average radon level in the air supplied by the facility is 20 mBq/m^3 [34]. Following the external lead shield, a 50 cm thick polyethylene shield is used to moderate the radiogenic neutron flux. A plastic scintillator based active muon veto system surrounds the whole experiment for muon tagging [35] (see Fig. 4).

2.1 Performances

CUPID-Mo has shown excellent detector performances in terms of energy resolution (7.4 $\pm$ 0.4) keV FWHM at 3034 keV [6] and α particle rejection > 99.9% [36], demonstrating that the CUPID requirements are within reach. Further details on the CUPID-Mo set-up and performances are given in [36].

3 Experimental data

The aim of our data processing is to convert the raw data stream into three calibrated energy spectra: β/γ like events with energy deposits in a single crystal ($\mathcal{M}_{1,\beta/\gamma}$), events with energy deposits in two crystals ($\mathcal{M}_2$) and of α-like events ($\mathcal{M}_{1,\alpha}$). These spectra will then be used in a simultaneous fit to extract radioactive contamination values and describe the observed spectra. The algorithms used for the data processing are described in detail in [6] but we will give a summary of the most important steps in the following. We also estimate the detector response parameters (energy resolution, energy bias, efficiencies, light yield) which are needed for post-processing the Monte Carlo spectral shapes.

3.1 Data taking

In this paper, we use the same dataset as in [6] with an exposure of 2.71 kg $\times$ year of LMO corresponding to

[1] Copper of 99.9975% purity, produced by Aurubis, Hamburg, Germany.

[2] Copper of > 99.990 % purity.

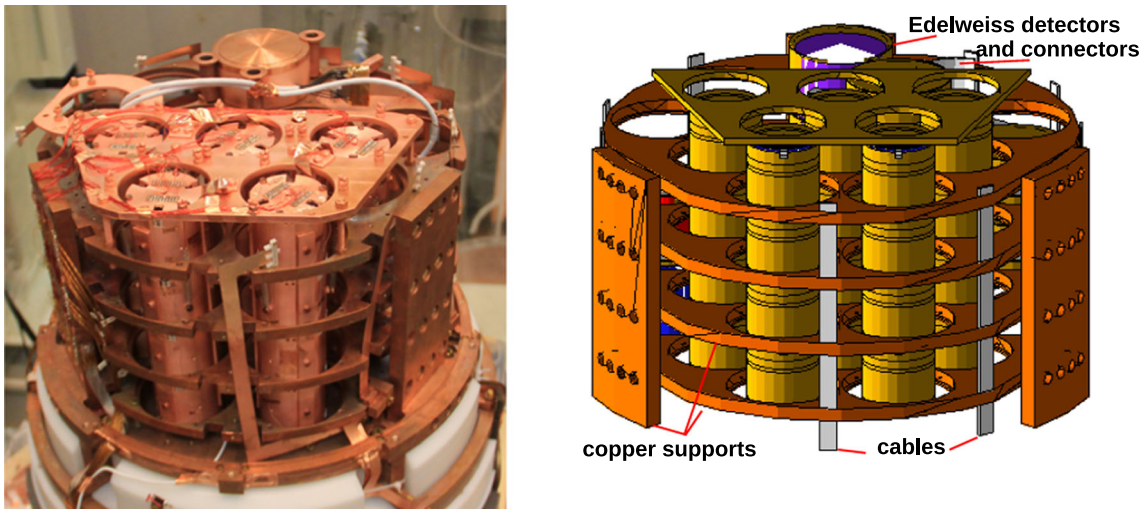

Fig. 2 Left: The CUPID-Mo experiment in the EDELWEISS cryostat. The five towers on the front contain the CUPID-Mo detectors and the EDELWEISS detectors can be seen behind. Right: GEANT4 rendering of the detector chamber in the Monte Carlo simulation geometry. Inside the five towers are placed the LMO crystals, the light detectors, the clamps and the reflective foils (not seen). The readout cables and the structure supporting the towers are indicated

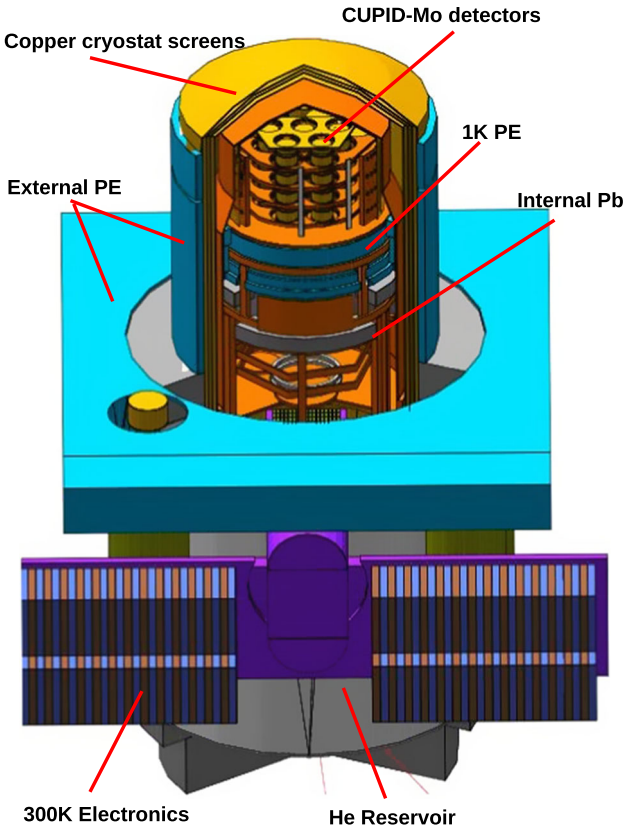

Fig. 3 GEANT4 rendering of the CUPID-Mo Monte Carlo simulation geometry, showing the cryogenic set-up

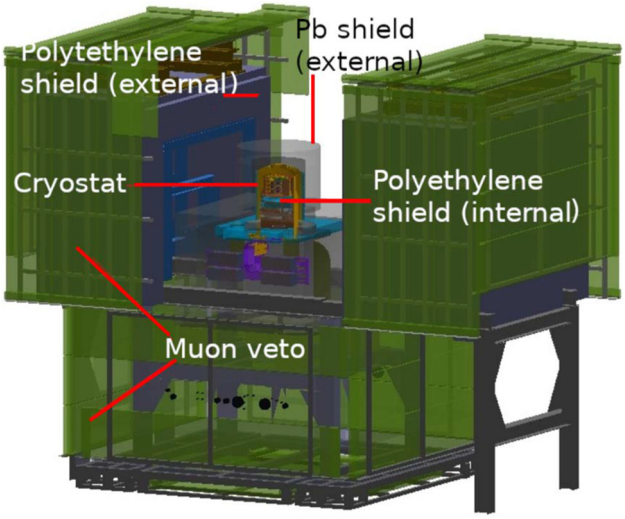

Fig. 4 Visualisation of the EDELWEISS cryostat and shielding as implemented in our MC simulations, we show the cryostat surrounded by the lead shield, the external polyethylene shielding and the muon veto panels. The muon panels are free to move to give a full geometric coverage

1.47 kg × year of ^{100}Mo. Our data is acquired as a continuous time-stream and digitized at 500 Hz by the EDELWEISS DAQ [36] and stored at both CC-IN2P3 (France) and NERSC (USA) for offline analysis. We acquire runs, periods of around 10–100 h of stable data taking, of both physics and calibration data, where a calibration source was placed in the vicinity of the experiment. We use regular calibrations with a ^{232}Th/^{238}U source to calibrate the LMO detectors and a high activity ^{60}Co source, which generates ^{100}Mo X-rays in the detectors, to calibrate the LDs. We divide the data into twelve periods of $\sim$ 1 month of stable data taking, called *datasets*.

We discard three short periods of data ($\approx$ 1 week each) due to the low statistics causing an inability to accurately calibrate this data.

3.2 Data processing

We process our data using the C++ softwares *Apollo* and *Diana* [37,38], first developed for the CUORE experiment and also used by CUORICINO, CUPID-0 and CUPID [39].

A complete description of the data processing can be found in [6]. We identify physics events using an optimal trigger, also used for previous CUPID-Mo analysis. This triggering is used for both the LDs and the LMO bolometers. We then store a 3 s waveform for both LDs and the LMO channels for each triggered events. For each LMO we associate (up to) two light detectors, called *side-channels*, which correspond to the LDs facing this LMO detector. These are numbered S1/S2 where S1 is the LD with the better detector performance (lower noise and higher detector light yield).

We estimate the amplitude of peaks using an optimal filter, which maximises the signal to noise ratio based on inputs of the known signal shape and spectral noise power density. This is done for all LMO events and also the corresponding LD events on the side-channels.

Next we correct for thermal gain changes and calibrate our data using dedicated ^{232}Th/^{238}U calibration measurements. This calibration is accurate to around $<$ 1 keV [6] which is sufficient for the binned background model fits. The LDs are calibrated using the dedicated ^{60}Co calibrations which produces $\sim$ 17 keV Mo X-rays.

3.3 Multiplicity

We define coincidences between physics events, where multiple detectors are triggered simultaneously. This provides useful information since events of $0\nu\beta\beta$ decay or $2\nu\beta\beta$ decay to the ground state are very likely ($>$ 75% probability [11]) to deposit energy in only one crystal. However, background events in particular from γ's are likely to deposit energy in multiple crystals simultaneously, for example due to Compton scattering in one crystal, or multiple γ's from the same decay. We estimate the multiplicity of an event as the number of pulses in different LMO detectors above our analysis energy threshold (set at 40 keV) within a $\pm$10 ms time window.

3.4 Data selection

Several cuts are used to remove non-physical events (for example noise spikes and cross-talk) or coincidences of two or more pulses generated by events very close in time within the same crystal, called pile-up events. We require that there is only one trigger in the 3 s LMO waveform. We then define a pulse shape discrimination (PSD) cut, described in detail in [6], using a principal component analysis method (PCA). We also define a cut on the pulse rise time and optimal filter based PSD variables[3] which help to cut pile-up like events. Details of the choice of the selection cuts is given in [6].

3.5 Particle identification

Since CUPID-Mo is a dual readout experiment we can discriminate α from β/γ particles. The use of light detectors also allows us to remove background events in which a particle deposits energy on our LDs. We select β/γ candidate events using the LD signal as following. We normalise the measured LD signals by defining the variable n, as the difference between the measured LD energy, E_{LD}, and the mean expected β/γ LD energy L, normalized by the light band width (σ). We compute n for $\mathcal{M}_1$ events. As each LD has different characteristics, the calculation is done for each channel (crystal) c, each dataset d and for both side channels s, i.e.:

$$n_{c,s,d} = \frac{E_{LD} - L_{c,d,s}(E)}{\sigma_{c,d,s}(E)}, \tag{1}$$

with E the measured LMO energy. The parameter $n_{c,s,d}$ has a distribution expected to be centered at zero for β/γ's and at a value different from zero for α particles. For details on the determination of the mean expected LD energies and its uncertainty, see [6].

For events with two LDs we expect the 2D distribution of $n_{c,1}$ against $n_{c,2}$ to be a bivariate Gaussian. As we observe no clear correlation we place a radial cut on the variable:

$$D = \sqrt{n_{c,1}^2 + n_{c,2}^2}. \tag{2}$$

If only one LD is available the cut is instead placed just on this $n_{c,s,d}$. We chose a cut of $D < 4$ to select β/γ events and call this data spectrum $\mathcal{M}_{1,\beta/\gamma}$. We also construct a spectrum of $\mathcal{M}_{1,\alpha}$ events comprised of high energy $\mathcal{M}_1$ events, $E >$ 3 MeV, with no light selection applied. This data comprises almost entirely α particles. The same events are obtained with a selection cut $D > 4$, thus, for simplification we have chosen only the energy cut to select α events.

Unlike most other analysis of scintillating bolometers we also develop a light selection cut for $\mathcal{M}_2$ events as described in detail in [18]. For a $\mathcal{M}_2$ event the scintillation light recorded can be the sum of that from the crystal above and below a given LD. We use the modeling described in [6] to compute the expected light detector energy for each physics event accounting for multiple contributions to the light yield. From this we can define the normalised LD energy for each

[3] The optimal filter test values or the χ^2 for rising and falling edges and for the pulse baseline.

pulse in a $\mathcal{M} > 1$ event. We require that each normalised LD energy (for each channel and side channel) is between -10 and 10 σ, for all but one LD. In this particular LD we observe an accidental contamination of ^{60}Co. Therefore we generally observe γ events in the LMO and β events in the LD with very large energy compared to scintillation light. For the two LMOs adjacent to this LD we make a cut of -10 to 3 σ, to take into account the energy directly deposited in the light detector. For more details see [18]. In addition, to further suppress events from this localized ^{60}Co source we make a *global LD anti-coincidence cut* to remove the γ background originating from this LD. We remove any events (on non-adjacent LMOs) with a trigger on this LD with energy > 2 keV within a 5 ms window.

3.6 Muon veto anti-coincidence

Despite the large rock overburden at LSM, which suppresses most muon events, they still form a possible background source. The EDELWEISS cryostat has a muon-veto system to remove these events, as shown in Fig. 4. We remove events, in each of the $\mathcal{M}_{1,\beta/\gamma}$, $\mathcal{M}_2$ and $\mathcal{M}_{1,\alpha}$ spectra, with a trigger in the veto system within a 5 ms window. With 98% geometric coverage and the operation voltage adjusted for the aging of the scintillator we expect an $\mathcal{O}(90\%)$ tagging efficiency of muons with a minimal impact on the β/γ acceptance [35]. Since this background was already subdominant and is strongly suppressed by the veto cut we do not include muons in our background model.

3.7 Delayed coincidences

Radioactivity from the ^{232}Th and ^{238}U decay chains in the LMO crystals could be a significant background in our data. Similar to other analyses of scintillating bolometers [5,40], we can exploit the time correlation of these decay chain events to reduce our experimental backgrounds. In particular, we veto events from the lower part of both chains where there are backgrounds from ^{214}Bi (^{238}U chain) and ^{208}Tl (^{232}Th chain). For ^{208}Tl we veto events in $10 \times T_{1/2}$ (1830 s) following a suspected ^{212}Bi α-decay. This time window contains $> 99.9\%$ of the ^{208}Tl decays.

The very low CUPID-Mo radioactivity also enables a novel delayed coincidence cut removing ^{214}Bi candidate events. The ^{222}Rn decay chain proceeds as follows:

$$^{222}\mathrm{Rn} \xrightarrow[\alpha\ 5590\ \mathrm{keV}]{3.8\ \mathrm{day}} {}^{218}\mathrm{Po} \xrightarrow[\alpha\ 6115\ \mathrm{keV}]{3.1\ \mathrm{min}} {}^{214}\mathrm{Pb} \xrightarrow[\beta^-\ 1018\ \mathrm{keV}]{27.1\ \mathrm{min}} {}^{214}\mathrm{Bi} \xrightarrow[\beta^-\ 3269\ \mathrm{keV}]{19.7\ \mathrm{min}} {}^{214}\mathrm{Po}. \quad (3)$$

We can therefore tag the event based on the ^{222}Rn or ^{218}Po α events and a fairly long dead time. We use energy cuts of 5985–6145 keV for ^{218}Po and 5460–5620 keV for ^{222}Rn to tag α candidates. For either type of α candidate events we then veto events within the same crystal within a time window containing 99% of events which is evaluated with MC sampling as 13860 s for ^{222}Rn and 13620 s for ^{218}Po. The two possible cuts on ^{222}Rn or ^{218}Po improve the rejection power for surface backgrounds. This cut has a small inefficiency (see Sect. 3.9), despite the long veto time.

3.8 Data spectra

Based on these cuts we construct the three data spectra used in our analysis:

- $\mathcal{M}_{1,\beta/\gamma}$: Events in one detector identified as β/γ,
- $\mathcal{M}_2$: Events in coincidence between 2 crystals, the two energies deposited in each crystal are summed,
- $\mathcal{M}_{1,\alpha}$: Events in one detector with alpha energy scale (> 3 MeV).

Because of the relatively fast half-life of $2\nu\beta\beta$ in ^{100}Mo ($\sim 7 \times 10^{18}$ year) and extremely low levels of contamination, relatively few peaks are observed in the $\mathcal{M}_{1,\beta/\gamma}$ spectrum, where the spectrum of $2\nu\beta\beta$ decays of ^{100}Mo is the dominant feature. The secondary datasets, $\mathcal{M}_2$ and $\mathcal{M}_{1,\alpha}$ however contain a lower fraction of $2\nu\beta\beta$ events and therefore provide useful information to determine the location of radioactive contaminations. The experimental spectra after all cuts are shown in Fig. 5.

3.9 Data selection efficiencies

We evaluate the efficiency of our cuts and correct the MC simulations by these values. In particular we use events in γ peaks from $\mathcal{M}_2$ and $\mathcal{M}_{1,\beta/\gamma}$ spectra to evaluate the efficiency of the PSD (Sect. 3.4), light yield and rise time cuts (Sect. 3.5). We do not observe that the cuts have any energy dependence in the range of the utilised γ peaks (236–2615 keV). For cuts where the inefficiency can be considered as a dead time, the multiplicity, muon veto, delayed coincidence and LD anti-coincidence, we evaluate the efficiency using the ^{210}Po peak. We evaluate the pile-up efficiency, the probability a pulse will be superimposed with another in a 3 s window, using random noise triggers. More details on each of these calculations can be found in [6], and the results are summarised in Table 1.

3.10 Energy scale and resolution

We use the observed γ peaks in both background and calibration data to predict the energy linearity and resolution. Each LMO detector in each dataset has a distinct energy resolution.

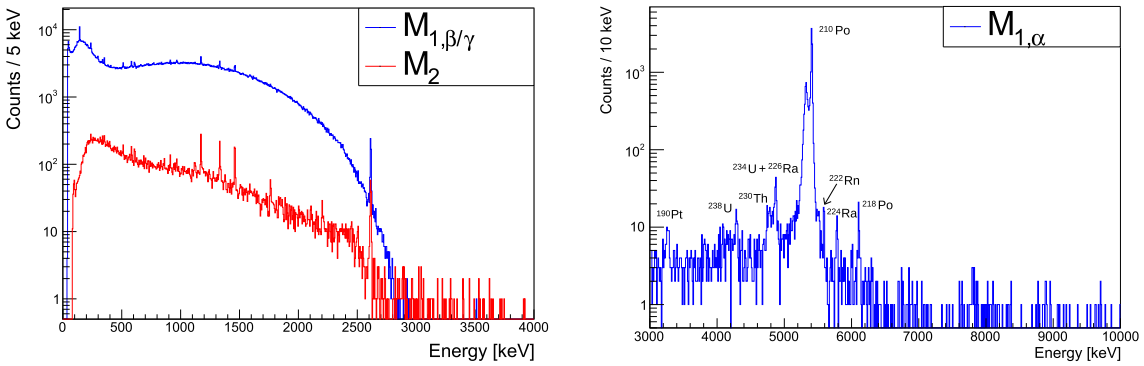

Fig. 5 CUPID-Mo experimental data. Left: $\mathcal{M}_{1,\beta/\gamma}$: events in one detector identified as γ/β. $\mathcal{M}_2$: events in coincidence between 2 crystals, the two energies deposited in the crystals are summed. Right: $\mathcal{M}_{1,\alpha}$: events in one detector with α energy scale

Table 1 Efficiencies for the cuts used on CUPID-Mo data. The PSD and Light Distance cut efficiencies are evaluated using γ peaks, and show no energy dependence in the range of the fit

Cut	Evaluation method	Efficiency [%]
PSD ($\mathcal{M}_{1,\beta/\gamma}$)	$\mathcal{M}_{1,\beta/\gamma}$ γ-peaks	95.2 ± 0.5
PSD ($\mathcal{M}_2$)	$\mathcal{M}_2$ γ-peaks	96.9 ± 0.5
Light distance ($\mathcal{M}_{1,\beta/\gamma}$)	$\mathcal{M}_{1,\beta/\gamma}$ γ-peaks	99.4 ± 0.4
Light distance ($\mathcal{M}_2$)	$\mathcal{M}_2$ γ-peaks	97.7 ± 1.8
Multiplicity	^{210}Po	99.55 ± 0.07
Rise time cut	$\mathcal{M}_{1,\beta/\gamma}$ γ-peaks	99.8 ± 0.2
LD anti-coincidence	^{210}Po	99.976 ± 0.017
Muon veto cut	^{210}Po	99.62 ± 0.07
Delayed coincidences	^{210}Po	99.16 ± 0.01
Pile-up	Noise	95.7 ± 1.0
Total $\mathcal{M}_{1,\beta/\gamma}$		88.9 ± 1.1
Total $\mathcal{M}_2$		83.3 ± 2.5
Total $\mathcal{M}_{1,\alpha}$		94.7 ± 1.0

As in [6,11] we perform a fit of the 2615 keV peak in calibration data to extract the resolution of each detector-dataset pair. We use these resolutions to build a function including a common scale factor $R(E)$ which will be determined for the peaks in background data. For our Monte Carlo simulations for each event we sample from a Gaussian with mean E and width $R \times \sigma_{c,d}$, where $\sigma_{c,d}$ is the energy resolution in channel c and dataset d. This energy calibration is discussed in detail in [6].

3.11 Features of data spectra

We observe in Fig. 5 that the spectrum of $2\nu\beta\beta$ decays of ^{100}Mo dominates the $\mathcal{M}_{1,\beta/\gamma}$ data, whereas the $\mathcal{M}_2$ spectrum has significant contributions from natural radioactivity, shown by prominent γ peaks. These consist predominantly of decays from the ^{238}U and ^{232}Th decay chains, however we also observe contributions from ^{40}K and cosmogenic activation products ^{60}Co and ^{57}Co. We also observe a short lived peak of ^{99}Mo, present for $\sim$ 1 dataset, from neutron activation after a calibration with an AmBe neutron source.

The spectrum $\mathcal{M}_{1,\alpha}$ is dominated by α decays from components very close to the detectors. As shown in Fig. 5, in our data we observe a large contribution of ^{210}Po, $E_\alpha = 5303$ keV, with both a large Q-value and α-energy peak and peaks from several other nuclides in the U/Th chains.

During α decay the energy released is shared between the α-particle and recoiling nucleus (NR), with energy $\mathcal{O}(100$ keV). In LMO crystals the range of α particles is about 10 μm and a few nm for nuclear recoils. Therefore we expect to observe a peak at the Q-value of the decay for a LMO bulk event. For surface activity the energy spectrum depends on the implantation depth. For shallow contribution $\mathcal{O}$(nm) in the crystal the α or recoil could escape, or both could be contained in the crystal. We therefore expect peaks at the NR energy, at the α energy, and at the Q-value, with a relatively low flat continuum from partial contained α's or NR. The ratio of these peaks depends on the depth of radioactive contamination. For a deeper contribution $\mathcal{O}(\mu$m) the NR is almost always contained but the α's can still escape after depositing some of its energy, giving rise to a continuum extending from low energies up to the Q-value.

Similarly, for materials facing the crystals we expect a dependence on the implantation depth: at shallow depths the spectrum will be characterised by peaks at the α-energy and NR energy, for a deep contribution this will become a flat spectrum from low energy up to the alpha energy. We note from Fig. 5 that we generally do not observe clear α-energy peaks in our data. However due to the limited statistics the data is still compatible with a full surface contamination. The lack of clear α-energy peaks creates a challenge for assessing the surface contamination.

4 Background sources

The background in our experiment is expected mainly from the natural radioactivity in the whole experimental setup, including the detectors. Other contributions from muons, neutrons and environmental gammas are expected to be subdominant, as explained in Sect. 4.1. To minimize the background, all the materials used to build the experiment have been carefully selected in terms of radiopurity. To this end, the daughters of ^{238}U and ^{232}Th decay chains, ^{40}K, and cosmogenic radionuclides have been measured by High Purity Ge γ-ray spectroscopy and ICPMS (Inductively Coupled Plasma Mass Spectrometry). The CUPID-Mo materials were chosen to minimize the ^{226}Ra and ^{228}Th contaminations, as the most critical radioactive backgrounds in the 3 MeV region relevant to $0\nu\beta\beta$ decay searches arise from ^{214}Bi and ^{208}Tl decays. Table 2 reports the radioactivity in the CUPID-Mo detector components resulting from CUPID-Mo and CUORE measurement campaigns [15]. The materials which are directly facing the crystals (all but the springs from Table 2) are referred to as *close components* in the following. The material choice in the EDELWEISS cryostat was done to minimize the contaminants at lower energies, $\mathcal{O}$(100 keV), which is the region of interest in dark matter searches. Table 3 shows the radioactivity in the EDELWEISS cryostat materials.[4] The NOSV copper is used for the CUPID-Mo detector holders, all the copper parts in the detector chamber and the cryostat screens (with the exception of the 1 K screen).

We identify the most significant contributions to our experimental background using the screening measurements and the analysis of experimental data from Sect. 3.11.

We can broadly categorise our background sources into four groups:

- *Close source*: Radioactivity in the LMO crystal, reflective foils, LDs, PTFE clamps and NTDs, directly facing the crystals;
- *10 mK source*: Sources of activity in the 10 mK stage of the cryostat but not directly facing the LMO crystals (springs, cables, connectors, copper plates for bolometer support), as shown in Fig. 2;
- *Infrastructure source*: The copper cryostat screens and the internal shieldings, see Fig. 3;
- *External*: Activity originating from outside the 300 K Cu shield.

[4] In Table 3, the Kapton connectors, MillMax connectors and Cu Kapton cables belong to the EDELWEISS readout system, while the NOMEX cables are used for the CUPID-Mo readout.

4.1 Other contributions – muons, neutrons and environmental gammas

The muon flux at the LSM is 5 muons/m^2/day [35]. Muons would generally deposit energy in multiple detectors and be strongly suppressed by anti-coincidence with the muon veto detector (see Sect. 3.6), therefore we do not include them in the background model.

Neutrons may induce background in the $0\nu\beta\beta$ region of interest (ROI) if they are captured in the materials of the setup, producing high energy gammas. The thermal neutron flux in LSM has been measured as $(3.6\pm0.05\ (\text{stat.})\pm0.27\ (\text{syst.}))\times 10^{-6}$ neutrons/s/cm^2 [43] and the ambient neutron flux (fast plus thermal) has been estimated $\sim 10^{-5}$ neutrons/s/cm^2 in [43,44]. Previous work [45] showed that 48 cm of polyethylene reduces the neutron flux by a factor 2×10^6. Taking into account the surface of the CUPID-Mo detectors, we get that the neutron flux expected is less than 1 neutron/year. Thus, ambient neutrons are not taken into account among our background sources.

The gamma flux at LSM has been measured with a portable Ge detector at several locations in the laboratory. At the place where the EDELWEISS set-up is installed, the flux of 2.6 MeV photons was measured as $5.1\pm0.2\ (\text{stat.})\times10^{-2}$ γ/s/cm^2 [46]. Considering that 20 cm of lead reduce the flux by about a factor 10^4, then the contribution of environmental gammas may not be negligible. We expect about 6 photons of 2.6 MeV on the detectors surface during the course of all data taking. We take them into account by generating decays at the level of the outermost cryogenic thermal shield, as the spectral shapes measured in the detector from a source generated outside the external lead and outside the outermost cryogenic thermal differ slightly only below 500 keV.

5 Monte Carlo simulations

The Monte Carlo simulation is developed in GEANT4 and implemented with version 10.04 [47]. The MC simulation program developed by the EDELWEISS collaboration [32], has been adapted to include the CUPID-Mo detectors and to include the features described below.

We generated $2\nu\beta\beta$ decay events, with energies sampled from the theoretical two-dimensional single electron energy spectrum from [48,49]. We consider separately both the HSD and SSD mechanisms.

The radioactive decays in the components of the experiment are generated using both Decay0 [50] and GEANT4. For decay chains in close sources we use the GEANT4 class G4RadioactiveDecay. This allows to generate sub-chains, for example ^{226}Ra to ^{210}Pb. We store the final position of the nuclear recoil, and use it as the initial condition for the next decay, along with the time difference. This allows for

Table 2 Radioactivity values of the components of the CUPID-Mo detectors. All measurements have been made by ICPMS, with the exception of the Springs, measured by γ-ray spectroscopy and the surface contamination of the Vikuiti™ reflective foil, measured with the BiPo-3 detector [41]

Element	Total mass [g]	Activity [mBq/kg]		
		^{238}U	^{232}Th	Others
Ge-LD [42]	27.4	$< 1.9 \times 10^{-2}$	$< 6 \times 10^{-3}$	
NTD [15]	2	< 12	< 4.1	
PTFE clamps [15]	216	$< 2.2 \times 10^{-2}$	$< 6.1 \times 10^{-3}$	
Reflectors (Vikuiti™)	10.08	$(1.7 \pm 0.5) \times 10^{-1}$	$(4.9 \pm 1.2) \times 10^{-2}$	^{214}Bi: (1.0 ± 0.4) nBq/cm^2
Springs	8.1	^{226}Ra: 11 ± 3	^{228}Th: 21 ± 5	^{228}Ra: 26 ± 9; ^{40}K: $(3.6 \pm 0.4) \times 10^3$

Table 3 Radioactivity of the components in the EDELWEISS setup. All measurements have been made by HPGe γ-spectroscopy. The MillMax connectors have also been measured by ICPMS

Element	Mass [g]	Activity [mBq/kg]		
		^{226}Ra	^{228}Th	Others
Kapton connectors	33.12	14 ± 7	67 ± 31	
Cu Kapton cables	510	8 ± 6	15 ± 10	
NOMEX cables	4	21	19	
MillMax connectors	0.5	$(1.0 \pm 0.6) \times 10^2$	$(1.0 \pm 0.2) \times 10^3$	^{238}U: $(1.2 \pm 0.2) \times 10^4$
Brass screws	2000	–	3.5 ± 0.9	^{210}Pb: $(6 \pm 3) \times 10^2$; ^{137}Cs: 2.6 ± 1.5
Cu NOSV[a]	2.89×10^5	< 0.040	$(2.4 \pm 1.2) \times 10^{-2}$	
Cu CUC2[a]	6.5×10^5	$(2.5 \pm 1.5) \times 10^{-2}$	$(3.3 \pm 1.6) \times 10^{-2}$	
PE internal	1.51×10^5	0.65 ± 0.08	0.30 ± 0.07	
Conn. 1K to 100K	430	$(2.6 \pm 0.4) \times 10^3$	450 ± 44	

[a] M. Laubenstein, private communication

the accurate consideration of pile-up from events out of the same decay chain and of the delayed coincidence cuts (see Sect. 3.7). From the simulations we then store the energy deposited in both the LMO and LDs. For the ^{232}Th decay chain, we generate separately ^{232}Th, ^{228}Ra to ^{228}Th and ^{228}Th to ^{208}Pb, since ^{228}Ra and ^{228}Th have long half-life and so secular equilibrium cannot be assumed. Similarly for the ^{238}U chain we generate separately ^{238}U to ^{234}U, ^{234}U, ^{230}Th, ^{226}Ra to ^{210}Pb and ^{210}Pb to ^{206}Pb.

We use Decay0 for most external sources, not directly facing the crystals, where pile-up events in the same crystal from subsequent decays in a chain are unlikely, and delayed coincidence cuts through the tagging of α events is impossible. For the ^{238}U decay chain we generate the β emitters ^{214}Pb and ^{214}Bi. Since they are in secular equilibrium, we combine their spectra to reduce the number of components in the background model fit. We also generate in some components ^{210}Bi which is not assumed to be in equilibrium. For the ^{232}Th decay chain we generate ^{212}Pb, ^{212}Bi and ^{208}Tl out of the ^{228}Th sub-chain and combine them into one spectrum. We also generate ^{228}Ac which is not assumed to be in equilibrium.

In addition to the ^{238}U and ^{232}Th chains, we simulate ^{40}K contamination in the springs and the outermost cryogenic thermal shield. We have also considered ^{60}Co from cosmogenic activation in copper as well as ^{87}Rb and ^{90}Sr+^{90}Y in the crystals. A ^{99}Mo contribution due to neutron activation in the first days of data taking is also simulated in the crystals.

The decays are generated in the bulk of the components and also the surface for close sources, where surface contaminants can produce a distinct energy spectrum compared to bulk contamination. Surface contaminations are modelled with an exponential density profile $e^{-x/\lambda}$, where λ is a variable depth parameter.

The particles are propagated through the experimental geometry using the Livermore low energy physics models [51]. We use production cut lengths[5] of 1 μm for e^-/e^+ and 10 μm for γ's. For LMO these correspond to 1 keV energy thresholds for both e^-/e^+ and γ's. This choice is based on a study of the impact of the production thresholds on the detected spectra. Thresholds of 1 keV and 250 eV for LMO

[5] Production cuts apply to the production of secondaries. Below the cut, the primary is tracked down to zero energy using a continuous energy loss.

give comparable spectra, while the computing time is significantly reduced for a 1 keV cut length.

5.1 Geometry

We implement a detailed geometry of the CUPID-Mo towers in the MC simulations. In particular, we reproduce the size of each LMO crystal [36] on an individual basis to take into account variations between the crystals. We also include the Ge LDs, the PTFE clamps, the reflective foils surrounding the crystals and the copper holders which are implemented as accurately as possible. Figure 2 shows the GEANT4 rendering of the simulation geometry of the 10 mK chamber, with the five towers of CUPID-Mo in the front. We included the readout cables, the springs, the EDELWEISS Ge detectors and their connectors. The copper structure supporting the crystals, composed of four copper plates and three copper columns made of NOSV copper, is also included in the simulated geometry. The four copper plates are held by brass screws with a relatively high mass (see Table 3) which have been modeled as well.

Figure 3 shows the simulated geometry of cryostat and electronics. The 10 mK, 1 K, 50 K, 100 K and 300 K thermal screens are included individually. The internal polyethylene shielding and lead shielding are also implemented in the geometry. We also note that the geometry extends and includes far components below the 1 K lead shield that are less radiopure, like the dilution unit, the 300 K electronics, the pumps and the He reservoir that is expected to be important for neutron simulations.

5.2 Detector response model

To compare the simulated spectra to the measured data we need to account for the finite energy resolution and response of the detectors. The following features are accounted for through a post processing of the MC simulation spectra:

- Energy resolution;
- Energy threshold of 40 keV;
- Event multiplicity;
- Scintillation light and LD resolution;
- Cut efficiencies;
- Inactive periods of detectors;
- Pile-up and delayed coincidences in decay chains.

We compute the energy resolution per detector-dataset pair as explained in Sect. 3.10. In particular, for a pulse with energy E_{MC} in channel c and dataset d we sample from a Gaussian with mean E_{MC} and standard deviation $R \times \sigma_{c,d}$. As is done in experimental data we discard pulses below the energy threshold, < 40 keV, and compute the multiplicity as the number of detectors with $E > 40$ keV for each simulated event.

We also reproduce the signals measured in the light detectors. We have parameterised the scintillation light energy measured by the LD in data as a function of LMO energy as a second order polynomial, for each LMO and side LD channel. We also parameterise the LD energy resolution as a Gaussian with standard deviation $\sqrt{p_0^2 + p_1 E}$. We use this parameterisation to generate a random scintillation light yield for each event which is summed with the energy deposited in MC from direct particle interactions. We use these light detector energies to reproduce the light yield cuts in the same way as in experimental data in Sect. 3.

To account for inactive detectors we assign a random timestamp from the data taking period to each simulated MC event. This allows us to apply the same cuts to the simulated data and remove events from detectors considered inactive and to account for the reduction of event multiplicity in these periods.

5.3 Simulated background sources

Some components produce indistinguishable spectra of energy deposits in the crystal, or in other words, they exhibit degenerate spectral shapes. In this case, we either group them, or generate the radioactive decays in only one, which accounts for all elements with degenerate spectra. This simplification reduces the number of free parameters in the fit of the simulations to the data, however, we need to keep in mind that the posterior distributions account for the sum of the grouped elements.

The reflective foils, the PTFE clamps, and all other passive elements directly facing the crystals produce degenerate spectra. For this reason we have generated radioactive decays only in the *Reflectors*. We simulated radioactive decays separately in the connectors, the cables and the springs in the detector chamber at 10 mK shown in Fig. 2, right. All the copper elements made of NOSV at the 10 mK stage (holders, four plates, three columns and 10 mK cryostat screen) have been grouped in one background source, which we refer to as *Copper supports*.

We have found that all thermal screens exhibit degenerate spectra, thus we group the screens made of NOSV copper and refer to as *Cryostat screens*. We have also found that the *internal polyethylene shielding* spectrum is degenerate with the one from internal lead shielding. Thus, we have chosen to include only the internal polyethylene shielding contribution in the fit. This element takes into account all contributions from background sources below the internal lead shielding, as the elements of the dilution unit or the 300 K electronics also shown in Fig. 3.

In addition we have considered as a source the outer cryostat screen, called *screen 300 K*. This volume also includes the contribution from radon present in the air between the 300 K screen and the external lead shielding.

6 Background model

The goal of the background model is to describe the data (Sect. 3) with the MC simulations (Sect. 5). The parameters of the model then tell us the radioactive contamination of various components of the experiment. We use a binned simultaneous maximum likelihood fit, performed in a Bayesian framework with a Markov Chain Monte Carlo (MCMC) approach [52], developed by CUORE and further optimized by CUPID-0 collaborations [15,42] using the JAGS software [53,54]. We model the data in spectra i ($\mathcal{M}_{1,\beta/\gamma}$, $\mathcal{M}_2$ and $\mathcal{M}_{1,\alpha}$) and energy bin b as:

$$f_i(E_b;\vec{N}) = \sum_{j=1}^{N_s} N_j \times f_{j,i}(E_b). \tag{4}$$

The sum j runs over the simulated MC sources, N_j is a scaling factor for each source (shared by all three spectra) and $f_{j,i}(E_b)$ are the simulated MC spectral shapes, with E_b the energy of bin b. The likelihood function for data $\mathcal{D}$, including the 3 spectra $\mathcal{M}_{1,\beta/\gamma}$, $\mathcal{M}_2$ and $\mathcal{M}_{1,\alpha}$ is then given by the product of Poisson distributions, $\text{Poiss}(n_{i,b};\, f(E_i(E_b;\vec{N})))$, for $n_{i,b}$ observed counts in bin b of spectrum i, and prediction $f_i(E_b;\vec{N})$ for the set of parameters $\vec{N}$:

$$\begin{aligned}\ln\mathcal{L}\big(\mathcal{D}|f(E_b;\vec{N})\big) &= \sum_{i=1}^{3}\sum_{b=1}^{N_b(i)} \ln\left(\text{Poiss}(n_{i,b};\, f_i(E_b;\vec{N}))\right)\\ &= \sum_{i=1}^{3}\sum_{b}^{N_b(i)} n_{i,b} \times \ln\left(f_i(E_b;\vec{N})\right) - f_i(E_b;\vec{N}) - \ln(n_{i,b}!).\end{aligned} \tag{5}$$

Here the sum i is over the three data spectra and b goes over the bins in each spectrum.

JAGS samples the full posterior probability distribution $p(\vec{N}|\mathcal{D})$ given by Bayes theorem:

$$p(\vec{N}|\mathcal{D}) = \frac{\mathcal{L}(\mathcal{D}|\vec{N}) \times \pi(\vec{N})}{p(\mathcal{D})}, \tag{6}$$

using MCMC. The prior probabilities, $\pi(\vec{N})$ are discussed in Sect. 6.3. For each parameter we also extract the marginalised posterior distribution by integrating over the parameter space Ω (excluding the parameter of interest):

$$p(N_j|\mathcal{D}) = \int_{\Omega} p(\vec{N}|\mathcal{D}) d\vec{\Omega}. \tag{7}$$

We choose the mode of the marginalised distribution as our point estimate of the parameter and we compute, by integrating, the smallest 68% Bayesian credible intervals, c.i., around the mode. If the lowest 68% includes the value zero, we give an upper limit at 90% c.i.

6.1 MC simulation of ^{56}Co calibration source

We have performed a calibration with a ^{56}Co source to validate the energy calibration and resolution of the CUPID-Mo detectors in the $0\nu\beta\beta$ ROI, at $\sim$ 3 MeV. The measurement is also useful to test and validate the implementation of the Monte Carlo simulations. Two ^{56}Co sources with an activity of 41 ± 8 Bq, measured with HPGe γ spectroscopy immediately after the calibration, were placed on the outer cryostat screen, inside the external shielding. The configuration was chosen to achieve the highest counting rate in the ROI for all detectors with a total rate below 0.125 Hz as an upper limit on the tolerable pile-up.

We have performed a fit of the calibration data to a MC simulation of the ^{56}Co sources summed with a background component (detailed later in this section) and pile-up, with only uniform priors. We describe in Sect. 6.3.1 how the spectral shape of the pile-up events is obtained. The fit has thus three parameters: the normalization factor of the background, the one of the ^{56}Co sources, and the one of the pile-up events. We know the normalization of the background from the background model fit. Comparing it to the normalization factor of the background in the calibration data, we obtain the efficiency of the cuts in the calibration data $(68.7 \pm 1.4)\%$. From the normalization factor of the ^{56}Co sources we obtain the activity of the sources without the efficiency correction. Using the estimated efficiency, we derive the final activity of the ^{56}Co source of (50 ± 1) Bq, which is in good agreement with the measured activities.

The model shows good agreement with the data in the whole energy range of the fit 200–4000 keV, as shown in Fig. 6. In Fig. 7 we present the region above 2800 keV with 2 keV binning, where the comparison in this region can be better appreciated. This fit shows that the MC implementation of the set-up is accurate and that the MC is able to describe well the data.

6.2 Background sources list

The background model fit includes 41 background sources associated to the bulk volume of the components identified in Sect. 5.3. We included 2 additional sources of surface

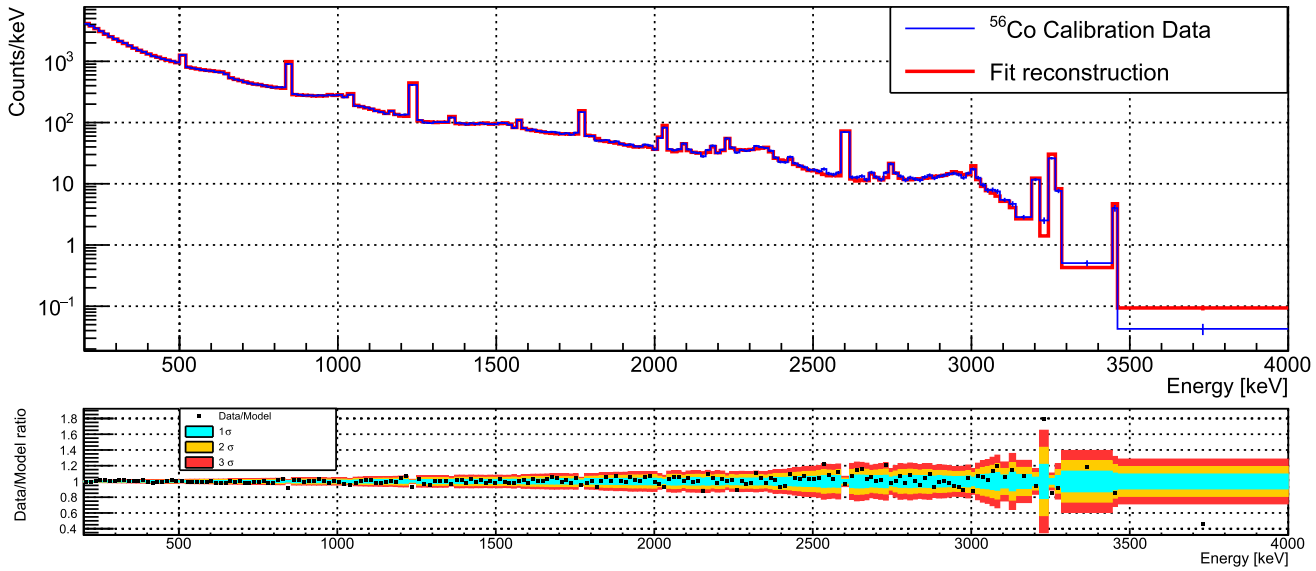

Fig. 6 Top: Comparison between the ^{56}Co calibration data and MC simulations, $\mathcal{M}_1$ data, with a variable binning in the region between 200–4000 keV. Bottom: Bin by bin ratio of data and MC. Most of the values are within 3 σ, with discrepancies below 20%

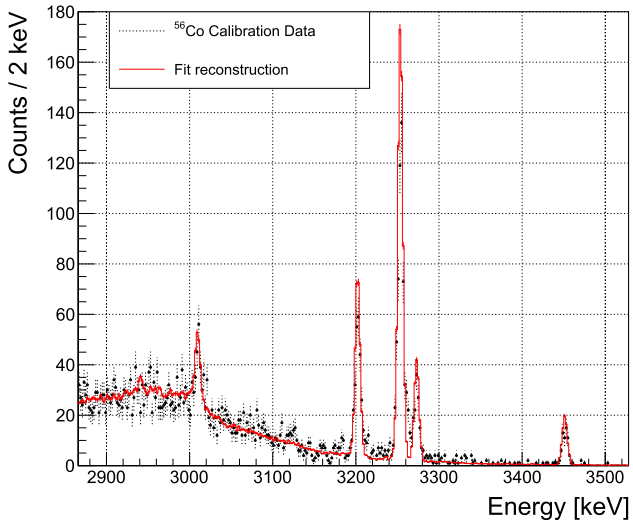

Fig. 7 Comparison between the ^{56}Co calibration data and MC simulations, $\mathcal{M}_1$ data in the region of interest

contamination: the LMO crystal and the Reflective foil (representing all sources facing the crystals). For a detailed list of the sources associated to radioactive contaminants we refer to Tables 4 and 5. The complete list of the background sources in our fit is:

- Crystal:
  - $2\nu\beta\beta$ decay of ^{100}Mo to ^{100}Ru ground state,
  - $2\nu\beta\beta$ decay of ^{100}Mo to ^{100}Ru 0_1^+ excited state,
  - pile-up (random coincidence of 2 events in the same crystal happening so close in time that the signal is equivalent to that of the sum of the two events),
  - ^{99}Mo,
  - 12 bulk sources of natural radioactivity detailed in Table 4,
  - 8 sources associated to surface contamination, listed in Table 4,
  - ^{210}Pb surface contamination with 1 nm and 1 μm implantation depth.
- Reflectors:
  - 3 sources associated to bulk contaminations, Table 5,
  - 8 sources associated to surface contaminations, Table 5,
  - ^{210}Pb surface contamination with 100 nm and 1 µm implantation depth.
- Close sources, 10 mK and infrastructure: 27 sources associated to the bulk volume of these components, listed in Table 5,
- Random coincidence of 2 events in two different crystals called accidentals.

A total of 67 sources are included in the fit. As mentioned in Sect. 5 we have modelled surface contaminations with an exponential density profile $e^{-x/\lambda}$. We have simulated surface contaminations with $\lambda = 10$ nm and 10 µm for all radionuclides in the U and Th chains. The choice 10 nm is driven by the fact the typical range of recoiling nuclei is of the order of some nm for α decays in the U and Th chains. The choice of 10 µm considers that mechanical crystal preparation including cutting, cleaning and polishing can lead to deep surface damage and implantation depths of $\sim$ µm, however depths $>$ 10 µm would be effectively equivalent to bulk contaminations. We observed that the component corre-

Table 4 Radioactive contaminations of the LMO crystals derived from the background model of the CUPID-Mo data, with 2.71 kg × year exposure. The upper table shows the bulk activities. We report also the results under the assumption of no surface contaminations, to study the effect in the fit of the anticorrelation between bulk and surface activities. The lower table shows the surface activities, we give the activities with MC simulation with 10 nm implantation depth (see text). The effect of including a contribution with a depth parameter of 10 μm is shown on the last column

Chain	Nuclide	Bulk activity [μBq/kg]	w/o surface cont. [μBq/kg]
^{232}Th	^{232}Th	< 0.22	$0.18^{+0.09}_{-0.05}$
	^{228}Ra to ^{228}Th	< 79	< 98
	^{228}Th to ^{208}Pb	$0.43^{+0.16}_{-0.15}$	0.57 ± 0.07
^{238}U	^{238}U to ^{234}U	$0.41^{+0.16}_{-0.28}$	$0.59^{+0.12}_{-0.11}$
	^{234}U	$1.15^{+0.33}_{-0.70}$	1.59 ± 0.20
	^{230}Th	< 0.58	$0.47^{+0.23}_{-0.24}$
	^{226}Ra to ^{210}Pb	< 0.21	0.39 ± 0.06
	^{210}Pb	96^{+6}_{-27}	105 ± 1
	^{190}Pt	$0.39^{+0.11}_{-0.10}$	
	^{87}Rb	< 103	
	^{90}Sr-^{90}Y	159^{+38}_{-34}	
	^{40}K	41^{+29}_{-22}	

		Surface activity [nBq/cm^2]	
		10 nm	10 nm + 10 μm
	^{232}Th	< 1.3	< 1.1
	^{228}Ra to ^{228}Th	< 389	< 449
	^{228}Th to ^{208}Pb	< 2.5	$0.9^{+0.9}_{-0.6}$
	^{238}U to ^{234}U	< 2.9	< 2.4
	^{234}U	< 7.3	< 5.9
	^{230}Th	< 2.2	< 2.3
	^{226}Ra to ^{210}Pb	2.0 ± 0.5	< 2.1
	^{210}Pb to ^{206}Pb[a]	62^{+109}_{-31}	

[a]Includes 1 μm and 1 nm implantation depth (see text for details)

sponding to the shallow surface contamination of the crystal, with $\lambda = 10$ nm, is needed to properly fit our data. Surface contaminations with $\lambda = 10$ μm give activities which are compatible with zero. Thus, for simplification to minimize the number of degrees of freedom, we choose to include in the fit only the crystal surface contaminations with $\lambda = 10$ nm implantation depth. Due to the small thickness (70 μm) and low density of the Reflectors, surface contaminations with $\lambda = 10$ μm are degenerate with bulk contaminations. Both produce continuous spectra due to the partial energy loss of α particles in the Reflector and the detection of the remaining kinetic energy in the crystal. We have therefore chosen to include only the surface contaminations with $\lambda = 10$ nm for the Reflectors in the background model fit.

To simulate surface and bulk contaminations in the crystal and the Reflectors, we have generated the decay chains to take into account time correlations and exploit the delay coincidences (see Sect. 5), as done for the data. We observed that the bulk contamination in the Reflectors produce a flat spectra independent of the specific part of the radioactive decay chain and our fits showed the activities of the various subchains (excluding ^{210}Pb to ^{206}Pb) were compatible. We hence simplify the fit model by assuming that the entirety of the U/Th (excluding ^{210}Pb to ^{206}Pb) chain is in secular equilibrium for the Reflectors.

In addition to the U/Th chains, other contaminations have been included in the crystals. In particular, ^{40}K can be found as a result of an initial contamination of the powder used to grow the crystals [31]. Some anthropogenic radionuclides due to fall out can also be found in enriched crystals [55], thus, we have included the bulk contaminations ^{87}Rb and ^{90}Sr+^{90}Y, which are pure β-emitters. ^{99}Mo was produced by activation during a neutron calibration with an AmBe source.

For all sources that aren't facing the crystals we have simulated decays of the daughters of ^{226}Ra and ^{228}Th. We identify in Table 3 a large content of ^{210}Pb in the brass screws holding the detector plates. We have simulated ^{210}Bi in this component and use it to account for this contamination in all 10 mK and infrastructure sources. Cobalt isotopes are expected to be primarily the result of cosmogenic activation in copper. We have therefore chosen to locate ^{60}Co and ^{57}Co in the *Copper supports* and use it to account for this contamination in all 10 mK and infrastructure sources. In all the components we use ^{228}Ac γ emitter with three main γ peaks clearly visible

in the data, not in equilibrium with ^{228}Th. In doing so, we have observed that for the 300 K screen the two values from the fit are compatible with equilibrium thus, to reduce the number of components in the fit we have combined ^{228}Ac and ^{228}Th.

6.3 Choice of priors

We consider informative priors both from screening measurements (Sect. 4) and from other independent measurements. We have informative priors on the contribution of the:

- $2\nu\beta\beta$ ^{100}Mo to ^{100}Ru 0_1^+ excited state, which has been taken as $T_{1/2} = (6.7 \pm 0.5) \times 10^{20}$ year (average value from [9]),
- Stainless steel springs included in the set-up to mitigate vibrational noise. These are modelled with high accuracy in the MC, and the values measured by HPGe and used as priors are given in Table 2,
- Random coincidence (pile-up and accidentals) events, determined from the rate of single events and from a measurement with a calibration source (see below).

6.3.1 Random coincidence events

Energy deposition in either one or two crystals randomly coinciding in time can cause non-negligible contributions to the high energy region both in $\mathcal{M}_{1,\beta/\gamma}$ and even more so in $\mathcal{M}_2$. This is a particular concern for ^{100}Mo, due to the fast rate of $2\nu\beta\beta$ decay of $T_{1/2} \sim 7 \times 10^{18}$ year [56], or around 2 mHz per detector. The events in two different detectors are referred to as accidentals and contribute to $\mathcal{M}_2$ spectrum. The random coincidences in the same detector are referred to as pile-up and contribute to the $\mathcal{M}_1$ spectrum.

We predict the spectral shape of these events by convolving the experimental $\mathcal{M}_{1,\beta/\gamma}$ spectrum with itself, i.e. by selecting randomly two energies in the experimental $\mathcal{M}_{1,\beta/\gamma}$ spectrum and summing them. The $\mathcal{M}_{1,\beta/\gamma}$ and the resulting random coincidences spectra are shown in Fig. 8.

The expected number of accidentals is then given by:

$$\hat{N}_{\text{acc}} = N^2 \frac{\Delta t}{t} \times \frac{N_{\text{LMO}} - 1}{N_{\text{LMO}}}, \tag{8}$$

where N is the total number of $\mathcal{M}_1$ events, $\Delta t/t$ is the ratio of the width of the coincidence time window, $\Delta t = \pm 10$ ms, to the total measurement time and N_{LMO} is the number of LMO detectors. For the accidental random coincidences we place a prior as a Gaussian function with mean $\hat{N}_{\text{acc}}$ and σ $\sqrt{\hat{N}_{\text{acc}}}$. We have used $N = 1.2 \times 10^6$, for a total measurement time of 2.2×10^7 s. We include this contribution only in the $\mathcal{M}_2$ spectrum.

The rate of pile-up events is generally lower than the rate of accidentals, but it is also less well constrained as the coincidence time, or effective time resolution, Δt_{eff}, is unknown a-priori and determined by the effectiveness of the pulse shape cuts used in the analysis. In general this time resolution will also be dependent on the energy of both the primary and secondary pulse as well as on their separation. However, since we are only interested in events in a narrow range of a high energy region (~ 3 MeV) we can treat this to a good approximation, as energy independent and simplify Eq. 8 to:

$$\hat{N}_{\text{pileup}} = N^2 \frac{\Delta t_{\text{eff}}}{t}. \tag{9}$$

For thermal detectors typically the timing resolution is between the inverse sampling frequency and detector rise time. In CUPID-Mo the inverse of the sampling rate is 2 ms and the median value of the rise-time is 24 ms, with 8 ms spread [36]. Similar LMO crystals to CUPID-Mo, tested at LNGS have achieved 1–2 ms effective timing resolution [57] also using PSD only on the LMO channel (as we have done in CUPID-Mo). However, this test has pulses with a higher sampling frequency with respect to CUPID-Mo, different operation temperature and noise conditions and slightly different rise time, so cannot be directly extrapolated.

For the prior on pile-up events in our fit we use a measurement with Th/U calibration sources. We consider all events between 4–5.5 MeV, and from Eq. 9 we can obtain a value for Δt_{eff}. As there are no events in the selected region, we obtain a prior for $\Delta t_{\text{eff}} < 7$ ms, at 90% c.i. As zero events are obtained, the corresponding probability density function is an exponential, that we use to place a prior on the pile-up rate. We include this contribution only in the $\mathcal{M}_{1,\beta/\gamma}$ spectrum.

6.4 Binning and choice of energy intervals

The energy range of the fit is 100–4000 keV for $\mathcal{M}_{1,\beta/\gamma}$, 400–4000 keV for $\mathcal{M}_2$ and 3000–10000 keV for $\mathcal{M}_{1,\alpha}$. We use a variable binning for the three spectra to have enough counts in each bin to minimize the effect of statistical fluctuations. We choose a minimum bin size of 15 keV for $\mathcal{M}_{1,\beta/\gamma}$ and $\mathcal{M}_2$, and 20 keV for $\mathcal{M}_{1,\alpha}$. We set the minimum number of counts in each bin to be 50 for $\mathcal{M}_{1,\beta/\gamma}$ and 30 for $\mathcal{M}_2$ and $\mathcal{M}_{1,\alpha}$. We choose each peak to be fully contained in one bin, to minimize the systematic effect of the detector response on our results.

7 Results

The result of the simultaneous fit of $\mathcal{M}_{1,\beta/\gamma}$, $\mathcal{M}_2$, and $\mathcal{M}_{1,\alpha}$ to the CUPID-Mo data with 2.71 kg $\times$ year exposure is

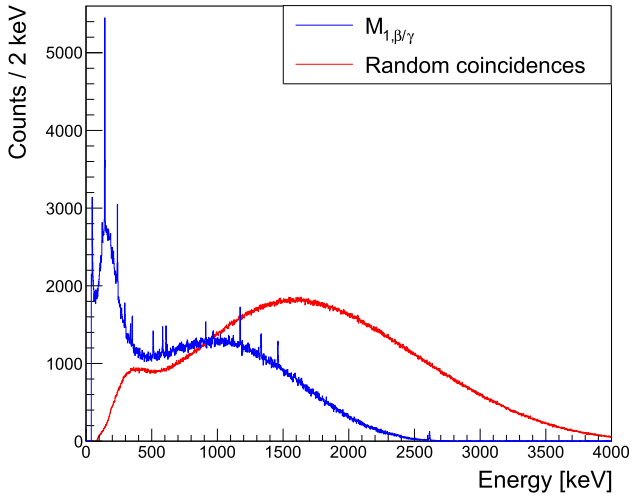

Fig. 8 Experimental $\mathcal{M}_{1,\beta/\gamma}$ and random coincidences (obtained by convolution of $\mathcal{M}_{1,\beta/\gamma}$, arbitrary normalization) spectral shapes. We observe that the random coincidences distribution is shifted to higher energies (as expected [58,59]) and could cause a background at the ROI

shown in Fig. 9. Tables 4 and 5 show the fit results, discussed in Sect. 7.2. We find that our background model is able to reconstruct well the 3 data spectra. On each spectrum the data over model ratio is shown, where the colors correspond respectively, to ± 1, ± 2, and ± 3 σ with:

$$\sigma_{i,b} = \frac{\sigma_{\text{data,i,b}}}{n_{\text{model,i,b}}}, \tag{10}$$

where $n_{\text{model,i,b}}$ is the predicted number of counts in bin b and spectrum i and $\sigma_{\text{data},i,b}$ is the standard deviation of the data in this bin, $\sqrt{n_{\text{data},i,b}}$.

To investigate the goodness of the fit we generate pseudo-experiments, or toy Monte Carlo simulations. We sample randomly according to a Poisson distribution the events in each energy bin of the background model best fit reproduction. We fit independently each pseudo experiment and obtain the likelihood $\mathcal{L}(\mathcal{D}|\vec{N})$, i.e. the probability of the experimental data $\mathcal{D}$ given the set of parameters $\vec{N}$ of our model. We show in Fig. 10 the result for $\mathcal{M}_{1,\beta/\gamma}$, $\mathcal{M}_2$ and $\mathcal{M}_{1,\alpha}$. The mean of the distributions of $\mathcal{M}_{1,\beta/\gamma}$ and $\mathcal{M}_2$ agree well with the value of the data. For $\mathcal{M}_{1,\alpha}$ the result demonstrate a modest incompatibility between the data and the model probably arising from an incomplete modelling of α detector response or an α miscalibration. This effect is visible for E > 6 MeV in Fig. 9 bottom panels. This modest incompatibility has driven the choice of a systematic in our model and we have thus performed a fit with an energy range 3000–6360 keV for $\mathcal{M}_{1,\alpha}$. We detail in Sect. 7.4 the results. The p value obtained are $p = 0.38$, $p = 0.04$ and $p \sim 0$ for $\mathcal{M}_{1,\beta/\gamma}$, $\mathcal{M}_2$ and $\mathcal{M}_{1,\alpha}$ respectively.

7.1 SSD and HSD $2\nu\beta\beta$ decay mechanisms

The transition between the ground states of ^{100}Mo and ^{100}Ru, with spin parity 0^+, is realized via virtual β transitions through 1^+ states of the intermediate nucleus ^{100}Tc. Nuclear theory does not predict a-priori whether this transition is realized dominantly through the 1^+ ground state (SSD hypothesis) or through higher excited states of ^{100}Tc (HSD hypothesis) [60].

We have found that the SSD mechanism of $2\nu\beta\beta$ decay to ^{100}Ru ground state reproduces fairly well the data with a $p = 0.38$, while the HSD model does not, $p \sim 0$. Since our data clearly favours SSD over HSD mechanism for $2\nu\beta\beta$, we have used the SSD model in our final fit.

7.2 Contaminations derived from the fit

7.2.1 LMO crystal contaminations

The $\mathcal{M}_{1,\alpha}$ spectrum is populated by α decays occurring in the crystals and in the elements directly facing them. As described in Sect. 3.11 we included bulk and surface contaminations in the crystals in our fit. We show in Fig. 11, the resulting components. Since we do not observe clear α-energy (NR escape) peaks due to the very low levels of contaminations and thus limited statistics, bulk and surface contaminations are anticorrelated. We performed studies concerning the effect of the location of the contaminations on bulk or surface in the fit results, which we discuss later.

The largest peak in the α region is the ^{210}Po peak. This peak is largely described by the Q-value component of the crystal bulk. For the ^{210}Po in order to fit as much as possible the particular shape peak in addition to 10 nm, implantation depths of 1 μm and 1 nm are used in the crystals, and implantation depths of 100 nm and 1 μm are used in the Reflectors. In Fig. 11 the left tail of the ^{210}Po peak is described by the surface contamination on the Reflectors.

The summary of the crystal activities extracted from the fit is presented in Table 4. The LMO crystal contaminations by radionuclides from the ^{238}U and ^{232}Th chains are all below 1 μBq/kg. As a study of the effect of the bulk versus surface location, we performed a fit without surface contaminations. These results show that, even under this extreme assumption, the results on the bulk activities do not vary significantly. As shown in Fig. 5 the peak at 4.8 MeV contains ^{234}U and ^{226}Ra alpha decays. In this analysis this peak is ascribed to ^{234}U, with a significant uncertainty (reported in Table 4) in the resulting contamination due to the anticorrelation with the ^{226}Ra contribution. Additionally, in this peak we could have a contribution from the neutron capture in ^{6}Li [31]. Neutrons captured in ^{6}Li produce an alpha particle plus tritium, ^{6}Li(n,α)^{3}H, with a total energy 4.782 MeV. We note also that the level of ^{228}Ra is not constrained by any α peak.

Table 5 Radioactive contaminations of the setup components derived from the posterior distribution of the background model fit. Uniform, non-informative priors are used except for the ^{228}Th, ^{226}Ra and ^{40}K contaminants in the springs. For surface contaminations, the simulated depth is 10 nm. The last column shows the activities from screening measurements when available (see Tables 2 and 3 in Sect. 4)

Component	Bulk	Posterior [mBq/kg]	Activity from screening [mBq/kg]
Reflectors[a]	^{238}U to ^{210}Pb	9.2 ± 1.0	Refl. only: 0.17 ± 0.05
	^{210}Pb	< 17	
	^{232}Th to ^{208}Pb	< 2.3	Refl. only: 0.05 ± 0.01
Springs	^{228}Ac	< 217	
	^{228}Th to ^{208}Pb	20 ± 5	21 ± 5
	^{226}Ra to ^{210}Pb	10 ± 3	11 ± 3
	^{40}K	3440^{+450}_{-340}	3600 ± 400
Kapton cables	^{228}Ac	< 139	
	^{228}Th to ^{208}Pb	< 28	15 ± 10
	^{226}Ra to ^{210}Pb	< 13	8 ± 6
Connectors[b]	^{228}Ac	< 442	
	^{228}Th to ^{208}Pb	< 339	82 ± 38
	^{226}Ra to ^{210}Pb	< 169	15 ± 8
Brass screws	^{228}Ac	< 24	
	^{228}Th to ^{208}Pb	< 18	3.5 ± 0.9
	^{210}Bi[c]	$(3.0 \pm 0.3) \times 10^4$	620 ± 254
Copper supports	^{228}Ac	< 0.051	
	^{228}Th to ^{208}Pb	< 0.052	0.024 ± 0.012
	^{226}Ra to ^{210}Pb	< 0.019	< 0.04
	^{60}Co[d]	0.47 ± 0.02	0.04
	^{57}Co[d]	0.029 ± 0.005	
Cryostat screens	^{228}Ac	< 0.38	
	^{228}Th to ^{208}Pb	< 0.40	0.024 ± 0.012
	^{226}Ra to ^{210}Pb	< 0.15	< 0.04
PE 1K[e]	^{228}Ac	< 4.4	0.5 ± 0.2
	^{228}Th to ^{208}Pb	$2.2^{+2.1}_{-1.6}$	0.3 ± 0.1
	^{226}Ra to ^{210}Pb	< 2.1	0.65 ± 0.08
Screen 300K	^{228}Ac to ^{208}Pb	(203^{+48}_{-51}) mBq	
	^{226}Ra to ^{210}Pb	(94 ± 13) mBq	
	^{40}K	(3200 ± 400) mBq	
Reflectors[a]	^{238}U to ^{234}U	$2.7^{+1.9}_{-1.6}$	
	^{234}U	< 9.5	
	^{230}Th	< 3.5	
	^{226}Ra to ^{210}Pb	$3.4^{+1.5}_{-1.2}$	(1.0 ± 0.4)[f] / (1.7 ± 0.5)[g]
	^{210}Pb to ^{206}Pb	1034^{+26}_{-33}	
	^{232}Th	< 3.9	
	^{228}Ra to ^{228}Th	< 504	
	^{228}Th to ^{208}Pb	$2.6^{+1.4}_{-1.5}$	(1.1 ± 0.4)[g]

[a]Reflectors take into account all passive elements directly facing the crystals: reflecting foils, PTFE, bonding wires, heaters
[b]Connectors refer to MillMax connectors plus Kapton connectors
[c]The ^{210}Bi in the Brass Screws accounts for this contamination in all 10 mK (Cables, Connectors, Springs, Copper supports) and infrastructure sources (cryostat screens and PE 1 K)
[d]Co in Copper supports account for this contamination also in Cryostat screens
[e]1K PE accounts for all sources below the 10 mK stage, e.g., 300 K electronics, dilution unit
[f] ^{214}Bi surface measurement with the BiPo-3 detector
[g]Extrapolation from ICPMS measurement, assuming all contamination on surface

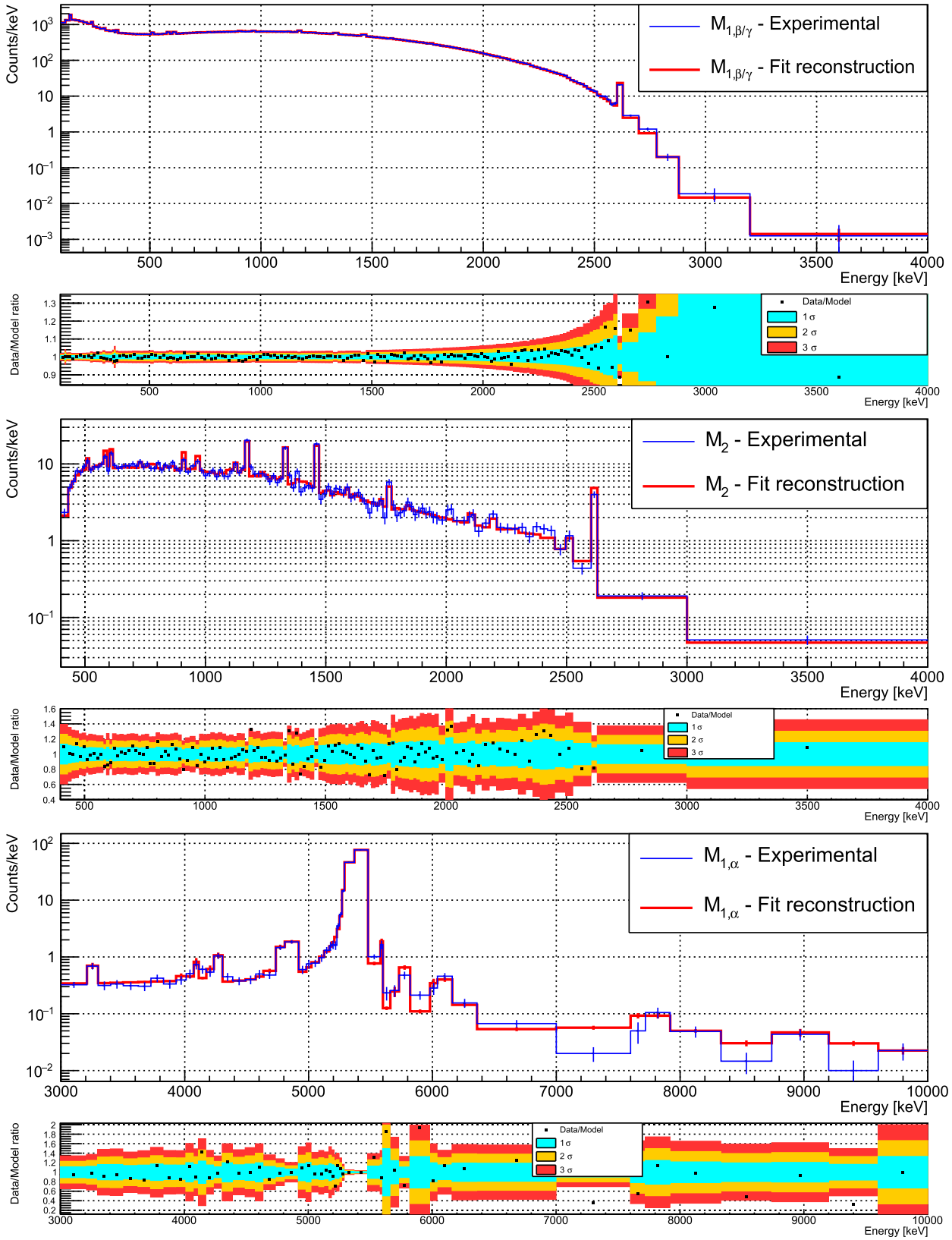

Fig. 9 Experimental data and background model simultaneous fit reconstruction of the 3 CUPID-Mo data spectra. Two upper panels: $\mathcal{M}_{1,\beta/\gamma}$, β/γ's spectrum with energy deposits in only one detector. Middle panels: $\mathcal{M}_2$, multiplicity 2 events, histogram of the 2 summed energies. Two bottom panels: $\mathcal{M}_{1,\alpha}$, multiplicity 1 events in α energy region. For each one, the lower panel shows the ratio between experimental counts and reconstruction counts for each bin. The colors indicate the uncertainties at ± 1, ± 2, and $\pm 3\,\sigma$

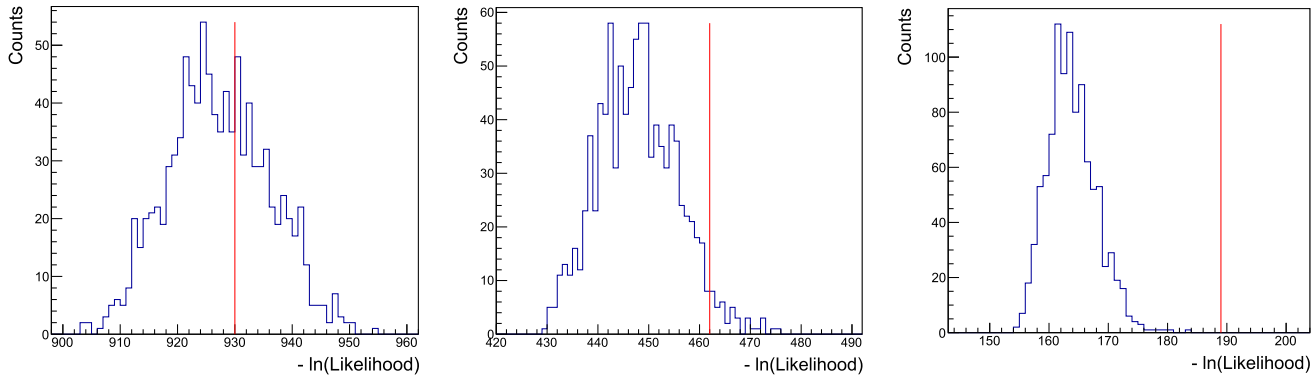

Fig. 10 Distribution of $-\ln \mathcal{L}(\mathcal{D}|\vec{N})$ from the toys for the $\mathcal{M}_{1,\beta/\gamma}$ (left), $\mathcal{M}_2$ (middle) and $\mathcal{M}_{1,\alpha}$ (right) spectra. The red line shows the $-\ln \mathcal{L}(\mathcal{D}|\vec{N})$ of the reference fit for each of the spectra

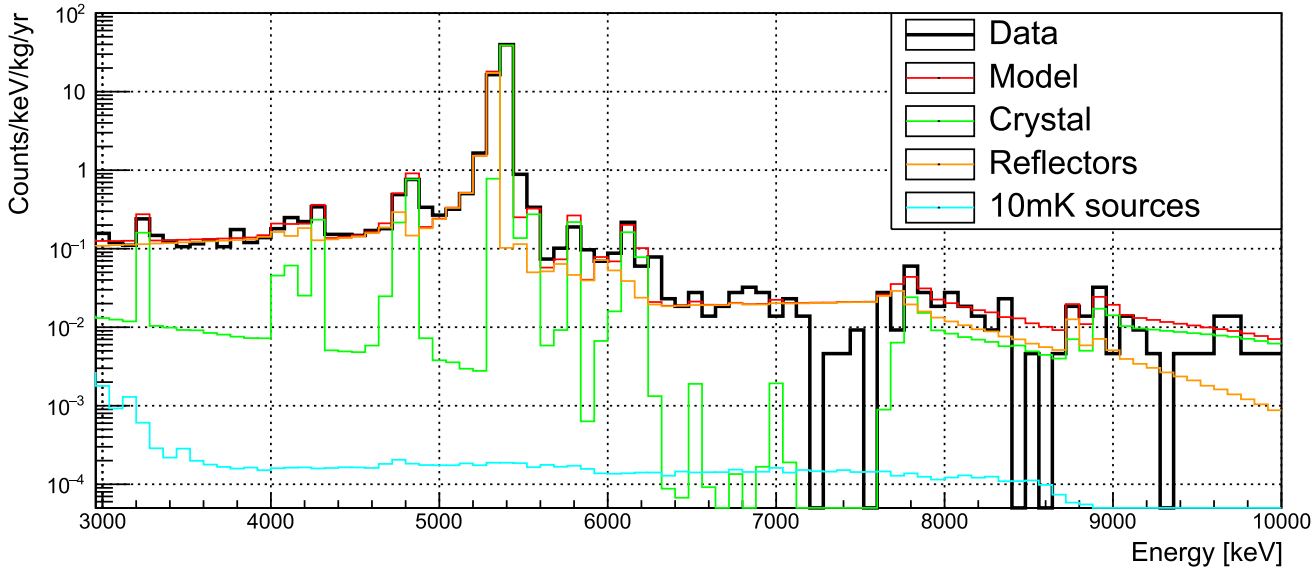

Fig. 11 Experimental $\mathcal{M}_{1,\alpha}$ spectrum reconstruction showing the components of the $\mathcal{M}_{1,\alpha}$ background model fit. Crystal and Reflector contaminations include bulk and surface. The surface contaminations are modelled with an exponential density profile and $\lambda = 10$ nm parameter depth. The peaks in the spectrum are described by the radioimpurities in the crystal and the continuum by the ones in the bulk of the Reflectors. The small contribution from 10 mK sources corresponds to the holders

There is clearly a larger ^{210}Po contribution than the rest of the ^{238}U chain, at the level of 96 μBq/kg, possibly introduced during the purification of the enriched material [61]. There are also traces of ^{190}Pt, caused by the crystal growth in a platinum crucible [62] and we find ^{40}K and ^{90}Sr+^{90}Y at the level of some hundreds of μBq/kg. We note that ^{210}Pb, ^{87}Rb, ^{90}Sr + ^{90}Y and ^{40}K do not represent a potential background for $0\nu\beta\beta$ search, as the Q_β of these radioisotopes is much lower than the $0\nu\beta\beta$ ROI at 3 MeV.

We show in Table 4 (bottom) the surface contaminations of the crystals derived from the fit. We studied the effect of including also a contribution with a depth parameter of 10 μm (i.e., including surface contaminations with $\lambda = 10$ nm and 10 μm) and the decay activity is shown in the third column of the table. The results are compatible with the fit including only 10 nm contributions. We observe clear anti-correlation for a given decay chain between the bulk and the surface contaminants in the crystal, but also with the surface of the Reflectors. These anti-correlations are taken into account in the uncertainties given in Table 4.

7.2.2 *Radioactive contaminations of the setup components*

A list of sources included in the fit and their resulting activities obtained from the marginalised mode and 68% c.i. are shown in Table 5.

The derived activities for the component called *Reflectors* are mainly constrained by the fit of the continuum in the α region. The values are larger than the measured radioactivities of the reflectors themselves, in particular, in ^{226}Ra.

We remind that this component takes into account all elements directly facing the crystals: PTFE, NTDs, LDs, bonding wires. A contamination of the reflecting foils introduced during the detector assembly could be conceived, explaining the activities obtained in the fit.

Concerning the surface activity on the reflecting foils, we performed a measurement with the BiPo-3 detector [41] which measures ^{214}Bi and ^{208}Tl levels through delay coincidences in the Bi-Po cascades. We can also convert the ICPMS results of the bulk measurement by assigning all the contamination to the surface. The surface activity of the *Reflectors* derived from the fit agrees well within uncertainties with both measurements.

The derived activities in the *Kapton cables*, the *Connectors*, the *Brass Screws* and the *Copper supports* agree well with the measured values. For the *Cryostat Screens* the activities obtained in the fit are higher than the measured levels from the raw copper. This points out to an additional contamination introduced during the fabrication of the screens for example due to the weldings. In particular, we have identified from the experimental data that the detectors facing the weldings in the cryostat screens have higher rates in the 2615 keV peak of ^{208}Tl.

The *Screen 300 K* accounts for the residual environmental γ's and the radon present in the gap between the outermost cryostat screen and the external lead shielding. The ^{226}Ra contamination derived from the fit shown in Table 5 can be translated into a radon level concentration resulting in (22 ± 3) mBq/m^3, which is in good agreement with measurements of 20 mBq/m^3 provided by the radon mitigation system in the LSM [34].

Figure 12 shows the breakdown of the components in the fit of $\mathcal{M}_{1,\beta/\gamma}$. In the region 0.8–3 MeV the dominant contribution is the $2\nu\beta\beta$ from ^{100}Mo and the most important contributions from the radioactivity in the materials are the cryostat and shields. We discuss in the next section the main sources in the $0\nu\beta\beta$ region.

7.3 Background index in the ^{100}Mo $0\nu\beta\beta$ ROI

We use our simultaneous fit to reconstruct the background index in the $0\nu\beta\beta$ region of interest. We chose to calculate the background index in the region ± 15 keV around 3034 keV. This range is much wider than the experimental energy resolution, without including any γ lines. We sample directly the full posterior distribution produced by JAGS for each step i in the Markov Chain by computing:

$$b_i = \sum_{\mathrm{j}=1}^{67} \mathrm{Pois}(N_j) \frac{w_{i,j}}{\Delta E \times Mt}. \tag{11}$$

Here b_i is the background index in the $0\nu\beta\beta$ region of interest, N_j is the integral of the spectrum of MC source j in the ROI, $w_{i,j}$ is the weight for source j in step i, ΔE is the width of the ROI and Mt is the experimental exposure. The sum goes over all background sources. The MC simulations are themselves the result of a stochastic process they have a statistical uncertainty, this is accounted for by Poisson smearing the MC ROI integrals per step of the Markov Chain. We then use the distribution of b_i for the full Markov Chain to estimate the marginalised posterior distribution of the background index. We perform this calculation for our maximal model with all parameters, we therefore naturally marginalise over all possible combinations of activities (for example surface or bulk radio-purity) consistent with our experimental data accounting for the systematic uncertainty due to source localisation.

From this calculation we extract the marginalised posterior of the background index shown in Fig. 13. This results in a measurement (mode $\pm$ smallest 68% interval) of:

$$b = 2.7^{+0.7}_{-0.6} \times 10^{-3} \text{ counts/keV/kg/year}. \tag{12}$$

or, in terms of the number of moles of isotope, $\mathrm{mol_{iso}}$, and energy resolution, ΔE_{FWHM}:

$$\mathcal{B} = 3.7^{+0.9}_{-0.8} \times 10^{-3} \mathrm{counts}/\Delta E_{\mathrm{FWHM}}/\mathrm{mol_{iso}}/\mathrm{year}. \tag{13}$$

This is the lowest background index achieved in a bolometric $0\nu\beta\beta$ decay experiment.

Next we reconstruct the contributions to the experimental background. We divide sources into five categories:

- Crystals U/Th;
- Pile-up;
- Reflectors;
- 10 mK sources;
- Cryostat and shields.

We emphasise that only the first three sources are relevant to CUPID. In the CUPID baseline the reflective foil is removed to improve background rejection. However, as it was noted before *Reflectors* include all the elements directly facing the crystals, PTFE, bonding wires, heaters. These elements will remain in CUPID. The final two are caused by materials in the EDELWEISS cryostat which is optimised for a dark matter rather than $0\nu\beta\beta$ decay search. The posterior distributions of background index from each source are shown in Fig. 14. We derive the background index for each of the sources in the same way as for the full posterior. We find that the crystals give the smallest contribution, with a background index:

$$8.1^{+3.5}_{-2.5} \times 10^{-5} \text{ counts/keV/kg/year}. \tag{14}$$

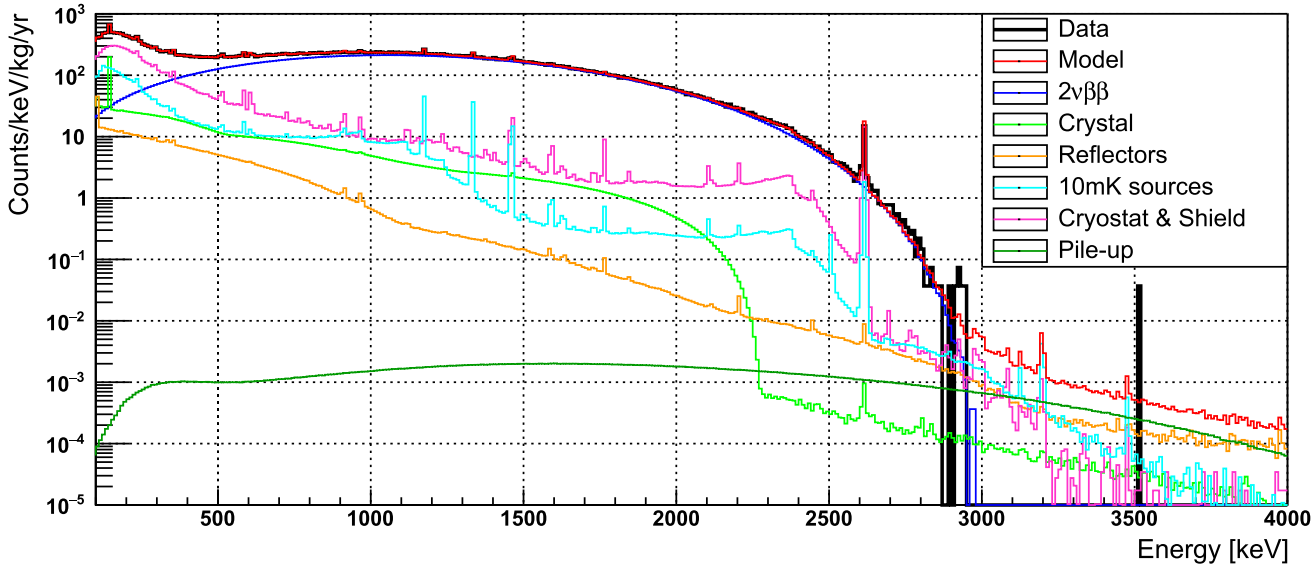

Fig. 12 Background sources reconstructing the experimental $\mathcal{M}_{1,\beta/\gamma}$ spectrum, grouped by source location. In blue, $2\nu\beta\beta$ is the dominant contribution in [350–3000] keV. The most important contribution from the materials, below 3 MeV, are the cryostat and shields, shown in magenta

As shown in Fig. 14, the posterior probability for pile-up allows us to set an upper limit for its background index, $< 1.4 \times 10^{-3}$ counts/keV/kg/year (90% c.i.). This is potentially the main background contribution, in particular due to the low CUPID-Mo sampling frequency (500 Hz) and lack of optimised cuts to remove pile-up. In CUPID, heat and light signals will be exploited together with optimised algorithms to remove pile-up events (see for example [63]). Figure 15 gives the background index extracted from Fig. 14 for each of the grouped components. They are obtained from the mode and the smallest 68.3% interval. For the pile-up the smallest 68.3% interval is compatible with zero, thus an upper limit is presented.

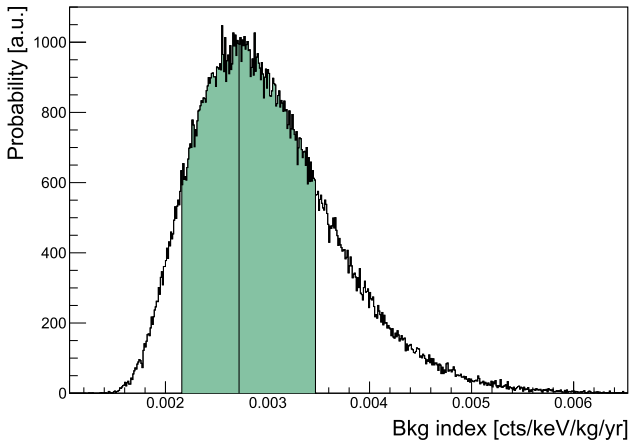

Fig. 13 Posterior distribution of background index, showing the mode and the smallest 68.3% c.i., $2.7^{+0.7}_{-0.6} \times 10^{-3}$ counts/keV/kg/year

7.4 Systematics

To check the stability of the model and the systematic uncertainties, we perform a series of different fits. To take into account the systematic uncertainty due to MC statistics, we add a nuisance parameter in Eq. 5:

$$\begin{aligned}&\ln(\mathcal{L}(D|(\vec{N}))) \\ &= \sum_{i=1}^{3} \sum_{b=1}^{N_b(i)} \ln\left(\text{Poiss}(n_{i,b};\, f_i(E_b;\, \vec{N}))\right) \\ &\quad + \ln\left(\text{Poiss}(N^{MC}_{j,i,b};\, N^{\hat{M}C}_{j,i,b})\right), \end{aligned} \tag{15}$$

where, $N^{MC}_{j,i,b}$ is the number of MC events in bin b of source j in spectra i, and $N^{\hat{M}C}_{i,b}$ is the expected number. These nuisance parameters added to the model account for the integer Poisson fluctuations in the MC. We find that the fit remains largely unchanged with only a small change in the value of the background index.

To check the stability of the fit, we perform different fits varying the binning, the energy fit region, the choice of background sources and, in particular, the bulk and surface contaminations in the crystals, as follow:

- Binning: we repeat the fit with 1, 2 and 20 keV fixed binning in $\mathcal{M}_{1,\beta/\gamma}$ and $\mathcal{M}_2$. In all cases, the overall goodness of the fit remains, and the value of the background index is compatible within uncertainties to that of the reference fit, as shown in Table 6. We did not repeat the fit with 1, 2 and 20 keV on $\mathcal{M}_{1,\alpha}$ due to the low statistics in each bin of the data;

- Fit energy region: our reference fit extends from 100 keV to 4 MeV for $\mathcal{M}_{1,\beta/\gamma}$ spectrum. We vary the energy threshold to 200 keV and find that the background index only varies slightly;
- Choice of background sources: our calculation of the background index is naturally marginalising over this uncertainty (see Sect. 7.3). However, as an additional check we perform the fit without including the crystal bulk contribution for the U and Th chains. The values of the activities of the sources change, but the goodness of the fit remains very similar and the value of the background index remains almost unchanged. We then remove the crystal surface contamination and still obtain a background index compatible within uncertainties to that of the reference fit;
- Energy region of $\mathcal{M}_{1,\alpha}$ fit: our reference fit extends from [3000–10000] keV. As described at the beginning of Sect. 7 the $\mathcal{M}_{1,\alpha}$ fit shows a modest incompatibility between the data and the model, mainly in the region E > 6 MeV. We thus performed a fit in [3000–6360] keV to account for this incompatibility as a systematic uncertainty in our model. In doing so, the U and Th contributions in the crystal get more degenerated, resulting in an increase of the Th contamination assigned in the fit. Still the background index is compatible, within uncertainties, to that of the reference fit.

The results of these tests are summarized in Table 6. As argued above, the result given in Eq. 17 is naturally marginalising over the uncertainty on the choice of the background sources. Considering all tests in Table 6 as a systematic uncertainty (with 2 keV fixed binning) and adding them in quadrature, the background index in (3034 ± 15) keV results in:

Table 6 Background Index in ROI for different fits. The tests allow to check the stability of the model and assess the systematic uncertainties

Fit	Background index [10^{-3} cts/keV/kg/year]
Reference fit	$2.7^{+0.7}_{-0.6}$
$\mathcal{M}_{1,\beta/\gamma}$ threshold = 200 keV	$2.8^{+0.7}_{-0.6}$
1 keV fixed binning for $\mathcal{M}_{1,\beta/\gamma}$ and $\mathcal{M}_2$	$2.5^{+0.6}_{-0.5}$
2 keV fixed binning for $\mathcal{M}_{1,\beta/\gamma}$ and $\mathcal{M}_2$	$2.5^{+0.7}_{-0.5}$
20 keV fixed binning for $\mathcal{M}_{1,\beta/\gamma}$ and $\mathcal{M}_2$	$2.9^{+0.8}_{-0.6}$
No crystal bulk ^{238}U and ^{232}Th chains	$2.8^{+0.7}_{-0.5}$
No crystal surface ^{238}U and ^{232}Th chains	$2.8^{+0.7}_{-0.6}$
No 10 mK sources ^{238}U and ^{232}Th chains	$2.2^{+0.7}_{-0.5}$
MC statistics (nuisance parameter)	$2.8^{+0.7}_{-0.6}$
$\mathcal{M}_{1,\alpha}$ range = 3000–6360 keV	3.8 ± 0.9

$$b = 2.7^{+0.7}_{-0.6}(\text{stat})^{+1.1}_{-0.5}(\text{syst}) \times 10^{-3}\ \text{counts/keV/kg/year}, \quad (16)$$

or:

$$\mathcal{B} = 3.7^{+0.9}_{-0.8}(\text{stat})^{+1.5}_{-0.7} (\text{syst}) \times 10^{-3}\text{counts}/\Delta E_{\text{FWHM}}/\text{mol}_{\text{iso}}/\text{year}. \quad (17)$$

We also verified that the reconstructed background index is not biased, by comparing the distribution of background indexes in toy Monte Carlo simulations to that of the reference fit.

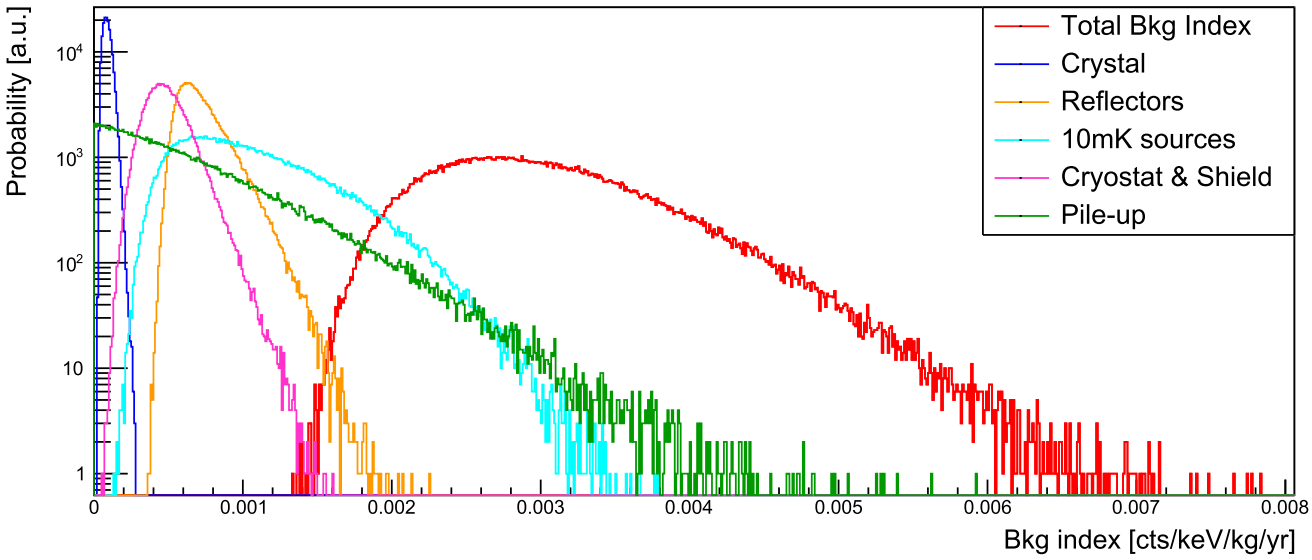

Fig. 14 Posterior distributions of background index of the several background sources grouped by source location. Also shown is the full posterior distribution

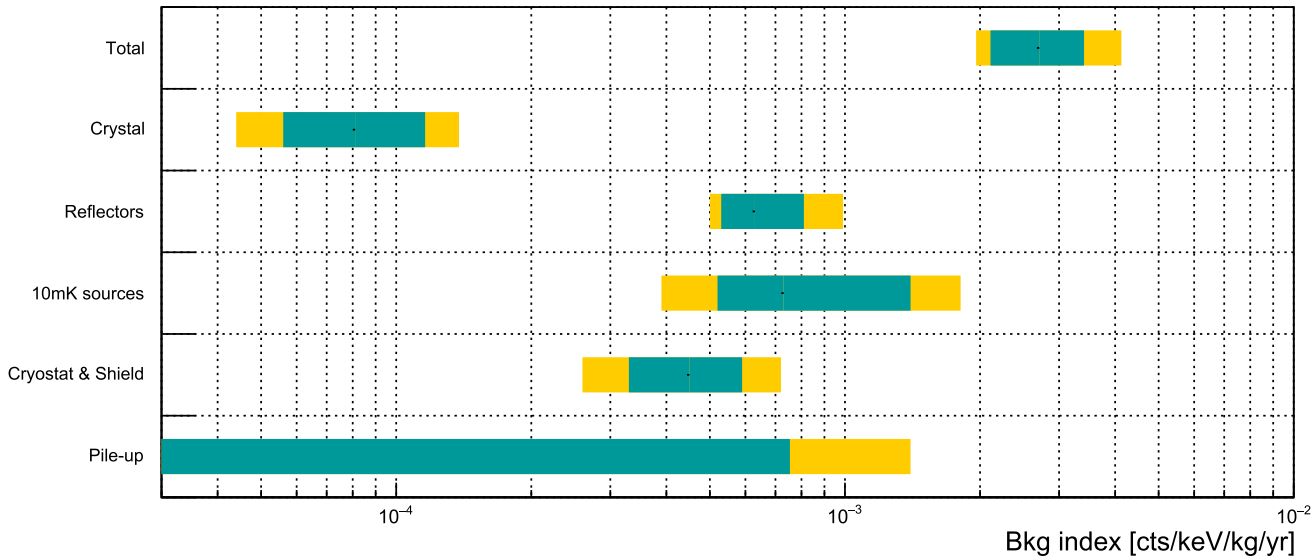

Fig. 15 Background index for the various groups of sources. The values are extracted from the mode of each distribution of Fig. 14, with their respective uncertainties. The green bars correspond to the smallest 68.3% interval around the mode, and the yellow bars to the smallest 90% interval around the mode. For the pile-up the distribution is compatible with zero, thus we give an upper limit to 68.3% c.i. in green and 90% c.i. in yellow

7.5 Residual alpha background

Due to our α particle rejection, background events in the ROI from ^{226}Ra and ^{228}Th subchains in the bulk and the surface of the crystals generally arise only from energy depositions of β or γ particles. However, ^{238}U, ^{234}U, ^{230}Th, ^{210}Po and ^{232}Th could also produce events in the ROI through energy deposits of α particles. Even if we apply a light yield cut to remove α background, it is still possible that some α events pass this selection cut.

From the background index distribution of the crystals, one can separate the background from β/γ decays from that coming from α decays, as shown in Fig. 16. One can observe that a non-negligible part of the crystal background index is coming from α's that passes the light yield cut. This α background is coming from surface contamination of the crystals. It corresponds to an α particle that deposits energy in the crystal and where the nuclear recoil deposits energy in the LD. This kind of events can pass the light yield cut mainly for the crystals that face only one LD. We show in Fig. 17, left, the experimental $\mathcal{M}_{1,\beta/\gamma}$ spectrum including all crystals, and the resulting spectrum selecting only the crystals that face two LDs. Such cut remove all the remaining alphas around 5.8 MeV. This effect is also visible in the background model. Figure 17, right, shows the reconstruction of the crystal component of $\mathcal{M}_{1,\beta/\gamma}$ spectrum, and the resulting spectrum selecting only the crystals that face two LDs. We remind that in CUPID-Mo 5 of the 20 LMOs are facing only one LD due to being in the bottom floor of the towers, one LD was not operational and one had a poor performance affecting a further 4 LMOs. We expect that in the case where all the crystals face two LDs, as in CUPID, the α background contribution should be negligible.

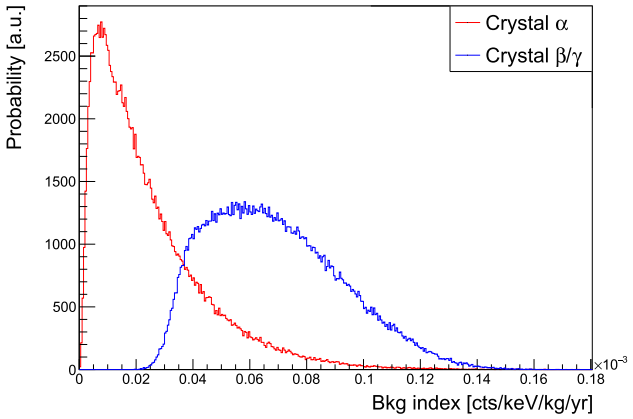

Fig. 16 Posterior distribution of background index of the crystal from α and β/γ contamination

8 Conclusion

In this work we present the development of a background model capable of describing very accurately the CUPID-Mo experimental data with 2.71 kg $\times$ year exposure. We have performed a simultaneous fit of three data spectra, $\mathcal{M}_{1,\beta/\gamma}$, $\mathcal{M}_2$ and $\mathcal{M}_{1,\alpha}$, to detailed Monte Carlo simulations. The model is performed in a Bayesian framework with a MCMC

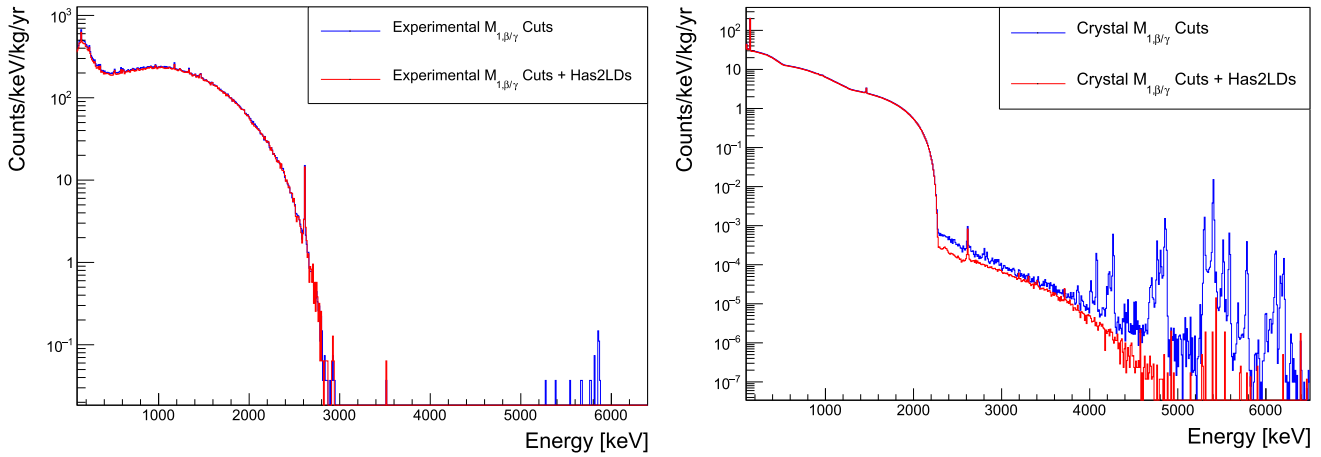

Fig. 17 Left: Experimental $\mathcal{M}_{1,\beta/\gamma}$ spectrum (in blue) adding a cut to select crystals that face two LDs (in red). Right: Fit reconstruction of the crystal component from $\mathcal{M}_{1,\beta/\gamma}$ spectrum (in blue), adding a cut to select crystals that face two LDs (in red)

approach. We have shown by a fit to a ^{56}Co calibration source that the MC implementation is accurate and that the MC is able to describe well the data. We used a total of 67 background sources including the bulk and surface radioactive contaminations in the crystal and the components of the set-up. We have performed systematic checks varying the binning, the energy fit region and the choice of background sources that showed the stability of the model.

We have found that the radiopurity of the $Li_2{}^{100}MoO_4$ crystals is sufficient to reach the goals of the future $0\nu\beta\beta$ experiment CUPID. The radiopurity levels of ^{226}Ra and ^{228}Th are below 0.5 μBq/kg. We obtain a background index in the region of interest of $3.7^{+0.9}_{-0.8}$ (stat)$^{+1.5}_{-0.7}$ (syst) $\times 10^{-3}$ counts/ΔE_{FWHM}/mol$_{\mathrm{iso}}$/year, the lowest in a bolometric $0\nu\beta\beta$ decay experiment.

The detailing of the background achieved in this work enables promising further studies. We can obtain the $2\nu\beta\beta$ decay rate of ^{100}Mo with high precision. It also allows for studies on various process which could distort the spectral shape, like Bosonic neutrinos, CP violation or $0\nu\beta\beta$ with Majoron(s) emission.

Acknowledgements This work has been performed in the framework of the CUPID-1 (ANR-21-CE31-0014) and LUMINEU programs, funded by the Agence Nationale de la Recherche (ANR, France). We acknowledge also the support of the P2IO LabEx (ANR-10-LABX0038) in the framework "Investissements d'Avenir" (ANR-11-IDEX-0003-01 Project "BSM-nu") managed by ANR, France. The help of the technical staff of the Laboratoire Souterrain de Modane and of the other participant laboratories is gratefully acknowledged. We thank the mechanical workshops of LAL (now IJCLab) for the detector holders fabrication and CEA/SPEC for their valuable contribution in the detector conception. F.A. Danevich, V.V. Kobychev, V.I. Tretyak and M.M. Zarytskyy were supported in part by the National Research Foundation of Ukraine Grant No. 2020.02/0011. A.S. Barabash, S.I. Konovalov, I.M. Makarov, V.N. Shlegel and V.I. Umatov were supported by the Russian Science Foundation under Grant No. 18-12-00003. J. Kotila is supported by Academy of Finland (Grant Nos. 314733, 320062, 345869). Additionally the work is supported by the Istituto Nazionale di Fisica Nucleare (INFN) and by the EU Horizon2020 research and innovation program under the Marie Sklodowska-Curie Grant Agreement No. 754496. This work is also based on support by the US Department of Energy (DOE) Office of Science under Contract Nos. DE-AC02-05CH11231, and by the DOE Office of Science, Office of Nuclear Physics under Contract Nos. DE-FG02-08ER41551, DE-SC0011091. This research used resources of the National Energy Research Scientific Computing Center (NERSC) and the IN2P3 Computing Centre. This work makes use of the *Diana* data analysis software and the background model based on JAGS, developed by the CUORICINO, CUORE, LUCIFER, and CUPID-0 Collaborations. Russian and Ukrainian scientists have given and give crucial contributions to CUPID-Mo. For this reason, the CUPID-Mo collaboration is particularly sensitive to the current situation in Ukraine. The position of the collaboration leadership on this matter, approved by majority, is expressed at https://cupid-mo.mit.edu/collaboration#statement. Majority of the work described here was completed before February 24, 2022.

Data Availability Statement This manuscript has no associated data or the data will not be deposited. [Authors' comment: This manuscript has associated raw and processed data. The data can be made available by signing an agreement with the CUPID-Mo collaboration.]

Funded by SCOAP^3. SCOAP^3 supports the goals of the International Year of Basic Sciences for Sustainable Development.

References

1. M. Agostini, G. Benato, J.A. Detwiler, J. Menéndez, F. Vissani Rev. Mod. Phys. **95**(2), 025002 (2023). https://doi.org/10.1103/RevModPhys.95.025002
2. S. Abe et al., Phys. Rev. Lett. **130**(5), 051801 (2023). https://doi.org/10.1103/PhysRevLett.130.051801
3. M. Agostini et al., Phys. Rev. Lett. **125**(25), 252502 (2020). https://doi.org/10.1103/PhysRevLett.125.252502
4. D.Q. Adams et al., Nature **604**(7904), 53 (2022). https://doi.org/10.1038/s41586-022-04497-4
5. O. Azzolini et al., Phys. Rev. Lett. **129**(11), 111801 (2022)
6. C. Augier et al., Eur. Phys. J. C **82**(11), 1033 (2022). https://doi.org/10.1140/epjc/s10052-022-10942-5
7. G. Anton et al., Phys. Rev. Lett. **123**(11), 161802 (2019)
8. I.J. Arnquist et al., Phys. Rev. Lett. **130**(11), 062501 (2023)
9. A. Barabash, Universe **6**(10), 159 (2020). https://doi.org/10.3390/universe6100159
10. E. Armengaud et al., Eur. Phys. J. C **77**(11), 785 (2017). https://doi.org/10.1140/epjc/s10052-017-5343-2
11. E. Armengaud et al., Phys. Rev. Lett. **126**(18), 181802 (2021). https://doi.org/10.1103/PhysRevLett.126.181802
12. D.Q. Adams, Prog. Part. Nucl. Phys. **122**, 103902 (2021)
13. C. Alduino et al., Eur. Phys. J. C **77**, 543 (2017)
14. D.Q. Adams et al., Phys. Rev. Lett. **126**(17), 171801 (2021). https://doi.org/10.1103/PhysRevLett.126.171801
15. C. Alduino et al., Eur. Phys. J. C **77**(1), 13 (2017). https://doi.org/10.1140/epjc/s10052-016-4498-6
16. D. Poda, Physics **3**(3), 473 (2021)
17. CUPID pre-CDR (2019). arXiv:1907.09376 [physics.ins-det]
18. C. Augier et al., Phys. Rev. C **107**(2), 025503 (2022). https://doi.org/10.1103/PhysRevC.107.025503
19. F. Simkovic, P. Domin, S.V. Semenov, J. Phys. G **27**, 2233 (2001). https://doi.org/10.1088/0954-3899/27/11/304
20. P. Domin, S. Kovalenko, F. Simkovic, S.V. Semenov, Nucl. Phys. A **753**, 337 (2005). https://doi.org/10.1016/j.nuclphysa.2005.03.003
21. Z.G. Berezhiani, A.Y. Smirnov, J.W.F. Valle, Phys. Lett. B **291**, 99 (1992). https://doi.org/10.1016/0370-2693(92)90126-O
22. R.N. Mohapatra, E. Takasugi, Phys. Lett. B **211**, 192 (1988). https://doi.org/10.1016/0370-2693(88)90832-5
23. C.P. Burgess, J.M. Cline, Phys. Lett. B **298**, 141 (1993). https://doi.org/10.1016/0370-2693(93)91720-8
24. C.P. Burgess, J.M. Cline, Phys. Rev. D **49**, 5925 (1994). https://doi.org/10.1103/PhysRevD.49.5925
25. P. Bamert, C.P. Burgess, R.N. Mohapatra, Nucl. Phys. B **449**, 25 (1995). https://doi.org/10.1016/0550-3213(95)00273-U
26. C.D. Carone, Phys. Lett. B **308**, 85 (1993). https://doi.org/10.1016/0370-2693(93)90605-H
27. R.N. Mohapatra, A. Perez-Lorenzana, C.A. de S Pires, Phys. Lett. B **491**, 143 (2000). https://doi.org/10.1016/S0370-2693(00)01031-5
28. A.S. Barabash et al., Nucl. Phys. B **783**, 90 (2007)
29. S.A. Ghinescu, O. Nitescu, S. Stoica, Phys. Rev. D **105**, 055032 (2022)
30. A. Abada, A. Hernandez-Cabezudo, X. Marcano, J. High Energy Phys. **01**, 041 (2019)
31. E. Armengaud et al., J. Instrum. **12**(08), P08010 (2017). https://doi.org/10.1088/1748-0221/12/08/P08010
32. E. Armengaud et al., Astropart. Phys. **47**, 1 (2013). https://doi.org/10.1016/j.astropartphys.2013.05.004
33. M. L'Hour, Revue archéologique de l'ouest **4**(1), 113 (1987)
34. R. Hodák et al., J. Phys. G **46**(11), 115105 (2019). https://doi.org/10.1088/1361-6471/ab368e
35. B. Schmidt et al., Astropart. Phys. **44**, 28 (2013)
36. E. Armengaud et al., Eur. Phys. J. C **80**(1), 44 (2020). https://doi.org/10.1140/epjc/s10052-019-7578-6
37. C. Alduino et al., Phys. Rev. C **93**(4), 045503 (2016). https://doi.org/10.1103/PhysRevC.93.045503
38. O. Azzolini et al., Eur. Phys. J. C **78**(9), 734 (2018). https://doi.org/10.1140/epjc/s10052-018-6202-5
39. K. Alfonso et al., Eur. Phys. J. C **82**(9), 810 (2022). https://doi.org/10.1140/epjc/s10052-022-10720-3
40. O. Azzolini et al., Eur. Phys. J. C **81**(8), 722 (2021). https://doi.org/10.1140/epjc/s10052-021-09476-z
41. A. Barabash et al., J. Instrum. **12**(06), P06002 (2017)
42. O. Azzolini et al., Eur. Phys. J. C **79**(7), 583 (2019). https://doi.org/10.1140/epjc/s10052-019-7078-8
43. S. Rozov et al. (2010). arXiv preprint. arXiv:1001.4383
44. S. Fiorucci et al., Astropart. Phys. **28**, 143 (2007). https://doi.org/10.1016/j.astropartphys.2007.05.003
45. R. Lemrani, M. Robinson, V.A. Kudryavtsev, M. De Jesus, G. Gerbier, N.J.C. Spooner, Nucl. Instrum. Methods A **560**, 454 (2006). https://doi.org/10.1016/j.nima.2005.12.238
46. R. Gurriaran, Personal communication
47. J. Allison et al., Nucl. Instrum. Methods Phys. Res. A **835**, 186 (2016)
48. J. Kotila, F. Iachello, Phys. Rev. C **85**(3), 034316 (2012). https://doi.org/10.1103/PhysRevC.85.034316
49. J. Kotila, Personal communication (2012)
50. O.A. Ponkratenko, V.I. Tretyak, Y.G. Zdesenko, Phys. Atom. Nucl. **63**, 1282 (2000). https://doi.org/10.1134/1.855784
51. Geant4 Physics Reference Manual
52. A. Gelman, J.B. Carlin, H.S. Stern, D.B. Dunson, A. Vehtari, D. Rubin, *Bayesian Data Analysis*, 3rd edn. (Chapman & Hall, London, 2013)
53. M. Plummer, in *3rd International Workshop on Distributed Statistical Computing (DSC 2003)* (2003), p. 124
54. M. Plummer, JAGS version 3.3.0 user manual (2012)
55. O.G. Polischuk, MDPI Phys. **3**(1), 103 (2021). https://doi.org/10.3390/physics3010009
56. A. Barabash, Universe **6**(10), 159 (2020)
57. A. Armatol et al., Phys. Rev. C **104**(1), 015501 (2021)
58. D. Chernyak et al., Eur. Phys. J. C **72**, 1989 (2012)
59. D.M. Chernyak, F.A. Danevich, A. Giuliani, M. Mancuso, C. Nones, E. Olivieri, M. Tenconi, V.I. Tretyak, Eur. Phys. J. C **74**, 2913 (2014). https://doi.org/10.1140/epjc/s10052-014-2913-4
60. R. Arnold et al., Eur. Phys. J. C **79**(5), 440 (2019). https://doi.org/10.1140/epjc/s10052-019-6948-4
61. E. Armengaud et al., J. Instrum. **10**(05), P05007 (2015)
62. V. Grigorieva et al., J. Mater. Sci. Eng. B **7**, 63 (2017). https://doi.org/10.17265/2161-6221/2017.3-4.002
63. G. Fantini et al., J. Low Temp. Phys. **209**, 1024 (2022). https://doi.org/10.1007/s10909-022-02741-9

5.2.3 Improved $2\nu\beta\beta$ model

As mentioned in section 1.2, since $0\nu\beta\beta$ and $2\nu\beta\beta$ share the same initial and final nuclear states, measurements of $2\nu\beta\beta$ are helpful for an accurate description of the nuclear structure and therefore to obtain reliable estimates of the $0\nu\beta\beta$ matrix elements. Together with my master student Toby Dixon and my PhD student Léonard Imbert, we performed spectral shape studies relying on the robust background model developed for CUPID-Mo, described in section 5.2.2. We obtained a first of its kind measurement of a novel nuclear structure observable, based on an improved description of the $2\nu\beta\beta$ decay process. We describe this improved model below.

We have introduced previously in section 1.2 that the rate of the $2\nu\beta\beta$ decay to the 0^+ ground state of the final nucleus is given in full generality by eq 1.16. With the appropriate constants the general expression for $2\nu\beta\beta$ decay reads [19, 136]:

$$\left(T_{1/2}^{2\nu}\right)^{-1} = \frac{m_e}{8\pi^7 \ln(2)} \left(G_\beta m_e^2\right)^4 \left(g_A^{\text{eff}}\right) I^{2\nu} \tag{5.5}$$

where $G_\beta = G_F \cos\theta_C$, with G_F the Fermi constant, θ_C the Cabibbo angle, and m_e the mass of the electron. The effective axial vector coupling constant g_A^{eff} indicates that the value can be tuned to reproduce the measured value of the $2\nu\beta\beta$ half life. The term $\mathrm{I}^{2\nu}$ contains the information on the energy dependence and the amplitude of the transition:

$$I^{2\nu} \propto \int_0^{E_i - E_f - E_1 - E_2} E_{\nu_1}^2 E_{\nu_2}^2 A^{2\nu} dE_{\nu_1}, \tag{5.6}$$

Also in section 1.2 we have shown that the $2\nu\beta\beta$ decay spectrum is typically described using two approximations, the Single State Dominance (SSD) and the High State Dominance (HSD) hypothesis. The description of the $2\nu\beta\beta$ spectrum was improved in [19, 136]. In this approach a Taylor expansion is performed in terms of the lepton energies. Recall that the lepton energies, introduced in section 1.2, enter in the factors $\epsilon_{K,L}$:

$$\epsilon_K = (E_{e_2} + E_{\nu_2} - E_{e_1} - E_{\nu_1})/2, \tag{5.7}$$

and

$$\epsilon_L = (E_{e_1} + E_{\nu_2} - E_{e_2} - E_{\nu_1})/2. \tag{5.8}$$

In the improved approach, the decay rate relates to the space phase factors and NMEs [19, 136] :

$$\Gamma^{2\nu} = \Gamma_0^{2\nu} + \Gamma_2^{2\nu} + \Gamma_{22}^{2\nu} + \Gamma_4^{2\nu}, \tag{5.9}$$

where :

$$\Gamma_0^{2\nu} = \left(g_A^{\text{eff}}\right)^4 M_0 G_0^{2\nu}, \tag{5.10}$$

$$\Gamma_2^{2\nu} = \left(g_A^{\text{eff}}\right)^4 M_2 G_2^{2\nu}, \tag{5.11}$$

$$\Gamma_{22}^{2\nu} = \left(g_A^{\text{eff}}\right)^4 M_{22} G_{22}^{2\nu}, \tag{5.12}$$

$$\Gamma_4^{2\nu} = \left(g_A^{\text{eff}}\right)^4 M_4 G_4^{2\nu}, \tag{5.13}$$

Here, M_0, M_2, M_{22}, M_4 are the nuclear matrix elements and G_0, G_2, G_{22}, G_4 are the space phase factors for the different terms in the Taylor expansion. This expansion allows to calculate

the phase space factors separately from the NMEs, as in the SSD and HSD approximations. The phase space factors are of the form [19, 136] :

$$G_N^{2\nu} \propto \int_0^{E_i - E_f - E_{e_1} - E_{e_2}} E_{\nu_1}^2 E_{\nu_2}^2 A_N^{2\nu} dE_{\nu_1}, \ (N = 0,\ 2,\ 4,\ 22) \tag{5.14}$$

with :

$$A_0^{2\nu} = 1, \tag{5.15}$$

$$A_2^{2\nu} = \frac{\epsilon_K^2 + \epsilon_L^2}{(2m_e)^2}, \tag{5.16}$$

$$A_{22}^{2\nu} = \frac{\epsilon_K^2 \epsilon_L^2}{(2m_e)^4}, \tag{5.17}$$

$$A_4^{2\nu} = \frac{\epsilon_K^4 + \epsilon_L^4}{(2m_e)^4}. \tag{5.18}$$

The nuclear matrix elements are given by [19, 136] :

$$M_0 = \left(M_{GT-1}^{2\nu}\right)^2, \tag{5.19}$$

$$M_2 = M_{GT-1}^{2\nu} M_{GT-3}^{2\nu}, \tag{5.20}$$

$$M_{22} = \frac{1}{3}\left(M_{GT-3}^{2\nu}\right)^2, \tag{5.21}$$

$$M_4 = \frac{1}{3}\left(M_{GT-3}^{2\nu}\right)^2 + M_{GT-1}^{2\nu} M_{GT-5}^{2\nu}, \tag{5.22}$$

with :

$$M_{GT-1}^{2\nu} = m_e \sum_n \frac{\left\langle 0_F^+ \right| \left|\tau_m^+ \vec{\sigma_m}\right| \left|1_n^+\right\rangle \left\langle 1_n^+ \right| \left|\tau_m^+ \vec{\sigma_m}\right| \left|0_I^+\right\rangle}{E_n - (E_i + E_f)/2}, \tag{5.23}$$

$$M_{GT-3}^{2\nu} = \sum_n \left\langle 0_F^+ \right| \left|\tau_m^+ \vec{\sigma_m}\right| \left|1_n^+\right\rangle \left\langle 1_n^+ \right| \left|\tau_m^+ \vec{\sigma_m}\right| \left|0_I^+\right\rangle \frac{4m_e^3}{(E_n - (E_i + E_f)/2)^3}, \tag{5.24}$$

$$M_{GT-5}^{2\nu} = \sum_n \left\langle 0_F^+ \right| \left|\tau_m^+ \vec{\sigma_m}\right| \left|1_n^+\right\rangle \left\langle 1_n^+ \right| \left|\tau_m^+ \vec{\sigma_m}\right| \left|0_I^+\right\rangle \frac{16m_e^5}{(E_n - (E_i + E_f)/2)^5}. \tag{5.25}$$

By introducing two ratios of nuclear matrix elements, [19]

$$\xi_{31} = \frac{M_{GT-3}^{2\nu}}{M_{GT-1}^{2\nu}}, \tag{5.26}$$

and

$$\xi_{51} = \frac{M_{GT-5}^{2\nu}}{M_{GT-1}^{2\nu}}, \tag{5.27}$$

the differential decay rate is expressed as :

$$\frac{d\Gamma}{dE} = \left(g_A^{\text{eff}}\right)^4 \left|M_{GT-1}^{2\nu}\right|^2 \left(\frac{dG_0^{2\nu}}{dE} + \xi_{31}\frac{dG_2^{2\nu}}{dE} + \frac{1}{3}\xi_{31}^2\frac{dG_{22}^{2\nu}}{dE} + \left(\frac{1}{3}\xi_{31}^2 + \xi_{51}\right)\frac{dG_4^{2\nu}}{dE}\right). \tag{5.28}$$

We can fit this model to the experimental $2\nu\beta\beta$ spectrum. The derivatives of the phase space factors $\frac{dG_N}{dE}$ are fixed from theoretical calculations, thus it is possible to obtain ξ_{31}, and ξ_{51} from the experimental spectral shape. Moreover we can compare the results with theoretical predictions, in particular the HSD and SSD hypotheses. The first term in the Taylor expansion (M_0, $A_0^{2\nu}$), where the lepton energies are neglected, corresponds to the HSD hypothesis, with $\xi_{31} = \xi_{51} = 0$. The SSD hypothesis does not correspond to a single term in the Taylor expansion. Recall that in this hypothesis the decay is supposed to proceed through the lowest 1^+ state of the intermediate nucleus and not through the sum over all possible intermediate states. $M^{2\nu}_{GT-3}$ and $M^{2\nu}_{GT-5}$ are expected to be dominated by lower-lying states due to the terms at the power 3 and 5 in the denominators. The SSD hypothesis would correspond to a particular combination of M_N and $G_N^{2\nu}$. Theoretical calculations using the SSD approximation can be performed to predict nonzero ξ_{31}, ξ_{51}, as in [19]. We can compare these values to the experimental results.

5.2.4 Measurement of the $2\nu\beta\beta$ decay rate and spectral shape of ^{100}Mo from the CUPID-Mo experiment

The work that we have performed with my two students has been published in Physical Review Letters [92] and it is included at the end of this section. However, some details of the work were not described in the publication, which we discuss in the following.

Measurement of the $2\nu\beta\beta$ half-life

We have built the background model of CUPID-Mo data with simulations of the contributions of the $2\nu\beta\beta$ decay and of various components of the experimental set-up. In our work described in section 5.2.2 we utilized the $2\nu\beta\beta$ spectrum from the SSD model. To measure the $2\nu\beta\beta$ decay rate, we replaced the SSD by the improved model spectrum in our background model, which again is well reproducing the experimental data. To extract the $2\nu\beta\beta$ decay rate, we simply integrate the $2\nu\beta\beta$ contribution to obtain:

$$T_{1/2} = (7.10 \pm 0.02) \times 10^{18} \text{ years}. \tag{5.29}$$

with a statistical uncertainty of 0.03%. The measurement is dominated by the systematic uncertainties, which are described in the article below. In particular, the anthropogenic isotope ^{90}Sr is a pure β emitter which decays to ^{90}Y. We have found that our background model is consistent with a ^{90}Sr/^{90}Y activity of 179^{+36}_{-32} μBq/kg. However, the ^{90}Y and the $2\nu\beta\beta$ spectra are anticorrelated in our model, as the shape of the spectrum of the ^{90}Y (Q-value= 2276 keV) is similar to that of the $2\nu\beta\beta$, as can be appreciated in Fig. 5.15. We thus considered the ^{90}Sr+^{90}Y contribution as a source of systematic uncertainty and we have rerun the fit without this contribution.

Considering all the systematics, we get the distribution for the decay rate shown in red in Fig.5.16. Extracting the mode and the smallest 68% interval:

$$(T_{1/2})^{-1} = (0.1414 \pm 0.0023) \times 10^{-18} \text{ years}^{-1} \text{ (stat+syst.)}, \tag{5.30}$$

which corresponds to a half-life for the $2\nu\beta\beta$ decay of ^{100}Mo of:

$$T_{1/2} = (7.07 \pm 0.02(\text{stat.}) \pm 0.11(\text{syst.}) \times 10^{18} \text{ yr}. \tag{5.31}$$

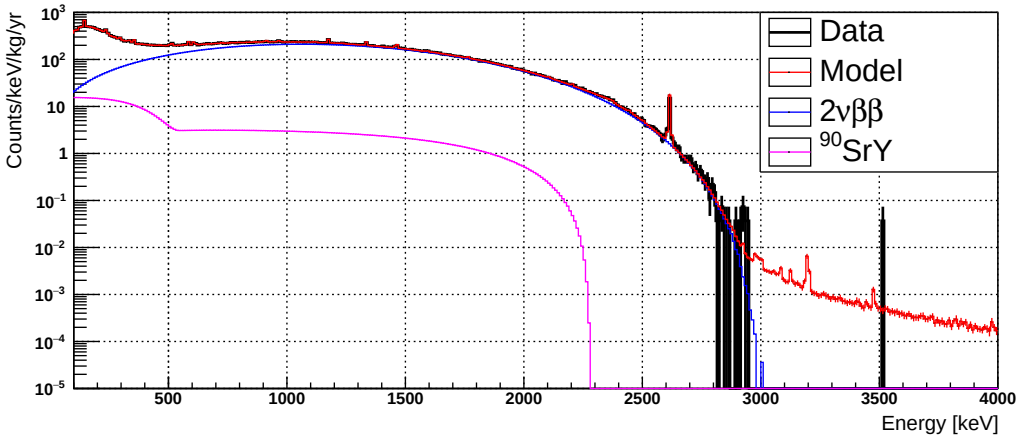

Figure 5.15: Experimental data $\mathcal{M}_{1,\beta/\gamma}$ in CUPID-Mo, compared to the background model reconstruction, the $2\nu\beta\beta$ spectrum and the ^{90}Sr+^{90}Y contribution. The shape of the spectrum of ^{90}Sr+^{90}Y is similar to that of the $2\nu\beta\beta$, therefore their contributions in the background model are anticorrelated.

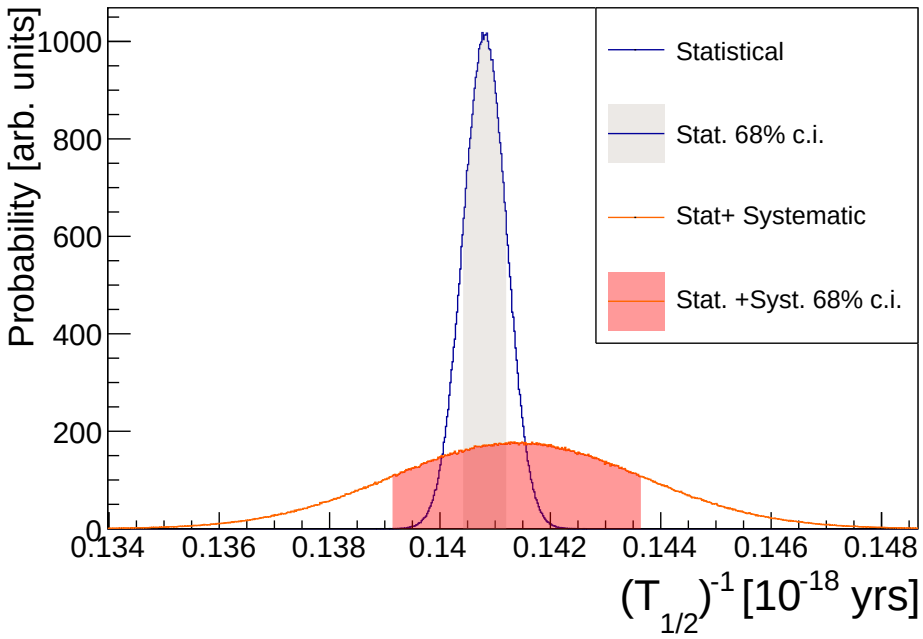

Figure 5.16: Probability posterior distributions of the decay rate of $2\nu\beta\beta$, with the statistical uncertainty in blue and the systematic uncertainty in red.

$2\nu\beta\beta$ spectral shape studies

As mentioned in section 5.2.3 we can extract the $\xi_{3,1}$ and $\xi_{5,1}$ using eq. 5.28 from the improved model description of the $2\nu\beta\beta$ decay, fitting this model to our experimental data. We have used the $2\nu\beta\beta$ NMEs computed by Fedor Šimkovic and collaborators within the pn-QRPA approach, and the spectral shapes $\frac{dG_N}{dE}$ computed by Šimkovic *et al*, considering Dirac wave functions with finite nuclear size and electron screening. The spectral shapes corresponding to the different terms in the Taylor expansion are shown in Fig 5.17 with arbitrary normalization.

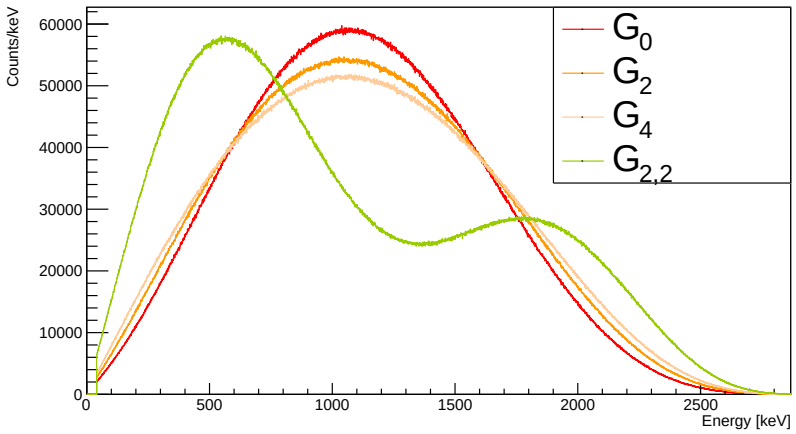

Figure 5.17: Comparison of the spectral shapes phase space factors corresponding to the Taylor expansion, with arbitrary normalization (Fedor Simkovic, personal communication).

Fig. 5.18 shows the distribution of $\xi_{5,1}$ as a function of $\xi_{3,1}$ obtained, showing a strong anti-correlation between both parameters. The fit favours values of $\xi_{5,1} > \xi_{3,1}$ which is theoretically not correct since according to the Taylor expansion $\xi_{3,1}$ corresponds to a lower order term than $\xi_{5,1}$, thus $\xi_{3,1} > \xi_{5,1}$. To constrain these two parameters we have taken advantage that the ratio $\xi_{5,1}/\xi_{3,1}$ can be reliably calculated. In particular $\xi_{51}/\ \xi_{31} = \mathrm{M}^{2\nu}_{GT-5}/M^{2\nu}_{GT-3} = 0.367$ [19] with SSD model, $\xi_{51}/\xi_{31} = 0.349$ according to shell model [137, 138], and ξ_{51}/ξ_{31} ranges from 0.364 to 0.368 in pn-QRPA models. Thus we have chosen to perform the fit with a Gaussian prior on ξ_{51}/ξ_{31}. The value of ξ_{31} from the fit results in:

$$\xi_{31} = 0.47 \pm 0.03 \text{ (stat.)}, \tag{5.32}$$

and

$$\xi_{51} = 0.17 \pm 0.02 \text{ (stat.)}. \tag{5.33}$$

The article below provides details on the comparison of these values with theoretical predictions. The value of ξ_{31} is found to be incompatible with HSD and compatible with the SSD hypothesis, mildly incompatible with predictions from the Interacting Shell Model, but compatible with pn-QRPA predictions.

As suggested in [20], a value for $g_{A,\text{eff}}$ can be obtained thanks to the combination of the experimental information on the half-life and of the shape of the spectrum:

$$g^4_{A,\text{eff}} = \frac{T^{-1}_{1/2} \times \xi^2_{3,1}}{M^2_{GT-3} G}., \tag{5.34}$$

where $G = G_0 + \xi_{3,1} G_2 + \xi_{3,1}^2 G_{22}/3 + (\xi_{3,1}^2/3 + \xi_{5,1}) G_4$. Assuming that M_{GT-3} is reliably calculated, we can thus use our experimental $T_{1/2}$ and $\xi_{3,1}$ to derive $g_{A,\text{eff}}$. The authors in [20] argue that the interactive shell model (ISM) calculates M_{GT-3} reliably since this model is able to describe accurately low lying states of nuclei. We have therefore used the value of M_{GT-3} from the ISM to reconstruct a value for $g_{A,\text{eff}}$. However, this result should be taken cautiously. According to theoreticians working with shell models different from the ISM, the value of M_{GT-3} derived in ISM is not reliable.

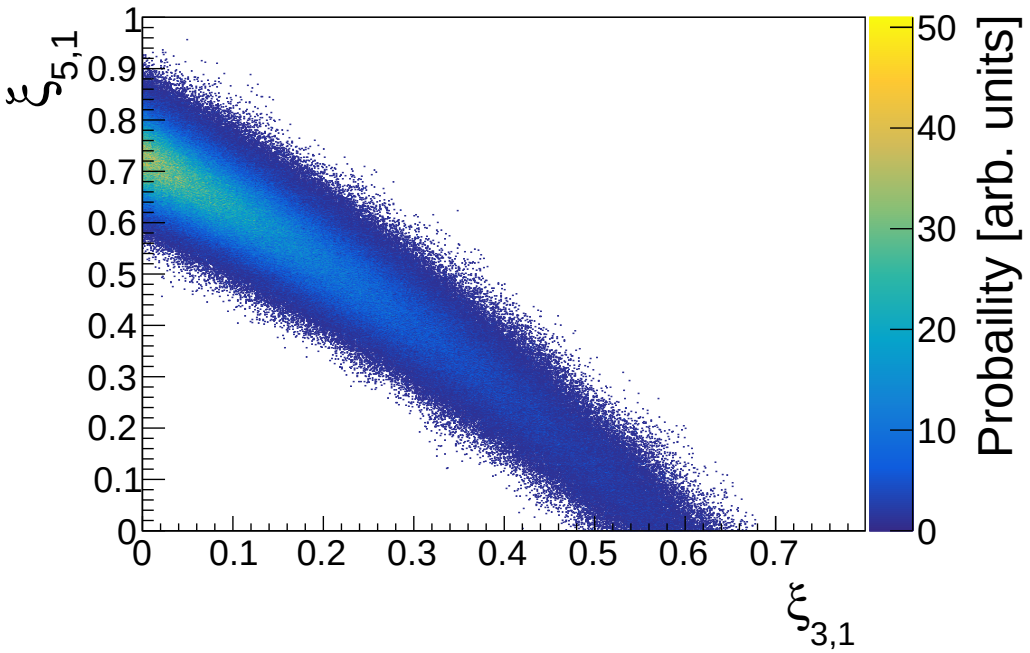

Figure 5.18: Two dimensional posterior distribution on ξ_{31} versus ξ_{51}. We observe a strong anticorrelation between both parameters.

We also extracted a value for $g_{A,\text{eff}}$ in the pn-QRPA model by sampling from the ξ_{31} distributions obtained in our fit. These two novel measurements of $g_{A,\text{eff}}$ are the first of their kind obtained from a spectral shape study of a $2\nu\beta\beta$ decay.

Article: C. Augier *et al* [CUPID-Mo coll.], Physical Review Letters 131, 162501 (2023)

Measurement of the $2\nu\beta\beta$ Decay Rate and Spectral Shape of ^{100}Mo from the CUPID-Mo Experiment

C. Augier,[1] A. S. Barabash,[2] F. Bellini,[3,4] G. Benato,[5,6] M. Beretta,[7] L. Bergé,[8] J. Billard,[1] Yu. A. Borovlev,[9] L. Cardani,[4] N. Casali,[4] A. Cazes,[1] E. Celi,[5,6] M. Chapellier,[8] D. Chiesa,[10,11] I. Dafinei,[4] F. A. Danevich,[12,13] M. De Jesus,[1] T. Dixon,[8,14,*] L. Dumoulin,[8] K. Eitel,[15] F. Ferri,[14] B. K. Fujikawa,[16] J. Gascon,[1] L. Gironi,[10,11] A. Giuliani,[8] V. D. Grigorieva,[9] M. Gros,[14] D. L. Helis,[14,5] H. Z. Huang,[17] R. Huang,[7] L. Imbert,[8] J. Johnston,[18] A. Juillard,[1] H. Khalife,[8] M. Kleifges,[19] V. V. Kobychev,[12] Yu. G. Kolomensky,[7,16] S. I. Konovalov,[20] J. Kotila,[21,22,23] P. Loaiza,[8] L. Ma,[17] E. P. Makarov,[9] P. de Marcillac,[8] R. Mariam,[8] L. Marini,[7,16,5] S. Marnieros,[8] X.-F. Navick,[14] C. Nones,[14] E. B. Norman,[7] E. Olivieri,[8] J. L. Ouellet,[18] L. Pagnanini,[6,5] L. Pattavina,[5,24] B. Paul,[14] M. Pavan,[10,11] H. Peng,[25] G. Pessina,[11] S. Pirro,[5] D. V. Poda,[8] O. G. Polischuk,[12,4] S. Pozzi,[11] E. Previtali,[10,11] Th. Redon,[8] A. Rojas,[26] S. Rozov,[27] V. Sanglard,[1] J. A. Scarpaci,[8] B. Schmidt,[14] Y. Shen,[17] V. N. Shlegel,[9] F. Šimkovic,[28,29] V. Singh,[7] C. Tomei,[4] V. I. Tretyak,[12,5] V. I. Umatov,[20] L. Vagneron,[1] M. Velázquez,[30] B. Ware,[31] B. Welliver,[7] L. Winslow,[18] M. Xue,[25] E. Yakushev,[27] M. Zarytskyy,[12] and A. S. Zolotarova[8]

(CUPID-Mo Collaboration)

[1]*Univ Lyon, Université Lyon 1, CNRS/IN2P3, IP2I-Lyon, F-69622 Villeurbanne, France*
[2]*National Research Centre "Kurchatov Institute," Kurchatov Complex of Theoretical and Experimental Physics, 117218 Moscow, Russia*
[3]*Dipartimento di Fisica, Sapienza Università di Roma, Piazzale Aldo Moro 2, I-00185 Rome, Italy*
[4]*INFN, Sezione di Roma, P.le Aldo Moro 2, I-00185 Rome, Italy*
[5]*INFN, Laboratori Nazionali del Gran Sasso, I-67100 Assergi (AQ), Italy*
[6]*INFN, Gran Sasso Science Institute, I-67100 L'Aquila, Italy*
[7]*University of California, Berkeley, California 94720, USA*
[8]*Université Paris-Saclay, CNRS/IN2P3, IJCLab, 91405 Orsay, France*
[9]*Nikolaev Institute of Inorganic Chemistry, 630090 Novosibirsk, Russia*
[10]*Dipartimento di Fisica, Università di Milano-Bicocca, I-20126 Milano, Italy*
[11]*INFN, Sezione di Milano-Bicocca, I-20126 Milano, Italy*
[12]*Institute for Nuclear Research of NASU, 03028 Kyiv, Ukraine*
[13]*INFN, Sezione di Roma Tor Vergata, Via della Ricerca Scientifica 1, I-00133 Rome, Italy*
[14]*IRFU, CEA, Université Paris-Saclay, F-91191 Gif-sur-Yvette, France*
[15]*Karlsruhe Institute of Technology, Institute for Astroparticle Physics, 76021 Karlsruhe, Germany*
[16]*Lawrence Berkeley National Laboratory, Berkeley, California 94720, USA*
[17]*Key Laboratory of Nuclear Physics and Ion-beam Application (MOE), Fudan University, Shanghai 200433, People's Republic of China*
[18]*Massachusetts Institute of Technology, Cambridge, Massachusetts 02139, USA*
[19]*Karlsruhe Institute of Technology, Institute for Data Processing and Electronics, 76021 Karlsruhe, Germany*
[20]*National Research Centre Kurchatov Institute, Institute of Theoretical and Experimental Physics, 117218 Moscow, Russia*
[21]*Department of Physics, University of Jyväskylä, P.O. Box 35, FI-40014 Jyväskylä, Finland*
[22]*Finnish Institute for Educational Research, University of Jyväskylä, P.O. Box 35, FI-40014 Jyvaäskylä, Finland*
[23]*Center for Theoretical Physics, Sloane Physics Laboratory, Yale University, New Haven, Connecticut 06520-8120, USA*
[24]*Physik Department, Technische Universität München, Garching D-85748, Germany*
[25]*Department of Modern Physics, University of Science and Technology of China, Hefei 230027, People's Republic of China*
[26]*LSM, Laboratoire Souterrain de Modane, 73500 Modane, France*
[27]*Laboratory of Nuclear Problems, JINR, 141980 Dubna, Moscow region, Russia*
[28]*Faculty of Mathematics, Physics and Informatics, Comenius University in Bratislava, 842 48 Bratislava, Slovakia*
[29]*Institute of Experimental and Applied Physics, Czech Technical University in Prague, 128 00 Prague, Czech Republic*
[30]*Université Grenoble Alpes, CNRS, Grenoble INP, SIMAP, 38420 Saint Martin d'Hères, France*
[31]*John de Laeter Centre for Isotope Research, GPO Box U 1987, Curtin University, Bentley, Western Australia, Australia*

(Received 26 July 2023; revised 29 August 2023; accepted 21 September 2023; published 18 October 2023)

Neutrinoless double beta decay ($0\nu\beta\beta$) is a yet unobserved nuclear process that would demonstrate Lepton number violation, a clear evidence of beyond standard model physics. The process two neutrino double beta decay ($2\nu\beta\beta$) is allowed by the standard model and has been measured in numerous experiments. In this Letter, we report a measurement of $2\nu\beta\beta$ decay half-life of ^{100}Mo to the ground state of ^{100}Ru of $[7.07 \pm 0.02(\text{stat}) \pm 0.11(\text{syst})] \times 10^{18}$ yr by the CUPID-Mo experiment. With a relative precision of $\pm 1.6\%$ this is the most precise measurement to date of a $2\nu\beta\beta$ decay rate in ^{100}Mo. In addition, we constrain higher-order corrections to the spectral shape, which provides complementary nuclear structure information. We report a novel measurement of the shape factor $\xi_{3,1} = 0.45 \pm 0.03(\text{stat}) \pm 0.05(\text{syst})$ based on a constraint on the ratio of higher-order terms from theory, which can be reliably calculated. This is compared to theoretical predictions for different nuclear models. We also extract the first value for the effective axial vector coupling constant obtained from a spectral shape study of $2\nu\beta\beta$ decay.

DOI: 10.1103/PhysRevLett.131.162501

For more than 20 years it has been known that neutrinos have mass via measurements of neutrino oscillations [1,2]. This raises the question of the nature of this mass. If the neutrino is its own antiparticle, a *Majorana* particle, then a decay mode of some nuclei would become possible, neutrinoless double beta decay ($0\nu\beta\beta$) (see reviews [3–5]). This decay could be observed in nuclei for which single beta decay is energetically disallowed (or disfavored by angular momentum). Two neutrons would be transformed into two protons, with the emission of only two electrons. The observation of this decay would have profound consequences for particle physics by showing that the Lepton number is not a fundamental symmetry of nature and providing clear evidence of beyond standard model physics.

The measurement of the decay rate could also provide a method to measure the effective neutrino mass [6]. Under the light Majorana neutrino exchange mechanism the decay rate would be related to the effective Majorana mass $\langle m_{\beta\beta} \rangle$ by

$$1/T^{0\nu}_{1/2} = G_{0\nu} \cdot g_A^4 \cdot |M_{0\nu}|^2 \cdot \langle m_{\beta\beta} \rangle^2 / m_e^2, \tag{1}$$

where $G_{0\nu}$ is the phase space factor, $M_{0\nu}$ the nuclear matrix element (NME), g_A the effective axial-vector coupling constant, and m_e the electron mass. While $G_{0\nu}$ can be calculated almost exactly [7], the NME is the result of complex many-body nuclear physics calculations (see the review [8]) and is only known to a factor of a few. To interpret the results of next-generation experiments these calculations must be improved. In addition, it has been observed that nuclear models often overpredict the decay rate of β^- and $2\nu\beta\beta$. To account for this g_A can be replaced with an effective value $g_{A,\text{eff}}$ [9–11]. Therefore there is still a possibility the $0\nu\beta\beta$ decay rate could be much lower than expected for an unrenormalized value of g_A (1.27). This would have significant impact on the discovery probability of next-generation experiments [12,13]. To constrain this possibility new measurements are needed.

Two neutrino double beta decay ($2\nu\beta\beta$) conserves Lepton number and is allowed within the standard model. It has been observed in a number of nuclei [14]. The decay rate of $2\nu\beta\beta$ decay can be described to a good approximation as

$$1/T^{2\nu}_{1/2} = G_{2\nu} \cdot g_A^4 \cdot |M_{2\nu}|^2, \tag{2}$$

where $G_{2\nu}$ is the phase space factor, $M_{2\nu}$ is the NME. Since $0\nu\beta\beta$ and $2\nu\beta\beta$ share the same initial and final nuclear states, an accurate prediction of $T^{2\nu}_{1/2}$ and therefore an accurate description of the nuclear structure, is a necessary condition to obtain reliable estimates of $M_{0\nu}$. These measurements are often used to tune the parameters of the nuclear models. However, they cannot alone answer questions about the value of $g_{A,\text{eff}}$ since only the product $M_{2\nu} \times g^2_{A,\text{eff}}$ is measured.

The $2\nu\beta\beta$ decay spectrum is typically described using two approximations: the single and higher state dominance hypotheses (SSD/HSD) [15]. In these approximations, the decay is supposed to proceed via a single intermediate 1^+ state. For the HSD model this state is an average higher energy state from the region of the Gamow-Teller resonance, while for SSD it is the lowest energy 1^+ state.

The description of the $2\nu\beta\beta$ decay spectrum was improved in [16,17]. In this approach, a Taylor expansion is performed in terms of the Lepton energies. The differential decay rate relates to phase space factors and NMEs as

$$\frac{d\Gamma}{dE} = g^4_{A,\text{eff}} |M_{GT-1}|^2 \left(\frac{dG_0}{dE} + \xi_{3,1} \frac{dG_2}{dE} + \frac{1}{3}\xi^2_{3,1} \frac{dG_{22}}{dE} + \left(\frac{1}{3}\xi^2_{3,1} + \xi_{5,1} \right) \frac{dG_4}{dE} \right). \tag{3}$$

Here, G_0, G_2, G_{22}, G_4 are the phase space factors for different terms in the Taylor expansion. $\xi_{3,1} = M_{GT-3}/M_{GT-1}$ and $\xi_{5,1} = M_{GT-5}/M_{GT-1}$ are ratios of NMEs. By fitting the energy distribution of electrons to

this model, constraints on $\xi_{3,1}, \xi_{5,1}$ can be obtained that can be compared to theoretical predictions. M_{GT-3} and M_{GT-5} are expected to be dominated by contributions from lower-lying states due to the higher power of the energy denominators so measurement of $\xi_{3,1}, \xi_{5,1}$ provide complementary nuclear structure information to the half-life. Within this model the HSD spectrum can be recovered by fixing $\xi_{3,1}, \xi_{5,1}$ to zero, and the SSD approximation can be used to predict nonzero $\xi_{3,1}, \xi_{5,1}$ as in [16]. ξ values larger than the SSD values would indicate mutual cancellation between lower and higher lying states.

As described in [16], a measurement of $\xi_{3,1}$ and the half-life can be used to extract a value for $g_{A,\mathrm{eff}}$ of

$$g^4_{A,\mathrm{eff}} = \frac{T^{-1}_{1/2} \times \xi^2_{3,1}}{M^2_{GT-3} G}, \tag{4}$$

where $G = G_0 + \xi_{3,1} G_2 + \xi^2_{3,1} G_{22}/3 + (\xi^2_{3,1}/3 + \xi_{5,1}) G_4$. M_{GT-3} can be computed reliably within the interacting shell model (ISM), which describes accurately low lying states of nuclei.

So far the analysis to extract the ξ factors has only been performed by the KamLAND-Zen experiment [18], which established an upper bound on $\xi_{3,1}$ in ^{136}Xe decays, which is still compatible with both the ISM and pn-QRPA calculations.

We compute $2\nu\beta\beta$ NMEs M_{GT-1}, M_{GT-3}, and M_{GT-5} within the proton-neutron quasiparticle random-phase approximation (pn-QRPA) [19,20] and described in more detail in the Supplemental Material [21]. These calculations are performed for a range of $g_{A,\mathrm{eff}}$ values. We compute the phase space factors G_0, G_2, G_4, G_{22} considering Dirac wave functions with finite nuclear size and electron screening as in [7].

The experimental signature of $2\nu\beta\beta$ decay is a continuous spectrum in the summed energies of the electrons. Differentiation of the signal from background is more challenging than for $0\nu\beta\beta$ decay: the decay rate must be extracted from a fit to the full spectrum using detailed simulations of the various contributions to the experimental background (see, for example, [22–25]).

Therefore, a very low background is imperative to make a precise measurement. Scintillating cryogenic calorimeters provide a technique to reach very low background rates [26–28]. In particular, a scintillation light signal in coincidence with a heat signal in the calorimeter can be used to remove α particle backgrounds [28–31].

In this Letter, we describe a measurement of the $2\nu\beta\beta$ decay rate and spectral shape of ^{100}Mo using the CUPID-Mo experiment, a demonstrator for the next-generation $0\nu\beta\beta$ decay experiment CUPID [32]. A detailed description of the experiment can be found in [33]. It consisted of an array of 20 lithium molybdate (LMO) cryogenic calorimeters, enriched in ^{100}Mo ($96.6 \pm 0.2\%$ isotope abundance) each of around 200 g mass. In addition, 20 germanium light detectors (LD), also operated as cryogenic calorimeters, were employed to readout the scintillation light signal used for particle identification to remove the α particle background. An individual module of CUPID-Mo consisted of an LMO crystal attached to a copper holder and a Ge LD. Both the LMO and LD signals were read out using neutron transmutation doped germanium thermistors [34]. These modules were then arranged into five towers of four LMOs each and installed in the EDELWEISS cryostat [35] at the Laboratoire Soutterain de Modane, France. It collected a total exposure of 1.48 kg × yr of ^{100}Mo between 2019 and 2020. The scintillation light signal allowed a complete rejection of α particles, while an excellent energy resolution of 7.7 ± 0.4 keV FWHM was measured at 3034 keV [36]. This performance lead to a limit on $0\nu\beta\beta$ in ^{100}Mo of $T^{0\nu}_{1/2} > 1.8 \times 10^{24}$ yr (90% credible interval) [36].

For this analysis we use the full data collected by CUPID-Mo. A detailed description of the data processing is given in [36] and was also used for [37,38]. An optimal filter based analysis chain [39], which maximizes the signal to noise ratio, is used to select physics events and estimate pulse amplitudes. Spurious events, such as pileup or spikes induced by electronics, are removed using a principal component analysis based pulse shape cut [36,40], normalized to ensure an energy independent efficiency. Because of the relatively short range of electrons in LMO, both $0\nu\beta\beta$ and $2\nu\beta\beta$ to ground states are likely to deposit energy in just a single LMO detector. However, background events induced by γ quanta are more likely to deposit energy in multiple crystals. As such we define the "multiplicity" ($\mathcal{M}$) of an event as the number of LMO detectors with a pulse above the 40 keV energy threshold within a ± 10 ms window. In addition, muon induced events are excluded using a dedicated muon veto system [41]. We select β, γ-like events using the scintillation light signal as described in detail in [36]. We also remove events with a trigger in one LD with high ^{60}Co contamination as described in [37,38]. Multiplicity one γ/β ($\mathcal{M}_{1,\gamma/\beta}$) events are used to extract the signal rates while $\mathcal{M}_2$ are used to constrain the γ background. We also extract the spectra at high energy without any α rejection, this dataset ($\mathcal{M}_{1,\alpha}$) is used to constrain the radioactivity of the LMO crystals and other nearby components.

The energy resolution and bias in the energy scale are measured using γ lines. The efficiency of all selection cuts has been estimated as $88.9 \pm 1.1\%$ for $\mathcal{M}_{1,\gamma/\beta}$ [36,38]. No evidence of energy dependence was found, over the range of the fit, and our cuts are normalized to have an energy-independent efficiency.

To extract the rate of $2\nu\beta\beta$ decay we construct a model of the data described in detail in [38]. We simulate using Geant4 [42] the $2\nu\beta\beta$ signal, using both the SSD and HSD models parametrized from [7] and the contributions to the

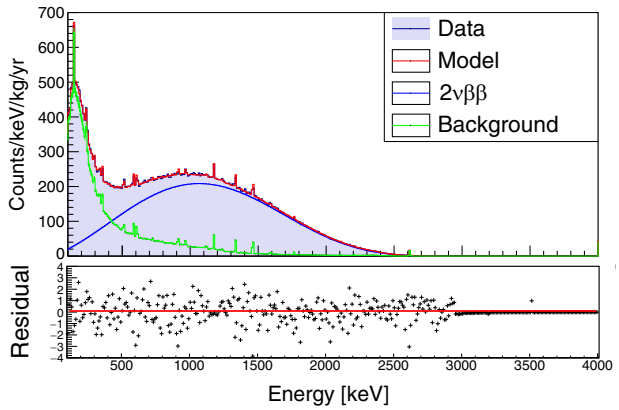

FIG. 1. Fit of the $\mathcal{M}_{1,\gamma/\beta}$ spectrum showing the main contributions to the model and the residuals defined as $(\text{data}-\text{fit})/\sqrt{\text{data}}$. The model describes well the experimental data and the spectrum above ~500 keV is dominated by $2\nu\beta\beta$ events.

improved $2\nu\beta\beta$ model from Eq. (3) [16]. We also simulate radioactive contaminations in the various components of the experimental setup. These simulations are then convolved with a detector response model consisting of the energy resolution of the detectors, energy threshold, coincidences, and dead times of the detectors.

We use a Bayesian analysis based on JAGS [43,44] to fit our three experimental spectra $(\mathcal{M}_{1,\gamma/\beta}, \mathcal{M}_{1,\alpha}, \mathcal{M}_2)$ to a sum of Monte Carlo (MC) simulations. The details of the choices of the model components are given in [38]. The fit to the $\mathcal{M}_{1,\gamma/\beta}$ spectrum uses a range of 100–4000 keV. A variable binning is used so that at minimum 15 keV bins are used in the continuum region and then bins are combined so at least 15 events are in each bin. Each γ or α peak is placed in one bin to avoid the systematic effect of the peak line shape. We show the $\mathcal{M}_{1,\gamma/\beta}$ fit in Fig. 1. We call this fit our "reference fit": we see that this model is able to describe all the features of the experimental data, and that the data are dominated by $2\nu\beta\beta$ decay events. While in [38] the SSD model of $2\nu\beta\beta$ was used by default, for this work we instead use the improved $2\nu\beta\beta$ model, and consider SSD as a cross-check. By using the improved model, which allows the spectral shape to vary during the fit, we marginalize over the theoretical uncertainty in the spectral shape.

We study the consistency between our model and data using pseudoexperiments. We generate from the best fit model a set of 1000 pseudoexperiments, and for each we perform the background model fit and extract $-\log(\mathcal{L})$. The value obtained for the $\mathcal{M}_{1,\gamma/\beta}$ data is consistent with the expected distribution. In particular, we extract a p value, or the probability of observing equal or larger fluctuations of 0.54.

From the background model fit we extract the $2\nu\beta\beta$ decay rate. We consider systematic uncertainties related to the number of reconstructed events and the efficiency and isotopic abundance conversion factors. We have performed a series of tests varying the assumptions of our background model to assess the dependence of $T_{1/2}$ on these choices. For each test a probability distribution is assumed for the systematic uncertainty based on the change in the best fit value with respect to our reference fit. We then compute a convolution of these distributions and the posterior distribution from the fit to obtain the posterior distribution considering all systematic uncertainties. This can be considered a generalization of adding in quadrature to non-Gaussian uncertainties.

First we perform tests to check the dependence of our results on the γ radioactivity source location. We remove far sources of Th/U radioactivity leading to a slightly lower $2\nu\beta\beta$ rate (−0.83%) and then close (10 mK) sources of Th/U radioactivity leading to a higher rate (+0.22%). In principle, this uncertainty is already marginalized over in our analysis. However, our fit favors far sources of radioactivity, possibly due to some other effects such as pure β decays, so we take a conservative approach considering an uncertainty of ±0.83% from the first test. This is assigned a Gaussian distribution to account for the possibility of even further sources than those included in our model.

Anthropogenic β^- decays could contribute to our background. In our model we include a source of $^{90}\text{Sr}+{}^{90}\text{Y}$, consisting of two pure β^- decays with Q values 546, 2276 keV and ~60 h delay. This is one of the only anthropogenic contaminations with a large enough Q value to correlate with $2\nu\beta\beta$ decay and a relatively long half-life. In our model the activity is constrained as 179^{+36}_{-32} μBq/kg. Since the convergence of this parameter is driven by events at low energy that could have several origins we repeat the fit without this contribution. We obtain a half-life value +1.0% higher than the reference and we assign a uniform probability distribution between the reference and this fit.

We repeat the fit removing any contributions where the smallest 68% interval contains zero activity, which we call the "minimal model." In our analysis, all the contributions are assigned non-negative uniform priors; therefore, a large number of parameters could bias the fit leading to a smaller $2\nu\beta\beta$ rate. We find a small shift of +0.24% in the $2\nu\beta\beta$ decay rate for this fit. We assign a Gaussian distribution with 0.24% uncertainty for this systematic uncertainty. We also check that our fit is not biased using our set of pseudoexperiments. The distribution of obtained $T_{1/2}$ is consistent with the fit to data.

We perform fits varying the energy scale by ∓ 1 keV resulting in a $2\nu\beta\beta$ decay rate shifted by $^{+0.11}_{-0.16}$%, which we assign an asymmetric-Gaussian distribution.

Our reference fit uses a variable binning described in [38]. We repeat the fit using fixed binning of 1, 2, 10, 20, and 30 keV. The largest effect is for a binning of 2 keV where the rate is reduced by −0.37%. We take a conservative approach considering a Gaussian distribution with ±0.37% standard deviation.

TABLE I. Systematic uncertainties in the determination of the $2\nu\beta\beta$ decay rate and $\xi_{3,1}$. All uncertainties are assigned either a Gaussian or asymmetric-Gaussian (for asymmetric uncertainties) posterior distribution with the exception of the $^{90}\mathrm{Sr} + {}^{90}\mathrm{Y}$, where we assign a uniform distribution.

Systematic test	Uncertainties $T_{1/2}$ [%]	Uncertainties $\xi_{3,1}$ [%]
Source location	0.83	0.9
$^{90}\mathrm{Sr} + {}^{90}\mathrm{Y}$	$+1.0^{a}$	-4.9^{a}
Minimal model	0.24	7.7
Binning	0.37	1.4
Energy bias	$^{+0.11}_{-0.16}$	$^{+3.5}_{-3.7}$
Bremsstrahlung	$^{+0.13}_{-0.22}$	$^{+6.0}_{-6.8}$
MC statistics	0.11	1.4
Efficiency	1.2	...
Isotopic abundance	0.2	...

[a]Uniform distribution.

To assess the dependence on the accuracy of the MC simulations we generate simulations of $2\nu\beta\beta$ decay where we vary the Bremsstrahlung cross section by $\pm 10\%$. These lead to $^{+0.13}_{-0.22}\%$ change in the $2\nu\beta\beta$ rate, to which we assign an asymmetric-Gaussian distribution.

To account for the statistical uncertainty in the MC simulations we perform a fit adding nuisance parameters to the model as is done in [22]. This leads to a -0.11% smaller $2\nu\beta\beta$ rate, which we consider a systematic with a Gaussian distribution.

The final systematic uncertainties are on selection efficiency and ^{100}Mo abundance, which are 1.2% and 0.2%, respectively, and are assigned Gaussian distributions. These systematic uncertainties are summarized in Table I.

Computing the convolution of all systematic uncertainties in Table I and converting to the decay rate we compute the posterior distribution of $T^{-1}_{1/2}$ (see Ref. [21]) for both the statistical only uncertainty and the combined uncertainty. From the central 68% credible interval we extract a measurement of

$$T^{2\nu}_{1/2} = [7.07 \pm 0.02(\mathrm{stat}) \pm 0.11(\mathrm{syst})] \times 10^{18}\ \mathrm{yr}. \quad (5)$$

With a relative uncertainty of $\pm 1.6\%$ this is one of the most precise determinations of a $2\nu\beta\beta$ decay half-life. The half-life is in agreement with our previous result obtained with a much smaller exposure [24], the value from NEMO-3 [45] and one obtained using the SSD $2\nu\beta\beta$ spectral shape model.

Next, we extract the values of the shape factors from the fit. We find a clear contribution from higher-order terms with a mild preference for a contribution from $\xi_{5,1}$ instead of $\xi_{3,1}$ (see more details in Supplemental Material [21]). However, the parameters $\xi_{3,1}$ and $\xi_{5,1}$ are strongly anti-correlated with $\rho = -0.92$. Thus, the fit is not sensitive to whether this contribution originates from $\xi_{3,1}$ or $\xi_{5,1}$.

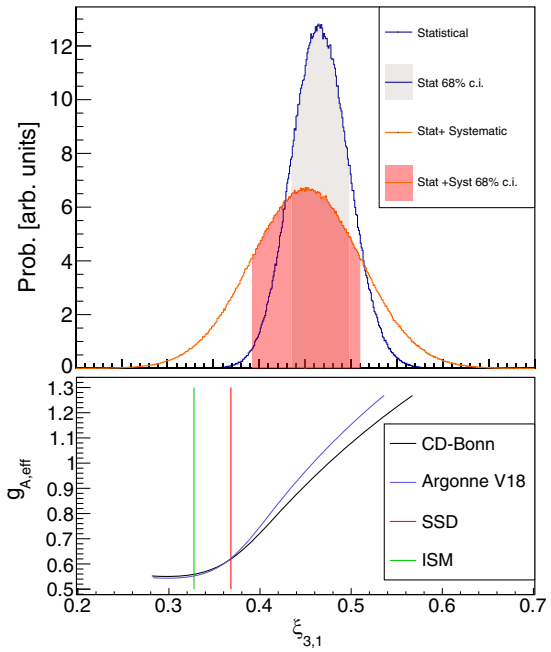

FIG. 2. Posterior distribution of $\xi_{3,1}$ both with and without convolution with the systematic uncertainties (upper figure). In the lower panel we compare to the pn-QRPA, ISM and SSD theoretical values as a function of $g_{A,\mathrm{eff}}$ for two potentials (CD-Bonn and Argonne V18; see Supplemental Material [21] for more details).

However, within nuclear structure calculations the value of $\xi_{5,1}/\xi_{3,1}$ can be calculated reliably since M_{GT-3} and M_{GT-5} depend on contributions from low lying states. The value of $\xi_{5,1}/\xi_{3,1}$ within pn-QRPA is 0.364–0.368 depending on $g_{A,\mathrm{eff}}$ and the nuclear potential. Within the SSD hypothesis the value is 0.367 [16] and within the ISM it is 0.349 [46,47]. To reduce the degeneracy in our model we perform a fit with a Gaussian prior on $\xi_{5,1}/\xi_{3,1}$ with a mean of the SSD prediction and a conservative 5% uncertainty.

From this fit we extract the value of $\xi_{3,1}$ to compare to theoretical predictions. We consider the same systematic uncertainties as for the half-life (also shown in Table I). The largest effects are found to be from the MC bremsstrahlung cross section and the choice of parameters of the model. The posterior distribution of this observable both before and after convolution with the systematics is shown in Fig. 2. We extract a measurement:

$$\xi_{3,1} = 0.45 \pm 0.03(\mathrm{stat}) \pm 0.05(\mathrm{syst}). \quad (6)$$

We compare our measurement of $\xi_{3,1}$ to pn-QRPA theoretical predictions in the lower panel of Fig. 2. Within pn-QRPA the g_{pp} parameter (the strength of the particle-particle interaction) is tuned using our measurement of the half-life for each $g_{A,\mathrm{eff}}$. Since the calculated values of $\xi_{3,1}$ depend on $g_{A,\mathrm{eff}}$, our measurement of $\xi_{3,1}$

provides complementary information on $g_{A,\mathrm{eff}}$. We find the experimental value is incompatible ($\sim 8\sigma$) with the prediction of the HSD hypothesis of $\xi_{3,1} = \xi_{5,1} = 0$, somewhat incompatible with that from the ISM ($\sim 2.1\sigma$) but mostly compatible with that from the SSD hypothesis ($\sim 1.4\sigma$) and the pn-QRPA predictions if the value of $g_{A,\mathrm{eff}}$ is moderately quenched (> 0.8) or unquenched. We encourage computation of $\xi_{3,1}$ and $\xi_{5,1}$ in additional theoretical frameworks such as the interacting boson model [48]. To extract a value for $g_{A,\mathrm{eff}}$ within the pn-QRPA framework, we sample from the distribution of $\xi_{3,1}$ from our fit and for each sample we extract the corresponding $g_{A,\mathrm{eff}}$ values. Assigning equal weights to the CD-Bonn and Argonne V-18 nuclear potentials we extract a posterior distribution on $g_{A,\mathrm{eff}}$ and thus we extract a value:

$$g_{A,\mathrm{eff}}(\text{pn-QRPA}) = 1.0 \pm 0.1(\mathrm{stat}) \pm 0.2(\mathrm{syst}). \quad (7)$$

As mentioned previously an analysis of $\xi_{3,1}$ and the half-life can be used to extract a measurement of $g_{A,\mathrm{eff}}$ if M_{GT-3} is known [see Eq. (4)]. Using the value of M_{GT-3} from the ISM [46,47] and our fit we reconstruct

$$g_{A,\mathrm{eff}}(\mathrm{ISM}) = 1.11 \pm 0.03(\mathrm{stat}) \pm 0.05(\mathrm{syst}). \quad (8)$$

The statistical uncertainty is obtained by sampling from the Markov chain; therefore, combining the uncertainties on $T_{1/2}$ and $\xi_{3,1}$, the systematic uncertainty is obtained from the same tests as previously considered. This is the first measurement of $g_{A,\mathrm{eff}}$ from a spectral shape study of $2\nu\beta\beta$ decay.

In this Letter, we have reported a measurement of the $2\nu\beta\beta$ decay half-life of ^{100}Mo. Utilizing excellent background rejection, a very clean spectrum is obtained that allowed us to obtain the most precise ever measurement of a $2\nu\beta\beta$ decay rate in this isotope. Special attention was paid to the systematic uncertainties affecting the result, particularly to the source location, model choices, and MC accuracy.

In addition, we obtained a first of its kind measurement of a novel nuclear structure observable $\xi_{3,1}$ based on an improved description of the $2\nu\beta\beta$ decay process. The value of this observable is found to be incompatible with an HSD prediction, mildly incompatible with predictions from the ISM, but compatible with pn-QRPA predictions and a moderately quenched or unquenched value of $g_{A,\mathrm{eff}}$. Finally, we report two novel measurements of $g_{A,\mathrm{eff}}$, the first of their kind obtained from a spectral shape study of a $2\nu\beta\beta$ decay.

This work has been performed in the framework of the CUPID-1 and P2IO LabEx programs, funded by the Agence Nationale de la Recherche (ANR, France). F. A. D., V. V. K., V. I. T., and M. M. Z. were supported in part by the National Research Foundation of Ukraine. A. S. B., S. I. K., I. M. M., V. N. S., and V. I. U. were supported by the Russian Science Foundation. J. K. is supported by Academy of Finland. F. D. was partly supported by the Slovak Research and Development Agency. Additionally the work is supported by the Istituto Nazionale di Fisica Nucleare (INFN), by the US Department of Energy (DOE) Office of Science. This work makes use of the *Diana* data analysis software and the background model based on JAGS, developed by the CUORICINO, CUORE, LUCIFER, and CUPID-0 collaborations.

*Corresponding author: toby.dixon@ijclab.in2p3.fr

[1] Y. Fukuda *et al.* (Super-Kamiokande Collaboration), Phys. Rev. Lett. **81**, 1562 (1998).
[2] Q. R. Ahmad *et al.*, Phys. Rev. Lett. **89**, 011301 (2002).
[3] S. Dell'Oro, S. Marcocci, M. Viel, and F. Vissani, Adv. High Energy Phys. **2016**, 2162659 (2016).
[4] M. Agostini, G. Benato, J. A. Detwiler, J. Menéndez, and F. Vissani, Rev. Mod. Phys. **95**, 025002 (2023).
[5] M. J. Dolinski, A. W. Poon, and W. Rodejohann, Annu. Rev. Nucl. Part. Sci. **69**, 219 (2019).
[6] G. Benato, Eur. Phys. J. C **75**, 563 (2015).
[7] J. Kotila and F. Iachello, Phys. Rev. C **85**, 034316 (2012).
[8] J. Engel and J. Menéndez, Rep. Prog. Phys. **80**, 046301 (2017).
[9] J. T. Suhonen, Front. Phys. **5**, 55 (2017).
[10] H. Ejiri, J. Suhonen, and K. Zuber, Phys. Rep. **797**, 1 (2019).
[11] G. Martínez-Pinedo, A. Poves, E. Caurier, and A. P. Zuker, Phys. Rev. C **53**, R2602 (1996).
[12] M. Agostini, G. Benato, and J. A. Detwiler, Phys. Rev. D **96**, 053001 (2017).
[13] M. Ettengruber, M. Agostini, A. Caldwell, P. Eller, and O. Schulz, Phys. Rev. D **106**, 073004 (2022).
[14] A. Barabash, Universe **6**, 159 (2020).
[15] F. Šimkovic, P. Domin, and S. V. Semenov, J. Phys. G **27**, 2233 (2001).
[16] F. Šimkovic, R. Dvornický, D. Stefánik, and A. Faessler, Phys. Rev. C **97**, 034315 (2018).
[17] O. Niţescu, R. Dvornický, S. Stoica, and F. Šimkovic, Universe **7**, 147 (2021).
[18] A. Gando *et al.* (KamLAND-Zen Collaboration), Phys. Rev. Lett. **122**, 192501 (2019).
[19] F. Šimkovic, V. Rodin, A. Faessler, and P. Vogel, Phys. Rev. C **87**, 045501 (2013).
[20] F. Šimkovic, L. Pacearescu, and A. Faessler, Nucl. Phys. **A733**, 321 (2004).
[21] See Supplemental Material at http://link.aps.org/supplemental/10.1103/PhysRevLett.131.162501 for a brief description of the proton-neutron quasiparticle random-phase approximation calculations of nuclear matrix elements and the posterior distributions from the fit.
[22] O. Azzolini *et al.* (CUPID-0 Collaboration), Eur. Phys. J. C **79**, 583 (2019).
[23] D. Q. Adams *et al.* (CUORE Collaboration), Phys. Rev. Lett. **126**, 171801 (2021).
[24] E. Armengaud *et al.*, Eur. Phys. J. C **80**, 674 (2020).
[25] M. Agostini *et al.* (GERDA Collaboration), J. High Energy Phys. 03 (2020) 139.

[26] S. Pirro, J. W. Beeman, S. Capelli, M. Pavan, E. Previtali, and P. Gorla, Phys. At. Nucl. **69**, 2109 (2006).
[27] D. Poda, Physics **3**, 473 (2021).
[28] E. Armengaud *et al.*, Eur. Phys. J. C **77**, 785 (2017).
[29] L. Cardani *et al.*, J. Instrum. **8**, P10002 (2013).
[30] O. Azzolini *et al.* (CUPID-0 Collaboration), Eur. Phys. J. C **78**, 428 (2018).
[31] J. W. Beeman *et al.* (LUCIFER Collaboration), Eur. Phys. J. C **75**, 591 (2015).
[32] W. R. Armstrong *et al.* (CUPID Collaboration), arXiv:1907.09376.
[33] E. Armengaud *et al.*, Eur. Phys. J. C **80**, 44 (2020).
[34] E. E. Haller, N. P. Palaio, M. Rodder, W. L. Hansen, and E. Kreysa, in *Neutron Transmutation Doping of Semiconductor Materials*, edited by R. D. Larrabee (Springer US, Boston, MA, 1984), pp. 21–36.
[35] E. Armengaud *et al.* (EDELWEISS Collaboration), J. Instrum. **12**, P08010 (2017).
[36] C. Augier *et al.*, Eur. Phys. J. C **82**, 1033 (2022).
[37] C. Augier *et al.* (CUPID-Mo Collaboration), Phys. Rev. C **107**, 025503 (2023).
[38] C. Augier *et al.* (CUPID-Mo Collaboration), Eur. Phys. J. C **83**, 675 (2023).
[39] E. Gatti and P. F. Manfredi, Riv. Nuovo Cimento **9N1**, 1 (1986).
[40] R. Huang *et al.* (CUPID-Mo Collaboration), J. Instrum. **16**, P03032 (2021).
[41] B. Schmidt *et al.* (EDELWEISS Collaboration), Astropart. Phys. **44**, 28 (2013).
[42] J. Allison *et al.*, Nucl. Instrum. Methods Phys. Res., Sect. A **835**, 186 (2016).
[43] M. Plummer, in *Proceedings of the 3rd International Workshop on Distributed Statistical Computing (DSC 2003)* (DSC proceedings, Vienna, 2003), p. 124.
[44] M. Plummer, JAGS version 3.3.0 user manual (2012).
[45] R. Arnold *et al.* (NEMO-3 Collaboration), Eur. Phys. J. C **79**, 440 (2019).
[46] L. Coraggio, N. Itaco, G. De Gregorio, A. Gargano, R. Mancino, and F. Nowacki, Phys. Rev. C **105**, 034312 (2022).
[47] L. Coraggio and G. De Gregorio (private communication).
[48] K. Nomura, Phys. Rev. C **105**, 044301 (2022).

Chapter 6

CUPID, the future bolometric $0\nu\beta\beta$ decay experiment

Te convido a creerme cuando digo futuro

Cuando digo futuro, Causas y Azares, Silvio Rodriguez

CUPID (CUORE Update with Particle IDentification) is a next generation experiment to search for neutrinoless double beta decay with scintillating bolometers. CUPID will exploit the existing CUORE [53] cryogenic infrastructure at the Laboratori Nazionali del Gran Sasso, in Italy, replacing the CUORE detectors by a new generation of scintillating bolometers. CUORE is at present the largest $0\nu\beta\beta$ bolometric detector. It is based on a pure bolometric technique, via the detection of the heat deposited in a particle interaction with the detection crystal. CUPID will explore the inverted mass ordering region thanks to a dramatic background improvement with respect to CUORE. Thanks to scintillating bolometers, with simultaneous readout of heat and light, CUPID will reject the surface α background that currently limits the CUORE sensitivity. The double beta isotope in CUPID is ^{100}Mo, embedded in scintillating $Li_2{}^{100}MoO_4$ crystals. One of the key features of the CUPID program is that the Q-value of ^{100}Mo (3034 keV) is higher than 2615 keV, implying a signal located outside the bulk of gamma natural radioactivity (the Q-value of ^{130}Te, the CUORE isotope, is 2526 keV). Thanks to the scintillating bolometer technique, the CUPID collaboration aims at reducing the background down to the 10^{-4} counts/(keV kg y) level, thus, achieving a sensitivity for discovery of neutrinoless double beta decay of $T_{1/2} > 10^{27}$ years and $m_{\beta\beta} < 12 - 20$ meV.

6.1 The CUPID Detector

The CUPID bolometric detectors will be placed inside the CUORE cryostat, a large dilution refrigerator able to cool down one ton of detectors below 10 mK, specially designed to ensure low-noise and low-radioactivity [114]. The CUORE cryostat consits of six nested vessels, with the innermost containing the experimental volume of about 1 m^3. Figure 6.1 shows a scheme of the CUORE cryostat [139]. The different stages, from outside to inside, are at decreasing temperatures of about 300 K, 40 K, 4 K, 600 mK, 50 mK, and 10 mK. Inside the 4-K vessel, two lead shields protect the detectors from external radioactivity sources. The internal lateral lead shield stands in between the 4-K and the 600-mK stage, while the top lead is positioned

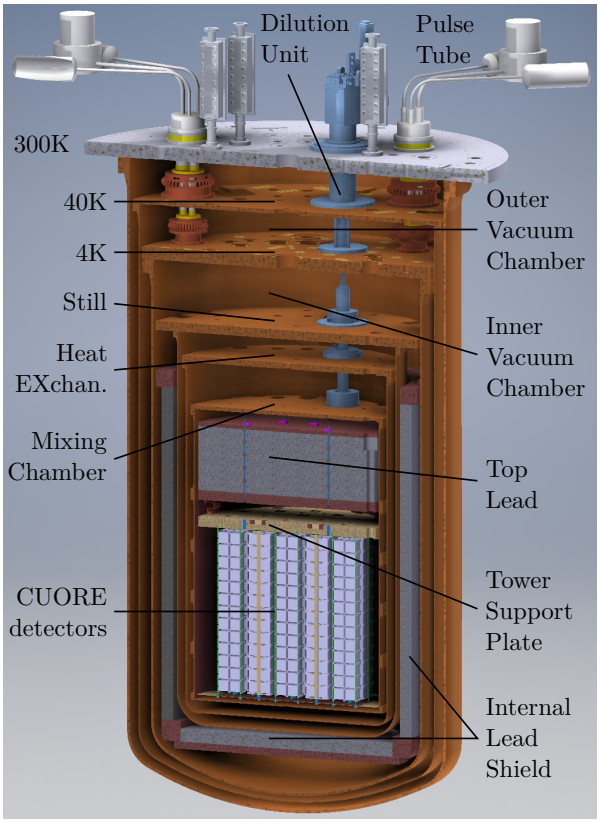

Figure 6.1: The CUORE/CUPID cryostat with the different thermal stages, the vacuum chambers, the cooling elements, the lead shields, and the detectors.

below the 10-mK plate. The detectors are attached to the Tower Support Plate placed right below the top lead shield.

The basic components of the CUPID detection system are the $Li_2{}^{100}MoO_4$ crystals coupled to thermal sensors, NTD, which reads the heat signal. The top and bottom of the crystals are facing the light detectors fabricated from Ge wafers, also instrumented with NTDs to read the light signal. Figure 6.2 shows a CUPID basic module. The crystals and the light detectors are supported by PTFE parts and a copper structure, with special care to minimize mechanical vibrations affecting the light detectors. In the baseline structure the crystals will be mounted on towers with 14 floors with 2 crystals per floor to maximize space occupancy (Fig. 6.3). This geometry allows to arrange the crystals in tightly-packed towers and to minimize the amount of passive material between crystals, to help to achieve the target background level of 10^{-4} counts/(keV kg y).

A first prototype tower was cooled down in July–October 2022 in the CUORICINO cryostat at LNGS. We could validate the assembly procedures and the thermal scheme. The light detectors [140] performances were affected by a large noise, whose origin is still under investigation.

The main bolometer crystals in CUPID will be grown from $Li_2{}^{100}MoO_4$ with ^{100}Mo enriched to $\geq 95\%$. The crystals will be cubic, with 45 x 45 x 45 mm^3 size, corresponding to a mass of ~ 280 g each. We selected this crystal volume to keep the pile-up of $2\nu\beta\beta$ decay of ^{100}Mo at a level compatible with the background goal.

The light detectors will be fabricated using high-purity Ge wafers, instrumented with NTD-Ge thermal sensors. This type of photon detectors provide a 99.9% rejection of α events

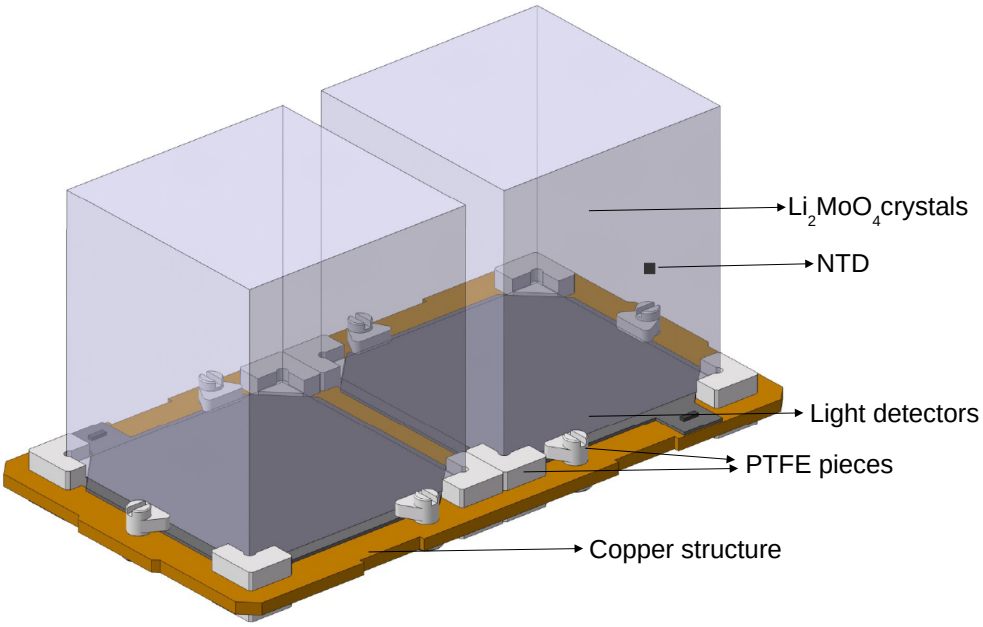

Figure 6.2: The CUPID basic detection module

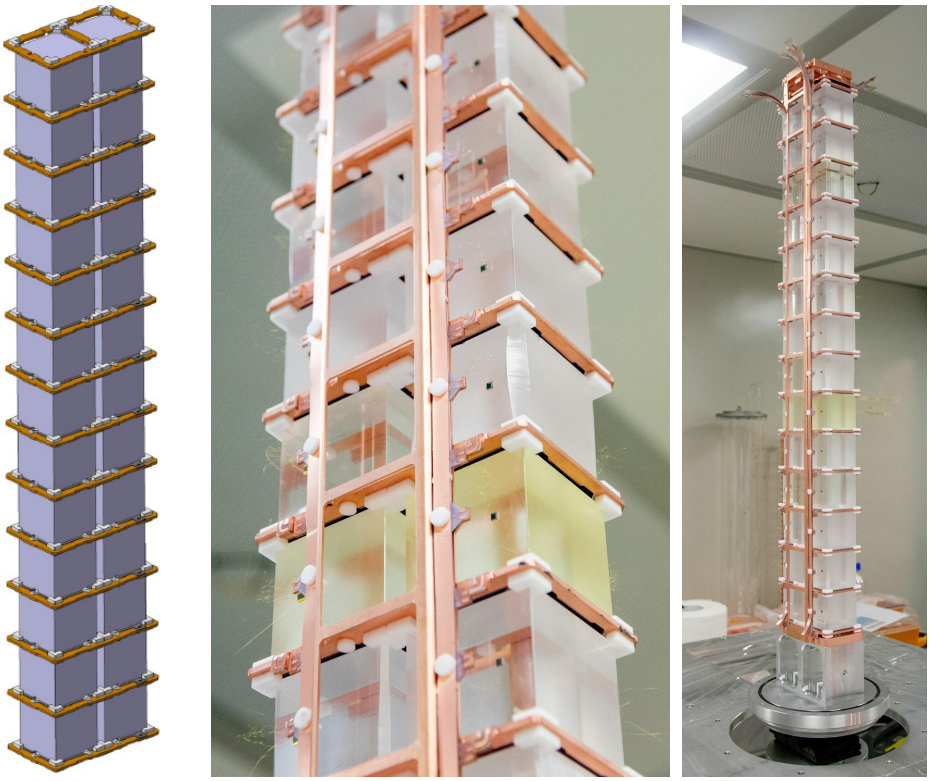

Figure 6.3: Left: Design of a CUPID tower consisting of 14 floors and 28 detection modules. Middle and Right: first prototype of a CUPID tower before installation in a cryostat at LNGS.

with 99.9% γ/β acceptance [58], and thus they meet the CUPID requirement. The rejection efficiency of pileup events depends on two parameters: the signal-to-noise ratio (SNR) at $Q_{\beta\beta}$ and the rise time ($\tau_{\rm rise}$). The SNR of a standard light detector is modest, ∼10 for a γ/β energy deposition of 3 MeV in the $Li_2{}^{100}MoO_4$ crystal. Thus, even if these detectors have a relatively fast rise-time, $\tau_{\rm rise} \sim 1$ ms, the rejection of the $2\nu\beta\beta$ pile-up events is insufficient. The heat detectors have typically SNR in ROI of about 1500 but $\tau_{rise} \sim 15$ ms, they are too slow to reach the required pile-up rejection. Therefore to enhance the SNR, the CUPID light detectors will be instrumented with Neganov-Trofimov-Luke (NTL) amplification [141]. This technology allows to operate light detectors with effective SNR amplification of the order of 15. We will further discuss the $2\nu\beta\beta$ pile-up background rejection in section 6.5.5.

We list in Table 6.1 the parameters of the CUPID baseline detector.

Table 6.1: Parameters of the baseline CUPID detector design.

Parameter	Baseline
Isotope	^{100}Mo
Q-value	$Q_{\beta\beta}$=3034 keV
Crystal	$Li_2{}^{100}MoO_4$
Crystal size	$45 \times 45 \times 45$ mm^3
Crystal mass (g)	280
Number of crystals	1596
Number of light detectors	1710
Detector mass (kg)	450
^{100}Mo mass (kg)	240
Energy resolution FWHM (keV)	5
Background index (counts/(keV·kg·yr))	10^{-4}
Containment efficiency	79%
Selection efficiency	90%
Livetime	10 years
Half-life exclusion sensitivity (Bayesian 90% C.I.)	1.6×10^{27} y
Half-life exclusion sensitivity (Frequentist 90% C.L.)	1.8×10^{27} y
$m_{\beta\beta}$ exclusion sensitivity (90% C.I.)	9.6–16 meV
$m_{\beta\beta}$ exclusion sensitivity (90% C.L.)	9.0–15 meV
Half-life discovery sensitivity (3σ)	1×10^{27} y
$m_{\beta\beta}$ discovery sensitivity (3σ)	12–21 meV

6.2 CUPID backgrounds

The $0\nu\beta\beta$ decay signature in CUPID will be a monochromatic line centered at $Q_{\beta\beta}$ =3034 keV. We group background sources that may produce events in the same energy region, hiding the expected peak, in the following categories:

- **Radioactive backgrounds**:
  - **Infrastructure**: radioactive contaminants in the cryostat, the inner lead shields, or the outer shields (made of lead and of polyethylene). The two contaminants of concern for the $0\nu\beta\beta$ signal are ^{214}Bi which has a Q-value= 3269 keV and a few γ's with

energy larger than $Q_{\beta\beta}$, and ^{208}Tl that contributes through the 2615 keV/583 keV cascade decay, when both γ's are simultaneously detected in the same crystal, with a small amount of lost energy.

  - **Close infrastructure**: the innermost cryostat thermal shield can contribute to the background via the emission of α and β particles emitted by radioactive contaminants on its inner surface, which has a direct line of sight to the detectors, or through γ rays emitted in the bulk.
  - **Close components**: radioactive isotopes in the components close to the detectors: the copper holder, the PTFE stands, and the cabling system. All the particles emitted by these radionuclei can reach the bolometers, even the short range α particles produced by ^{238}U and ^{232}Th and their daughters, or β particles produced by ^{214}Bi and ^{208}Tl decays.
  - **Detectors**: radioimpurities in the $Li_2{}^{100}MoO_4$ crystals and Ge wafers themselves. Relevant backgrounds include β decays, primarily of ^{214}Bi and ^{208}Tl decays, and surface ^{238}U and ^{232}Th chain contaminants.

- **$2\nu\beta\beta$ in the crystals**: The random coincidence of two or more $2\nu\beta\beta$ events from ^{100}Mo in the same crystal happening so close in time that the signal is equivalent to that of the sum of the two events.

- **Muons:** There are several types of external background sources that we consider. However, γ rays which originate outside the experimental infrastructure are efficiently shielded and contribute negligibly to the $0\nu\beta\beta$ region. So we focus our discussion of external background sources on muons which pass through the rock overburden and interact with our detector.

- **Neutron induced backgrounds:** The backgrounds that could contribute to the ^{100}Mo ROI arise mainly from (n,γ) reactions, which can produce γ's up to 10 MeV, or by inelastic scattering of a nucleus, which may deposit $\sim$MeVs of energy.

The CUPID detector will use several passive and active technologies to reduce the background. Passive techniques includes the selection, cleaning, and storage of all the materials involved in the detector construction. Active techniques include anti-coincidence, delayed coincidence, and particle identification. These active mitigation techniques are described in the following sections.

6.3 Active background rejection: anticoincidences and delayed coincidences

Active techniques were successfully exploited in CUORE [57, 142] and CUPID-Mo (Sec. 5.2.2). Other than its energy, the $0\nu\beta\beta$ decay signature has another distinguishing characteristic: the energy is deposited by electrons. In 79% of the cases, the energy deposited by the two electrons will be contained in a single crystal, while background γ events are more likely to undergo Compton scattering and full absorption in different crystals. The capability of operating the detector in anti-coincidence allows us to exploit the high granularity of the device to reject

multi-site events, such as μ's either crossing the detector, or inducing showers in the shields or multi-Compton interactions induced by γ rays. This technique applies, with different efficiency, to any contaminant or environmental flux. The delayed coincidence technique can be used only in the case of ^{214}Bi and ^{208}Tl contaminants in the detector, since it requires the detection of the α decay of the mother. We can exploit the time correlation of these decay chains events to reduce our experimental backgrounds. In particular, we veto events from the lower part of both chains, from ^{214}Bi (^{238}U chain) and ^{208}Tl (^{232}Th chain). Fig. 6.4 shows a scheme of the delayed coincidence cut. For ^{208}Tl we can veto events following a suspected ^{212}Bi α-decay. This isotope decays to ^{208}Tl, which has a short half-life of 3.05 minutes. As a consequence, the β/γ interactions produced by ^{208}Tl decay can be efficiently suppressed by opening a time-veto after the detection of the α from ^{212}Bi. For example in CUPID-Mo we applied a time-veto of $10 \times T_{1/2}$= 1830 s, which contains $> 99.9\%$ of the ^{208}Tl decays.

The very low radioactivity of the $Li_2{}^{100}MoO_4$ crystals enables an extended delayed coincidence cut to remove ^{214}Bi candidate events. The ^{222}Rn decay chain proceeds as follows:

$$\begin{aligned} {}^{222}\mathrm{Rn} &\xrightarrow[\alpha\ 5590\ \mathrm{keV}]{3.8\ \mathrm{day}} {}^{218}\mathrm{Po} \xrightarrow[\alpha\ 6115\ \mathrm{keV}]{3.1\ \mathrm{min}} {}^{214}\mathrm{Pb} \\ &\xrightarrow[\beta^-\ 1018\ \mathrm{keV}]{27.\ \mathrm{min}} {}^{214}\mathrm{Bi} \xrightarrow[\beta^-\ 3269\ \mathrm{keV}]{19.9\ \mathrm{min}} {}^{214}\mathrm{Po}. \end{aligned} \tag{6.1}$$

We can therefore tag the event based on the ^{222}Rn or ^{218}Po α events and a fairly long dead time. In CUPID-Mo we use energy cuts of $5985 - 6145$ keV for ^{218}Po and $5460 - 5620$ keV for ^{222}Rn to tag α candidates. For either type of α candidate events we then veto events within the same crystal within a time window 13860 s for ^{222}Rn and 13620 s for ^{218}Po. These time windows contain 99% of events, as evaluated with a Monte Carlo sampling. The delayed coincidence cut is particularly efficient to reject surface backgrounds.

While the described techniques are available for all the arrays of cryogenic calorimeters, CUPID will offer an additional tool for particle identification, the simultaneous readout of heat and light.

6.4 Active background rejection: α/β discrimination

The leading contribution to the CUORE background in the $0\nu\beta\beta$ ^{100}Mo ROI comes from energy degraded α particles. These are produced in decays that occur on surfaces of the crystal or passive materials near the crystals. A particle from an α decay on a passive surface near a crystal may lose a fraction of its energy in the passive surface before depositing a fraction of its kinetic energy in the crystal. Similarly, an α on the surface of the crystal may deposit some of its energy in the crystal, before escaping and terminating in a passive material. Both scenarios lead to a relatively flat background at energies well below the α decay energy, which generates backgrounds in the $0\nu\beta\beta$ signal region. In CUORE, this is the dominant contribution to the background index (BI) of 10^{-2} counts/(keV·kg·yr).

The major technical advancement of CUPID is the ability to do particle discrimination based on measured scintillation light. Each $Li_2{}^{100}MoO_4$ crystal is coupled to two light detectors consisting of Ge wafers instrumented with temperature sensors. The anticipated performance of this technique in CUPID is demonstrated in CUPID-Mo [58], and the LUMINEU program [143] and has been reproduced in dedicated test runs in the Hall C cryostat at LNGS [144], and in the CROSS cryostat at LSC. Figure 6.5 shows the performance of the particle discrimination

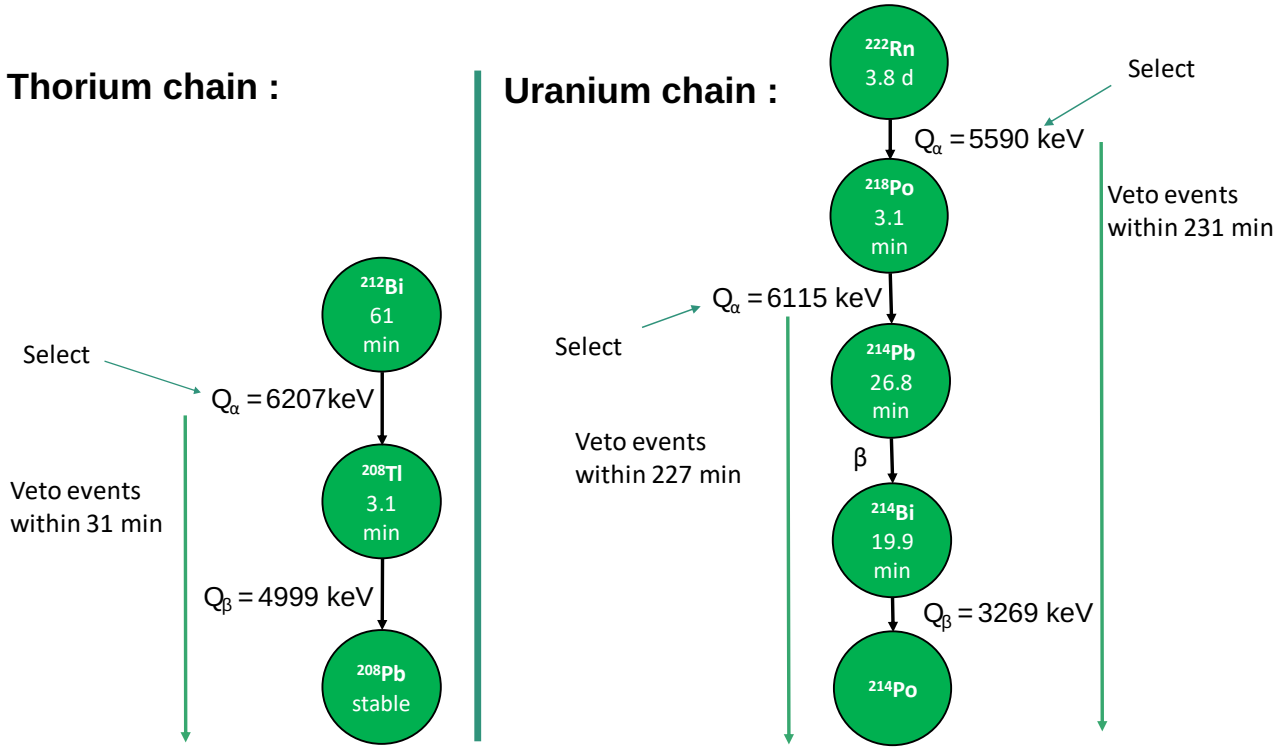

Figure 6.4: Scheme of the delayed coincidences time-veto cut. We identify certain α's from the uranium and thorium chain to reject the β's from ^{208}Tl and ^{214}Bi, respectively.

with a $Li_2{}^{100}MoO_4$ bolometer and Ge light detector in recent measurements at Canfranc using a CUPID-like configuration. In the left graph, we plot the energy measured on the $Li_2{}^{100}MoO_4$ crystal (the 'heat') as the event energy on the horizontal axis, and the measured light amplitude, normalized by the heat, as a proxy for the light yield on the vertical axis.

To quantify the power of the α-tagging ability we define the Discrimination Power (DP) defined as

$$DP = \frac{|\mu_{\beta/\gamma} - \mu_\alpha|}{\sqrt{\sigma^2_{\beta/\gamma} + \sigma^2_\alpha}} \tag{6.2}$$

where μ and σ are, respectively, the average value and RMS of the β/γ and α light distributions. Both of these parameters depend on the energy. In order to satisfy the requirement on BI= 10^{-4} counts/(keV·kg·yr) we require DP(E=$Q_{\beta\beta}$)> 3.1 [145].

A Note about Reflector Foils In the CUPID-Mo and CUPID-0 arrays, the crystals were surrounded by a reflective foil around the curved cylindrical face to maximize light collection. In CUPID, the removal of the reflecting foil will allow the reduction of the background thanks to the tagging of the events in coincidence between crystals, but to the expense of a reduction in the light collection. R&D tests proved that the light yield, in the configuration without reflective foils, is sufficient to reach the required discrimination power [144].

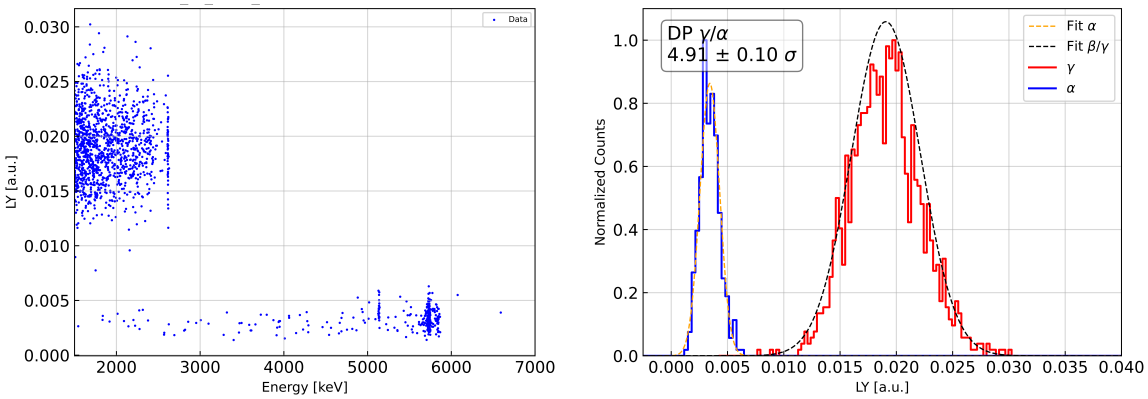

Figure 6.5: Left: Light/Heat signal ratio from a typical CUPID-like $45 \times 45 \times 45$ mm^3 $Li_2{}^{100}MoO_4$ crystal. The light signal comes from a single light detector operated at LSC with NTL amplification. The upper band shows the β/γ events with a LY$\approx$ 0.3 keV/MeV, and the lower band the α events, with much lower LY. Right: The discrimination power of this detector is evaluated as DP$= 4.9 \pm 0.1$.

6.5 Predicted CUPID backgrounds

We evaluate the background index as the expected number of events, induced by any background source, in a 30 keV region around $Q_{\beta\beta}$ =3034 keV, normalized by the total detector mass, measurement livetime, and keV of energy. We have chosen our region of interest (ROI) to exclude two γ lines at 3000 and 3053 keV emitted in ^{214}Bi decay (both of which have an intensity at the 10^{-4} level). Our chosen ROI is 6 times our goal energy resolution (FWHM=5 keV). The availability of such a wide region free from γ lines allows us to mildly relax our requirement in energy resolution without significantly affecting the detector sensitivity. Fig. 6.6 shows for illustration a simulated spectrum of the CUPID backgrounds and the chosen ROI region.

We evaluated the CUPID backgrounds with dedicated GEANT4 [146] simulations. We implemented a detailed detector geometry of the CUPID towers, including the crystals, copper holders, PTFE stands and cabling. This geometry is embedded in the implementation of the geometry of the CUORE cryostat. A rendering of the CUPID geometry in the GEANT4 simulation is shown in Fig. 6.7. Since secular equilibrium is often broken at the ^{226}Ra or ^{228}Th level (respectively for the ^{238}U and ^{232}Th chains), it is important to keep in mind that activities bounds must be considered independently. To simulate bulk and surface contaminations in the crystal, detector holders and close infrastructure, we have generated the decay chains ^{226}Ra or ^{228}Th to take into account time correlations and exploit the delayed coincidences (see Sect. 6.3).

We account for the detector response through a post processing of the Monte Carlo simulated spectra. We reproduce the detector energy resolutions and process the time correlations in the decay chains, necessary for the delayed coincidences analysis. In the study presented here, we do not simulate the production and collection of scintillation light, but reconstruct the expected light signal as follows. In the simulation, we tag energy deposition in the crystals according to the kind of interacting particle. For each event we know the fraction of energy deposited from β/γ's and the energy deposited by α particles. We construct a variable as the ratio between the energy deposited by β/γ's and the energy deposited by α's, GBF. A more realistic approach is in progress, based on the implementation of a light yield distribution for β/γ's and α's extracted from experimental data, as was done in CUPID-Mo.

Several cuts are used for background suppression. To evaluate the BI in the ROI, we require

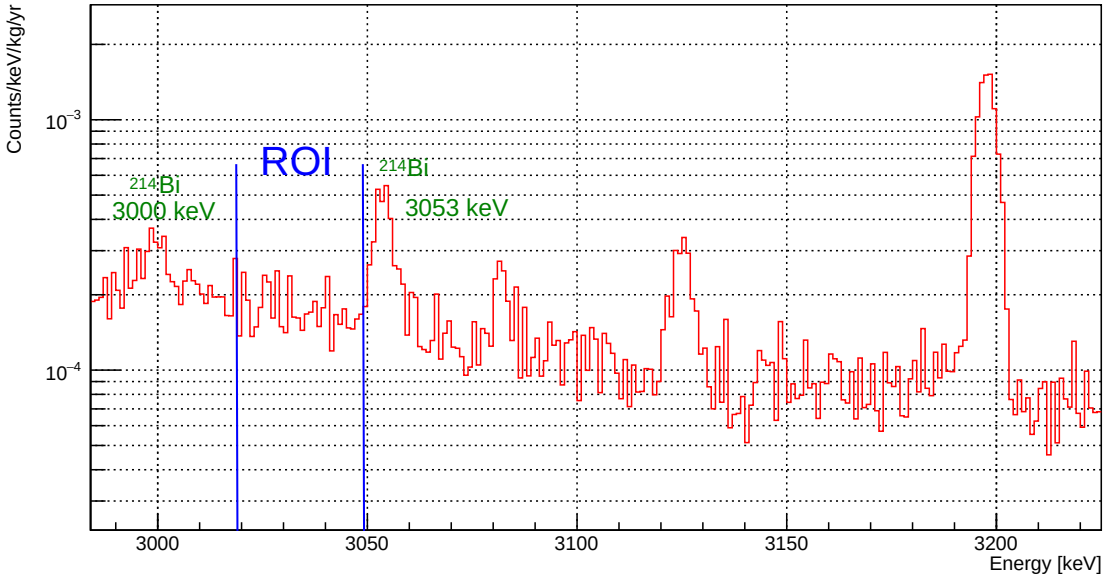

Figure 6.6: Monte Carlo simulated spectrum of the CUPID background (arbitrary normalization), illustrating the choice of the region of interest for the evaluation of the background index. The ROI is defined as 3034 ± 15 keV to exclude two γ lines of ^{214}Bi at 3000 and 3053 keV.

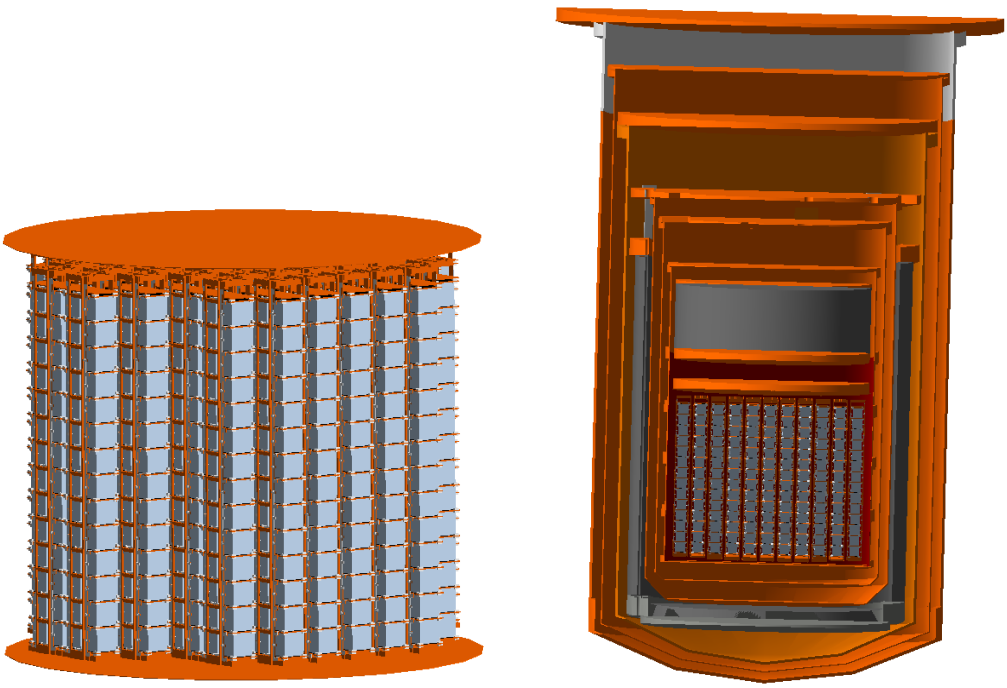

Figure 6.7: Geometry of the CUPID baseline detector array as implemented in the GEANT4 simulation software.

that the energy be deposited in only one crystal. In addition, the capability to perform particle identification is extremely powerful and we require that the GBF be higher than 90%. We also apply the delayed coincidences cut to remove events from ^{208}Tl and ^{214}Bi decays. In addition, to reject direct energy deposits in the light detector, we require this energy < 5 keV. We show in Fig. 6.8 two examples of background simulations. The left plot corresponds to ^{226}Ra - ^{210}Pb on the surface of the CuPEN cables. The selection requiring the energy deposits in a single crystal and the particle identification largely reduces the background, while the delayed coincidence cut has a small effect because the probability to observe an α particle plus a β from the same decay in components other than the crystals is small. The right plot shows the ^{228}Th - ^{208}Pb decay in the bulk of the crystals. In this case, the delayed coincidence cut is very powerful to suppress the background.

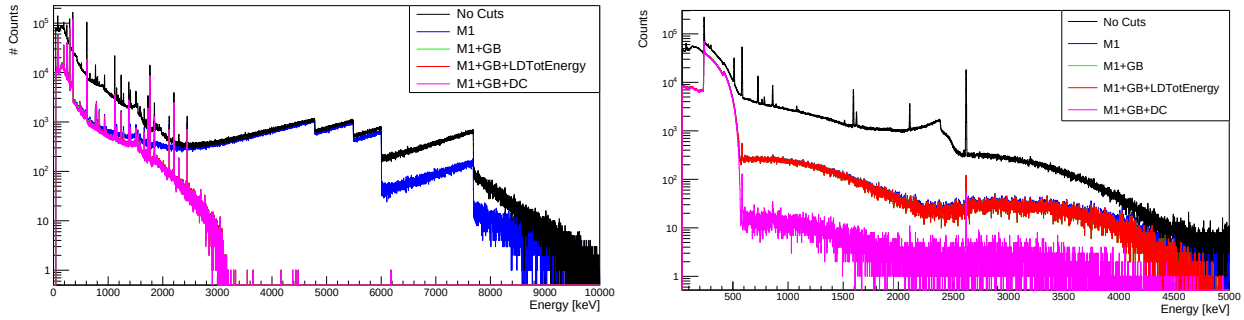

Figure 6.8: Monte Carlo simulations of two background contributions. Left: ^{226}Ra - ^{210}Pb on the surface of the CuPEN cables. The simulation assumes an exponential density profile, $e^{-x/\lambda}$ with a depth parameter $\lambda = 10\mu$m. Right: ^{228}Th - ^{208}Pb in the bulk of the crystals. The effect of the cuts is shown.

6.5.1 Method to combine the background contributions

The MC simulations give us the shape of the expected background spectrum for each source. To calculate the background index in the ROI, we need the absolute number of events and thus we need to know the radioactive contaminations, i.e, the number of decays per unit of time. The background models developed in CUORE and CUPID-Mo reproduce well the features of the experimental data and the resulting parameters of the model then tell us the radioactive contamination of various components of the experiment. Our results for the CUPID projections rely on the radioactivities obtained from the background models of CUORE and CUPID-Mo (section 5.2.2) [147]. As a result of the background models, we obtain the probability distributions for the activities of the different components. These results suffer from correlations between background sources with similar spectral shapes. To take into account the correlations, we combine the contributions by directly sampling the full posterior distribution for each step i in the Markov Chain. We compute the background index b_i in the step i summing over all sources:

$$b_i = \sum_{\mathrm{j=1}}^{\mathrm{Nsources}} \mathrm{Pois}(N_j) \frac{w_{i,j}}{\Delta E \times N_{gen}}. \tag{6.3}$$

Here $w_{i,j}$ is the probability value for the activity, from the background models, for source j in step i (it can be thought as a 'weight'). N_j is the integral of the spectrum of source j in the ROI, obtained from the CUPID simulations for which N_{gen} events were generated. ΔE

is the width of the ROI. The simulations are themselves the result of a stochastic process and they have a statistical uncertainty, this is accounted for by Poisson smearing the Monte Carlo ROI integrals. We then use the distributions of b_i to estimate the marginalised posterior distribution of the background index, and give the mode $\pm$ the smallest 68% interval. If the smallest interval includes the zero value, then a limit is given at 90 % confidence interval. We show in Fig 6.9 an example of the distribution of background index for ^{226}Ra on the surface of the crystal. The distribution was obtained applying the method describe above, using the probability distribution for the activity from the CUPID-Mo background model.

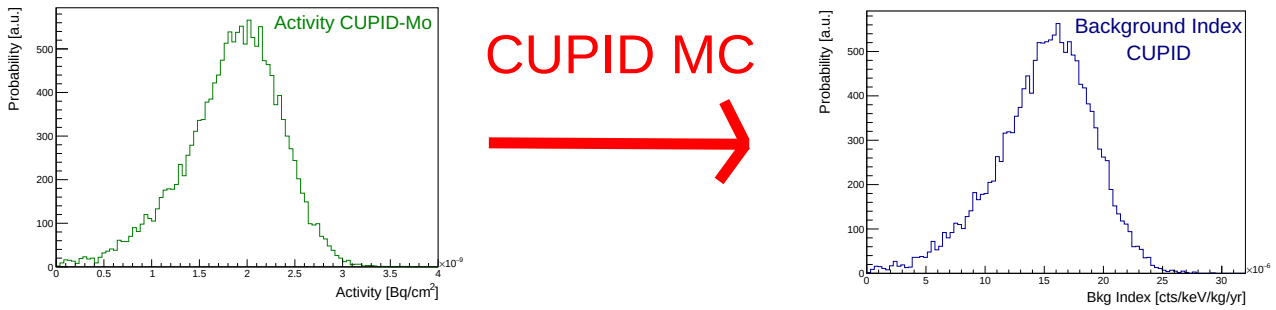

Figure 6.9: Probability distributions of the activity of ^{226}Ra on the surface of the $Li_2{}^{100}MoO_4$ crystals, from the CUPID-Mo background model. Applying the method described in 6.5.1, we obtain the probability distributions of the background index in CUPID.

6.5.2 ^{238}U and ^{232}Th in the bulk and on the surface of the crystals

Bulk and surface contaminations in the $Li_2{}^{100}MoO_4$ crystals are inferred from the CUPID-Mo background model. The model is built from the simultaneous fit of : $\mathcal{M}_{1,\beta/\gamma}$, events in one crystal identified as β/γ; $\mathcal{M}_2$, events in coincidence between 2 crystals, and $\mathcal{M}_{1,\alpha}$, events in one detector with alpha energy scale (> 3 MeV), (see section 5.2.2). The crystal contamination is deduced to a large extent from the $\mathcal{M}_{1,\alpha}$ spectrum, populated by α decays occurring in the crystals and in the elements directly facing them, shown in Figure 6.10.

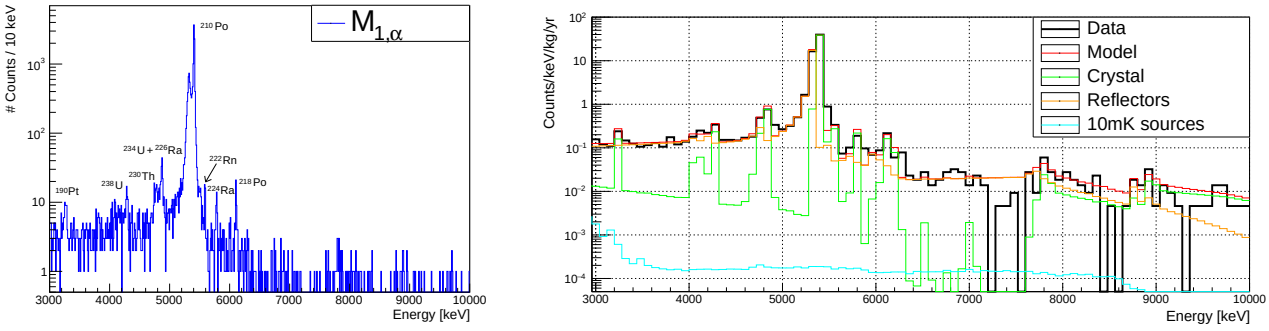

Figure 6.10: Left: CUPID-Mo $\mathcal{M}_{1,\alpha}$ experimental data. Right: background model reconstruction [147].

All the contaminations in the radionuclides that are relevant for the CUPID background from the ^{238}U and ^{232}Th chains are below 1 μBq/kg (see Table 4 in [147] included in section 5.2.2). The peak at 4.8 MeV contains ^{234}U and ^{226}Ra alpha decays. In the CUPID-Mo analysis

Table 6.2: Radioactive bulk and surface contaminations of the LMO crystals derived from the background model of the CUPID-Mo data, with 2.71 kg × yr exposure. The corresponding background index contributions are also shown.

^{226}Ra to ^{210}Pb	^{228}Th to ^{208}Pb	BI ^{226}Ra [ckky]	BI ^{228}Th [ckky]	BI Tot [ckky]
< 0.2 μBq/kg	$0.43^{+0.16}_{-0.15}$ μBq/kg	0	$(2.9 \pm 1.1) \cdot 10^{-6}$	$(2.9 \pm 1.1) \cdot 10^{-6}$
2.0 ± 0.5 nBq/cm^2	< 2.5 nBq/cm^2	$(1.6^{+0.5}_{-0.3}) \cdot 10^{-5}$	$< 1.6 \cdot 10^{-5}$	$(2.2 \pm 0.7) \cdot 10^{-5}$
Total				$(2.6 \pm 0.6) \cdot 10^{-5}$

this peak is ascribed to ^{234}U, with a significant uncertainty in the resulting contamination due to the anticorrelation with the ^{226}Ra contribution. Additionally, in this peak we could have a contribution from the neutron capture in ^{6}Li[148]. Neutrons captured in ^{6}Li produce an alpha particle plus tritium, ^{6}Li(n,α)^{3}H, with a total energy 4.782 MeV. We note also that the level of ^{228}Ra is not constrained by any α peak. The largest peak in the α region is the ^{210}Po peak. The fit ascribes a large part of this peak to the Q-value component of the crystal bulk. The ^{210}Po contamination, much larger than the rest of the ^{238}U chain, is at the level of 96 μBq/kg, possibly introduced during the purification of the enriched material [143]. There are also traces of ^{190}Pt, caused by the crystal growth in a platinum crucible [149]. We find ^{40}K introduced by the contamination in the lithium carbonate powder employed in the crystal growth. We find also anthropogenic ^{90}Sr+^{90}Y at the level of some hundreds of μBq/kg. We note that ^{210}Pb, ^{87}Rb, ^{90}Sr+^{90}Y and ^{40}K do not represent a potential background for $0\nu\beta\beta$ search, as the Q_β of these radioisotopes is much lower than the $0\nu\beta\beta$ ROI at 3 MeV. The contaminants that are relevant for the CUPID background in the ROI are ^{226}Ra and ^{228}Th, shown in Table 6.2.

Bulk contaminations contribute to the BI in the ROI with $\sim 3 \cdot 10^{-6}$counts/(keV·kg·yr). Surface contaminations contribute with $\sim 2 \cdot 10^{-5}$counts/(keV·kg·yr), one order of magnitude larger than the bulk. Both bulk and surface contaminations in the crystals sum up to $2.6 \cdot 10^{-5}$counts/(keV·kg·yr). Such value is a factor ~ 4 lower than in CUPID-Mo thanks to the higher granularity of CUPID, and to the absence of reflector foils, yielding a higher anti-coincidence efficiency.

Contaminations in the $Li_2{}^{100}MoO_4$ crystals inferred from CUPID-Mo crystals are sufficiently low to achieve the BI goal. Surface contaminations, which are the dominant background, can be further reduced by a strictly controlled crystal production chain, similar to the one adopted for the CUORE crystals, and the deployment of assembly procedures in dedicated high-end clean rooms like in CUORE.

6.5.3 Cosmogenic isotopes in $Li_2{}^{100}MoO_4$ crystals

The cosmogenic activation of $Li_2{}^{100}MoO_4$ crystals was estimated using the ACTIVIA [150] code, assuming a sea level exposure of 90 days [151, 152, 145]. As discussed previously in section 2.1, among all the materials present in the CUPID setup, only molybdenum contributes with cosmogenically activated isotopes emitting radiation with energy high enough to give events in the ROI. The crystals are going to be 95% enriched in ^{100}Mo, with the remaining

isotope being only ^{98}Mo. The only potentially dangerous activated isotopes in ^{100}Mo are ^{42}K, ^{82}Rb, ^{56}Co and ^{88}Y. Assuming an underground cooling period of 1 year (as is the case in the CUPID baseline plan), the contributions of ^{42}K, ^{82}Rb and ^{88}Y to the ^{100}Mo ROI becomes $\sim 10^{-7}$ counts/(keV·kg·yr), and ^{56}Co contributes at the level of 9×10^{-7} counts/(keV·kg·yr) (Fig. 6.11). The total background expected from cosmogenic activation isotopes is $2.3 \cdot 10^{-6}$ counts/(keV·kg·yr).

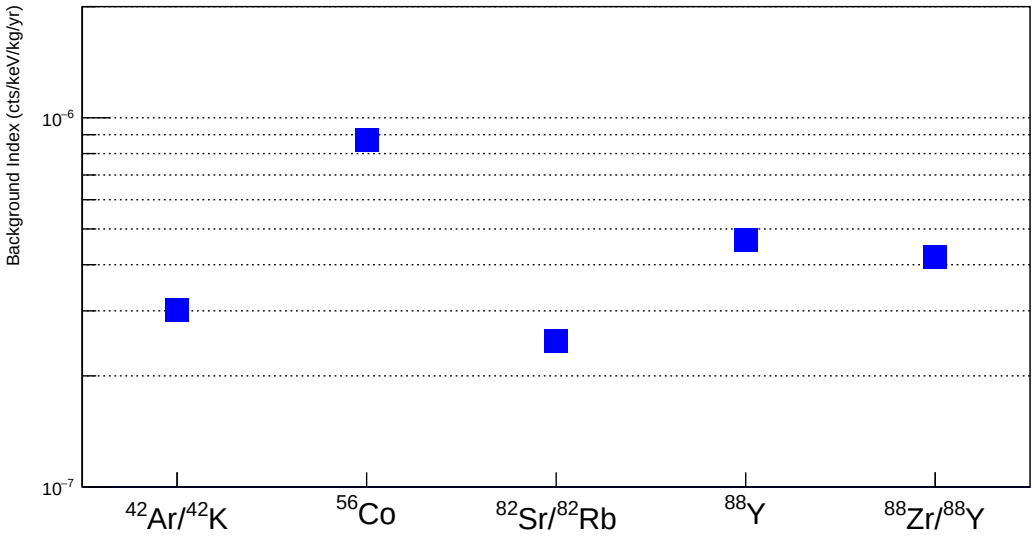

Figure 6.11: Expected background in the $0\nu\beta\beta$ ROI from cosmogenic radionuclides in $Li_2{}^{100}MoO_4$ crystals, after 90 days of exposure at sea level and 1 year underground. ^{88}Y can be produced either directly, or as the decay product of ^{88}Zr.

6.5.4 Total background from radioactivity in the crystals

The total expected background from the radioactivity in the crystals considering ^{238}U and ^{232}Th in the bulk and surface, cosmogenics and anthropogenic radionuclides results in $(2.8 \pm 0.6) \cdot 10^{-5}$counts/(keV·kg·yr). Fig. 6.12 shows a breakdown of the contributions and the total expected background from the crystals. The total probability density function is shown in Fig. 6.13.

6.5.5 $2\nu\beta\beta$ pile up in the crystals

As discussed previously, we define pile-up as the random coincidence of 2 events in the same crystal happening so close in time that the signal is equivalent to that of the sum of the two events. This is a particular concern for ^{100}Mo, due to the fast rate of $2\nu\beta\beta$ decay of $T_{1/2} \sim 7 \times 10^{18}$ yr [153]. As mentioned previously, the rejection efficiency of pileup events depends on two parameters: the signal-to-noise ratio at $Q_{\beta\beta}$ and the pulse rise time (τ). A same value of rejection efficiency can be achieved with different combinations of these parameters. Thus, a 3D space with axes (τ, SNR, BI_{Pileup}) can be built. The points in this 3D space can be identified with dedicated measurements and detector response simulations, as shown in Fig. 6.14. The data points show the performances of Neganov-Trofimov-Luke light detectors [154] and TES instrumented light detectors from dedicated measurements [155]. The solid line corresponds to $BI_{Pileup} = 0.5 \cdot 10^{-4}$counts/(keV·kg·yr).

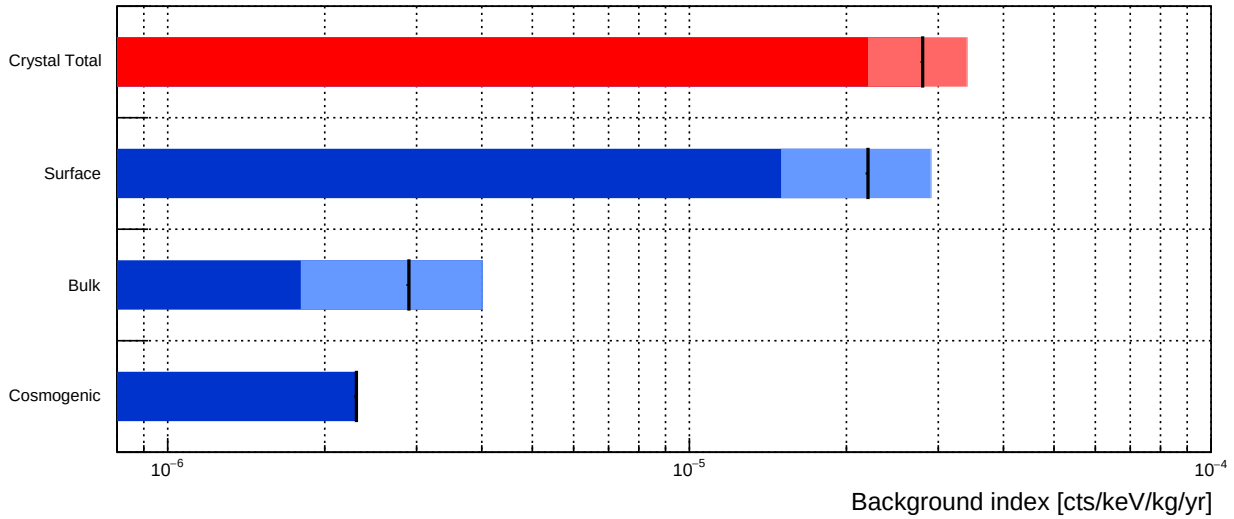

Figure 6.12: Breakdown of the expected backgrounds from radioactive contamination in the $Li_2{}^{100}MoO_4$ crystals. The black line shows the mean value, the light band the $\pm\sigma$ uncertainty.

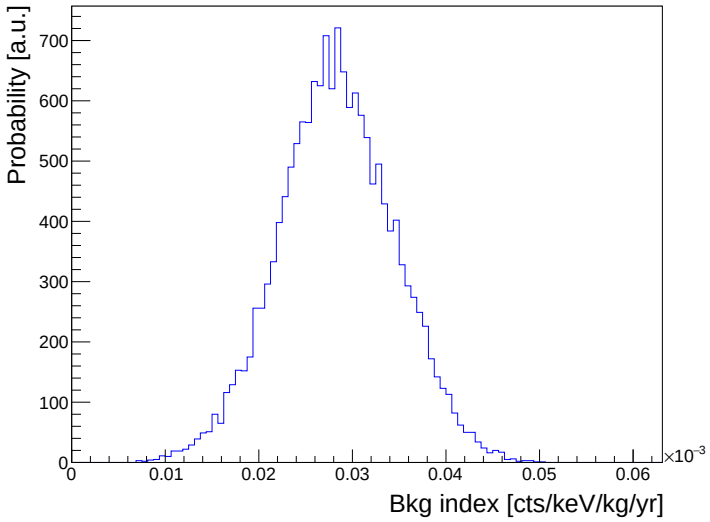

Figure 6.13: Probability density function for the BI contribution from the $Li_2{}^{100}MoO_4$ crystals. We obtain the pdf distribution using Monte Carlo Markov Chains from the CUPID-Mo background model convoluted with the results of the CUPID simulations.

To reach the CUPID background goal of 10^{-4} counts/(keV·kg·yr), the pile up contributions should be $\leq 5 \cdot 10^{-5}$ counts/(keV·kg·yr). The heat signals present a high SNR (∼1500) but have a slow τ of $\sim$ 15 ms. The pileup background goal can therefore be reached only using light detectors. Standard NTD-based light detectors can reach τ of $\sim$ 1 ms [154], but are limited by the SNR, which is $\sim$ 900 eV/100 eV$\sim$ 9 for energy depositions in $Li_2{}^{100}MoO_4$, at $Q_{\beta\beta}$. As described in Sec. 4.3.1, light detectors instrumented with Neganov-Trofimov-Luke amplification can provide the needed signal amplification. Results obtained at the Canfranc Underground Laboratory (LSC) on several NTL light detectors, developed for CROSS, proved an excellent performance both for alpha/beta-gamma and pile-up rejection. A R&D program on NTL-boosted detectors is ongoing.

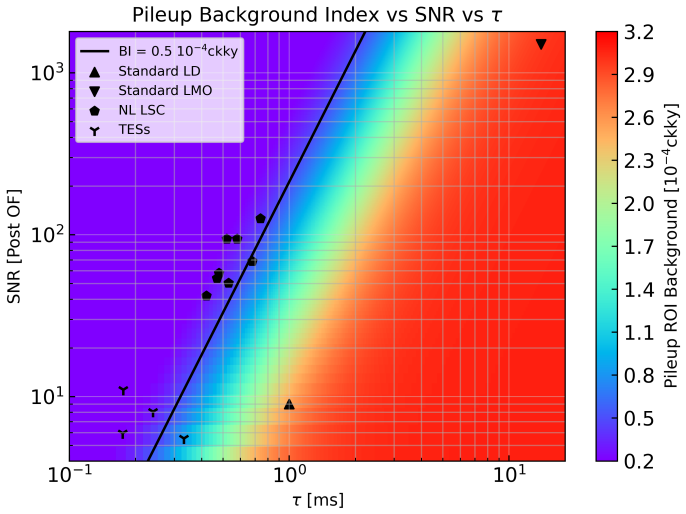

Figure 6.14: 3D plot of (τ, SNR, $\mathrm{BI_{Pileup}}$). The data points show the performances of Neganov-Trofimov-Luke light detectors (dots, from tests performed at LSC in the CROSS cryostat, see section 4.3.1), TES (small crosses), light detectors without NTL amplification (Standard LD, upward-pointing triangle), and LMO (downward-pointing triangle). The solid black line identifies the boundary $\mathrm{BI_{Pileup}} = 0.5 \cdot 10^{-4}$counts/(keV·kg·yr).

6.5.6 ^{238}U, ^{232}Th from close sources

Close sources include all elements directly facing the crystals, the copper holders, PTFE clamps and cabling system made of PEN bands with copper tracks. Since the ^{100}Mo ROI lies above the majority of the γ backgrounds, the only contributions to the BI from bulk copper, PTFE and PEN contamination comes from multiple scattering of cascade decays, which tend to be subdominant. As with the crystals, the primary contribution to the BI comes from surface contamination through the β decays of ^{214}Bi and ^{208}Tl. In CUORE-0 and CUORE, we developed a rigorous cleaning procedure to clean the copper parts [156, 157]. For CUPID, the cleaning of the detector holder parts will be based on similar procedures.

We evaluate ^{238}U and ^{232}Th contribution from close sources simulating the radionucleides in ^{226}Ra or ^{228}Th subchains and using the activities reported in Table 6.3.

For copper holders we use the activities inferred from the CUORE background model[1]. In this model, the contributions from all elements made of NOSV copper directly facing the crystals are considered together, since they yield degenerated spectra. These elements include the copper holders, the tiles that cover the inside of the 10 mK vessel, the tower support plate, the copper plates on top and bottom of the detectors, the flange of the 10 mK vessel and the 10 mK vessel sides, see Fig. 6.1. Though the spectra from PTFE and CuPEN cables are not explicitly included in the background sources, their contribution is taken into account in the copper holders, since the three spectra are completely degenerated. We combine the activities from the CUORE background model with CUPID simulations to obtain the probability distribution shown in Fig. 6.15. The background indexes are reported in Table 6.3.

To get an estimation of the background from PTFE and CuPEN cables, we have used measured radioactivities. We measured by ICPMS a PTFE sample from Plastic & Seals, from which we obtained the bulk radioactivity. Since we could not asses the activity on the surface, we assumed all the contamination measured by ICPMS to be on the surface, to obtain a

[1] publication in preparation

Table 6.3: Radioactive contaminations of the close components and the corresponding background index expected in the CUPID ROI. For copper frames we consider the activities derived from the background model of CUORE data, with 1038 kg × yr exposure. For PTFE and CuPEN cables we consider the radioactivities measured by ICPMS and HPGe gamma spectroscopy, respectively.

	^{226}Ra to ^{210}Pb	^{228}Th to ^{208}Pb	BI [ckky]	BI Tot. [ckky]
Cu frames	< 0.5 μBq/kg 9.3 ± 0.8 nBq/cm^2	< 1.3 μBq/kg 9.5 ± 0.7 nBq/cm^2	$< 1.6 \cdot 10^{-6}$ $3.9 \pm 0.4 \cdot 10^{-5}$	$3.9 \pm 0.4 \cdot 10^{-5}$
PTFE	< 120 μBq/kg < 26 nBq/cm^2	< 40 μBq/kg < 8.7 nBq/cm^2	$< 7.4 \cdot 10^{-6}$ $< 2.2 \cdot 10^{-5}$	$< 2.2 \cdot 10^{-5}$
CuPEN cables	< 1000 μBq/kg < 11 nBq/cm^2	< 800 μBq/kg < 9 nBq/cm^2	$< 1.4 \cdot 10^{-5}$ $< 6.4 \cdot 10^{-6}$	$< 1.4 \cdot 10^{-5}$

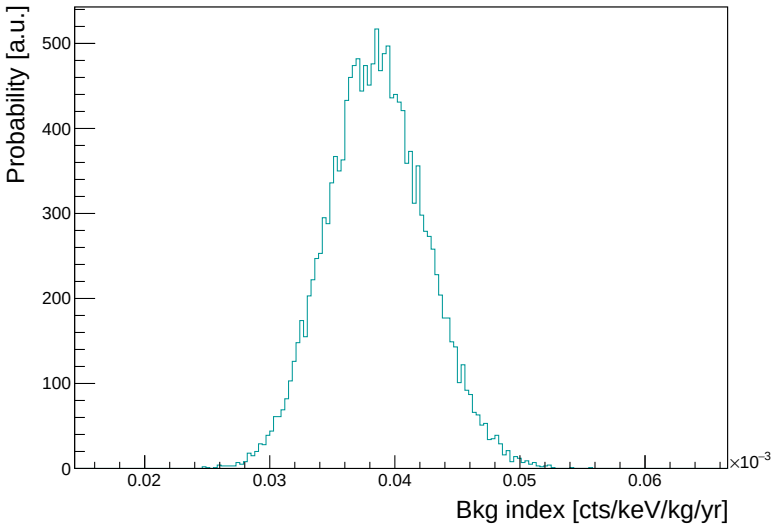

Figure 6.15: Probability density function for the BI contribution from the copper holders. We obtain the pdf distribution using Monte Carlo Markov Chains from the CUORE background model convoluted with the results of the CUPID simulations.

conservative estimation. For CuPEN we have measured a sample (with the full copper layer) with a HPGe detector at LNGS. As with PTFE, to obtain the surface radioactivity we translated the bulk radioactivity assigning all the contamination to the surface. For this reason, in order not to double count, we indicate in Table 6.3 only the largest contribution for the evaluation of the total BI from these elements. For both PTFE and CuPEN we got only upper limits for the activity levels. The corresponding probability density distribution functions are thus exponentials. The distribution of the expected BI, obtained from the combination of ^{226}Ra to ^{210}Pb and ^{228}Th to ^{208}Pb distributions, are shown in Fig. 6.16.

However, in the evaluation of the CUPID background budget, we chose to consider only the copper frames. In the CUORE background model, the activity of the copper holders takes into account the activity of the PTFE and CuPEN, as mentioned previously. Thus, including those components would lead to double counting their contributions. We remark

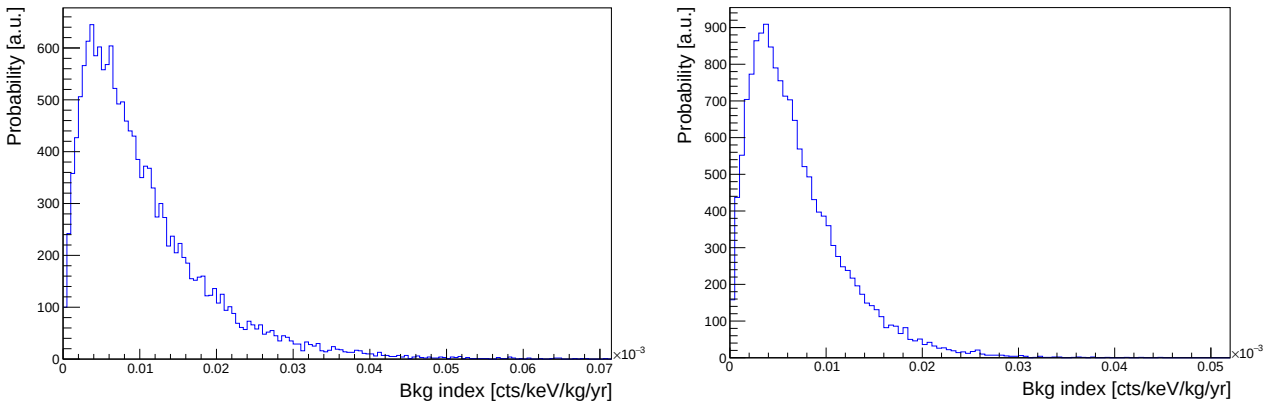

Figure 6.16: Probability density functions for the BI of the PTFE clamps (left) and CuPEN cables (right).

that CuPEN and PTFE contributions are subdominant, which can be appreciated in Fig. 6.17. In the total budget, we consider thus a BI from the close components $3.9 \pm 0.4 \cdot 10^{-5}$ counts/keV/kg/y, entirely due to surface contamination on copper frames. We plan to further reduce this background by the reduction of the copper surface contaminations with respect to CUORE. In CUPID, we have radically changed the design of the copper frames in order to reduce the machining operations, and succeeded to design copper frames that can be produced exclusively by lamination, bending and laser cutting, thus fully avoiding the need of milling or drilling, likely to introduce contaminants on the surface. In addition, we will improve the control of the storage conditions.

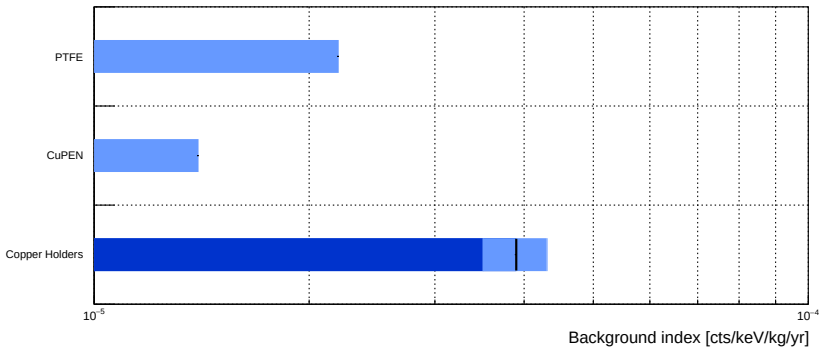

Figure 6.17: Estimations of the BI for close components. For PTFE and CuPEN the prediction are upper limits, shown in light blue.

6.5.7 ^{238}U, ^{232}Th in the close infrastructure

The innermost cryostat thermal shield (10 mK shield) can further contribute to the background via the emission of β and α particles emitted by radioactive contaminants on its inner surface, which has a direct line of sight to the detectors. In the CUORE cryostat, the innermost shield consists of a copper cylinder (10 mK vessel), internally paved with copper tiles (10 mK tiles). The detector towers are attached to a Tower support plate (TSP). A copper plate is placed at the top and bottom of the detectors (Cu plate). A flange on the top of the 10 mK vessel ensures the vacuum tightness (10 mK flange). To evaluate the CUPID background from these

Table 6.4: Background index estimated for the close infrastructure components. (We did not consider surface backgrounds for Tower Support Plate and the 10 mK flange since the location of the source indicates that their contribution is negligible. For the Cu plate, we did not perform bulk simulations because its mass is much smaller than the other components.). * extrapolated from CUORE background model.

Activity	^{226}Ra to ^{210}Pb < 0.5 μBq/kg	^{228}Th to ^{208}Pb < 1.3 μBq/kg	
	BI bulk [ckky]	BI surface (10 μm) [ckky]	BI Tot. [ckky]
10 mK tiles	$< 2.9 \cdot 10^{-8}$	$5.1 \pm 0.5 \cdot 10^{-6}$	$5.1 \pm 0.5 \cdot 10^{-6}$
10 mK vessel	$< 2.7 \cdot 10^{-7}$	$6.6 \pm 1.6 \cdot 10^{-7}$	$7.8^{+2.1}_{-1.4} \cdot 10^{-7}$
Cu plate	-	$5.5^{+1.0}_{-0.8} \cdot 10^{-7}$	$5.5^{+1.0}_{-0.8} \cdot 10^{-7}$
TSP*	$< 2.3 \cdot 10^{-7}$	-	$< 2.3 \cdot 10^{-7}$
10 mK flange	$< 10^{-8}$	-	$< 10^{-8}$
			$6.4\ ^{+0.6}_{-0.5} \cdot 10^{-6}$

components, we have used the activities inferred from the CUORE background model. In this model the above mentioned components are grouped, together with the copper holders, as mentioned above. Thus, the activities are the same as in Table 6.3. We have simulated ^{226}Ra or ^{228}Th subchains with the CUPID Monte Carlo and obtained the background index reported in Table 6.4. The dominant contribution is the surface contamination from the tiles covering the inside of the 10 mK thermal shield. The total expected background from the 10 mK chamber results in $6.4\ ^{+0.6}_{-0.5} \cdot 10^{-6}$ counts/(keV·kg·yr).

6.5.8 ^{238}U, ^{232}Th in the cryostat and radiation shields

As previously discussed, the only contaminants present in the infrastructure that may yield a background in the ^{100}Mo ROI are ^{214}Bi and ^{208}Tl in the shields and cryostat.

The components considered in the evaluation of the CUPID background are: the 50 mK (Heat Exchan in Fig 6.1), 600 mK (Still in Fig 6.1) and 4 K, 40 K and 300 K shields, made of oxygen-free copper, the Internal Lead Shield, made of Roman lead and the Top lead, made of low radioactivity lead. Following the approach in CUORE we have simulated radioactive decays in the 600 mK thermal shield and use this simulation as a proxy for the 50 mK shield, since both spectra are expected to be degenerated. Similarly, we use the simulated spectra for the 4 K shield as a proxy for the 40 K and 300 K shields. The BI from these elements is subdominant, at the level of 10^{-6} counts/keV/kg/y. Table 6.5 gives the activities considered, from the CUORE background model, and the background contributions.

6.5.9 Neutron-induced backgrounds

The dominant neutron background for the $0\nu\beta\beta$ search in CUPID comes from the radioactivity in the surrounding rock. As we have mentioned in section 2.3, the uranium and thorium in the rock produces neutrons with energies of some MeV by (α, n) reactions and spontaneous

Table 6.5: Radioactive contaminations of the CUORE cryostat and shields and the expected background in CUPID. * extrapolated from CUORE background model.

	^{226}Ra to ^{210}Pb	^{228}Th to ^{208}Pb	BI [ckky]
50mK + 600mK	13.1 ± 7.1 μBq/kg	48.5 ± 3.9 μBq/kg	$< 3.8 \cdot 10^{-6}$ ($\sim 1.8 \pm 1.5 \cdot 10^{-6}$)
4K + 40K + 300K	< 43 μBq/kg	< 34 μBq/kg	$< 3.2 \cdot 10^{-7}$
Roman Lead*	< 1.66 μBq/kg	15.4 ± 1.9 μBq/kg	$5.4 \pm 0.7 \cdot 10^{-7}$
Total			$2.4 \pm 1.5 \cdot 10^{-6}$

fission, mainly of ^{238}U. The CUORE infrastructure includes an external passive shield consisting of 18 cm of polyethylene to thermalize neutrons, 2 cm of H_3BO_3 powder to capture thermal neutrons, and at least 25 cm of lead in all directions to absorb γ rays. Residual neutrons that go through the shieldings and arrive inside the cryostat can be captured at the resonance of (n,γ) cross sections and produce γ's up to 10 MeV, in the $0\nu\beta\beta$ signal region. These neutrons have energies between 0.5 eV and 0.5 MeV. Neutrons may also scatter inelastically of nuclei which may deposit MeVs of energy. However neutron inelastic scattering will give a similar signature as an α particle, and can thus be efficiently discriminated.

First simulations were run to assess the neutron induced background due to (n,γ) capture by $Li_2{}^{100}MoO_4$ crystals and by copper components. We expect these components to produce most of the (n,γ) background because of their position in the experimental setup. Preliminary results predict a background in the ROI of the order of 2.65×10^{-5} counts/(keV·kg·yr) with a statistical uncertainty of $\sim 2\%$ and a systematic uncertainty (mainly due to a poor knowledge of the intermediate-energy neutron flux inside the Gran Sasso cavern) up to $\sim 30\%$. This result indicate the need to add an additional polyethylene shielding to further moderate the environmental neutrons. According to the simulations, a 10 cm thick borated-polyethylene layer installed around the existing shields would reduce the (n,γ) background by a factor of ~ 15.

6.5.10 Muon-induced background

Muons underground may produce gammas through radiative energy loss. If the energy of the gamma is ~ 3 MeV, they can mimic a $0\nu\beta\beta$ signal in CUPID. The CUORE background model predicts a BI from muons of $1.26 \pm 0.01 \cdot 10^{-3}$ counts/(keV·kg·yr) if no selection cuts are applied. Thanks to the large granularity in CUPID and CUORE, most of the muons deposit energies in more than one crystal, thus the selection of events with energy deposits in only one crystal largely suppresses this background, reducing it to $5 \cdot 10^{-5}$ counts/(keV·kg·yr) (coincidence time window=5 ms). In CUPID we plan to install a muon veto consisting of plastic scintillator panels to further reduce the muon background. According to simulations the muon veto will have an efficiency ~ 98 %, decreasing the muon background to 1.3×10^{-6} counts/(keV·kg·yr), making it subdominant.

6.5.11 Summary of Backgrounds for CUPID Baseline

The background index probability distributions are shown in Fig. 6.18 for the radioactivity from materials. As discussed previously, the driving background is the surface contaminations in the detector holders (close components) and the next-to-leading contribution is the crystal surface. From the total probability distribution we get the BI in the CUPID ROI expected from radioactive contaminations:

$$B = 0.74^{+0.08}_{-0.07} \cdot 10^{-4} \text{ counts/(keV·kg·yr)} \tag{6.4}$$

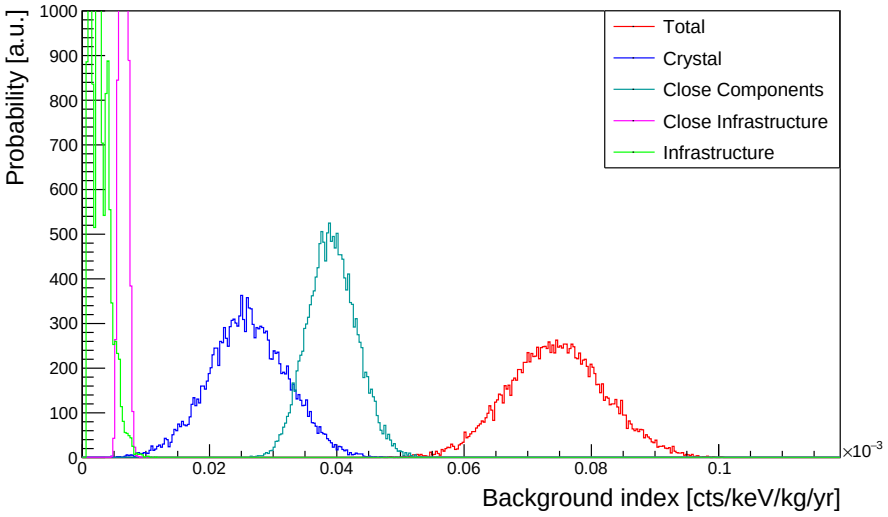

Figure 6.18: Background index distributions in the CUPID ROI from radioactive contaminations.

The total background considers $2\nu\beta\beta$ pile-up, muons and neutrons, which gives the expected BI in the CUPID ROI:

$$B = 1.27^{+0.08}_{-0.07} \cdot 10^{-4} \text{ counts/(keV·kg·yr)} \tag{6.5}$$

As discussed previously we plan to further reduce the background by the reduction of the copper and crystal surface contaminations. We plan to machine the cooper parts by bending and laser cutting to avoid introducing contaminants on the surface. We plan also to have a strict control of the radon and dust during the long-term storage, in addition of the control during the assembly of the detectors. We are pursuing as well a series of tests on crystal surface treatment to further reduce this contamination.

Although the discovery of $0\nu\beta\beta$ is the primary goal of CUPID, the spectrum down to lower energies will allow to study new physics processes outside the Standard Model, which could distort the spectral shape of the $2\nu\beta\beta$ spectrum. This includes $0\nu\beta\beta$ decay with emisson of Majoron(s), $2\nu\beta\beta$ decay with emission of Bosonic neutrinos, Lorentz invariance violation or sterile neutrinos. Spectral shapes studies of $2\nu\beta\beta$ decay, as the one performed with CUPID-Mo, are also extremely helpful to constrain nuclear structure models.

We have considered in our simulations also radionuclides with Q-value lower than 3 MeV to reconstruct the background spectrum down lower energies. The reconstructed spectrum is shown in Fig. 6.20.

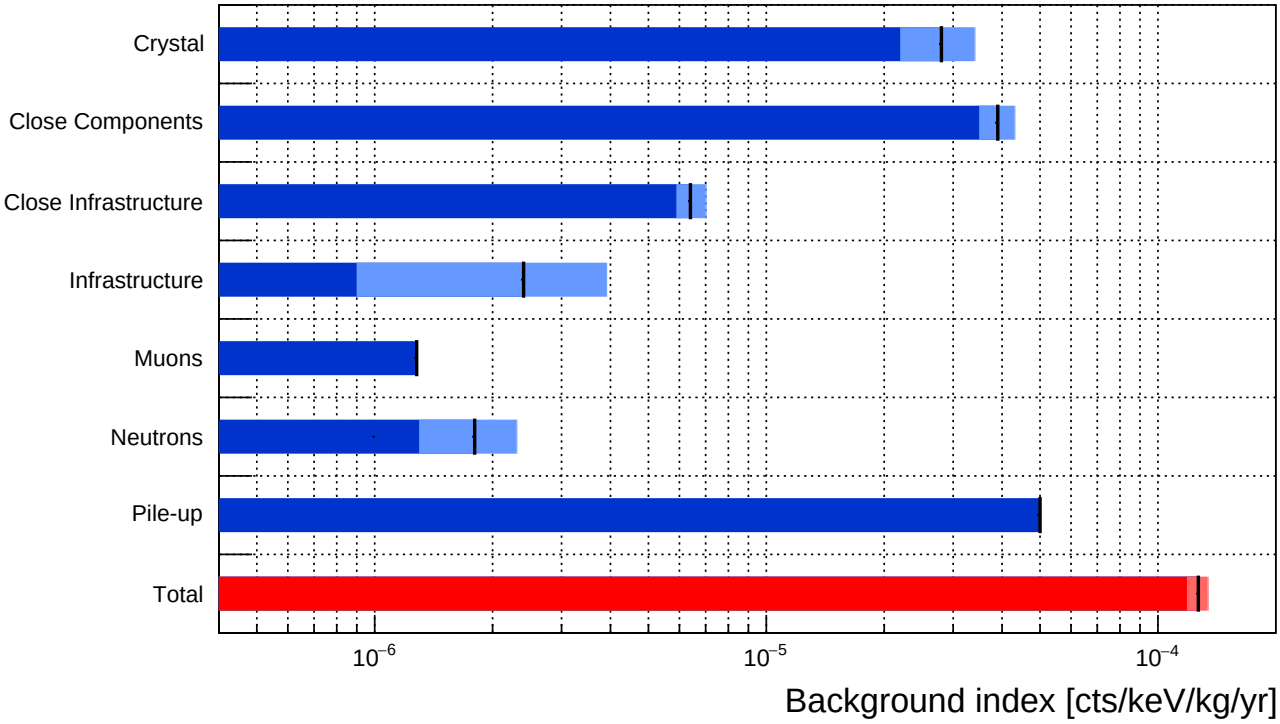

Figure 6.19: Breakdown of the predicted BI in CUPID, in 3034 ± 15 keV around the $Q_{\beta\beta}$ of ^{100}Mo. The backgrounds from radioactive contamination are derived from dedicated simulations combined with results of background models. The crystal contribution is based on activities from the CUPID-Mo background model [147]; the close components, close infrastructure and infrastructure, on the CUORE background model. Muon and neutron predictions are based on simulations and on CUORE data. The $2\nu\beta\beta$ pile-up estimate relies on current extrapolations of results of recent R&D measurements. The black line shows the mean value, and the light band the $\pm 1\sigma$ uncertainty.

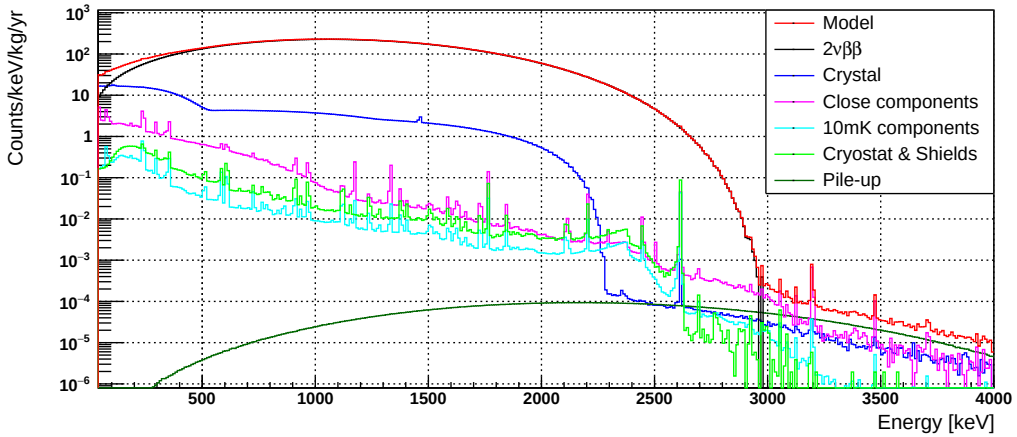

Figure 6.20: Reconstructed simulated background spectrum in CUPID.

6.6 Sensitivity

Considering the parameters given in Table 6.1, the CUPID sensitivity both in terms of $0\nu\beta\beta$ decay half life ($T^{0\nu}_{1/2}$) and $m_{\beta\beta}$ was evaluated. The collaboration used a frequentist and a Bayesian approach to compute exclusion sensitivity and the discovery sensitivity, defined as the value of $T^{0\nu}_{1/2}$ at which there is a 50% probability to make a 3σ discovery. The numerical

calculation is performed by generating toy Monte Carlo pseudo experiments and fitting each with a statistical analysis similar to that we will use in CUPID. In this way we compute the distribution of possible limits and the probability of discovery. For all cases, we convert the sensitivity in $T^{0\nu}_{1/2}$ into a sensitivity in $m_{\beta\beta}$, using a set of nuclear matrix elements (NME) computed with different nuclear models [158, 64, 129, 159, 160, 161, 130]. In a Bayesian analysis the results can depend strongly on the choice of prior. In this analysis we consider a flat prior on the decay rate, or equivalently in $m^2_{\beta\beta}$, this choice is standard in the $0\nu\beta\beta$ community. As a result of the Bayesian exclusion sensitivity analysis, we obtain the distribution of limits shown in Fig 6.21 left, from which we extract the median sensitivity of:

$$T^{0\nu}_{1/2} > 1.6 \cdot 10^{27}\,\text{yr at 90\% confidence level.} \tag{6.6}$$

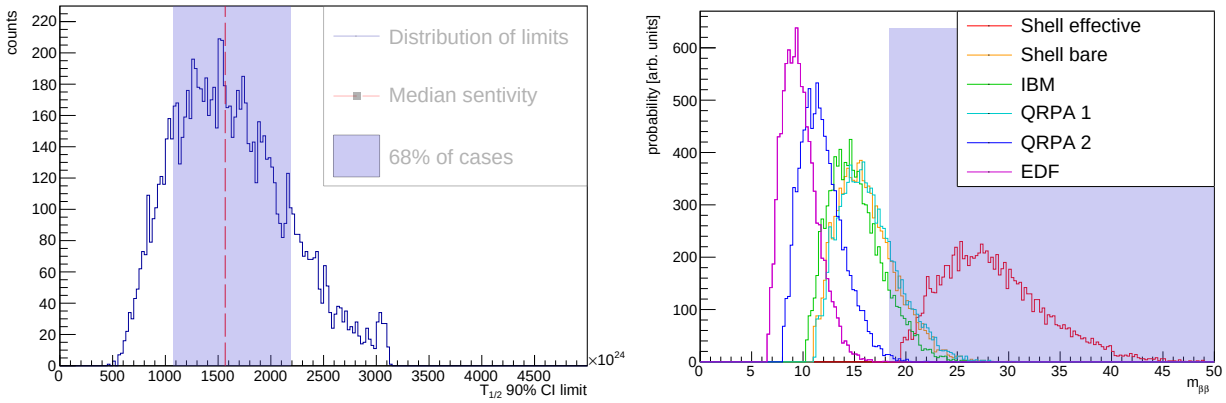

Figure 6.21: Distribution of $T_{1/2}$limits for CUPID. The median sensitivity and interval containing 68 % is also shown (left), and distribution of $m_{\beta\beta}$. The band corresponds to the Inverted Ordering mass region (right), obtained with a Bayesian analysis.

This value corresponds to a set of different $m_{\beta\beta}$ values, shown in Fig 6.21 (right). The lower value is obtained with the EDF model [158], and corresponds to 9.6 meV. The upper value can be obtained by the IBM and QRPA models [130, 64] and corresponds to 16.3 meV. Recently, an effective shell model calculation, which has not yet been validated by any independent calculation, resulted in a smaller NME value [161], which would further increase the upper $m_{\beta\beta}$ value to 28.3 meV.

In the frequentist approach we obtain an exclusion sensitivity of $T_{1/2} > 1.8 \cdot 10^{27}$ yr at 90% confidence level. In terms of effective Majorana mass, this becomes $m_{\beta\beta}$ <9–26 meV (or $m_{\beta\beta}$ <9–15 meV if we exclude the effective shell model).

For the discovery sensitivity we observed that in the Bayesian analysis the result is strongly dependent on the choice of prior. Since different choices would largely impact the results, the discovery case was not computed in the Bayesian framework. From the frequentist analysis, we get that, with a 10 yr livetime, CUPID will reach a 3σ discovery sensitivity of $T^{0\nu}_{1/2} = 1.0 \cdot 10^{27}$ yr. This value corresponds to a set of different $m_{\beta\beta}$ values that range in $m_{\beta\beta}$ =12–36 meV (or $m_{\beta\beta}$ =12–21 meV if we exclude the shell model). We use the output of the $T^{0\nu}_{1/2}$ discovery sensitivity to extract the discovery probability as a function of $m_{\beta\beta}$, shown in Fig. 6.22.

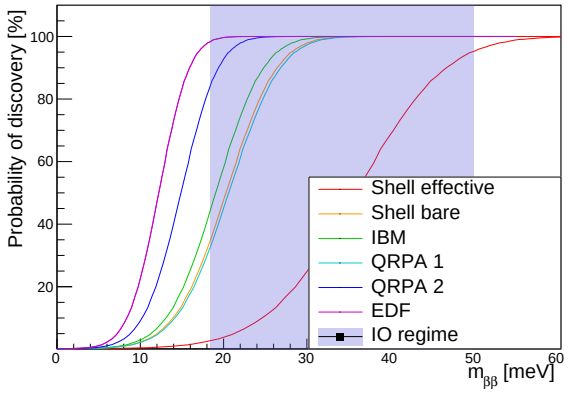

Figure 6.22: Probability of discovery in the frequentist approach, as a function of $m_{\beta\beta}$, assuming different values of NME. The shaded area corresponds to the allowed $m_{\beta\beta}$ range in the inverted ordering,

6.7 Perspectives

CUPID will contain 450 kg of $Li_2{}^{100}MoO_4$ crystals, corresponding to 240 kg of ^{100}Mo, expected to be operated at a background index of $\sim 10^{-4}$ counts/(keV·kg·yr). The sensitivity to the $0\nu\beta\beta$ half-life of ^{100}Mo will be $\sim 10^{27}$ years in 10 years of data taking, corresponding to ~ 10 meV in terms of the effective Majorana mass. The original plan for the purchase of the enriched isotope and the crystal growing was to go on with the scheme followed in CUPID-Mo, which involved Russian providers for both the enriched isotope and the crystal growers. However, the geopolitical situation caused by the Russian war against Ukraine prevented us from purchasing the crystals and isotopes from Russia. Presently, the CUPID collaboration has found a crystal vendor and we will be able to proceed. The CUPID timeline is defined to a large extent by the time needed for isotope enrichment and crystal growth. These will span over 4- 5 years. Starting the isotope enrichment in 2025, we expect to deploy the CUPID detectors by 2030.

After the completion of CUPID, we may consider a possible scenario, in the framework of a phased approach in an enlarged CUPID program. A new detector, with the same parameters as CUPID, could be deployed in the CUORE cryostat, but with a further reduction of the background down to $2 \cdot 10^{-5}$ counts/(keV·kg·yr). Reaching this background could be possible with a reduction of the $2\nu\beta\beta$ pileup through faster sensors, plus a reduction of the surface background from the crystals and copper, through pulse shape discrimination. The discovery sensitivity that could be reached with such a detector, named CUPID-reach, is shown in Fig. 6.23.

Next-to-next generation $0\nu\beta\beta$ decay experiments, at time scales of 15 - 25 years from now, aim at a discovery of a $0\nu\beta\beta$ signal. The sensitivities of next-to-next generation experiments would be $\sim 10^{29}$ years for the $0\nu\beta\beta$ decay half-life, and the corresponding sensitivities for $m_{\beta\beta}$ of ~ 2.5 meV, see Fig. 6.24. The discovery of a signal at such scales has some 'theoretical' arguments. Some theoretical models focusing on the coarse structure of the mass matrix predict that $m_{\beta\beta} = \mathcal{O}(1) + \sqrt{\Delta m^2_{atm}} \cdot \theta_c^n$ with n=1, 2 $\rightarrow m_{\beta\beta} \sim 10$ meV for n=1 [8].

In view of an ultimate bolometric $0\nu\beta\beta$ decay experiment, we may consider "CUPID-1T", consisting of 1.8 tons of $Li_2{}^{100}MoO_4$ crystals, corresponding to 1000 kg of ^{100}Mo. Such detector would need a new cryostat approximately 4 times larger than CUORE. To reach the required sensitivity (Fig. 6.23), the backgrounds should be reduced to the level of $5 \cdot$

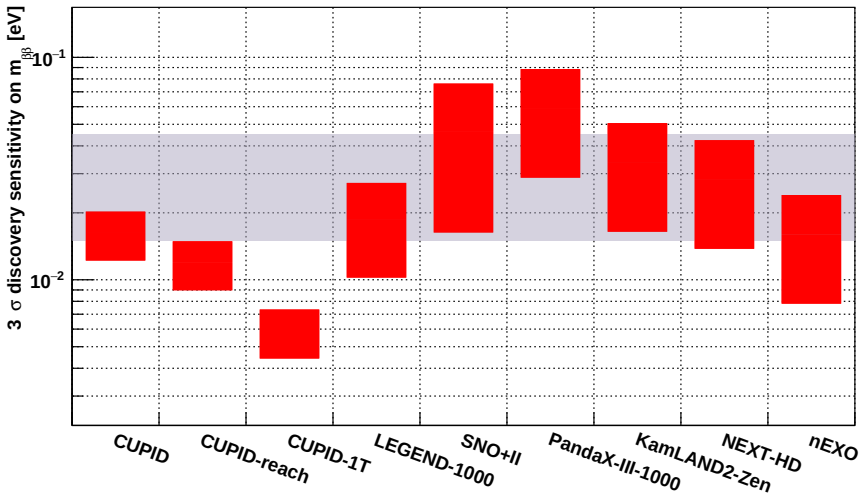

Figure 6.23: Discovery sensitivity for a selected set of next-generation ton-scale experiments.The grey shaded region corresponds to the parameter region allowed in the Inverted Hierarchy of the neutrino mass. The red error bars show the $m_{\beta\beta}$ values such that an experiment can make at least a 3σ discovery, within the range of the nuclear matrix elements for a given isotope. Note that the shell model NME is not included in the CUPID program estimations. The parameters of other experiments are taken from Refs. [40, 41, 42]. Reproduced from [43].

10^{-6}counts/(keV·kg·yr).

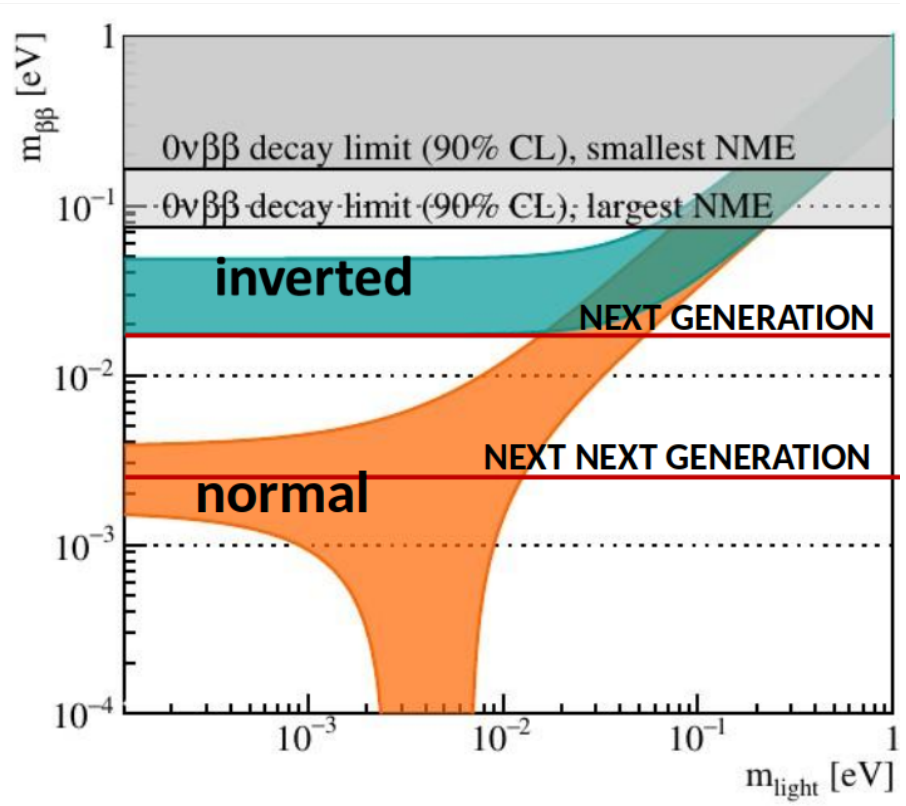

Figure 6.24

Conclusion

Neutrinoless double beta decay and dark matter searches poses an experimental challenge as in both searches the hypothetical signals are expected to happen at very low rates, competing with the background from natural radioactivity that populates the region of interest. However, the reward is worth the effort. If neutrinoless double beta decay is observed, it would demonstrate that neutrino is the only fermion to be a Majorana particle, and thus, that lepton number is non conserved, opening the door to physics beyond the Standard Model. The dark matter paradigm sets its basis on cosmology and astrophysical observations, rather than on particle physics. Both searches need to understand and to reduce the backgrounds to extremely low levels. My work is dedicated to such background studies. We need, in the first place, to build the detectors with radiopure materials. We developed two ultra-low background HPGe γ-ray spectrometers, today in operation at the Laboratoire Souterrain de Modane. One of them is among the most sensitive γ-ray Ge spectrometers world-wide. The most sensitive detector to my knowledge for the measurement of ^{208}Tl and ^{214}Bi contamination on surfaces is the BiPo-3 detector, developed in the frame of the SuperNEMO $0\nu\beta\beta$ decay experiment, which we have employed for the measurement of the $0\nu\beta\beta$ sources in the experiment. However, at present the low radioactivity techniques are not sensitive enough to measure the levels of radioactivity needed in $0\nu\beta\beta$ decay and dark matter experiments. We need to develop new techniques based on innovative technologies.

The EDELWEISS-II dark matter experiment, located at LSM, aimed at the direct detection of WIMPs with masses in the range 10 GeV to a few TeV. The elastic collision with the target nuclei would generate energy deposits $\leq$ 100 keV. EDELWEISS detectors were germanium crystals equipped with dual heat and ionization measurement to discriminate γ/β-induced electronic recoils from potential WIMP-induced nuclear recoils. Thanks to the so-called 'interleaved detectors', EDELWEISS-II was also able to reject the surface backgrounds that were limiting the sensitivity. We continued with the EDELWEISS-III phase, which consisted of 36 Ge detectors of 800 g each, in order to increase the exposure. We upgraded the set-up with more radiopure materials and additional shieldings, selected through a vast screening campaign. We developed a background model of the gamma background, which could reproduce the spectrum of the EDELWEISS-II data, and used the results for the design of EDELWEISS-III.

CUORE is at present the largest $0\nu\beta\beta$ bolometric detector, operating at LNGS. It is based on a pure bolometric technique, via the detection of the heat deposited in a particle interaction with the detection crystal. The CUORE background is dominated by surface α's from the surfaces facing the crystals. Thanks to scintillating bolometers, CUPID will reduce the background by two orders of magnitude. The performance of this technique was demonstrated in the CUPID-Mo experiment, located in the Laboratoire Souterrain de Modane, operating between 2019 and 2020. In our continuous quest to understand the background, we have developed a background model which reproduces well the CUPID-Mo data. We could determine the

radiopurity levels of the $Li_2{}^{100}MoO_4$ crystals, which were proven to be sufficient to reach the CUPID background goals. In case of a discovery of $0\nu\beta\beta$ decay we will need to better constrain the nuclear models. At present, the nuclear matrix elements are calculated with differences in the results up to a factor 3. The possibility of a quenching of the axial vector coupling constant g_A would have a significant - negative- impact on the $m_{\beta\beta}$ predictions, as the rate relates to $m_{\beta\beta}$ through g_A^4. The 'quenching' is in fact observed in some β and $2\nu\beta\beta$ decays, but the case in $0\nu\beta\beta$ decay remains an open issue. $2\nu\beta\beta$ decay is an allowed Standard Model process which can give complementary information to constrain the nuclear physics uncertainties affecting $0\nu\beta\beta$ decay. Thanks to the robust background model developed for CUPID-Mo we were able to obtain the first of its kind measurement of a novel nuclear structure observable based on an improved description of the $2\nu\beta\beta$ decay. So far, a similar analysis has been performed by the KamLand-Zen experiment [162], but they could only establish upper bounds. These measurements can provide experimental data to help theorists improve the nuclear physics calculations which will be needed to interpret a possible discovery of $0\nu\beta\beta$ decay.

Bibliography

[1] Fireman, "A Measurement of the Half-Life of Double Beta-Decay from ^{124}Sn," *Phys. Rev.*, no. 45, pp. 323–324, 1949.

[2] E. L. Fireman and D. Schwarzer, "A Re-Investigation of the Double Beta-Decay from ^{124}Sn," *Phys. Rev.*, vol. 4, no. 86, pp. 451–453, 1952.

[3] E. Der Mateosian and M. Goldhaber, "Limits for Lepton-Conserving and Lepton-Nonconserving Double Beta Decay in ^{48}Ca," *Phys. Rev.*, vol. 4, no. 146, p. 810, 1966.

[4] A. Drukier and L. Stodolsky, "Principles and applications of a neutral-current detector for neutrino physics and astronomy," *Phys. Rev. D*, vol. 30, pp. 2295–2309, Dec 1984.

[5] M. W. Goodman and E. Witten, "Detectability of Certain Dark Matter Candidates," *Phys. Rev. D*, vol. 31, p. 3059, 1985.

[6] K. Borer *et al.*, "First results with the ORPHEUS dark matter detector," *Astropart. Phys.*, vol. 22, pp. 199–210, 2004.

[7] S. P. Ahlen, F. T. Avignone, R. L. Brodzinski, A. K. Drukier, G. Gelmini, and D. N. Spergel, "Limits on Cold Dark Matter Candidates from an Ultralow Background Germanium Spectrometer," *Phys. Lett. B*, vol. 195, pp. 603–608, 1987.

[8] M. Agostini, G. Benato, J. A. Detwiler, J. Menéndez, and F. Vissani, "Toward the discovery of matter creation with neutrinoless $\beta\beta$ decay," *Rev. Mod. Phys.*, vol. 95, no. 2, p. 025002, 2023.

[9] S. Bilenky, "Neutrino Masses from the Point of View of Economy and Simplicity," *Phys. Part. Nucl.*, vol. 50, no. 6, pp. 645–662, 2019.

[10] E. Akhmedov, "Majorana neutrinos and other Majorana particles:Theory and experiment," *arXiv e-prints*, p. arXiv:1412.3320, Dec. 2014.

[11] M. Fukugita and T. Yanagida, "Baryogenesis Without Grand Unification," *Phys. Lett. B*, vol. 174, pp. 45–47, 1986.

[12] T. Tomoda, "Double beta decay," *Rept. Prog. Phys.*, vol. 54, pp. 53–126, 1991.

[13] C. Giganti, S. Lavignac, and M. Zito, "Neutrino oscillations: The rise of the PMNS paradigm," *Progress in Particle and Nuclear Physics*, vol. 98, pp. 1–54, 2018.

[14] A. Cabrera *et al.*, "Synergies and prospects for early resolution of the neutrino mass ordering," *Sci. Rep.*, vol. 12, no. 1, p. 5393, 2022.

[15] K. Sakashita, "Neutrino physics," *Journal of Physics: Conference Series*, vol. 2446, no. 012026, 2023.

[16] J. Engel and J. Menéndez, "Status and Future of Nuclear Matrix Elements for Neutrinoless Double-Beta Decay: A Review," *Rept. Prog. Phys.*, vol. 80, no. 4, p. 046301, 2017.

[17] J. T. Suhonen, "Value of the Axial-Vector Coupling Strength in β and $\beta\beta$ Decays: A Review," *Front. in Phys.*, vol. 5, p. 55, 2017.

[18] J. Kotila and F. Iachello, "Phase space factors for double-β decay," *Phys. Rev. C*, vol. 85, p. 034316, 2012.

[19] F. Šimkovic, R. Dvornický, D. Stefánik, and A. Faessler, "Improved description of the $2\nu\beta\beta$ -decay and a possibility to determine the effective axial-vector coupling constant," *Phys. Rev. C*, vol. 97, no. 3, p. 034315, 2018.

[20] F. Šimkovic, V. Rodin, A. Faessler, and P. Vogel, "$0\nu\beta\beta$ and $2\nu\beta\beta$ nuclear matrix elements, quasiparticle random-phase approximation, and isospin symmetry restoration," *Phys. Rev. C*, vol. 87, no. 4, p. 045501, 2013.

[21] J. Suhonen and O. Civitarese, "Probing the quenching of g_A by single and double beta decays," *Phys. Lett. B*, vol. 725, pp. 153–157, 2013.

[22] P. Gysbers *et al.*, "Discrepancy between experimental and theoretical β-decay rates resolved from first principles," *Nature Phys.*, vol. 15, no. 5, pp. 428–431, 2019.

[23] J. Suhonen, "Electron spectra of forbidden β decays and the effective value of the axial-vector coupling constant g_A," *AIP Conf. Proc.*, vol. 1894, no. 1, p. 020024, 2017.

[24] J. Kostensalo, J. Suhonen, J. Volkmer, S. Zatschler, and K. Zuber, "Confirmation of gA quenching using the revised spectrum-shape method for the analysis of the 113Cd β-decay as measured with the COBRA demonstrator," *Phys. Lett. B*, vol. 822, p. 136652, 2021.

[25] A. F. Leder *et al.*, "Determining g_A/g_V with High-Resolution Spectral Measurements Using a $LiInSe_2$ Bolometer," *Phys. Rev. Lett.*, vol. 129, no. 23, p. 232502, 2022.

[26] M. Haaranen, J. Kotila, and J. Suhonen, "Spectrum-shape method and the next-to-leading-order terms of the β-decay shape factor," *Phys. Rev. C*, vol. 95, p. 024327, 2017.

[27] D. Mund, B. Maerkisch, M. Deissenroth, J. Krempel, M. Schumann, H. Abele, A. Petoukhov, and T. Soldner, "Determination of the Weak Axial Vector Coupling from a Measurement of the Beta-Asymmetry Parameter A in Neutron Beta Decay," *Phys. Rev. Lett.*, vol. 110, p. 172502, 2013.

[28] B. Märkisch *et al.*, "Measurement of the Weak Axial-Vector Coupling Constant in the Decay of Free Neutrons Using a Pulsed Cold Neutron Beam," *Phys. Rev. Lett.*, vol. 122, no. 24, p. 242501, 2019.

[29] L. Jokiniemi, B. Romeo, P. Soriano, and J. Menéndez, "Neutrinoless $\beta\beta$-decay nuclear matrix elements from two-neutrino $\beta\beta$-decay data," *Phys. Rev. C*, vol. 107, no. 4, p. 044305, 2023.

[30] G. Adhikari *et al.*, "nEXO: neutrinoless double beta decay search beyond 10^{28} year half-life sensitivity," *J. Phys. G*, vol. 49, no. 1, p. 015104, 2022.

[31] J. Martín-Albo *et al.*, "Sensitivity of NEXT-100 to Neutrinoless Double Beta Decay," *JHEP*, vol. 05, p. 159, 2016.

[32] C. Adams *et al.*, "Sensitivity of a tonne-scale NEXT detector for neutrinoless double beta decay searches," *JHEP*, vol. 2021, no. 08, p. 164, 2021.

[33] J. Renner *et al.*, "Energy calibration of the NEXT-White detector with 1% resolution near $Q_{\beta\beta}$ of^{136}Xe," *JHEP*, vol. 10, p. 230, 2019.

[34] X. Chen *et al.*, "PandaX-III: Searching for neutrinoless double beta decay with high pressure^{136}Xe gas time projection chambers," *Sci. China Phys. Mech. Astron.*, vol. 60, no. 6, p. 061011, 2017.

[35] Y. Gando *et al.*, "The nylon balloon for xenon loaded liquid scintillator in KamLAND-Zen 800 neutrinoless double-beta decay search experiment," *JINST*, vol. 16, no. 08, p. P08023, 2021.

[36] S. Abe *et al.*, "Search for the Majorana Nature of Neutrinos in the Inverted Mass Ordering Region with KamLAND-Zen," *Phys. Rev. Lett.*, vol. 130, no. 5, p. 051801, 2023.

[37] J. Shirai, "Results and future plans for the KamLAND-Zen experiment," *J. Phys. Conf. Ser.*, vol. 888, no. 1, p. 012031, 2017.

[38] V. Albanese *et al.*, "The SNO+ experiment," *JINST*, vol. 16, no. 08, p. P08059, 2021.

[39] N. Abgrall *et al.*, "The Large Enriched Germanium Experiment for Neutrinoless $\beta\beta$ Decay: LEGEND-1000 Preconceptual Design Report," 2021.

[40] M. Agostini, G. Benato, and J. Detwiler, "Discovery probability of next-generation neutrinoless double- β decay experiments," *Phys. Rev. D*, vol. 96, no. 5, p. 053001, 2017.

[41] J. J. Gomez-Cadenas, "Status and prospects of the NEXT experiment for neutrinoless double beta decay searches," in *54th Rencontres de Moriond on Electroweak Interactions and Unified Theories*, pp. 201–206, 2019.

[42] J. Galan *et al.*, "Topological background discrimination in the PandaX-III neutrinoless double beta decay experiment," *J. Phys. G*, vol. 47, no. 4, p. 045108, 2020.

[43] "CUPID-pre-CDR," *CUPID pre-CDR, arXiv:1907.09376 [physics.ins-det]*, 2019.

[44] S. Andringa *et al.*, "Current Status and Future Prospects of the SNO+ Experiment," *Adv. High Energy Phys.*, vol. 2016, p. 6194250, 2016.

[45] T. Kaptanoglu *et al.*, "Neutrino Physics with SNO+," *Talk at TAUP 2023*, 2023.

[46] P. Novella *et al.*, "Measurement of the ^{136}Xe two-neutrino double beta decay half-life via direct background subtraction in NEXT," *Phys. Rev. C*, vol. 105, no. 05501, 2022.

[47] E. Fiorini, A. Pullia, G. Bertolini, F. Cappellani, and G. Restelli, "A Search for Lepton Nonconservation in Double Beta Decay With a Germanium Detector," *Phys. Lett. B*, vol. 25, pp. 602–603, 1967.

[48] H. V. Klapdor-Kleingrothaus *et al.*, "Latest results from the Heidelberg-Moscow double beta decay experiment," *Eur. Phys. J. A*, vol. 12, pp. 147–154, 2001.

[49] M. Agostini *et al.*, "Final Results of GERDA on the Search for Neutrinoless Double-β Decay," *Phys. Rev. Lett.*, vol. 125, no. 25, p. 252502, 2020.

[50] E. Andreotti *et al.*, "130Te Neutrinoless Double-Beta Decay with CUORICINO," *Astropart. Phys.*, vol. 34, pp. 822–831, 2011.

[51] D. Adams *et al.*, "Improved Limit on Neutrinoless Double-Beta Decay in ^{130}Te with CUORE," *Phys. Rev. Lett.*, vol. 124, no. 12, p. 122501, 2020.

[52] D. Q. Adams *et al.*, "Measurement of the $2\nu\beta\beta$ Decay Half-Life of ^{130}Te with CUORE," *Phys. Rev. Lett.*, vol. 126, no. 17, p. 171801, 2021.

[53] D. Q. Adams *et al.*, "Search for Majorana neutrinos exploiting millikelvin cryogenics with CUORE," *Nature*, vol. 604, no. 7904, pp. 53–58, 2022.

[54] D. Q. Adams *et al.*, "New direct limit on neutrinoless double beta decay half-life of ^{128}Te with cuore," *Phys. Rev. Lett.*, vol. 129, p. 222501, Nov 2022.

[55] K. Alfonso [CUORE collab.], "Latest results from the CUORE experiment," *Talk at TAUP 2023*, August 2023.

[56] E. Armengaud *et al.*, "Development of ^{100}Mo-containing scintillating bolometers for a high-sensitivity neutrinoless double-beta decay search," *Eur. Phys. J. C*, vol. 77, no. 11, p. 785, 2017.

[57] O. Azzolini *et al.*, "Final Result on the Neutrinoless Double Beta Decay of ^{82}Se with CUPID-0," *Physical Review Letters*, vol. 129, no. 11, p. 111801, 2022.

[58] E. Armengaud *et al.*, "The CUPID-Mo experiment for neutrinoless double-beta decay: performance and prospects," *Eur. Phys. J. C*, vol. 80, no. 1, p. 44, 2020.

[59] H. B. Kim *et al.*, "Status and Performance of the AMoRE-I Experiment on Neutrinoless Double Beta Decay," *J. Low Temp. Phys.*, vol. 209, no. 5-6, pp. 962–970, 2022.

[60] O. Yoomin, "AMoRE-II preparation and status," *Talk at TAUP 2023*, August 2023.

[61] R. Arnold *et al.*, "Results of the search for neutrinoless double-β decay in ^{100}Mo with the NEMO-3 experiment," *Phys. Rev. D*, vol. 92, no. 7, p. 072011, 2015.

[62] A. S. Barabash *et al.*, "Calorimeter development for the SuperNEMO double beta decay experiment," *Nucl. Instrum. Meth. A*, vol. 868, pp. 98–108, 2017.

[63] D. Moore, "Double beta decay review, theory and experiment," *Talk at TAUP 2023*, August 2023.

[64] J. Hyvärinen and J. Suhonen, "Nuclear matrix elements for $0\nu\beta\beta$ decays with light or heavy Majorana-neutrino exchange," *Phys. Rev. C*, vol. 91, no. 2, p. 024613, 2015.

[65] F. Šimkovic, A. Smetana, and P. Vogel, "$0\nu\beta\beta$ and $2\nu\beta\beta$ nuclear matrix elements evaluated in closure approximation, neutrino potentials and su(4) symmetry," *Phys. Rev. C*, vol. 98, p. 064325, 2018.

[66] J. Terasaki, "Strength of the isoscalar pairing interaction determined by a relation between double-charge change and double-pair transfer for double-β decay," *Phys. Rev. C*, vol. 102, p. 044303, Oct 2020.

[67] N. Aghanim *et al.*, "Planck 2018 results. VI. Cosmological parameters," *Astron. Astrophys.*, vol. 641, p. A6, 2020. [Erratum: Astron.Astrophys. 652, C4 (2021)].

[68] J. Billard, M. Boulay, S. Cebrián, L. Covi, G. Fiorillo, A. Green, J. Kopp, B. Majorovits, K. Palladino, F. Petricca, L. Roszkowski (chair), and M. Schumann, "Direct detection of dark matter—APPEC committee report," *Reports on Progress in Physics*, vol. 85, p. 056201, Apr. 2022.

[69] M. Battaglieri *et al.*, "US cosmic visions: New ideas in dark matter 2017: Community report,"

[70] G. Heusser, "Low-radioactivity background techniques," *Ann. Rev. Nucl. Part. Sci.*, vol. 45, pp. 543–590, 1995.

[71] A. Ianni, "Underground laboratories possibilitties," *Talk at workshop: Fostering citizens role in the advance of ground-breaking research in Fundamental Science, Pisa*, September 2022.

[72] P. Loaiza, "The ANDES deep underground laboratory project," *Talk at Low Radioactivity Techniques, LRT 2019, Jaca,*, May 2019.

[73] M. Ambrosio *et al.*, "Measurement of the residual energy of muons in the Gran Sasso underground laboratories," *Astropart. Phys.*, vol. 19, pp. 313–328, 2003.

[74] D. Mei and A. Hime, "Muon-induced background study for underground laboratories," *Phys. Rev. D*, vol. 73, p. 053004, 2006.

[75] H. O. Back, W. Bonivento, M. Boulay, E. Church, S. R. Elliott, F. Gabriele, C. Galbiati, G. K. Giovanetti, C. Jackson, A. McDonald, A. Renshaw, R. Santorelli, K. Scholberg, M. Simeone, R. Tayloe, and R. V. de Water, "A facility for low-radioactivity underground argon," 2022.

[76] M. J. Carson, J. C. Davies, T. J. Sumner, H. M. Araujo, V. A. Kudryavtsev, M. Robinson, and N. J. C. Spooner, "Veto performance for large-scale xenon dark matter detectors," *Nucl. Instrum. Meth. A*, vol. 548, pp. 418–426, 2005.

[77] "SRIM - The Stopping and Range of Ions in Matter." http://www.srim.org/. Accessed: 2008.

[78] A. Lubashevskiy, "PhD thesis: Results of WIMP search with Edelweiss." http://edelweiss.in2p3.fr/Publications/Docs/Lubashevskiy_thesis.pdf. in Russian.

[79] M. Wójcik and G. Zuzel, "Behaviour of the ^{222}Rn daughters on copper surfaces during cleaning," in *Proceedings, 2nd Topical Workshop on Low Radioactivity Techniques (LRT 2006), October 1-4 , 2006* (P. Loaiza, ed.), vol. 897, p. 53, AIP, 2007.

[80] P. Loaiza, V. Brudanin, J.-L. Reyss, I. Stekl, G. Warot, and M. Zampaolo, "Air radioactivity levels following the Fukushima reactor accident measured at the Laboratoire de Modane, France," *Journal of Environmental Radioactivity*, vol. 114, p. 66, 2012.

[81] O. Masson *et al.*, "Tracking of airborne radionuclides from the damaged Fukushima Daiichi nuclear reactors by European networks," *Environ Sci Technol.*, vol. 45(18), pp. 7670–7, 2011.

[82] A. Gando *et al.*, "Limit on Neutrinoless $\beta\beta$ Decay of Xe-136 from the First Phase of KamLAND-Zen and Comparison with the Positive Claim in Ge-76," *Physical Review Letters*, vol. 110, Feb. 2013.

[83] A. Gando *et al.*, "Search for Majorana Neutrinos Near the Inverted Mass Hierarchy Region with KamLAND-Zen," *Physical Review Letters*, vol. 117, Aug. 2016.

[84] J. A. Formaggio and C. J. Martoff, "Backgrounds to sensitive experiments underground," *Ann. Rev. Nucl. Part. Sci.*, vol. 54, pp. 361–412, 2004.

[85] Wilson *et al.*, "SOURCES4A," *Technical Report LA-13639-MS*, vol. Los Alamos, 1999.

[86] V. Chazal, B. Chambon, M. De Jesus, D. Drain, C. Pastor, L. Vagneron, R. Brissot, J. F. Cavaignac, A. Stutz, and Y. Giraud-Heraud, "Neutron background measurements in the underground laboratory of Modane," *Astropart. Phys.*, vol. 9, pp. 163–172, 1998.

[87] R. Lemrani, M. Robinson, V. A. Kudryavtsev, M. De Jesus, G. Gerbier, and N. J. C. Spooner, "Low energy neutron propagation in MCNPX and GEANT4," *Nucl. Instrum. Meth. A*, vol. 560, pp. 454–459, 2006.

[88] Y. F. Wang, V. Balic, G. Gratta, A. Fasso, S. Roesler, and A. Ferrari, "Predicting neutron production from cosmic ray muons," *Phys. Rev. D*, vol. 64, p. 013012, 2001.

[89] M. Neuberger, L. Pertoldi, S. Schönert, and C. Wiesinger, "The cosmic muon-induced background for the LEGEND-1000 alternative site at LNGS," *J. Phys. Conf. Ser.*, vol. 2156, no. 1, p. 012216, 2021.

[90] C. Wiesinger, L. Pandola, and S. Schönert, "Virtual depth by active background suppression: revisiting the cosmic muon induced background of Gerda Phase II," *The European Physical Journal C*, vol. 78, July 2018.

[91] J. Billard, E. Figueroa-Feliciano, and L. Strigari, "Implication of neutrino backgrounds on the reach of next generation dark matter direct detection experiments," *Phys. Rev. D*, vol. 89, p. 023524, Jan 2014.

[92] C. Augier *et al.*, "Measurement of the $2\nu\beta\beta$ Decay Rate and Spectral Shape of ^{100}Mo from the CUPID-Mo Experiment," *Phys. Rev. Lett.*, vol. 131, no. 16, p. 162501, 2023.

[93] C. Arpesella *et al.*, "Measurements of extremely low radioactivity levels in BOREXINO," *Astropart. Phys.*, vol. 18, pp. 1–25, 2002.

[94] R. Arnold *et al.*, "Technical design and performance of the NEMO 3 detector," *Nucl. Instrum. Meth. A*, vol. 536, pp. 79–122, 2005.

[95] M. Hult *et al.*, "Recent developments in ultra low-level gamma-ray spectrometry at IRMM," *Appl. Rad. and Isotopes*, vol. 53, p. 225, 2000.

[96] J. Autran, D. Munteanu, P. Roche, G. Gasiot, S. Martinie, S. Uznanski, S. Sauze, S. Semikh, E. Yakushev, S. Rozov, P. Loaiza, G. Warot, and M. Zampaolo, "Soft-errors induced by terrestrial neutrons and natural alpha-particle emitters in advanced memory circuits at ground level," *Microelectronics Reliability*, vol. 50, no. 9, pp. 1822–1831, 2010.

[97] J.-L. Autran, P. Roche, S. Sauze, G. Gasiot, D. Munteanu, P. Loaiza, M. Zampaolo, and J. Borel, "Altitude and Underground Real-Time SER Characterization of CMOS 65 nm SRAM," *IEEE Transactions on Nuclear Science*, vol. 56, pp. 2258–2266, Aug. 2009.

[98] H. Neder, G. Heusser, and M. Laubenstein, "Low level γ-ray germanium-spectrometer to measure very low primordial radionuclide concentrations," *Appl. Rad. and Isot.*, vol. 53, p. 191, 2000.

[99] G. Heusser, M. Laubenstein, and H. Neder, "Low-level germanium gamma-ray spectrometry at the μBq/kg level and future developments towards higher sensitivity," *In Radionucleides in the Environment Int. Conference on Isotopes and Environmental Studies,*, vol. 8, p. 495, 2006.

[100] M. Laubenstein *et al.*, "Underground meaurements of radioactivity," *Applied Radiation and Isotopes*, vol. 61, pp. 167–172, 2004.

[101] P. Loaiza, C. Chassaing, P. Hubert, A. Nachab, F. Perrot, J. L. Reyss, and G. Warot, "Low background germanium planar detector for gamma-ray spectrometry," *Nucl. Instrum. Meth. A*, vol. 634, pp. 64–70, 2011.

[102] V. Brudanin, V. Egorov, R. Hodák, A. Klimenko, P. Loaiza, F. Mamedov, F. Piquemal, E. Rukhadze, N. Rukhadze, I. Štekl, Y. Shitov, G. Warot, E. Yakushev, and M. Zampaolo, "Development of the ultra-low background HPGe spectrometer OBELIX at Modane underground laboratory," *Journal of Instrumentation*, vol. 12, p. P02004, feb 2017.

[103] P. Loaiza, V. Brudanin, F. Piquemal, E. Rukhadze, N. Rukhadze, I. Stekl, G. Warot, and M. Zampaolo, "Obelix, a new low-background HPGe at Modane Underground Laboratory," *AIP Conf. Proc.*, vol. 1672, no. 1, p. 130002, 2015.

[104] R. Arnold *et al.*, "Investigation of double beta decay of ^{100}Mo to excited states of ^{100}Ru," *Nucl. Phys. A*, vol. 925, pp. 25–36, 2014.

[105] E. Rukhadze *et al.*, "Investigations of 2β decay of ^{106}Cd and ^{58}Ni with HPGe spectrometer OBELIX," *AIP Conf. Proc.*, vol. 1672, no. 1, p. 130005, 2015.

[106] V. N. Epov *et al.*, "Direct determination of ^{226}Ra in environmental matrices using collision cell inductively coupled plasma mass-spectrometry.," *Journal of Radioanalytical and Nuclear Chemistry*, vol. 256, pp. 53–60, 2003.

[107] I. J. Arnquist and E. W. Hoppe, "The quick and ultrasensitive determination of K in NaI using inductively coupled plasma mass spectrometry," *Nuclear Instruments and Methods in Physics Research Section A: Accelerators, Spectrometers, Detectors and Associated Equipment*, vol. 851, pp. 15–19, 2017.

[108] N. Abgrall *et al.*, "The Majorana Demonstrator radioassay program," *Nuclear Instruments and Methods in Physics Research Section A: Accelerators, Spectrometers, Detectors and Associated Equipment*, vol. 828, pp. 22–36, 2016.

[109] M. Sisti, "Neutron Activation Analysis for low background experiments, GDR Deep Underground Physics kick-off meeting, 1 June 2021."

[110] G. Zuzel *et al.*, "Removal of Long-Lived Radon Daughters From Surfaces," *Talk at LRT 2022*, 2022.

[111] G. Benato *et al.*, "Development of an ultralow-background bolometric alpha detector for the measurement of surface contamination," *Talk at LRT 2022*, 2022.

[112] A. Barabash *et al.*, "The BiPo-3 detector for the measurement of ultra low natural radioactivities of thin materials," *Journal of Instrumentation*, vol. 12, no. 06, p. P06002, 2017.

[113] P. Loaiza *et al.*, "The BiPo-3 detector," *Appl. Rad. and Isot.*, vol. 123, p. 54, 2017.

[114] D. Q. Adams, "CUORE Opens the Door to Tonne-scale Cryogenics Experiments ," *Prog. Part. Nucl. Phys.*, vol. 122, no. 103902, 2021.

[115] C. Alduino *et al.*, "The projected background for the CUORE experiment ," *Eur. Phys. J. C*, vol. 77, no. 543, 2017.

[116] D. Poda, "Scintillation in Low-Temperature Particle Detectors ," *Physics*, vol. 3, no. 3, p. 473, 2021.

[117] P. Lecoq, A. Annenkov, A. Gektin, C. Korzhik, and Pedrini, *Inorganic Scintillators for Detector Systems*. Springer, 2006.

[118] M. Barucci, J. W. Beeman, V. Caracciolo, L. Pagnanini, L. Pattavina, G. Pessina, S. Pirro, C. Rusconi, and K. Schäffner, "Cryogenic light detectors with enhanced performance for rare event physics," *Nucl. Instrum. Meth. A*, vol. 935, pp. 150–155, 2019.

[119] P. N. Luke, "Voltage-assisted calorimetric ionization detector," *J. Appl. Phys.*, vol. 64, p. 6858, 1988.

[120] V. Kozlov *et al.*, "A detection system to measure muon-induced neutrons for direct dark matter searches," *Astroparticle Physics*, vol. 34, no. 2, pp. 97–105, 2010.

[121] A. Benoit *et al.*, "First results of the EDELWEISS WIMP search using a 320-g heat-and-ionization Ge detector," *Phys. Lett. B*, vol. 513, pp. 15–22, 2001.

[122] E. Armengaud *et al.*, "Final results of the EDELWEISS-II WIMP search using a 4-kg array of cryogenic germanium detectors with interleaved electrodes," *Phys. Lett. B*, vol. 702, pp. 329–335, 2011.

[123] E. Armengaud *et al.*, "Background studies for the EDELWEISS dark matter experiment," *Astropart. Phys.*, vol. 47, pp. 1–9, 2013.

[124] A. Rakhimov, V. Brudanin, D. Filosofov, P. Loaiza, G. Marinov, A. Mirsagatova, D. Medvedev, N. Mukhamedshina, S. Rozov, I. Sadikov, G. Warot, and E. Yakushev, "Neutron activation analysis of polyethylene from neutron shield of EDELWEISS experiment," *Radiochimica Acta*, vol. 103, no. 9, pp. 673–678, 2015.

[125] E. Armengaud *et al.*, "Constraints on low-mass WIMPs from the EDELWEISS-III dark matter search," *Journal of Cosmology and Astroparticle Physics*, vol. 2016, p. 019, may 2016.

[126] C. Augier *et al.*, "Final results on the $0\nu\beta\beta$ decay half-life limit of ^{100}Mo from the CUPID-Mo experiment," *Eur. Phys. J. C*, vol. 82, no. 11, p. 1033, 2022.

[127] E. Armengaud *et al.*, "New Limit for Neutrinoless Double-Beta Decay of ^{100}Mo from the CUPID-Mo Experiment," *Phys. Rev. Lett.*, vol. 126, no. 18, p. 181802, 2021.

[128] M. Mirea, T. Pahomi, and S. Stoica, "Values of the phase space factors involved in double beta decay," *Rom. Rep. Phys.*, vol. 67, no. 3, p. 872, 2015.

[129] L. S. Song, J. M. Yao, P. Ring, and J. Meng, "Nuclear matrix element of neutrinoless double-β decay: Relativity and short-range correlations," *Phys. Rev. C*, vol. 95, no. 2, p. 024305, 2017.

[130] J. Barea, J. Kotila, and F. Iachello, "$0\nu\beta\beta$ and $2\nu\beta\beta$ nuclear matrix elements in the interacting boson model with isospin restoration," *Phys. Rev. C*, vol. 91, no. 3, p. 034304, 2015.

[131] P. K. Rath, R. Chandra, K. Chaturvedi, P. Lohani, P. K. Raina, and J. G. Hirsch, "Neutrinoless $\beta\beta$ decay transition matrix elements within mechanisms involving light Majorana neutrinos, classical Majorons, and sterile neutrinos," *Phys. Rev. C*, vol. 88, no. 6, p. 064322, 2013.

[132] P. K. Rath, R. Chandra, K. Chaturvedi, and P. K. Raina, "Nuclear Transition Matrix Elements for Double-β Decay Within PHFB Model," *Front. in Phys.*, vol. 7, p. 64, 2019.

[133] P. Pirinen and J. Suhonen, "Systematic approach to β and $2\nu\beta\beta$ decays of mass $a = 100 - -136$ nuclei," *Phys. Rev. C*, vol. 91, p. 054309, 2015.

[134] N. López Vaquero, T. R. Rodríguez, and J. L. Egido, "Shape and pairing fluctuations effects on neutrinoless double beta decay nuclear matrix elements," *Phys. Rev. Lett.*, vol. 111, no. 14, p. 142501, 2013.

[135] C. Augier *et al.*, "The background model of the CUPID-Mo $0\nu\beta\beta$ experiment," *Eur. Phys. J. C*, vol. 83, no. 7, p. 675, 2023.

[136] O. Niţescu, R. Dvornický, S. Stoica, and F. Šimkovic, "Angular Distributions of Emitted Electrons in the Two-Neutrino $\beta\beta$ Decay," *Universe*, vol. 7, no. 5, p. 147, 2021.

[137] L. Coraggio, N. Itaco, G. De Gregorio, A. Gargano, R. Mancino, and F. Nowacki, "Shell-model calculation of ^{100}Mo double-β decay," *Phys. Rev. C*, vol. 105, no. 3, p. 034312, 2022.

[138] L. Coraggio and G. D. Gregorio, 2023. Personal communication.

[139] C. Alduino *et al.*, "The CUORE cryostat: An infrastructure for rare event searches at millikelvin temperatures," *Cryogenics*, vol. 102, pp. 9–21, 2019.

[140] K. Alfonso *et al.*, "A first test of CUPID prototypal light detectors with NTD-Ge sensors in a pulse-tube cryostat," *JINST*, vol. 18, no. 06, p. P06033, 2023.

[141] B. S. Neganov and V. N. Trofimov, "Colorimetric method measuring ionizing radiation," *Otkryt. Izobret.*, vol. 146, p. 215, 1985.

[142] O. Azzolini *et al.*, "Background identification in cryogenic calorimeters through $\alpha - \alpha$ delayed coincidences," *Eur. Phys. J. C*, vol. 81, no. 8, p. 722, 2021.

[143] E. Armengaud *et al.*, "Development and underground test of radiopure ZnMoO4 scintillating bolometers for the LUMINEU $0\nu2\beta$ project," *Journal of Instrumentation*, vol. 10, no. 05, p. P05007, 2015.

[144] K. Alfonso *et al.*, "Optimization of the first CUPID detector module," *Eur. Phys. J. C*, vol. 82, no. 9, p. 810, 2022.

[145] D. Poda and A. Giuliani, "Low background techniques in bolometers for double-beta decay search," *Int. J. Mod. Phys. A*, vol. 32, no. 30, p. 1743012, 2017.

[146] J. Allison *et al.*, "Recent developments in Geant4," *Nuclear Instruments and Methods in Physics Research A*, vol. 835, p. 186, 2016.

[147] C. Augier *et al.*, "The background model of the CUPID-Mo $0\nu\beta\beta$ experiment," *Eur. Phys. J. C*, vol. 83, no. 7, p. 675, 2023.

[148] E. Armengaud *et al.*, "Performance of the EDELWEISS-III experiment for direct dark matter searches," *Journal of Instrumentation*, vol. 12, p. P08010, aug 2017.

[149] V. Grigorieva *et al.*, "Li2MoO4 Crystals Grown by Low-Thermal-Gradient Czochralski Technique," *Journal of Materials Science and Engineering B*, vol. 7, 04 2017.

[150] J. J. Back and Y. A. Ramachers, "ACTIVIA: Calculation of Isotope Production Cross-sections and Yields," *Nucl. Instrum. Meth.*, vol. A586, pp. 286–294, 2008.

[151] D. Chernyak, *Development of cryogenic low background detector based on enriched zinc molybdate crystal scintillators to search for neutrinoless double beta decay of ^{100}Mo*. PhD thesis, CSNSM, Orsay, 2015.

[152] F. A. Danevich *et al.*, "Status of LUMINEU program to search for neutrinoless double beta decay of ^{100}Mo with cryogenic $ZnMoO_4$ scintillating bolometers," *AIP Conf. Proc.*, vol. 1686, no. 1, p. 020007, 2015.

[153] A. Barabash, "Precise half-life values for two-neutrino double-β decay: 2020 review," *Universe*, vol. 6, no. 10, p. 159, 2020.

[154] A. Ahmine *et al.*, "Enhanced light signal for the suppression of pile-up events in Mo-based bolometers for the $0\nu\beta\beta$ decay search.," *Eur. Phys. J. C*, vol. 83, no. 5, p. 373, 2023.

[155] V. Singh *et al.*, "Large area photon calorimeter with Ir-Pt bilayer transition-edge sensor for the CUPID experiment," 10 2022.

[156] F. Alessandria *et al.*, "Validation of techniques to mitigate copper surface contamination in CUORE," *Astroparticle Physics*, vol. 45, pp. 13 – 22, 2013.

[157] C. Alduino *et al.*, "CUORE-0 detector: design, construction and operation," *JINST*, vol. 11, no. 07, p. P07009, 2016.

[158] N. López Vaquero, T. R. Rodríguez, and J. L. Egido, "Shape and pairing fluctuations effects on neutrinoless double beta decay nuclear matrix elements," *Phys. Rev. Lett.*, vol. 111, no. 14, p. 142501, 2013.

[159] F. Šimkovic, A. Smetana, and P. Vogel, "$0\nu\beta\beta$ nuclear matrix elements, neutrino potentials and SU(4) symmetry," *Phys. Rev. C*, vol. 98, no. 6, p. 064325, 2018.

[160] F. F. Deppisch, L. Graf, F. Iachello, and J. Kotila, "Analysis of light neutrino exchange and short-range mechanisms in $0\nu\beta\beta$ decay," *Phys. Rev. D*, vol. 102, no. 9, p. 095016, 2020.

[161] L. Coraggio, N. Itaco, G. De Gregorio, A. Gargano, R. Mancino, and F. Nowacki, "Shell-model calculation of ^{100}Mo double-β decay," *Phys. Rev. C*, vol. 105, no. 3, p. 034312, 2022.

[162] A. Gando *et al.*, "Precision measurement of the ^{136}Xe two-neutrino $\beta\beta$ spectrum in KamLAND-Zen and its impact on the quenching of nuclear matrix elements," *Phys. Rev. Lett.*, vol. 122, no. 19, p. 192501, 2019.